


10-2021

SOLITON BASED ALL-OPTICAL DATA PROCESSING IN WAVEGUIDES

Amaria Javed

Follow this and additional works at: https://scholarworks.uaeu.ac.ae/all_dissertations

 Part of the [Physics Commons](#)

United Arab Emirates University

College of Science

SOLITON BASED ALL-OPTICAL DATA PROCESSING IN
WAVEGUIDES

Amaria Javed

This dissertation is submitted in partial fulfillment of the requirements for the degree of
Doctor of Philosophy

Under the Supervision of Prof. Usama Al Khawaja

October 2021

Declaration of Original Work

I, Amaria Javed, the undersigned, a graduate student at the United Arab Emirates University (UAEU), and the author of this dissertation, entitled "*Soliton Based All-Optical Data Processing in Waveguides*", hereby, solemnly declare that this dissertation is my own original research work that has been done and prepared by me under the supervision of Prof. Usama Al Khawaja, in the College of Science at the UAEU. This work has not previously been presented or published, or formed the basis for the award of any academic degree, diploma or a similar title at this or any other university. Any materials borrowed from other sources (whether published or unpublished) and relied upon or included in my dissertation have been properly cited and acknowledged in accordance with appropriate academic conventions. I further declare that there is no potential conflict of interest with respect to the research, data collection, authorship, presentation and/or publication of this dissertation.

Student's Signature _____


Date 25/02/2022

Copyright © 2021 Amaria Javed
All Rights Reserved

Advisory Committee

1) Advisor: Usama Al Khawaja

Title: Professor

Department of Physics

College of Science

2) Member: Amrane Nouredine

Title: Professor

Department of Physics

College of Science

3) Member: Maamar Benkraouda

Title: Professor

Department of Physics

College of Science

Approval of the Doctorate Dissertation

This Doctorate Dissertation is approved by the following Examining Committee Members:

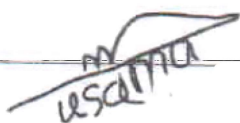
1) Advisor (Committee Chair): Usama Al Khawaja

Title: Professor

Department of Physics

College of Science

Signature _____



Date 26/01/2022

2) Member: Ehab Malkawi

Title: Associate Professor

Department of Physics

College of Science

Signature _____



Date 27/01/2022

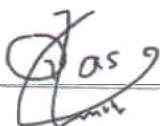
3) Member: Qasem Al Mdallal

Title: Associate Professor

Department of Mathematical Sciences

College of Science

Signature _____



Date 27/01/2022

4) Member (External Examiner): Bakhtiyor Baizakov

Title: Professor

Physical-Technical Institute

Uzbekistan Academy of Sciences, Uzbekistan

Signature _____



Date 28/01/2022

This Doctorate Dissertation is accepted by:

Dean of the College of Science: Professor Maamar Benkraouda

Signature Maamar Benkraouda Date March 14, 2022

Dean of the College of Graduate Studies: Professor Ali Al-Marzouqi

Signature Ali Hassan Date March 14, 2022

Copy _____ of _____

Abstract

The growing demand for higher data processing speed and capacity motivates the replacement of the current electronic data processing by optical data processing in analogy with the successful replacement of electronic data communication by optical data communication. In a quest to achieve a comprehensive optical data processing we aim at using solitons in waveguide arrays to perform all-optical data processing operations. Solitons are special nonlinear waves appreciated for their ability to conserve their shape and velocity before and after scattering. They are observed naturally in diverse fields of science, namely, nonlinear physics, mathematics, hydrodynamics, biophysics and quantum field theory, etc with potential applications in telecommunication systems, routers, switches, multiplexors, logic gates and computers.

The dissertation deals with solitons and we target to design waveguide arrays that allow for useful data processing such as switching, routing, steering, logic gating, unidirectional flow, and ultimately computing. The dissertation is started by characterizing the discrete solitons dynamical behaviour, including their interaction and scattering off potentials, and then exploiting these properties to design the optical data processing devices. Theoretical method such as variational method, and numerical computation has been used to investigate the performance of the designed devices. Chapter 1 provides a brief overview about the topic and shows significance of the study. Chapter 2, is devoted to present a protocol for adding binary numbers using discrete solitons in waveguide arrays where it is shown that the nonlinear interaction between discrete solitons in waveguide arrays can be exploited to design half and full adders. Chapter 3 deals with a protocol to achieve an essential feature of an optical transistor, namely the amplification of input signal with the use of discrete solitons in waveguide arrays. Chapter 4, studies a bound state of two discrete solitons in a two-dimensional waveguide array to investigate the effect of binding on the mobility of the two solitons. Chapter 5 deals with Skyrmion-like topological excitations for a two-dimensional spin-1/2 system mapped to a Manakov system. Chapter 6 is devoted to investigate the dynamics of two component bright-bright (BB) solitons through reflectionless double potential barrier and well in the framework of a Manakov system governed by the coupled nonlinear Schrödinger equations to achieve unidirectional flow. Chapter 7 provides a protocol for the quantum controlled-NOT gate which is based on two qubits operation by investigating the soliton scattering through a reflectionless potential well in an optical system. This protocol demonstrates the prospect of soliton scattering by a potential well for quantum information processing. Chapter 8 concludes the whole learned lessons and future directions of research.

We believe that this dissertation is an important contribution to the effort made towards the realization of optical devices in achieving a soliton based all-optical data processing.

Keywords: Solitons, Discrete solitons, Optical solitons, Waveguide arrays, All-optical data processing, All-optical devices.

Title and Abstract (in Arabic)

معالجة البيانات الضوئية المعتمدة على سوليتون في الموجات

الملخص

يحفز الطلب المتزايد على سرعة وسعة معالجة البيانات الأعلى على استبدال معالجة البيانات الإلكترونية الحالية بمعالجة البيانات الضوئية بالتماثل مع الاستبدال الناجح لاتصالات البيانات الإلكترونية عن طريق اتصالات البيانات الضوئية. في محاولة لتحقيق معالجة شاملة للبيانات الضوئية ، نهدف إلى استخدام solitons في مصفوفات الدليل الموجي لأداء جميع عمليات معالجة البيانات الضوئية. Solitons هي موجات غير خطية خاصة تُقدر لقدرتها على الحفاظ على شكلها وسرعتها قبل وبعد التشتت. يتم ملاحظتها بشكل طبيعي في مجالات متنوعة من العلوم ، وهي الفيزياء غير الخطية والرياضيات والديناميكا المائية والفيزياء الحيوية ونظرية المجال الكمومي وما إلى ذلك مع التطبيقات المحتملة في أنظمة الاتصالات والموجهات والمفاتيح ومضاعفات الإرسال والبوابات المنطقية وأجهزة الكمبيوتر.

تتعامل الأطروحة مع solitons ، ونستهدف تصميم مصفوفات الدليل الموجي التي تسمح بمعالجة البيانات المفيدة مثل التبديل والتوجيه والتوجيه والبوابة المنطقية والتدفق أحادي الاتجاه والحوسبة في النهاية. تبدأ الرسالة من خلال توصيف السلوك الديناميكي للسولتون المنفصل ، بما في ذلك تفاعلها ، وتشتت الإمكانات ، ثم استغلال هذه الخصائص لتصميم أجهزة معالجة البيانات الضوئية. تم استخدام الطريقة النظرية مثل طريقة التباين والحساب العددي للتحقق من أداء الأجهزة المصممة. يقدم الفصل الأول لمحة موجزة عن الموضوع ويوضح أهمية الدراسة. تم تخصيص الفصل 2 لتقديم بروتوكول لإضافة أرقام ثنائية باستخدام solitons المنفصلة في مصفوفات الدليل الموجي حيث نوضح أنه يمكن استغلال التفاعل غير الخطي بين solitons المنفصلة في مصفوفات الدليل الموجي لتصميم إضافة نصف وكاملة. يتعامل الفصل 3 مع بروتوكول لتحقيق ميزة أساسية للترانزستور البصري ، ألا وهي تضخيم إشارة الدخل باستخدام solitons المنفصلة في مصفوفات الدليل الموجي. الفصل 4 يدرس حالة منظمة لاثنتين من السولتونات المنفصلين في مصفوفة دليل موجي ثنائي الأبعاد لاستقصاء تأثير الارتباط على حركية السولتونات. يتعامل الفصل 5 مع الإثارات الطوبولوجية الشبيهة بـ Skyrmion لنظام ثنائي الأبعاد تدور -1 / 2 تم تعيينه لنظام ماناكوف. تم تخصيص الفصل 6 لدراسة ديناميكيات مكونين من السوليتون الساطع الساطع (BB) من خلال حاجز مزدوج محتمل غير عاكس وبئر في إطار نظام ماناكوف تحكمه معادلات شرودنجر غير الخطية المقترنة لتحقيق تدفق أحادي الاتجاه. يوفر الفصل 7 بروتوكولاً للبوابة التي يتم التحكم فيها كمياً - NOT والتي تستند إلى عملية اثنتين كيوبت من خلال التحقيق في تشتت السوليتون من خلال بئر محتمل غير عاكس في نظام بصري. يوضح هذا البروتوكول احتمالية تشتت soliton بواسطة بئر محتمل لمعالجة المعلومات الكمية. الفصل 8 يختتم الدروس المستفادة بأكملها والتوجهات المستقبلية للبحث. نعتقد أن هذه الرسالة هي مساهمة مهمة في الجهد المبذول نحو تحقيق الأجهزة البصرية في تحقيق معالجة البيانات الضوئية القائمة على السوليتون.

مفاهيم البحث الرئيسية: solitons ، solitons المنفصلة ، solitons الضوئية ، صفائف الدليل الموجي ، معالجة البيانات الضوئية بالكامل ، جميع الأجهزة البصرية.

Acknowledgements

It is a pleasure to thank my mentor Prof. Usama Al Khawaja, for introducing me to the Soliton and Nonlinear Optics. His encouragement and support throughout this project is greatly appreciated. I would also like to thank the Nonlinear Physics research group for the many helpful talks and seminars which benefited my work.

I would also like to thank all the faculty members of Department of Physics, College of Science, College of Graduate Studies (CGS) at UAEU, and the coordinator of PhD program for their support and cooperation during my study.

It has been great pleasure working with several colleagues. Special thanks to all of my research fellows, departmental staff and administrative personnel at UAEU.

Finally, I would like to express my utmost gratitude to my parents, family members, and friends for their patience, persistent support, and love.

Dedication

To my beloved husband 'Waqar', and my lovely kids 'Shayan' and 'Hania'

Table of Contents

Title	i
Declaration of Original Work	ii
Copyright	iii
Advisory Committee	iv
Approval of the Doctorate Dissertation	v
Abstract	vii
Title and Abstract (in Arabic)	ix
Acknowledgments	x
Dedication	xi
Table of Contents	xii
List of Tables	xv
List of Figures	xvi
List of Abbreviations	xx
Chapter 1: Introduction	1
1.1 Overview	1
1.2 Aim and Objectives	2
1.3 Literature Review	3
1.4 Research Methodology	10
1.4.1 Analytical Tools	10
1.4.2 Numerical Techniques	12
1.5 Structure of the Dissertation	16
Chapter 2: Logic Gates and Adders	20
2.1 Introduction	20
2.2 Theoretical Framework and Setup	21
2.3 The XOR Gate	24
2.3.1 The OR Gate	24
2.3.2 The XOR Gate: A Modified OR Gate	27
2.4 One-bit Half Adder and Full Adder	31

2.5 Conclusion	34
Chapter 3: Optical Amplifier	35
3.1 Introduction	35
3.2 Theoretical Model	36
3.3 Results and Discussion	39
3.3.1 Reflectionless Potential	39
3.3.2 Modulated Potential	41
3.4 Conclusion	43
Chapter 4: Discrete Soliton Molecules	45
4.1 Introduction	45
4.2 Model Equation	46
4.3 Equilibrium Width and Energy: Numerical Solution	47
4.4 Variational Calculation	50
4.4.1 Equilibrium Width and Energy	52
4.4.2 Characteristics of PN Potential	55
4.4.3 Soliton-Soliton Interaction	56
4.5 Anisotropic Waveguide Arrays	58
4.5.1 Equilibrium Profiles and Mobility	58
4.5.2 Formation of Soliton Molecule	59
4.5.3 Soliton Fission	64
4.6 Conclusions	66
Chapter 5: Mapping the Spin-1/2 System to 2D Manakov System	67
5.1 Introduction	67
5.2 Two-Dimensional Skyrmions	68
5.3 Mapping the Spin-1/2 System to 2D Manakov System	73
5.4 Solving the Manakov System	74
5.4.1 Similarity Transformation	74
5.4.2 Power Series Method	76
5.4.3 Numerical Solutions	78
5.5 Stability of the Non-Trivial Skyrmions	82
5.6 Conclusion	86
Chapter 6: Unidirectional Flow and Unidirectional Segregation	88
6.1 Introduction	88
6.2 Theoretical Model	89
6.3 Propagation of Bright-Bright Solitons through RM Potential Barriers	92
6.3.1 Unidirectional Flow for Uncoupled Components with $g_{12} = 0$	93

6.3.2 Polarity Reversal in Unidirectional Flow with $g_{12} > 0$	96
6.3.3 Unidirectional Segregation with $g_{12} < 0$	99
6.3.4 Special Case: $g_1 \neq g_2$	106
6.4 Variational Approach Versus Numerical Computation	112
6.5 Results and Discussion	116
Chapter 7: All-Optical Quantum Controlled-NOT Gate	119
7.1 Introduction	119
7.2 Theoretical Framework and Setup	120
7.3 The CNOT Gate Protocol	122
7.4 Discussion and Conclusion	127
Chapter 8: Conclusion and Recommendations	128
References	132
List of Publications	143
Appendices	144
Appendix A: Energy Functional	144
Appendix B: Solutions of the 2D Manakov system	151
Appendix C: Similarity Transformation	152
Appendix D: Asymmetric Gaussian Potential Barriers	154
Appendix E: Equations of Motion	161

List of Tables

Table 5.1:	All possible cases of rotations in the xz -plane.	72
Table 5.2:	All possible cases of rotations in the xy -plane.	72
Table 6.1:	The velocity window for unidirectional flow of composite BB solitons with different coupling strengths for the case of RM potential barriers.	102
Table 7.1:	Truth table for CNOT gate	122
Table D.1:	The velocity window for unidirectional flow of composite BB solitons with different coupling strengths for the Gaus- sian potential barriers.	157

List of Figures

Figure 2.1: Schematic figure representing the OR gate having two potential wells injected with two control solitons.	25
Figure 2.2: Spacio-temporal plots representing the function of OR gate with initial soliton speed $v = 0.22$	27
Figure 2.3: Transport Coefficients of OR gate.	27
Figure 2.4: Spacio-temporal plot representing the free propagation of a signal soliton in the setup of OR gate.	28
Figure 2.5: The effect of the potential wells on the speed of signal soliton in the OR gate.	29
Figure 2.6: Schematic figure for the XOR gate.	30
Figure 2.7: Spacio-temporal plots representing the function of XOR gate.	30
Figure 2.8: Transport Coefficients of XOR gate.	31
Figure 2.9: Profiles for waveguides separation and waveguides coupling.	32
Figure 2.10: Scheme for half adders.	33
Figure 2.11: Scheme for full adders.	33
Figure 3.1: Reflectionless potential (Ideal case): 3D plot representing the dependence of the output intensity, R , on the input intensity, I_{in} , and signal soliton speed, v	40
Figure 3.2: 3D plot representing the dependence of the output intensity, R , on the signal soliton speed, v	41
Figure 3.3: Modulated potential (non-reflectionless potential).	42
Figure 3.4: The relation between the output intensity, R , and the input intensity of control soliton, I_{in}	43
Figure 4.1: Soliton molecule profiles for In-phase and out-of-phase with isotropic waveguide array.	48
Figure 4.2: Soliton molecule profiles for In-phase and out-of-phase with anisotropic waveguide array.	49
Figure 4.3: Comparison between the cross-sections of isotropic and anisotropic in-phase soliton-molecule profile.	50
Figure 4.4: In-phase and out-of-phase isotropic soliton molecules obtained by both numerical and variational method.	52
Figure 4.5: In-phase PN potential for the isotropic case.	53
Figure 4.6: Out-of-phase PN potential for the isotropic case.	54
Figure 4.7: The variational PN potential for separation of solitons.	54
Figure 4.8: The PN potential versus the molecule's position for different solitons separation.	55
Figure 4.9: The PN potential for different orientations.	57

Figure 4.10: The soliton-soliton interaction.	58
Figure 4.11: In-phase PN potential for the anisotropic case and its two cross section profiles.	59
Figure 4.12: Out-of-phase PN potential for the anisotropic case and its two cross section profiles.	60
Figure 4.13: In-phase and out-of-phase anisotropic soliton molecules.	60
Figure 4.14: Soliton molecule in anisotropic PN potential (in-phase).	61
Figure 4.15: Trajectories of the two solitons corresponding to the soli- ton molecule.	62
Figure 4.16: The potential of interaction between two solitons in a soli- ton molecule.	63
Figure 4.17: Splitting of the soliton molecule.	65
Figure 4.18: Trajectories of the two solitons forming the soliton molecule.	66
Figure 5.1: Schematic figure representing the action of the spin rota- tion operator for a maximally symmetric skyrmion.	70
Figure 5.2: Stationary power series solutions with different nodes.	77
Figure 5.3: The numerical solutions of the spinor components.	78
Figure 5.4: In-plane and out-of-plane vector representations of skyrmions in spin-1/2 system.	79
Figure 5.5: The average spin texture modulated by the total density.	80
Figure 5.6: The total density for the case of rotation around ρ in xy - plane with initial spin along z -axis.	81
Figure 5.7: The average spin for a skyrmion in a spin-1/2 system with the rotation around ρ in xy -plane.	83
Figure 5.8: The vector representation of skyrmions in spin-1/2 system for the case of rotation around ρ in xy -plane with initial spin along z -axis.	84
Figure 5.9: The average spin for a skyrmion in a spin-1/2 system with the rotation around ρ in xy -plane with initial spin orienta- tion along y -axis.	85
Figure 5.10: The energy for the case of rotation around y -axis with ini- tial spin along z -axis.	86
Figure 6.1: The Gaussian and Rosen-Morse asymmetric double poten- tial barriers.	91
Figure 6.2: Transport coefficients in terms of velocity for the propaga- tion of the ψ_1 component through asymmetric RM poten- tial barriers.	92
Figure 6.3: Propagation of composite BB soliton through asymmetric RM potential barriers.	94

Figure 6.4: Transmission and reflection coefficients of the component ψ_1 through RM potential barriers versus v and g_{12}	96
Figure 6.5: Propagation of composite BB soliton through asymmetric RM potential barriers for $g_{12} = 0.3$	98
Figure 6.6: Propagation of composite BB soliton through asymmetric RM potential barriers for $g_{12} = 0.325$	100
Figure 6.7: Propagation of composite BB soliton through asymmetric RM potential barriers for $g_{12} = 0.33$	101
Figure 6.8: Borders of velocity window for the unidirectional flow with $g_1 = g_2 = 1$, through the RM potential barriers.	101
Figure 6.9: Reflection coefficients of the components ψ_1 and ψ_2 propagating through RM potential barriers.	104
Figure 6.10: Propagation of components through asymmetric RM potential barriers for $g_{12} = -0.004$	105
Figure 6.11: Reflection and transmission coefficients of the components ψ_1 and ψ_2 propagating through RM potential barriers from $x_0 = -10$	107
Figure 6.12: Reflection and transmission coefficients of the components ψ_1 and ψ_2 propagating through RM potential barriers from $x_0 = 10$	108
Figure 6.13: Unidirectional segregation of composite BB soliton.	108
Figure 6.14: Reflection and transmission coefficients of the components ψ_1 and ψ_2 propagating through RM potential barriers from $x_0 = -10$ with $g_{12} = -0.5$	110
Figure 6.15: Reflection and transmission coefficients of the components ψ_1 and ψ_2 propagating through RM potential barriers from $x_0 = 10$ with $g_{12} = -0.5$	111
Figure 6.16: Bidirectional segregation of composite BB soliton.	111
Figure 6.17: Asymmetric double well potential.	113
Figure 6.18: Unidirectional segregation of composite BB soliton with an agreement between variational and numerical method.	115
Figure 6.19: Analytically calculated transport coefficients in terms of velocity for the propagation of two right moving components through asymmetric double square potential well.	115
Figure 6.20: Analytically calculated transport coefficients in terms of velocity for the propagation of two left moving components through asymmetric double square potential well.	116

Figure 6.21: Numerically calculated transport coefficients in terms of velocity for the propagation of two right moving components through asymmetric double square potential well.	116
Figure 6.22: Numerically calculated transport coefficients in terms of velocity for the propagation of two left moving components through asymmetric double square potential well.	117
Figure 7.1: Schematic figure representing the solitons' scattering implementation of the controlled-NOT gate.	123
Figure 7.2: Transport Coefficients of CNOT gate.	124
Figure 7.3: Density plots for the function of CNOT gate.	125
Figure 7.4: Initial and final profiles of target solitons in the absence and presence of control soliton.	126
Figure A.1: The full and approximate PN potential with $n_{2y}=1$	147
Figure A.2: The full and approximate PN potential with $n_{2x}=1$	147
Figure B.1: Graphical representation of $\psi_1(\rho)$ and $\psi_2(\rho)$ for solution-1.	151
Figure B.2: Graphical representation of $\psi_1(\rho)$ and $\psi_2(\rho)$ for solution-2.	151
Figure D.1: Transport coefficients in terms of velocity for the propagation of the ψ_1 component through asymmetric Gaussian barriers.	154
Figure D.2: Propagation of composite BB soliton through asymmetric Gaussian potential barriers for $g_{12} = 0$	155
Figure D.3: Transmission and reflection coefficients of the component ψ_1 through Gaussian barriers.	156
Figure D.4: Propagation of composite BB soliton through asymmetric Gaussian potential barriers for $g_{12} = 0.3$	156
Figure D.5: Propagation of composite BB soliton through asymmetric Gaussian potential barriers for $g_{12} = 0.315$	158
Figure D.6: Propagation of composite BB soliton through asymmetric Gaussian potential barriers for $g_{12} = 0.317$	159
Figure D.7: Borders of velocity window for the unidirectional flow through the Gaussian potential barriers.	159
Figure D.8: Reflection coefficients of the components ψ_1 and ψ_2 propagating through Gaussian potential barriers.	160

List of Abbreviations

AL	Ablowitz-Ladik
BB	Bright-Bright
CNOT	Controlled-NOT
DNLSE	Discrete Nonlinear Schrödinger Equation
FEM	Finite Element Method
LVM	Lagrangian Variational Method
NLSE	Nonlinear Schrödinger Equation
PN	Peierls-Nabarro
PT	Pöschl-Teller
RM	Rosen-Morse
SSFM	Split Step Fourier Method

Chapter 1: Introduction

1.1 Overview

Solitons are localized solitary waves which have very special properties such as a) they propagate at constant speed without change in their shape, b) they are extremely robust to perturbations, and in particular to collisions with small amplitude linear waves and c) they are even stable with respect to collisions with other solitons. When two solitons collide, they pass through each other and emerge with their original speed and shape after the interaction. It is to be noted that the interaction is not a simple superposition of the two waves. Moreover, after the collision, the trajectories of the two waves will be shifted with respect to the trajectories without the collision. In other words, the outcome of the collision of two solitons is only a simple phase shift of individual waves [3, 2, 1].

In addition to the soliton in telecommunications, they also find application in the construction of optical splitters, routers and switches [4, 5, 6, 7]. In case of optical switches, the propagation of one optical pulse affects the other, the ‘signal’ pulse by the ‘control’ pulse. Here it behaves like the control pulse opening a gate for a signal pulse, so as to allow it to pass through. Photonic logic gates operate on this principle. Hence, logic gates can also be realized using solitons. In medicine, they are recently applied in neuroscience to describe the signal transfer between the cell membranes [8]. Solitary type solutions are also used to explore the minute suspended particles in the dusty plasmas [9]. Also, topological type of solitons also found to occur in different parts of super gravity as well as string theory to investigate the defects in cosmic strings and domain walls [10]. They also found to occur in fluid dynamics and exploited to understand the sophisticated and complicated rogue wave dynamics [11]. They also paved the way for the rapid development in the field of Bose-Einstein condensates for the creation of 2D and 3D solitary waves for higher order nonlinear system [12].

Other very important applications of optical solitons are generating ultrashort pulses through pulse compression technique. Ultrashort pulses are needed in many branches of science, which have been using nanosecond and picosecond pulses. Optical solitons help in the generation of ultrashort pulses through pulse compression technique in fiber [13]. An optical sensor based on Kerr induced phase shift is also developed for measurement of pressure, speed, temperature and intensity [14].

1.2 Aim and Objectives

We aim at using solitons in waveguide arrays to perform all-optical data processing operations. To the applied level, we target to design waveguide arrays that allow for useful data processing such as switching, routing, steering, logic gating, unidirectional flow, and ultimately computing. The dissertation is started by characterizing the discrete solitons dynamical behaviour, including their interaction and scattering off potentials, and then exploiting these properties to design the optical data processing devices. Theoretical method such as variational method, and numerical computation has been used to investigate the performance of the designed devices.

The major challenge is to design devices that perform logic gating, diode behaviour, transistor, and ultimately lead to data processing including filtering, routing, and computation. The devices have to be robust against the different kinds of perturbations in real systems such as all kinds of noise, imperfections in the array, energy losses, etc.

Specifically, we use the idea of modulating the coupling, dispersion, and nonlinearity of the waveguides to manipulate the solitons dynamics. This dissertation is distinguished by: i) the focus on soliton-soliton interaction and soliton-potential interaction, ii) the utilization of the solitons dynamics in designing clear and realistic optical components for all-optical technologies. In addition, the unique feature of solitons dispersionless propagation is favorable for designing optical instruments that control the data in a network. This is the main reason that we consider solitons in this dissertation.

There are many fundamental issues involved including the quantum effects of the solitons' dynamics. Unlike classical transport, the phase of the soliton plays here an important role in, for instance, creating an effective repulsive force between colliding solitons, the low-velocity quantum reflection from an attractive potential well, the quantum reflection from surfaces, the nonlinear soliton tunneling and soliton ejection, and the resonant tunneling in potential barriers and wells. All of these phenomena are of valuable importance for the advancement of our understanding of the quantum nature of such macroscopic objects.

There are important technological applications that exploit the novel nonclassical features of solitons. Due to their dispersionless nature, optical solitons have proven to be a reliable, robust, and efficient data communication and memory storage systems. In addition, solitons can be used as ultrafast clean optical switches, logic gates, and optical routers which are essential for optical communication networks and quantum computation. In comparison with electronic components, all-optical operations are much faster and more efficient. Although soliton-soliton and soliton-impurity interaction is a well-studied subject, much less is known about designing all optical components for data processing. In summary, the topics addressed by this dissertation are of both fundamental depth and important technological impact.

1.3 Literature Review

Solitons appear in diverse fields of science and engineering, most importantly in nonlinear physics, data communication systems, biophysics, hydrodynamics, quantum field theory, etc., owing to their invariant shape and velocity, before and after collisions [15]. In optical systems, they manifest themselves as 'optical solitons', realized through a delicate balance between nonlinearity and dispersion/diffraction which play an indispensable role in long haul communications systems, data processing devices, switching devices, routers and computers [16, 17, 18, 19, 20]. In order to realize these functionalities, diverse configurations, namely, photonic circuitry [21], silicon-on-silicon waveguides [22],

X-junctions [23], fused-fiber couplers [24], liquid crystals [25, 26], nonlinear waveguide arrays [27, 28], Mach-Zehnder interferometer [29], etc., [30, 31, 32, 33, 34, 35] have been proposed.

The increasing demand on higher speed and capacity of data processing motivates replacing current electronic data processing by optical data processing in an analogy with the successful replacement of electronic data communication by optical data communication [16, 17, 18, 19]. In a quest to achieve a comprehensive optical data processing, many of the main ingredients have been already proposed in the literature considering various setups [21, 22, 23, 24, 25, 26, 27, 28, 29, 30, 31, 32]. Prominent among these is discrete solitons in waveguide arrays [21, 22]. Optical solitons have been suggested as data carriers due to their unique feature of preserving their integrity over long distances of propagation and their particle-like inelastic scattering with each other and with external potentials [36, 37, 38, 39, 40]. Discrete solitons are also characterised by this appealing feature. In addition, the propagation of discrete solitons in waveguide arrays can be most feasibly controlled through the dispersion or nonlinearity management [41, 42]. Dispersion management is achieved by varying the separations between the waveguides resulting in an effective potential [43]. The profile of separations' variations can be set such that a particular type of reflectionless potential is realized [41]. In such a case, the soliton will scatter off the potential elastically with minimized radiation losses. This results in clean particle-like soliton scattering. The nonlinear interaction together with the dispersion management allow for a host of setups where various data processing components can be devised. For instance, unidirectional flow has been shown to exist in waveguide arrays with dispersion management [43] and nonlinearity management [44] in a similar manner as for the continuum cases in optical fibers with double potential wells [45], PT-symmetric potentials [46], and nonlinearity management [47].

Discrete solitons were shown to exist in arrays of coupled waveguides [48, 49] exhibiting unique behaviour in contrast with their continuum counterparts. This was revealed

through a number of phenomena [50, 51, 52, 50, 53, 54, 55, 56, 57, 58]. Prominent among these is the dissipative flow due to the presence of the Peierls-Nabarro (PN) effective potential [54, 55, 56, 57]. Due to its crucial effect on the solitons' stability and dynamics, the height and profile of the PN potential were extensively investigated by many authors [55]. Interest in discrete solitons was then boosted by their application in the all-optical operations [59]. The experimental observation of discrete solitons in two-dimensional (2D) optically-induced nonlinear photonic lattices [60], stimulated further interest due to the additional advantages brought by the dimensionality [61, 62, 63]. Three fundamental types of 2D stationary solitons were found, namely the site-centred, bond-centred, and hybrid solitons [64]. Recently, we have shown that with anisotropic waveguide arrays the hybrid soliton splits into two types named as hybrid-X and hybrid-Y solitons [65]. We have also shown that anisotropy enhances greatly on the mobility of discrete solitons. In general, two dimensional discrete solitons exhibit poor or no mobility due to their strong pinning by the PN potential. Several ideas have been proposed to enhance the mobility for both one-dimensional [66] and two-dimensional [67] waveguide arrays including also modulated nonlinearity [68], defects [69], PT symmetric couplers [70], etc. The binding mechanism between solitons in optical fibres is a subject of interest from both the fundamental and applied point of views due to the increase of data rates in optical telecommunication [71]. Similarly, it is interesting to investigate the possibility of forming a bound state of two solitons in 2D waveguide arrays.

The vector nonlinear Schrödinger equation (NLSE) describes spinor systems and the interaction between its field components. The model has also various applications in different areas of physics, for instance, the propagation of electromagnetic waves with arbitrary polarization in a self-focusing media [72], and the evolution of waves in plasma [73]. It is also shown [74] that the vector NLSE governs the average dynamics of dispersion-managed solitons which are considered as a key element for optical communication. The soliton robustness to polarisation-mode dispersion has a strong dependence on both chromatic dispersion and soliton energy [75]. It is known that the two-component vector

NLSE or the Manakov system is completely integrable and is solvable by the inverse scattering transform (IST) method. Recently, Manakov spatial solitons were observed in AlGaAs planar waveguides [76]. More recently, the Si-based waveguides using similar phenomena are served as optical biosensors [77]. The similarity reductions of the 2D coupled NLSE have been studied by Lie's method. It is shown that the 2D coupled NLSE is reduced to the 1D-NLSE by the similarity transformations [78]. The theoretical investigation for the evolution of and interaction between collective excitations in the two-dimensional NLSE was numerically studied by using shooting method and split-step Fourier method as well as the modulation instability method [79]. The analytical bright one- and two-soliton solutions of the (2+1)-dimensional coupled NLSE under certain constraints were presented in [80] by employing the Hirota method. Hirota method was also applied on the mixed-type solitons for a (2+1)-dimensional N -coupled nonlinear Schrödinger system in nonlinear optical-fiber communication [81]. The exact soliton solutions for the (2+1)-dimensional coupled higher-order NLSE in birefringent optical-fiber communication is given in [82]. The dynamical evolution of two-component Bose-Einstein condensates trapped in cylindrical well is numerically investigated by solving the coupled Gross-Pitaevskii equations and different numbers of unstable ring dark (gray) solitons were generated [83]. The study of dark-bright (DB) ring solitons in two-component Bose-Einstein condensates is conducted in [84]. The Newton relaxation method was used in [85] to obtain stationary discrete vector solitons in two-dimensional nonlinear waveguide arrays. These results may also be applicable to two-component Bose-Einstein condensates trapped in a two-dimensional optical lattice. The two dimensional discrete solitons in optically induced nonlinear photonic lattices were observed in [86]. The homotopy analysis method was also used to solve cubic and coupled nonlinear Schrödinger equations [87]. The interaction of optical beams with arbitrary polarizations in self-focusing media is studied in [88] by using the direct scattering problem. Their physical schemes deal with spatial solitons, and the dynamics is formally described by the initial value problem for the Manakov system. The ferromagnetic Bose-Einstein condensate allows for pointlike topological excitations, i.e., skyrmions [89]. The stability of

skyrmions in a fictitious spin-1/2 condensate is investigated in [90]. The monopoles in an antiferromagnetic Bose-Einstein condensate and their static and dynamic properties were shown in [91]. Topological protection of photonic mid-gap defect modes is demonstrated in [92]. The description of topological phase transitions in photonic waveguide arrays is discussed in [93].

The evolution and scattering of solitons through various external scattering potentials, namely, walls or barriers [94, 95, 96, 97, 98, 99, 100], steps [101, 102, 103, 104, 105, 106, 107], wells [108, 109, 110], and surfaces [111, 112] necessitates the nonlinear interaction and wave nature of the solitons. Optimal channelization of such potentials allow the possibility to procure soliton based switches, signal processing devices, routers, and diodes [21, 27, 113, 45]. Diverse studies in nonlinear materials also reported enhancing the nonlinear properties for applications in photonic devices, optoelectronics and optical amplifier [114, 115, 116]. Nonlinear control and soliton management, employing complex Ginzburg-Landau equation has been investigated for diverse nonlinear systems to explore their role on the transmission speed, pulse width and period of the solitons [117, 118, 119, 120, 121]. Analytical form for an external potential has been used to investigate the possibility of stable solitonic propagation regimes as well as an unstable regime, where the initial soliton profile decays to breathing decaying solitons [122]. Two-dimensional self-trapped optical waves in the presence of Laguerre-Gaussian and harmonic potentials were also investigated considering the closed-form expressions for the soliton solutions and the conservation laws for the norm and the Hamiltonian. The nonlinear modes obtained are found to be stable below a certain threshold norm value [123]. Further, the parameter which allows controllability of the solitonic properties in PT-symmetric Mathieu lattices, namely, shape, dynamics and stability has also been pointed out for efficient light control [124]. Recently, the unidirectional flow of bright solitons through a specific combination of asymmetric potential wells was demonstrated where transmission of solitons were defined by the critical velocity, below which reflection dominates [45]. Moreover, such special flow of solitons were also found to occur in

the solitons scattering through the parity-time symmetric potentials. The physics behind such phenomenon was found to be related to an energy exchange interaction that occurred between the soliton internal modes and its center of mass dynamics during unidirectional scattering [46]. Furthermore, Reference [43] predicted the realization of such unidirectional flow through photonic waveguide arrays with two asymmetric potential wells by appropriate modulation of the coupling coefficients. In this line of research, [125] realized the discrete version of this problem and accomplished the discrete solitons based operation of all-optical logic gates, switches, filters and optical diodes through suitable adjustment of a control soliton power in the waveguide arrays with an effective potential. A detailed study describing the interplay between the bound states of the potential well and incident soliton revealed the insignificance of trapping on the unidirectional flow of the solitons. Moreover, it hints to the origin of the unidirectional flow as being related to the excitation of breathing modes in the scattering region [47].

Recently, the atomic interactions in a two-component Bose-Einstein condensate through the propagation of vector two solitons like matter waves passing across a Gaussian barrier were investigated [126]. This study reported the importance of the interspecies interactions which allows the wave packet to propagate like a breather. Also, elaborated the role of the interspecies interaction, relative velocity, barrier and relative phase on the collision dynamics. Furthermore, the splitting of composite solitons scattering through a narrow potential barrier were proposed for designing a two-component soliton interferometer in presence of self-attraction and cross-attraction between the components. This analysis identified the existence of substantial parameter range over which one component undergoes full transmission through the barrier, while the other one undergoes full reflection [127]. Additionally, the diode functionality has also been realized through diverse nonlinear discrete lattices, such as a layered nonlinear, non-mirror-symmetric model [128], two parallel-coupled discrete nonlinear Schrödinger inhomogeneous chains [129], and nonlinear lattice with asymmetric defects [130]. Further numerical and analytical investigations reported the significance of the scattering of solitons as well as plane waves through the

localized nonlinear potentials to account for the best operational regimes of the interferometer [131]. The one-dimensional model for a cavity equipped with saturated gain and Kerr nonlinearity has also been investigated to sustain the state of shuttle motion of the solitons [132].

Lastly, the promise of tremendous computational power, coupled with the development of robust error-correcting schemes [133], has fuelled extensive efforts [134] to build a quantum computer. The requirements for realizing such a device are confounding: scalable quantum bits (two-level quantum systems, or qubits) that can be well isolated from the environment, but also initialized, measured and made to undergo controllable interactions to implement a universal set of quantum logic gates [135]. The usual set consists of single qubit rotations and a controlled-NOT (CNOT) gate, which flips the state of a target qubit conditional on the control qubit being in the state 1.

In this dissertation, we also achieve an unambiguous numerical demonstration and comprehensive implementation of quantum CNOT operation in an optical system where we consider soliton scattering by a reflectionless potential well. In particular, the interactions of solitons through different external scattering potentials, namely, potential barriers [94, 95, 96, 97, 98, 99, 100], step potentials [101, 102, 103, 104, 105, 106, 107], potential wells [108, 109, 110], and surfaces [111, 112] demand the interplay of nonlinearity and waveform of the solitons. Through suitable engagement of these potentials with selective parameters allowed the implementation of the logic gates, switches, signal processing devices and diodes [21, 27, 113, 45]. Through the optical soliton switches, a function for controlled-NOT (CNOT) gate has been proposed through logic gates conversion using reversible logic elements [136]. Through the optical soliton switches, a function for controlled-NOT (CNOT) gate has been proposed through logic gates conversion using reversible logic elements [136]. The difficulty in achievement of optical quantum computing with two-photon interactions via a two qubit gate through quantum phase gate, has been also addressed (although considerable progress has been made in the cavity quan-

tum electrodynamics systems, the field transformation is considered only through a simple model [137]). The collisions of the Manakov solitons in a nonlinear system allowed the description of a polarization state through linear fractional transformations, where a sequence of solitons operates on other sequences. Such collisions of solitons allowed the realization of diverse logic gates including CNOT gates. Such a study is found to be fruitful for implementing quantum computation in the bulk nonlinear medium with self-restoring as well as reusable qualities, without interconnecting components [138].

Further considerable efforts have been made to achieve collision based computing in diverse substrates involving, physical, chemical and biological systems, where there exists localization [139]. Furthermore, the possibility of quantum logic through the numerical investigation of the vector solitons collision is demonstrated, where the qubit is defined by the polarization of a vector soliton and its state change is determined through colliding with a register soliton [140]. Conversely, the simulated quantum logic is not completely error-free, owing to the variation in the system parameters during propagation. A further study, offered an algorithm for minimizing the information processing error in diverse situations and two soliton transmission lines [141, 142].

1.4 Research Methodology

1.4.1 Analytical Tools

In order to gain physical insight of optical pulse dynamics through the guiding medium, many of the researchers mostly relied on numerical methods and analytical techniques like the Lagrangian variational method (LVM) [1], Hamiltonian method [143], projection operator method (POM) [144, 145], non-Lagrangian collective variable (CV) approach [146], CV technique [147] and the moment method [1] to study the pulse dynamics in fiber systems of various pulse parameters with respect to the fiber parameters. The LVM was first introduced for solitons in plasma physics and it was applied in optical fibers to estimate interaction length and to find the solution of optical beam propagation described

by the NLS equation [148]. In the variational methods, a variational functional is formulated; the minimization based on Ritz-optimization procedure gives rise to a set of Euler-Lagrange equations, which are then solved numerically. The CV treatment reduces the dynamics of the pulse field, which involves an infinite number of degrees of freedom, to the dynamics of a simple mechanical system having only a few degrees of freedom, each called a collective variable, which could be then associated with a relevant physical parameter of the pulse. The achievement of this approach results in the possibility of transforming the partial differential equation for the original field into a set of ordinary differential equations (ODEs) for the collective variables. Among the aforementioned techniques, we have chosen the LVM to investigate the pulse propagation in fiber. Hence, a short description of this method will be provided.

1.4.1.1 Lagrangian Variational Method

The variational method was first applied to the NLSE by Anderson and that for coupled NLSE by Pare to derive the first order dynamical equations [149, 150]. From suitable input trial wave function and by employing a Ritz optimization procedure, approximate dynamical solutions are obtained for the evolution of pulse parameters during propagation. The results obtained by using Lagrangian formulation was in good agreement with that achieved from inverse scattering techniques and numerical methods. Hence, LVM has been used obtaining dynamical equations to explore the physical insight of the system. The dynamical equations for the pulse parameters of an optical pulse propagating through fiber governed by NLSE can be obtained by employing LVM as follows. The Lagrangian for the NLSE is provided by

$$L = \frac{1}{2} \left(U \frac{\partial U^*}{\partial z} - U^* \frac{\partial U}{\partial z} \right) + \frac{i\beta_2}{2} \left| \frac{\partial U}{\partial T} \right|^2 - \frac{i\gamma}{2} |U|^4 \quad (1.1)$$

considering the suitable input wave function $U(z, T)$. For our illustration, we consider the Gaussian pulse of the following form;

$$U(z, T) = A(z) \exp(-\rho T^2 + i\theta(z)) \quad (1.2)$$

where $A(z)$ and $\theta(z)$ represents the amplitude and phase of the input pulse with constant ρ . The reduced Lagrangian for the problem is given by

$$\langle L \rangle = \int_{-\infty}^{\infty} L dT \quad (1.3)$$

Substituting (1.2) in (1.1) and applying (1.3), we reach at reduced Lagrangian

$$\langle L \rangle = \left(i\sqrt{\pi}A(z)^2 \left(-2\gamma A(z)^2 + \sqrt{2}(e^{2i\theta(z)}\rho\beta_2 - 2\theta'(z)) \right) \right) / (8\sqrt{\rho}) \quad (1.4)$$

By substituting above reduced Lagrangian in the Euler-Lagrange equations and varying with respect to variational parameters, we obtain two differential equations for $A(z)$ and $\theta(z)$ as follows

$$A'(z) = -\frac{1}{2} i e^{2i\theta(z)} \rho A(z) \beta_2 \quad (1.5)$$

$$\theta'(z) = \frac{-4\gamma A(z)^2 + \sqrt{2} e^{2i\theta(z)} \rho \beta_2}{2\sqrt{2}} \quad (1.6)$$

From the obtained dynamical equations, the evolution of pulse parameters over a desired length can be achieved by employing Runge-Kutta method. Hence, the variational method provides a very convenient way for finding an explicit approximate solutions. And they provide simple expression for any physical quantities at desired problem where exact analytical solutions are not obtainable.

1.4.2 Numerical Techniques

1.4.2.1 Finite Element Method

The finite element method (FEM) is widely accepted as a very powerful computational technique for electromagnetic problems, in particular, for modeling and simulation of wave propagation in guided wave optics. It is well suited numerical approach to design photonic crystal fiber (PCF) for the calculation of propagation constants in particular, effective refractive index and leakage loss. Using FEM, one can obtain comparable and

accurate propagation constants of PCF which has been verified by experiments. The major advantage of the FEM is its ability to work with complex design of PCF in solving Maxwell's equation for obtaining propagation constants. This direct approach of FEM can treat PCFs with arbitrarily shaped and arbitrarily arranged air holes. In particular, the FEM can select the order and the number of triangular elements, depending on the required computational accuracy [151, 152].

The time dependent Maxwell's equations are

$$\nabla \cdot \bar{E} = \frac{\rho}{\varepsilon}; \quad \nabla \times \bar{E} = -\mu \frac{\partial \bar{H}}{\partial t}; \quad (1.7)$$

$$\nabla \cdot \bar{H} = 0; \quad \nabla \times \bar{H} = \bar{J} + \varepsilon \frac{\partial \bar{E}}{\partial t}, \quad (1.8)$$

where \bar{E} and \bar{H} are the electric and magnetic field vectors, respectively, ε and μ are the permittivity and permeability of the medium, ρ is the electric charge density, and \bar{J} is the electric current density. For the electric field, since $\rho = 0$ and $\bar{J} = \sigma \bar{E}$, we can derive the equation for \bar{E} by taking the curl:

$$\nabla^2 \bar{E} - \mu \sigma \frac{\partial \bar{E}}{\partial t} - \mu \varepsilon \frac{\partial^2 \bar{E}}{\partial t^2} = 0, \quad (1.9)$$

where σ is the electrical conductivity. From the above equation, the basic equation for the FEM analysis can be reduced by setting $\bar{E}(x, y, z, t) = \bar{E}_0(x, y, z)e^{i\omega t}$. It follows that [152]

$$\frac{1}{\mu} \nabla^2 \bar{E} + \omega^2 \varepsilon_c \bar{E} = 0, \quad (1.10)$$

where $\varepsilon_c = \varepsilon - i\frac{\sigma}{\omega}$ is complex permittivity and $\omega = \frac{2\pi c}{\lambda}$. c is the speed of the light and λ is the wavelength. When applying full-vector FEM, the PCF cross section domain is divided into sub-domain with triangular element where any refractive index profiles can be properly represented. Dividing the PCF cross section into a number of triangular elements, from (1.10) we can obtain the following eigenvalue equation:

$$([A] - n_{eff}^2[B])\{h\} = 0 \quad (1.11)$$

where [A] and [B] are the finite element matrices, $\{h\}$ is the discretized electric field vector consisting of the edge and nodal variables. The matrices [A] and [B] are sparse allowing an efficient resolution of the equation by means of high performance algebraic solvers for both real and complex problems. The boundaries of the triangles can be connected with the help of the transition conditions just mentioned. This scheme leads to a matrix eigenvalue system, which can be solved numerically.

1.4.2.2 Split Step Fourier Technique

As the NLSE does not have an analytical solution for the case of arbitrarily shaped pulses introduced through the fiber. However, numerical tools have been developed over the years to solve it. There are two major numerical schemes that are generally applied to the NLSE, the finite difference methods, namely the Ablowitz and Ladik [153, 154] and Crank-Nicolson [155] schemes and the function approximation method such as split step fourier method (SSFM). Out of these techniques, the SSFM has been found to be the more robust. Ever since the study by Hasegawa and Tappert [156] in 1973, the SSFM is the most commonly used, and also chosen for our present study. The main attraction of SSFM for solving the NLSE are its speed and easy implementation compared to other techniques, particularly time domain finite difference methods [1].

In SSFM, the first step involves the separation of the dispersion and nonlinearity terms in the NLSE. The operators \hat{D} represents dispersion and loss in the linear medium and the nonlinear operator \hat{N} accounts for the fiber nonlinearities and both are assumed to be act independently from each other over a short fiber distances Δz .

$$\hat{D} = -\frac{\alpha}{2}U - \sum_{n=2}^4 \beta_n \frac{i^{n-1}}{n!} \frac{\partial^n U}{\partial T^n} \quad (1.12)$$

and

$$\hat{N} = i\gamma \left(|U|^2 U + \frac{i}{\omega_0} \frac{\partial(|U|^2 U)}{\partial T} - T_R U \frac{\partial |U|^2}{\partial T} \right) \quad (1.13)$$

where $U(z, T)$ is the complex field envelope at time T and step z . The NLSE can be further written in the operator form as

$$\frac{\partial U}{\partial z} = (\hat{D} + \hat{N}) U \quad (1.14)$$

The algorithm involves the splitting of fiber in terms of Δz steps of numerical integration, in which only the terms that account for nonlinearity $\hat{N} = 0$ in NLSE are considered at the first step and terms of dispersion alone $\hat{D} = 0$ in NLSE are considered in the second step. And the corresponding equations obtained are solved by transformation using Fourier transform at the subsequent stage.

Mathematically expressed by

$$U(z+h, T) \approx \exp(h\hat{D}) \exp(h\hat{N}) U(z, T) \quad (1.15)$$

The exponential operator ($\exp(h\hat{D})$) can be estimated in the Fourier domain by using

$$\exp(h\hat{D}) B(z, T) = F_T^{-1} \exp(h\hat{D}(-i\omega)) F_T B(z, T) \quad (1.16)$$

where F_T denotes the Fourier transform, $\hat{D}(-i\omega)$ is obtained from (1.12) by replacing the operator $\partial/\partial T$ by $-i\omega$, and ω is the frequency in the Fourier domain. As $\hat{D}(i\omega)$ is just a magnitude in the Fourier space, the evaluation of (1.16) is much simple. The linear operator \hat{D} is most effectively solved in the spectral domain, and for nonlinear operator \hat{N} can be favorably solved in the temporal domain. Assuming a discrete signal in the time and frequency domain, the Fast Fourier Transform (FFT) can be used for converting between both domains. The advantage of the FFT algorithm is it makes the numerical evaluation relatively fast. Hence, for this reason SSFM is faster by up to two orders of magnitude compared with most finite difference schemes. The accuracy of the SSFM can be improved by adopting a different procedure for optical pulse propagation over one segment from z to the other $z+h$. In this procedure (1.15) can be replaced by

$$U(z+h, T) \approx \exp\left(\frac{h}{2}\hat{D}\right) \exp\left(\int_z^{z+h} \hat{N}(z') dz'\right) \exp\left(\frac{h}{2}\hat{D}\right) U(z, T) \quad (1.17)$$

The effectiveness of the SSFM depends on the time (or frequency) domain resolution as well as on the distribution of step sizes considered along the fiber. If Δz , the split step size, becomes too large, the condition for separable calculation of \hat{D} and \hat{N} breaks, and the algorithm ends with wrong results. Hence, a careful determination of the optimal split step size is considered to be much important in case of minimal computational effort for a particular accuracy. Typically, step size is adaptively adjusted towards very small value. The Δz should be a minimum fraction, thereby involves > 1000 steps/(shortest linear or nonlinear length) along the length of the fiber. As the speed of the FFT is proportional to $N_t \log_2 N_t$, where N_t is the number of signal samples in the time or frequency domain, careful determination of the simulation bandwidth and the time window is vital for minimizing computational effort with given specific accuracy constraints. For temporal and spectral computation windows spanning T_{span} and F_{span} , respectively, the sampling theorem imposes the condition $T_{span}F_{span}=N_p$, where N_p is the number of discretization points.

1.5 Structure of the Dissertation

This dissertation investigates the study of the all optical data processing through solitons in waveguides arrays by employing analytical and numerical methods. The summary of the chapters are provided below.

Chapter 2 presents a design to add binary numbers using discrete solitons in waveguide arrays. We show that the nonlinear interaction between discrete solitons in waveguide arrays can be exploited to design half and full adders. By modulating the separation between waveguides and introducing control solitons, we achieve the performance of an XOR gate. We construct the half and full adders using the XOR gate together with the previously- designed OR and AND gates. To facilitate the experimental realization, we calculate the profile of separations between the waveguides that will lead to the performance of the XOR gate.

Chapter 3 presents a protocol to achieve an essential feature of an optical transistor, namely the amplification of input signal with the use of discrete solitons in waveguide arrays. We consider the scattering of a discrete soliton by a reflectionless potential in the presence of a control soliton. We show that at the sharp transition region between full reflectance and full transmittance, the intensity of the reflected or transmitted soliton is highly sensitive to the intensity of the control soliton. This suggests a setup of signal amplifier. For realistic purposes, we modulate the parameters of the reflectionless potential well to achieve a performance of amplifier with a controllable amplification. To facilitate the experimental realization, we calculate the amplification factor in terms of the parameters of the potential well and the input power of the control soliton. The suggested signal amplifier device will be an important component in the all-optical data processing.

In Chapter 4, we consider a bound state of two discrete solitons in a two-dimensional waveguide array. Using numerical and variational calculations we investigate the effect of binding on the mobility of the two solitons, which we found to be marginal. Considering anisotropic waveguides, where coupling in one direction is stronger than in the other, we show that mobility is enhanced considerably along the weaker-coupling direction. We show also that a stable bound state of two solitons exists in such a setup where each one of the two solitons is located at a different waveguide. The stability of the resulting soliton molecule is provided by the Peierls-Nabarro potential and the mobility of the individual solitons is facilitated by the anisotropy. Considering a combination of two out-of-phase solitons we find that they form a metastable state of a single soliton that suddenly splits into two solitons propagating away from each other.

In Chapter 5, we find Skyrmion-like topological excitations for a two-dimensional spin-1/2 system. Expressing the spinor wavefunction in terms of a rotation operator maps the spin-1/2 system to a Manakov system. We employ both analytical and numerical methods to solve the resulting Manakov system. Using a generalized similarity transformation, we reduce the two-dimensional Manakov system to the integrable one-dimensional Manakov

system. Solutions obtained in this manner diverge at the origin. We employ a power series method to obtain an infinite family of localized and nondiverging solutions characterized by a finite number of nodes. A numerical method is then used to obtain a family of localized oscillatory solutions with an infinite number of nodes corresponding to a skyrmion composed of concentric rings with intensities alternating between the two components of the spinor. We investigate the stability of the skyrmion solutions found here by calculating their energy functional in terms of their effective size. It turns out that indeed the skyrmion is most stable when the phase difference between the concentric rings is π , i.e., alternating between spin up and spin down. Our results are also applicable to doubly polarized optical pulses.

In Chapter 6, we investigate the dynamics of two component bright-bright (BB) solitons through reflectionless double barrier and double well potentials in the framework of a Manakov system governed by the coupled nonlinear Schrödinger equations. The objective is to achieve unidirectional flow and unidirectional segregation/splitting, which may be used in the design of optical data processing devices. We observe how the propagation of composite BB soliton is affected by the presence of interaction coupling between the two components passing through the asymmetric potentials. We consider Gaussian and Rosen-Morse double potential barriers in order to achieve the unidirectional flow. Moreover, we observe a novel phenomenon which we name "*Polarity Reversal*" in the unidirectional flow. In this situation, the polarity of the diode is reversed. To understand the physics underlying these phenomena, we perform a variational calculation where we also achieve unidirectional segregation/splitting using an asymmetric double square potential well. Our comparative study between analytical and numerical analysis lead to an excellent agreement between the two methods.

Chapter 7 presents a protocol for the quantum controlled-NOT gate which is based on two qubits operation by investigating the soliton scattering through a reflectionless potential well in an optical system. We consider the set up of two input solitons with different

intensities scattered by a reflectionless potential well with a control soliton placed at the centre of the potential. The two input solitons correspond to the target qubit while presence or absence of control soliton corresponds to the control qubit. We achieve the desired performance of the quantum logic gate by exploiting the intensity difference between the two input solitons and we find this to be possible within a finite width of a velocity of incidence for the two solitons. The calculation of transport coefficients ensures the feasibility of building a quantum controlled-NOT gate. This protocol demonstrates the prospect of soliton scattering by a potential well for quantum information processing. Chapter 8 concludes the whole learned lessons and recommendations for this dissertation.

Chapter 2: Logic Gates and Adders

In this chapter, we present a design and protocol to add binary numbers using discrete solitons in waveguide arrays. We show that the nonlinear interaction between discrete solitons in waveguide arrays can be exploited to design half and full adders. By modulating the separation between waveguides and introducing control solitons, we achieve the performance of an XOR gate. We construct the half and full adders using the XOR gate together with the previously- designed OR and AND gates. To facilitate the experimental realization, we calculate the profile of separations between the waveguides that will lead to the performance of the XOR gate.

2.1 Introduction

Logic gates have been proposed using the same dispersion management method mentioned in last chapter [72]. Control solitons were introduced to propagate through the potential wells and were shown to be an effective tool to modulate the depth of the potential well. The output was then controlled by the intensity of the control solitons and the AND, OR, NAND, and NOR logic gates were all achieved with a single device but different protocols. Here, we follow the same procedure building on this previous work and achieve the XOR gate which is instrumental in realising half and full adders of binary number. The XOR gate is designed out of a modification on the OR gate where we introduce a third potential well and control soliton that further disperses the outputs of the OR gate based on small center-of-mass speed difference. When a soliton scatters off the potential wells it will suffer from a reduction in its center-of-mass speed due to exciting internal modes. The third potential well and control soliton are capable of detecting this reduction in speed and directing the soliton to an opposite direction compared with the case in OR gate. The propagation of solitons in the proposed device is modeled by the discrete nonlinear Schrödinger equation in the tight-binding approximation with site-dependent dispersion coefficients. The potentials are introduced through pre-calculated

profiles for the waveguides' separations. At first, the stationary solutions are obtained which were then used as control and signal solitons for the time evolution of solitons in the waveguide. Transport coefficients in terms of the soliton's speed are then calculated and the window in the velocity domain for which the device functions in the desired manner are identified.

To construct half and full adders, a number of gates have to be connected, namely the output of a certain gate needs to be the input of another gate. Since the typical output of a gate is a reflected or transmitted signal soliton and the input is a control soliton, which are in general different in intensity, we invoke the concept of a converter. This is a pulse source that generates an output of standard intensity. It is triggered by an input pulse of any intensity. The intensity of the output pulse is a characteristic of the converter and is independent of that of the input pulse. We believe such a pulse source is realisable. One-bit half adder can be connected in this manner to result in a one-bit full adder and, hence, one-bit full adder can be connected to obtain an n -bit full adder. In the present paper, we show only how one-bit half and one-bit full adders can be constructed since it is well-established how to obtain the n -bit adders from the one-bit adders.

The rest of the chapter is organized as follows. In Section 2.2, we present the setup and theoretical model. In Section 2.3, we show how the OR gate can be modified to generate an XOR gate. This section starts with a review of the setup and performance of the OR gate followed by the setup modification and performance of the XOR gate. In Section 2.4, we show how the gates can be connected to give half and full adders. Finally, in Section 2.5, we summarize our main conclusions.

2.2 Theoretical Framework and Setup

The propagation of solitons in a one-dimensional array of N waveguides with focusing nonlinearity can be described, in the tight-binding approximation, by the following dis-

crete nonlinear Schrödinger equation (DNLSE) [157],

$$i\frac{\partial\Psi_n}{\partial z} + C_{n,n-1}\Psi_{n-1} + C_{n,n+1}\Psi_{n+1} + \gamma|\Psi_n|^2\Psi_n = 0, \quad (2.1)$$

where Ψ_n is the normalized mode amplitude and n is an integer associated with the waveguide channel, z is the propagation distance, $C_{n,m}$ are the coupling coefficients between different waveguide channels n and m , and γ is the strength of the focusing nonlinearity. Here we used $\gamma = 1$ for numerical simulation.

The modulation of the coupling constants via changing the separation between waveguides leads to an effective potential and Equation (3.1) will be rewritten as [41]:

$$i\frac{\partial\Psi_n}{\partial z} = -C_{n-1}^S\Psi_{n-1} - C_{n+1}^S\Psi_{n+1} - \gamma|\Psi_n|^2\Psi_n, \quad (2.2)$$

where

$$C_{n\pm 1}^S = \sqrt{(C + |\Psi_n^{AL}|^2)(C + |\Psi_{n\pm 1}^{AL}|^2)}. \quad (2.3)$$

For the effective potential to be reflectionless, we use the integrable Ablowitz-Ladik model

$$i\frac{\partial\Psi_n}{\partial z} + (\Psi_{n-1} + \Psi_{n+1})(C + |\Psi_n|^2) = 0, \quad (2.4)$$

with the exact soliton solution

$$\Psi_n^{AL} = \sqrt{c} \sinh(\mu) \operatorname{sech}[\mu(n - n_0)] \exp(i\beta z), \quad (2.5)$$

where $\beta = 2c \cosh(\mu)$, μ is the inverse width of the soliton, n_0 corresponds to the location of the soliton peak, and c is an arbitrary real constant. We refer to reflectionless as a clean

scattering where all of the soliton intensity is either transmitted or reflected. The coupling strength between pulses in neighboring waveguides decays exponentially in terms of the waveguides separation, as [73, 158]

$$C_{n,n\pm 1}^S = C \exp\left(1 - \frac{D_{n,n\pm 1}}{D_0}\right), \quad (2.6)$$

where $D_{n,n\pm 1}$ is the separation between waveguides n and $n \pm 1$, and D_0 and C are positive constants. Thus, the separation between waveguides that gives rise to an effective potential is obtained by inverting the last equation, namely

$$D_{n,n\pm 1} = D_0 \left[1 - \log\left(\frac{C_{n,n\pm 1}^S}{C}\right) \right]. \quad (2.7)$$

This practical relation is used to design specific effective potentials.

All solitons used here are the stationary states of Equation (3.1). They are generated using the Newton-Raphson method and trial solution is given by $\Psi_n = A \exp(-\alpha|n - n_0|)$, where α^{-1} and n_0 are parameters that set the width and peak location of the soliton respectively. As usual, two stationary modes result out of this procedure, namely, the Page mode and the Sievers-Takeno mode [159]. Therefore, the initial soliton used in our protocol can be written generally as

$$\Psi = \Psi_s e^{ivn} + r \Psi_{c_1} + s \Psi_{c_2} + p \Psi_p, \quad (2.8)$$

where Ψ_s , Ψ_{c_1} , Ψ_{c_2} , and Ψ_p are signal soliton, input-1 control soliton, input-2 control soliton, and partitioner control soliton, respectively, which are generated by the scheme described above. Their profiles are given by the AL solution, Equation (2.5). The coefficient e^{ivn} corresponds to the kick-in velocity of the signal soliton with velocity, v . The parameters r , s , and p control the intensities of the control solitons. Typically we use $r = s = 0.16$ and $p = 0.1$.

The intensity of the control soliton is $\text{sech}^2(x)$ -shaped and the modulation of the dispersion coefficients is also $\text{sech}^2(x)$ -shaped. The control soliton is located at the region where the dispersion is modulated. Therefore, the incident soliton will encounter two effective potentials when it is scattered. The first comes from the modulation in the dispersion coefficients and the second comes from the nonlinear interaction with the control soliton. Since the two effective potentials have the $\text{sech}^2(x)$ shape, the net interaction energy will be determined by the relative values of the strengths of the two potentials. By controlling the intensity of the control soliton, we tune the strength of the effective potential resulting from the modulation in dispersion coefficients.

The consideration of input and output of the logic gate with this scheme is described in next section. The use of discrete solitons for the addition of binary numbers requires an XOR gate which is designed in the next section by modifying our previous scheme for the OR gate [72].

2.3 The XOR Gate

The XOR gate we are proposing here is a variation of the OR gate by [72]. We start in the next subsection by reviewing the OR gate and showing how it can be modified to function as an XOR gate.

2.3.1 The OR Gate

We follow a similar scheme of controlling the scattering of the signal soliton by injecting a control soliton into a potential well as described in [72]. The schematic figure representing the OR gate that includes two potential wells, is shown in Figure 2.1. An effective single potential well can be obtained from Equation (3.3) with the modulated coupling constants

$$C_{n\pm 1}^S = C\{[1 + \sinh^2(\mu) \text{sech}^2 \mu(n - n_0)] \times [1 + \sinh^2(\mu) \text{sech}^2 \mu(n \pm 1 - n_0)]\}^{1/2} \quad (2.9)$$

This is achieved by the waveguides separations profile given by Equation (2.7), namely

$$D_{n,n\pm 1} = D_0 \left[1 - \frac{1}{2} \log[1 + \sinh^2(\mu) \operatorname{sech}^2(\mu(n - n_0))] \right. \\ \left. - \frac{1}{2} \log[1 + \sinh^2(\mu) \operatorname{sech}^2(\mu(n \pm 1 - n_0))] \right]. \quad (2.10)$$

Similarly, a double potential well is obtained by generalizing Equation (2.9) as follows

$$C_{n,n\pm 1}^S = [(C + |\Psi_{1,n}^{AL}|^2 + |\Psi_{2,n}^{AL}|^2) \times (C + |\Psi_{1,n\pm 1}^{AL}|^2 + |\Psi_{2,n\pm 1}^{AL}|^2)]^{1/2}, \quad (2.11)$$

where $\Psi_{1,2}^{AL}$ are two exact solitonic solutions centered at different waveguides which take the form

$$\Psi_{i,n}^{AL} = \sqrt{c} \sinh(\mu_i) \operatorname{sech}[\mu_i(n - n_i)] \exp(i\beta_i z), \quad i = 1, 2, \quad (2.12)$$

with $\beta_i = 2c \cosh(\mu_i)$, μ_i is the inverse width of the i -th soliton and n_i corresponds to the location of the i -th soliton's peak.

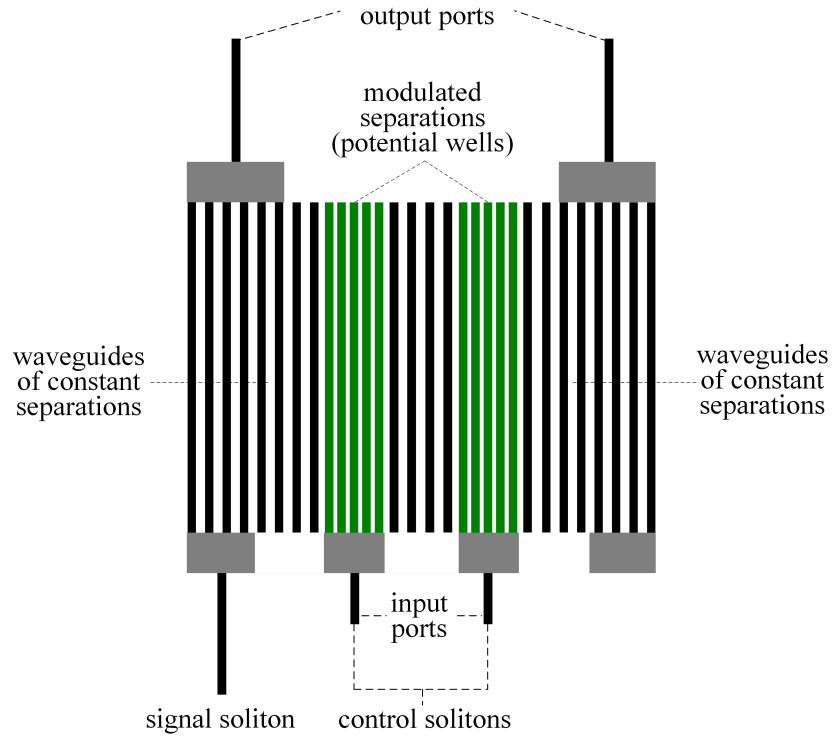


Figure 2.1: Schematic figure representing the OR gate having two potential wells injected with two control solitons.

To achieve the performance of OR gate, we solve Equation (3.1) using the above mentioned coupling coefficients. All solitons used at the start of the time evolution, whether signal or control solitons, are the stationary solitons of Equation (3.1). The input signals of the logic gate are taken as 1 if there is a control soliton in the potential well and 0 otherwise, such that 11 corresponds to two equal control solitons in the two potential wells, 01(10) corresponds to a control soliton in the right (left) potential well, and 00 corresponds to no control solitons in the potential wells. The output is taken from the scattered soliton which can be reflected, transmitted, or trapped. It is clear from the spacio-temporal plots shown in Figure 2.2 that for the 00 case the scattered soliton is reflected while for all other options of the input, the scattered soliton is transmitted. The performance of the OR gate is thus obtained if the output is taken from the transmission port. Hence, obeying the Boolean expression for the OR gate.

Now, we present the calculation of the transport coefficients which are defined as follows: reflection $R = \sum_1^{n_1 - \delta n} |\Psi_n|^2 / \sum_1^N |\Psi_n|^2$, transmission $T = \sum_{n_2 + \delta n}^N |\Psi_n|^2 / \sum_1^N |\Psi_n|^2$ and trapping $L = \sum_{n_1 - \delta n}^{n_2 + \delta n} |\Psi_n|^2 / \sum_1^N |\Psi_n|^2$, where N is the number of waveguides and δn is roughly equal to the width of the soliton in order to avoid the inclusion of the tails of the trapped soliton with the reflected or transmitted ones. It should be noted that we use throughout all numerical calculated solutions that are in-phase with each other. We realize that phase differences may affect in the output of the scattering of solitons. Therefore, we chose for simplicity not to incorporate this additional factor in our protocol. A preliminary investigation of the scattering outcomes in terms of the potential and soliton parameters including potential depth, width, location, soliton initial speed, phase, and type, gives an idea of the ranges of parameters for which the useful applications could be obtained. The transport coefficients curves for the OR gate are presented in Figure 2.3 which show a reasonably wide window of velocity for the operation of OR gate.

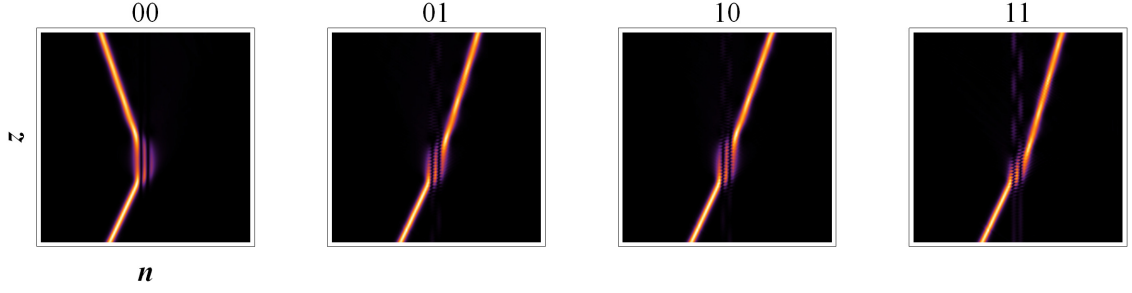


Figure 2.2: Spacio-temporal plots representing the function of OR gate with initial soliton speed $v = 0.22$. The two potential wells are separated by 4 waveguides, $\Delta n = 4$, the amplitude of the control soliton is multiplied by the power control parameter $r = 0.16$, as defined by Equation (3.7) the waveguide arrays range from $n = 1$ to $n = 124$ and time ranges from $z = 0$ to $z = 317$. Other parameters used are $c = 1$ and $\mu = 1.5$. For clarity purpose, the control solitons are not shown here.

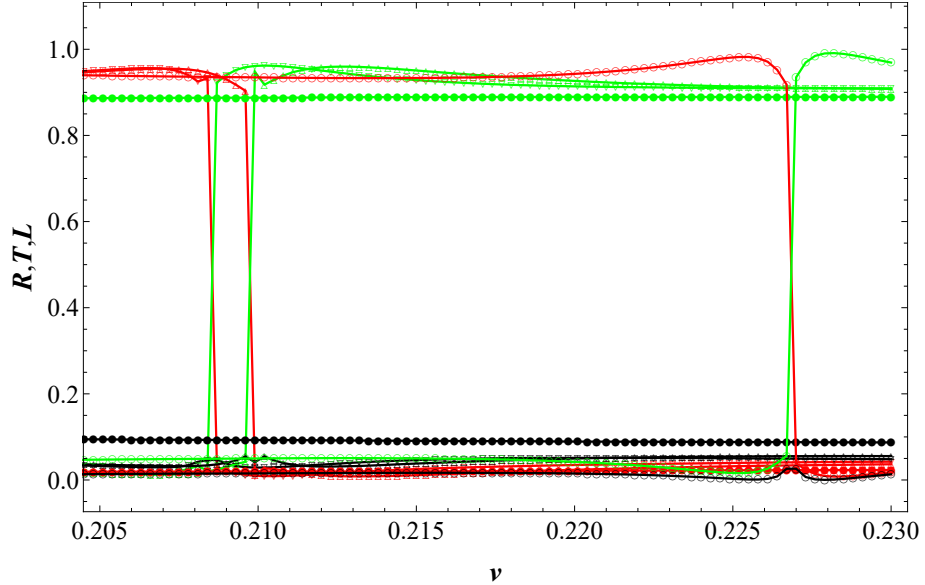


Figure 2.3: Transport Coefficients of OR gate. Red curves correspond to reflection (R), green curves correspond to transmission (T), and black curves correspond to trapping (L). Filled circles correspond to the presence of control solitons in both wells (11). Up and lower triangles correspond to the presence of a control soliton in the left or right well (10 or 01), respectively. Empty circles correspond to the absence of control solitons from both wells (00). All parameters used are the same as in Figure 2.2.

2.3.2 The XOR Gate: A Modified OR Gate

The modification we make on the OR gate is based on distinguishing the scattered solitons according to their center-of-mass speeds. The trajectories of discrete solitons are characterized by quick jumps between the waveguides (large speed) and temporary pinning at

the waveguides (small speeds), as shown in Figure 2.4. The speed will then have two different values and an averaging procedure is therefore needed. We conduct this averaging by calculating the speed over a time interval corresponding to a number of waveguides. The result is shown in Figure 2.4. Applying the averaging procedure to all possible cases for the action of OR gate, we notice a clear difference in the speeds of the output soliton, as shown in Figure 2.5.

The free propagation of signal soliton, which we take as a benchmark, preserves the highest state of velocity among all. This is of course expected due to the absence of potential wells which are main sources of dissipation. The speed of the (11) case is noticeably lower than that of the (01) and (10) cases. The speed for the (00) case is negative since it is reflection. This difference in speeds is the key element for designing the XOR gate.

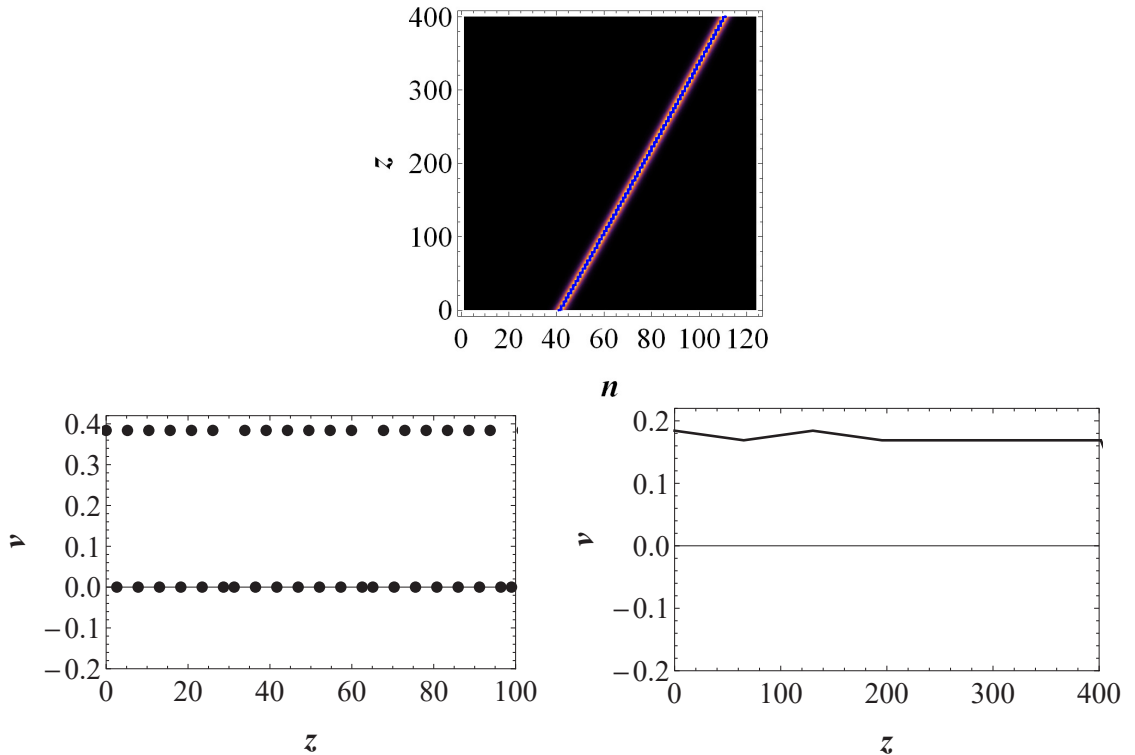


Figure 2.4: Spacio-temporal plot representing the free propagation of a signal soliton in the setup of OR gate with both potential wells and control solitons switched off. The trajectory of the signal soliton with initial speed $v = 0.214$ is represented by blue line. The left subfigure in lower panel shows two possible values of speed, namely $v = 0$ corresponding to soliton pinning, and $v \approx 0.39$ corresponding to transition from site to site. The right subfigure in lower panel shows the averaging of the two speeds over several waveguides. Waveguides range from $n = 1$ to $n = 124$ and time ranges from $z = 0$ to $z = 400$. Other parameters used are $c = 1$ and $\mu = 1.5$.

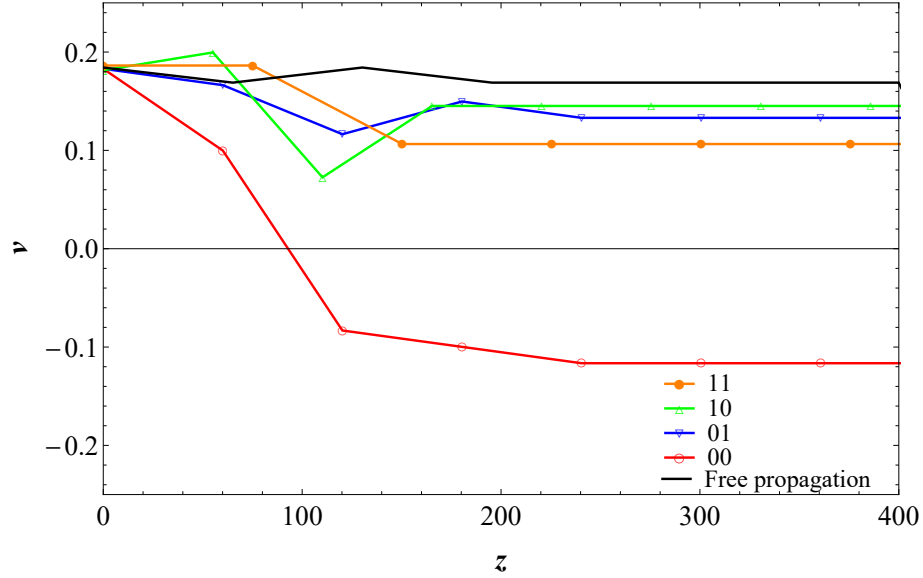


Figure 2.5: The effect of the potential wells on the speed of signal soliton in the OR gate. All cases have same initial the speed $v = 0.214$. The free propagation of signal soliton leads the highest state among all. The (00) corresponds to reflection. The speeds of the 01 and 10 are closer to each other and are noticeably larger than the (11) state.

We exploit this difference by introducing a third potential well and control soliton that reflect the (11) case but not the (01) and (10). This is possible due to the fact that the critical speed at which the solitons reflect or transmit can be controlled by the intensity of the control soliton. Tuning the intensity of the third control soliton, we managed to achieve the function of the XOR gate. Schematically, the XOR gate is represented by Figure 2.6.

The distribution of control solitons for the XOR gate are as follows: For the 00 gate, we have no control solitons in the input ports, for the 01 gate we have only one control soliton in the second input port, for the 10 gate, we have only one control soliton in the first input port, and for the 11 gate, we have two control solitons in the input ports. The third control soliton on the right side of the input ports with different control power is used particularly to reflect the (11) case in order to achieve the performance of XOR gate. In Figure 2.7, the desired performance is clearly seen to have been achieved. The (00) and (11) reflect while (01) and (10) transmit. The transport coefficients for the XOR gate are presented in Figure 2.8. It is seen from the figure that the working window of velocity for the XOR gate is reasonably comparable to and overlaps with the OR gate.

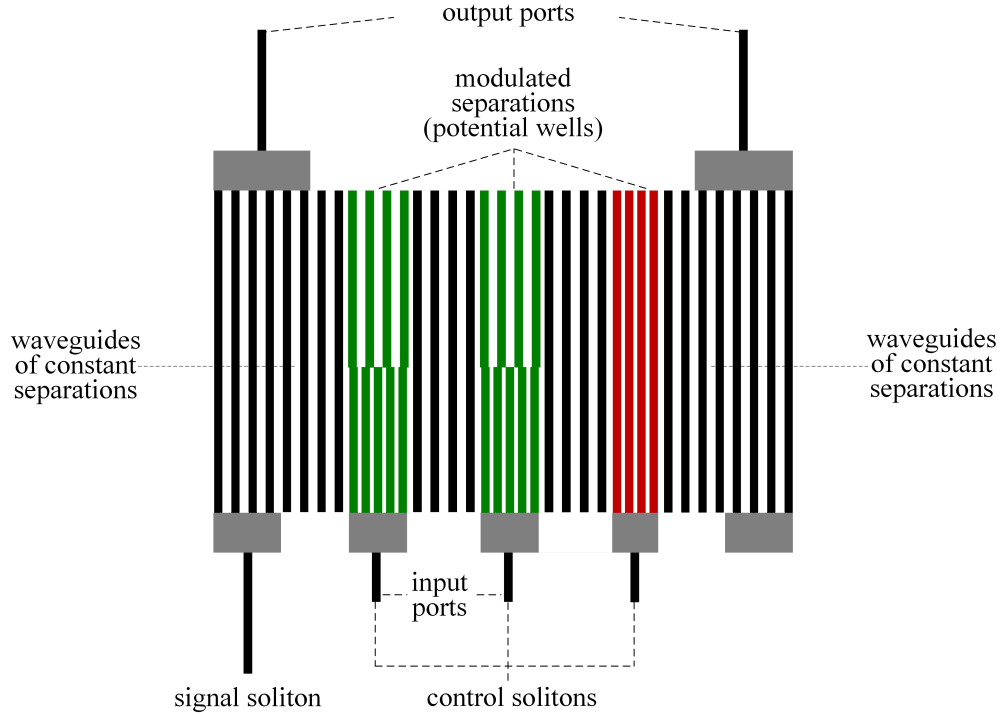


Figure 2.6: Schematic figure showing the XOR gate having two modified potential wells of the same control power and a third potential well is introduced with different control power to reflect the (11) case in order to achieve the performance of XOR gate. The first two potential wells extend only up to about half of the evolution time in order not to affect the reflected signal in the (11) case. Beyond this point, the separations return back to their uniform values away from the potentials.

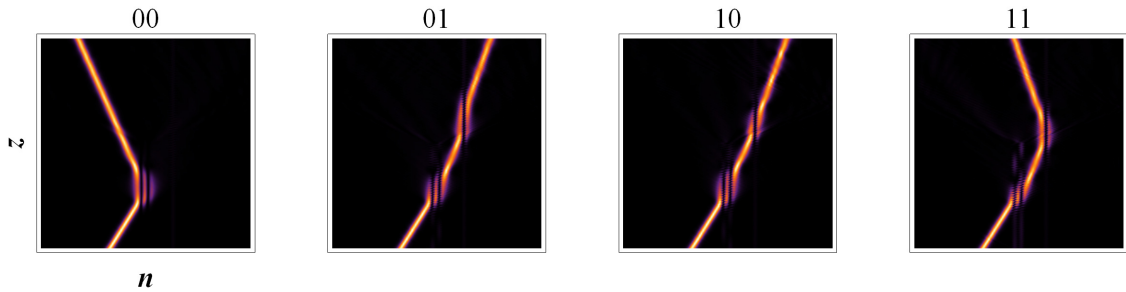


Figure 2.7: Spacio-temporal plots representing the function of XOR gate with initial soliton speed $v = 0.22$. The two modified potential wells are separated by 4 waveguides, $\Delta n = 4$, and take the same position as in the OR gate. The third potential well is placed at 15 waveguides from the centre. The control solitons are invisible for clear density plots. The parameter setting the power of the control solitons in the first two wells is $r = 0.16$, as in the OR gate, while in the third well $p = 0.1$. Time ranges from $z = 0$ to $z = 423$. The reflection for the (11) case is enhanced by cutting off the first two potential wells at $z = 212$. Other parameters used are $c = 1$ and $\mu = 1.5$.

For the feasibility of experimental realization, we plot the waveguides separation in μm and the corresponding coupling strength in mm^{-1} corresponding to potential wells used in Figure 2.8, as calculated by using Equations (2.6) and (2.7) and shown in Figure 2.9.

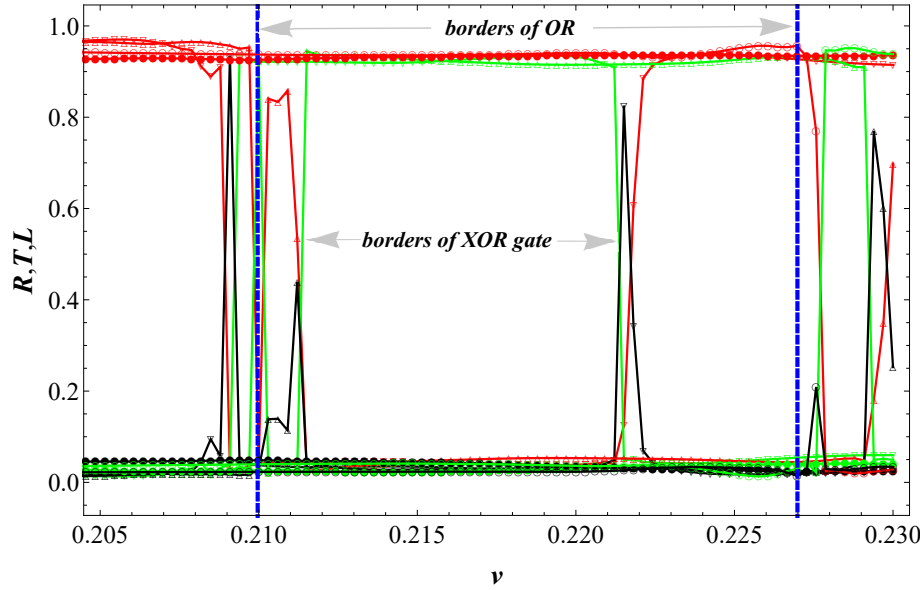


Figure 2.8: Transport Coefficients of XOR gate: Red curves correspond to reflection (R), green curves correspond to transmission (T), and black curves correspond to trapping (L). Filled circles correspond to the presence of control solitons in both wells (11). Up and lower triangles correspond to the presence of a control soliton in the left or right well (10 or 01), respectively. Empty circles correspond to the absence of control solitons from both wells (00). The working window of velocity for OR and XOR gate are considerably comparable. All parameters used here are the same as in Figure 2.7.

2.4 One-bit Half Adder and Full Adder

Adders are type of digital circuits designed to perform the addition of numbers. There are two types: half adders and full adders. As shown in the left subfigure in Figure 2.10, the half adder has two inputs, assigned A and B, and two outputs S (Sum) and C (Carry). The half adder is able to add two single binary digits and provides two digit outputs (sum and carry). The C (carry) value is an AND output of the inputs A and B while the S (Sum) value is the output from XOR gate. Therefore, the common representation of the half adder simply uses an XOR logic gate and an AND logic gate [160]. Similarly, we design our scheme for the half adder with the use of discrete solitons in waveguides arrays, composed of an AND gate and an XOR gate. Our half adder takes two inputs, A and B, and delivers two outputs S (sum) and C (carry). A and B inputs are attached to the potential wells by injecting the control solitons. The output S is collected from the XOR gate upon the transmittance of the discrete soliton.

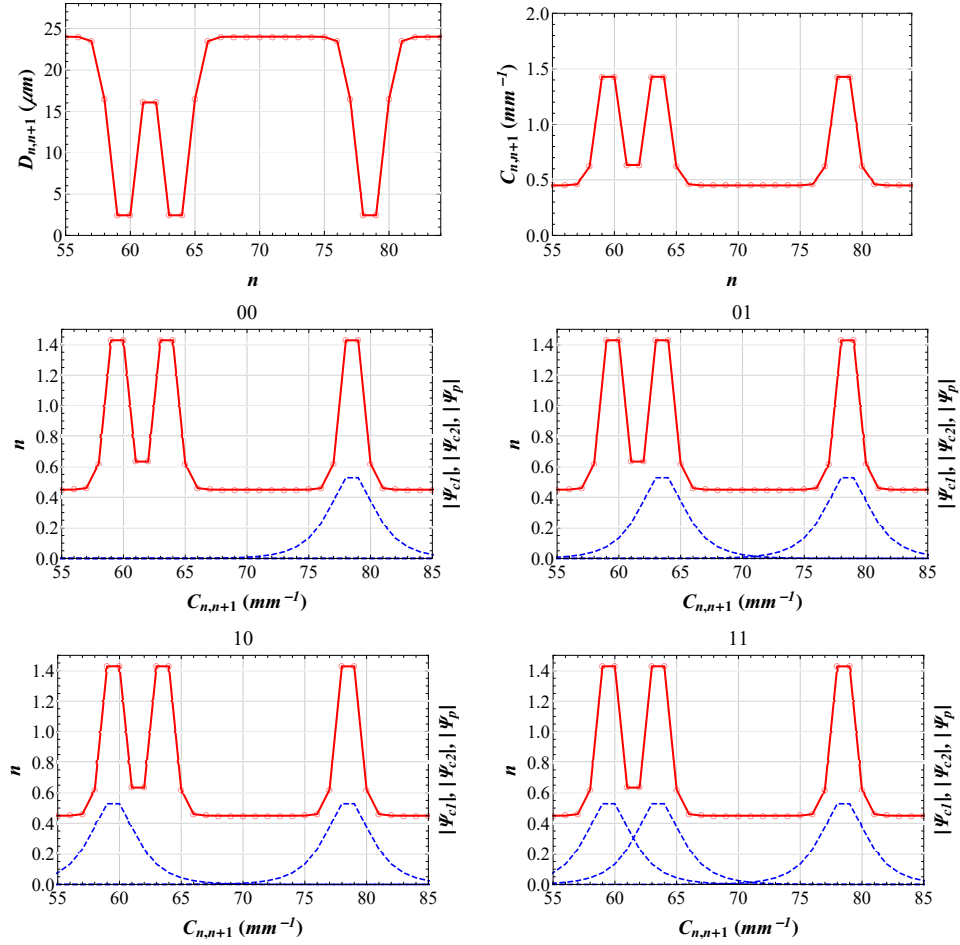


Figure 2.9: Left subfigure in the upper panel shows waveguides separation, $D_{n,n+1}$. The right subfigure in the upper panel shows waveguides coupling, $C_{n,n+1}$. The calibration values $D_0 = 24 \mu\text{m}$ and $C_0 = 0.45 \text{mm}^{-1}$ were taken from the experiment of [73] for the $\lambda = 543 \text{nm}$ pulse. The lower panel consist of four subfigures corresponding to 00, 01, 10, and 11. The blue dashed line represents the intensity of the control solitons.

In addition, the output C is taken from the AND gate upon the transmittance. In order to maintain the universal features of the signal soliton, a converter is introduced in our scheme. The purpose of the converter is to allow for devices connectivity and hence scalability. It refers to a pulse generator that produces an output signal that is always of the same characteristics regardless of the input signal. For instance, the input signal of a converter can be an output (reflected or transmitted) soliton. It takes the output signal of a device and converts it to an input signal to another device. Our half adder scheme is shown in Figure 2.10.

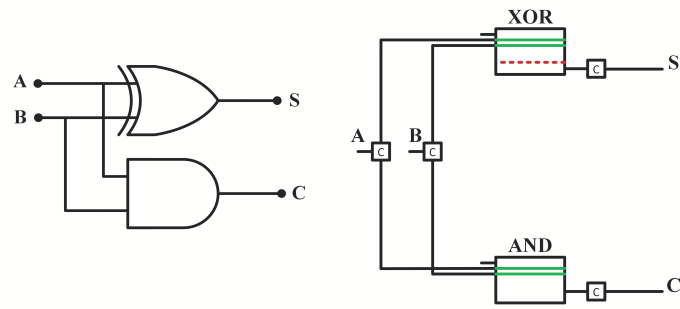


Figure 2.10: Left subfigure shows the typical electronic scheme of half adder designed with the combination of AND and XOR gate. A and B are the two inputs while S (sum) and C (carry) are the outputs. Right subfigure shows our scheme of half adder designed with the discrete solitons in waveguide arrays. c in box is a converter modulates the intensity of a input soliton to match that of a control soliton.

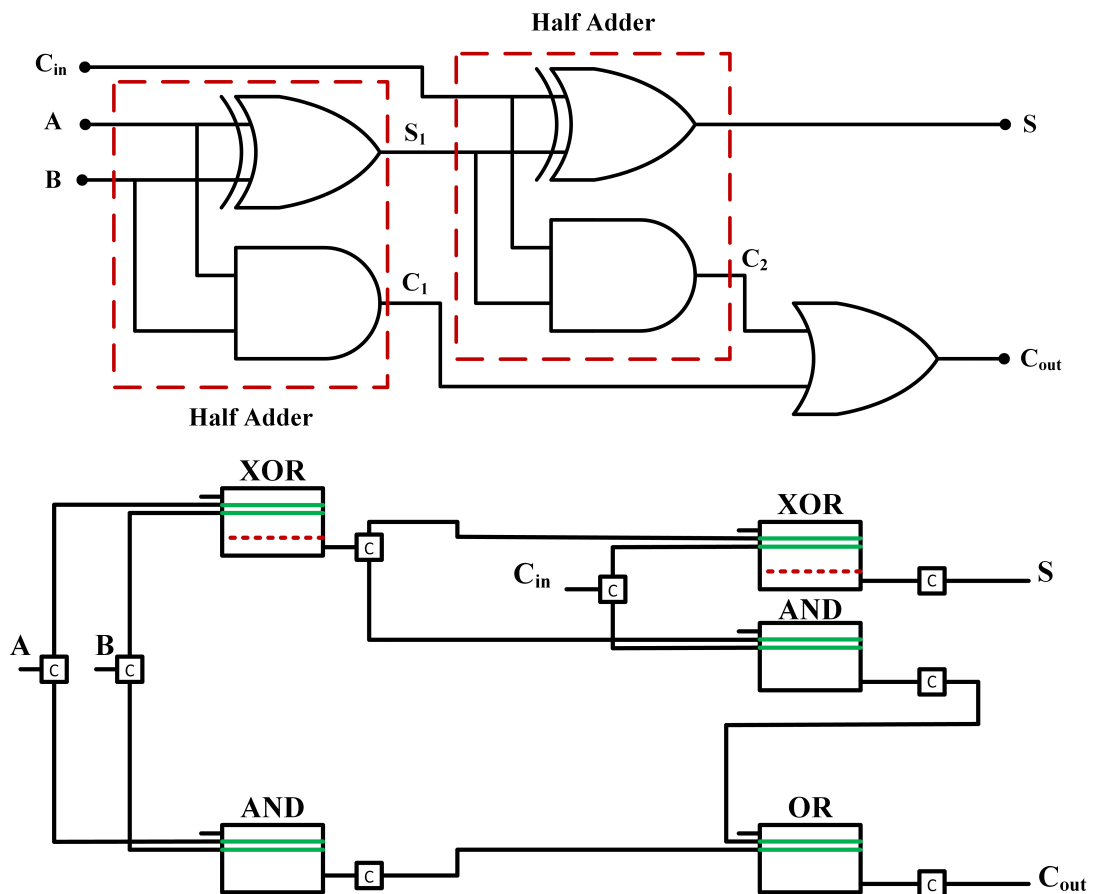


Figure 2.11: Upper subfigure shows the electronic scheme of full adder designed with the combination of two half adders. A, B and C_{in} are the three inputs while S (sum) and C_{out} (carry) are the outputs. Lower subfigure represents our scheme of full adder designed with the combination of two half adders shown in Figure 2.10.

The full adder extends the concept of the half adder by providing an additional carry-in (C_{in}) input [161]. It adds three single-digit binary numbers, two inputs and a carry-in

bit. The third input makes it eligible for scaling n -bits. The full adder outputs two numbers, a Sum and a Carry bit. Upper subfigure in Figure 2.11 shows the electronic scheme of full adder with three inputs: A, B and C_{in} , which adds the three input numbers and generates a Carry out (C_{out}) and a Sum (S). As a result, placing two half adders together with the use of an OR gate results in a one-bit full adder. In order to add more n -bits, n -full adders are connected in cascade to perform the addition. We construct the full adder by following the electronic scheme in structure. It has three inputs, A, B, and C_{in} , and two outputs the S (sum) and C (carry) as shown in the lower subfigure in Figure 2.11. A converter is also introduced in this scheme.

2.5 Conclusion

We have shown that by modifying the setup of the previously-proposed OR gate in a waveguide array, an XOR gate can be obtained. The modification includes the introduction of a third potential well in addition to the two potential wells in the OR gate. A control soliton is injected into the new potential well. The role of the new potential well and its control soliton is to disperse the (11) output signal from the (10) and (01) outputs exploiting a difference in their center-of-mass speed. We found this to be possible within a finite width of a velocity of incidence that is comparable with that of the OR gate. To facilitate the experimental realization, the profiles of the waveguides separations have been calculated in real units, as given by Figure 2.9. We have also shown how the AND, OR, and XOR gates can be connected to result in half and full adders. We believe this proposal will be a useful step towards achieving all-optical data processing.

Chapter 3: Optical Amplifier

This chapter presents a design and protocol to achieve an essential feature of an optical transistor, namely the amplification of input signal with the use of discrete solitons in waveguide arrays. We consider the scattering of a discrete soliton by a reflectionless potential in the presence of a control soliton. We show that at the sharp transition region between full reflectance and full transmittance, the intensity of the reflected or transmitted soliton is highly sensitive to the intensity of the control soliton. This suggests a setup of signal amplifier. For realistic purposes, we modulate the parameters of the reflectionless potential well to achieve a performance of amplifier with a controllable amplification. To facilitate the experimental realization, we calculate the amplification factor in terms of the parameters of the potential well and the input power of the control soliton. The suggested signal amplifier device will be an important component in the all-optical data processing.

3.1 Introduction

The main objective of the present work is to achieve amplification which is an essential feature of an optical transistor in all-optical operations. The main functions of an optical transistor are switching and amplifying optical signals. The device is the optical analog of the electronic transistor that forms the basis of modern electronic devices. Optical transistors introduce the possibility of controlling light using only light and has applications in optical computing and fiber-optic communication networks. Such technology has the potential to exceed the speed of electronics, while saving more power [162]. The present work is a continuation of our previous works in which switch, diode and logic gates have been proposed [43, 72], in addition to our recent design of a scheme and protocol to add binary numbers using discrete solitons in waveguide arrays [34].

We consider a discrete nonlinear Schrödinger equation with dispersion management through modulating the separations between waveguides and in the presence of a control soliton

located at the minimum of the potential. We solve the equation numerically and calculate the transport coefficients from which the amplification factor is determined at the transition region between full reflection and full transmission. As the ideal reflectionless potential leads to an output power that is very sensitive to the input power, we propose lowering such unrealistic sensitivity by perturbing the parameters of the potential such that the scattering of the soliton will not be totally reflectionless. In other words, we allow for some radiation to be emitted resulting in cross-over-like type of transition rather than a sharp transition.

The rest of the chapter is organized as follows. In Section 3.2, we present the setup and theoretical model. In Section 3.3, we present our main results and discussion. Finally, in Section 3.4, we summarize our main conclusions.

3.2 Theoretical Model

The propagation of solitons in a one-dimensional array of N waveguides with focusing nonlinearity can be described, in the tight-binding approximation, by the following discrete nonlinear Schrödinger equation (DNLSE) [157],

$$i \frac{\partial \Psi_n}{\partial z} + C_{n,n-1} \Psi_{n-1} + C_{n,n+1} \Psi_{n+1} + \gamma |\Psi_n|^2 \Psi_n = 0, \quad (3.1)$$

where Ψ_n is the normalized mode amplitude and n is an integer associated with the waveguide channel, z is the propagation distance, $C_{n,m}$ are the coupling coefficients between different waveguide channels n and m , and γ is the strength of the focusing nonlinearity. Here we used $\gamma = 1$ for numerical simulation. The discrete nonlinear Schrödinger equation is also associated with the supratransmission phenomenon which is characterized by the propagation of nonlinear localized modes (gap solitons) [163, 164]. The modulation of the coupling constants through changing the separation between waveguides leads to

an effective potential and Equation (3.1) will be rewritten as [41]:

$$i\frac{\partial\Psi_n}{\partial z} + C_{n-1}^S\Psi_{n-1} + C_{n+1}^S\Psi_{n+1} + \gamma|\Psi_n|^2\Psi_n = 0, \quad (3.2)$$

where

$$C_{n\pm 1}^S = \sqrt{(C + |\Psi_n^{AL}|^2)(C + |\Psi_{n\pm 1}^{AL}|^2)}. \quad (3.3)$$

For the effective potential to be reflectionless, we use the integrable Ablowitz-Ladik (AL) model

$$i\frac{\partial\Psi_n}{\partial z} + (\Psi_{n-1} + \Psi_{n+1})(C + |\Psi_n|^2) = 0, \quad (3.4)$$

The above equation is one of the basic discrete equations of the integrable hierarchy. As such, it serves as a model for the application of a range of techniques for obtaining exact solutions. The Ablowitz-Ladik equation is one of the early examples of an equation to which the inverse scattering technique has been applied. Various other methods, such as Darboux and Bäcklund transformations, have also been applied to solve this equation. Generally speaking, every technique applicable to the basic NLSE equation can also be applied, with some modifications, to the AL equation. Here, we find a stationary bright soliton solution to the AL model, Equation (3.4), using the ansatz method. Substitute the following ansatz in Equation (3.4):

$$\psi_n = A \operatorname{sech}(\beta(n - n_0)) e^{i\mu z}, \quad (3.5)$$

where A , β , and μ are unknown real constants. Then, expand the resulting equation in powers of $n - n_0$. Equating coefficients of powers of $n - n_0$ to zero, gives $A = \sqrt{C} \sinh\beta$ and $\mu = 2C \cosh\beta$. For these two expressions, the whole power series vanishes and thus

the solution of Equation (3.4) will be given by

$$\Psi_n^{AL} = \sqrt{C} \sinh(\beta) \operatorname{sech}[\beta(n - n_0)] \exp(i\mu z), \quad (3.6)$$

where β is the inverse width of the soliton, n_0 corresponds to the location of the soliton peak, and C is an arbitrary real constant. A similar procedure, with the ansatz $\psi_n = A \tanh(\beta(n - n_0)) e^{i\mu t}$, leads to the dark soliton solution. All solitons used here are the stationary states of Equation (3.1). They are generated using the Newton-Raphson method and trial solution is given by $\Psi_n = A \exp(-\alpha|n - n_0|)$, where α^{-1} and n_0 are parameters that set the width and peak location of the soliton respectively. As usual, two stationary modes result out of this procedure, namely, the Page mode and the Sievers-Takeno mode [159]. Therefore, the initial condition used in our protocol can be written generally as

$$\Psi_n(0) = \Psi_s e^{i\nu n} + r \Psi_c, \quad (3.7)$$

where Ψ_s is the signal soliton and Ψ_c represents input control soliton, they are both generated by the Newton-Raphson method. The coefficient $e^{i\nu n}$ corresponds to the kick-in velocity of the signal soliton with velocity, ν , used to control the motion of discrete soliton. This method has the benefit of preserving the norm and it is the same kick or thrust which is used in [165] to control the evolution of two solitons solution in time. The parameter r controls the intensity of the input control soliton I_{in} , related by $I_{in} = r^2$. The intensity of the control soliton is $\operatorname{sech}^2(x)$ -shaped and the modulation of the dispersion coefficients is also $\operatorname{sech}^2(x)$ -shaped. The control soliton is located at the region where the dispersion is modulated. Therefore, the incident soliton will encounter two effective potentials when it is scattered. The first comes from the modulation in the dispersion coefficients and the second comes from the nonlinear interaction with the control soliton. Since the two effective potentials have the $\operatorname{sech}^2(x)$ shape, the net interaction energy will be determined by the relative values of the strengths of the two potentials. By controlling the intensity of the control soliton, we tune the strength of the effective potential resulting

from the modulation in dispersion coefficients. The parameter r refers to an external control on the intensity of the input soliton. It can be done through tuning the intensity of the laser pulse injected into the waveguide. A more sophisticated control could be achieved by injecting the control soliton into a beam splitter where only a fraction of the soliton transmits. That fraction can be used as the input control soliton in our scheme. The calculation of amplification factor is obtained through transport coefficients which are defined as: reflection $R = \sum_1^{n_1 - \delta n} |\Psi_n|^2 / \sum_1^N |\Psi_n|^2$, transmission $T = \sum_{n_2 + \delta n}^N |\Psi_n|^2 / \sum_1^N |\Psi_n|^2$ and trapping $L = \sum_{n_1 - \delta n}^{n_2 + \delta n} |\Psi_n|^2 / \sum_1^N |\Psi_n|^2$, where N is the number of waveguides and δn is roughly equal to the width of the soliton in order to avoid the inclusion of the tails of the trapped soliton with the reflected or transmitted ones. In our amplification protocol, we consider the intensity of the control soliton, I_{in} , as the input signal and the intensity of the reflected soliton, R , as the output signal. Amplification is thus measured by the rate of change in the output intensity, ΔR , with respect to a change in the input intensity, ΔI_{in} , namely

$$M = \frac{\Delta R}{\Delta I_{in}}. \quad (3.8)$$

3.3 Results and Discussion

3.3.1 Reflectionless Potential

We consider the ideal situation with a reflectionless potential. As expected and shown in Figure 3.1, sharp transitions occur at a critical speed, v_c . The intensity of control soliton will merely shift the location at which the sharp transition occurs. Since the amplification factor is proportional to the slope of transport coefficient at the transition region, unrealistically high amplification values will be obtained. Smearing the curve is thus needed. We will achieve this in the following by perturbing the potential such that the scattering of the soliton will not be totally reflectionless.

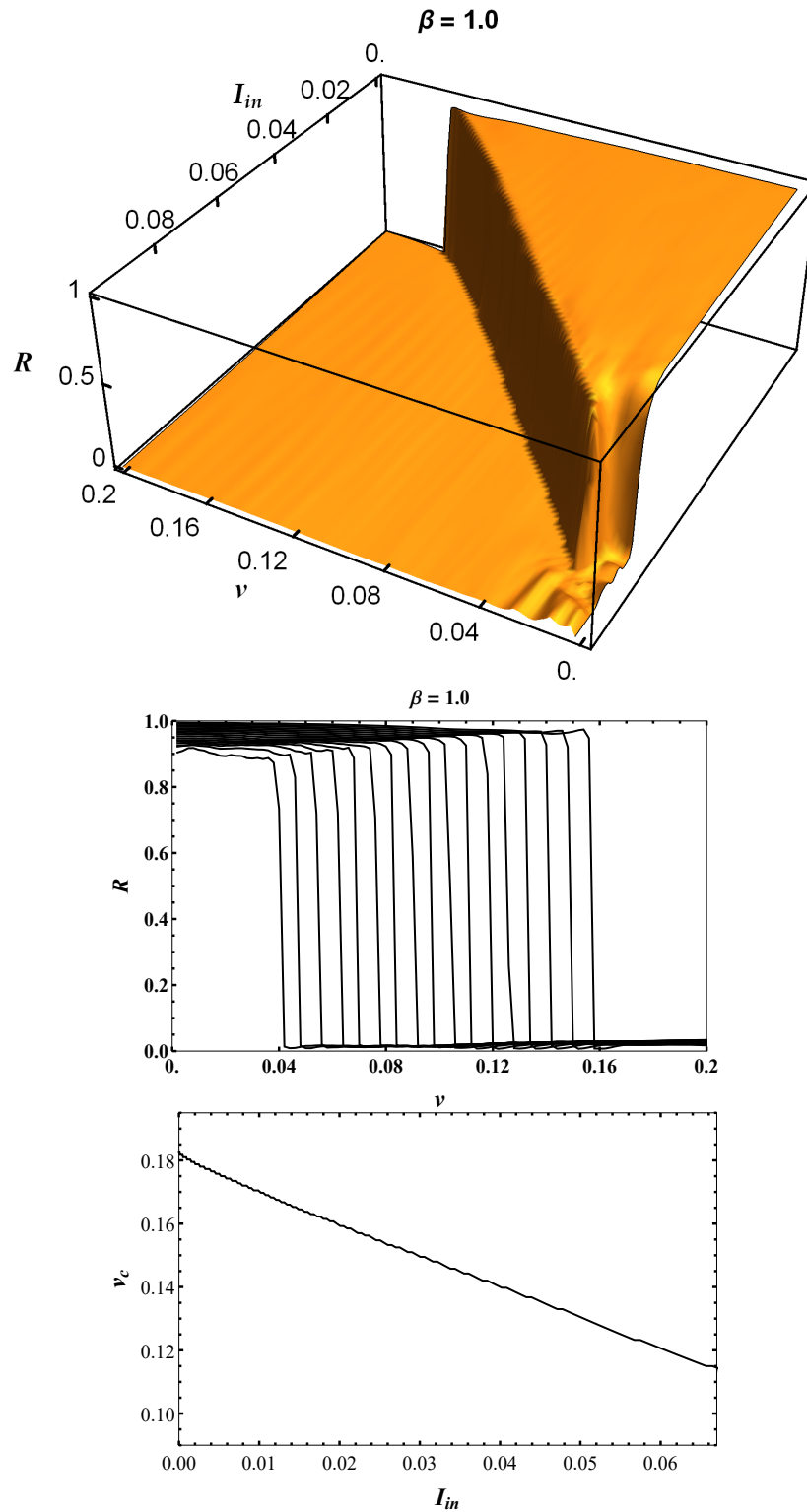


Figure 3.1: Reflectionless potential (Ideal case): 3D plot representing the dependence of the output intensity, R , on the input intensity, I_{in} , and signal soliton speed, v . The left subfigure in the lower panel corresponds to constant- I_{in} cross sections from the 3D plot with I_{in} reaching to $I_{in} = 0.12$, for the curve with lowest critical speed, from 0.02 by an increment of 0.006. The right subfigure in the lower panel shows the critical speed in terms of the control soliton intensity. A reflectionless potential with $\beta = 1$ is used.

3.3.2 Modulated Potential

In order to design the device with an amplification feature, we need to have a finite slope in the transition region replacing the sudden jump in the transport coefficients, as shown previously in Figure 3.1. This can be achieved by using a potential that is not fully reflectionless such as using $\Psi_n^{AL} = \sqrt{C} \sinh(\beta) \operatorname{sech}[\beta(n - n_0)] \exp(i\mu z)$ with $\beta \neq 1$. Using values of β other than 1, leads to smearing the sharp transition in the transport coefficient, as shown in Figure 3.2.

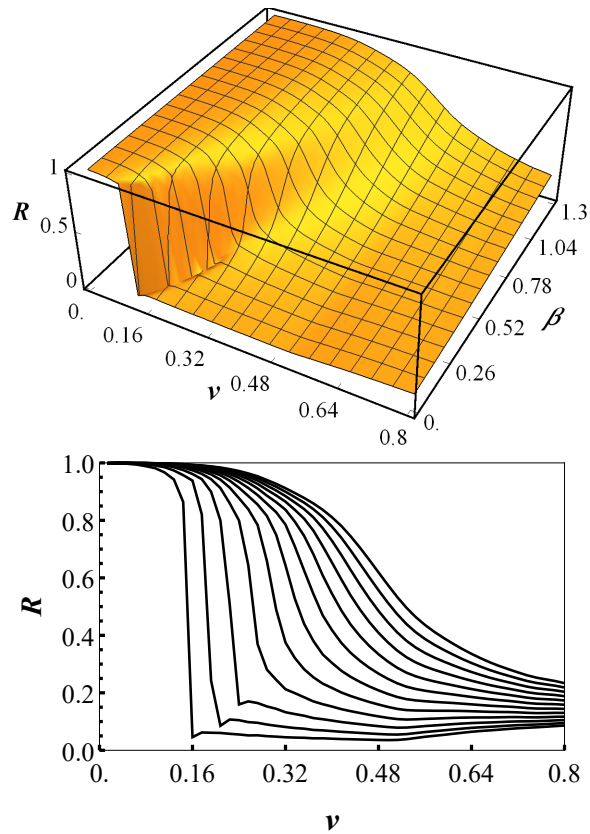


Figure 3.2: 3D plot representing the dependence of the output intensity, R , on the signal soliton speed, v , and the parameter of the potential well, β , for $I_{in} = 0$ (no control soliton). The right subfigure shows constant- β cross-sections.

To investigate in more detail the effect of modulating the potential, we monitor the changes in the intensity of the reflected soliton in terms of changes in the intensity of control soliton and signal soliton speed for three different cases of modulated potential.

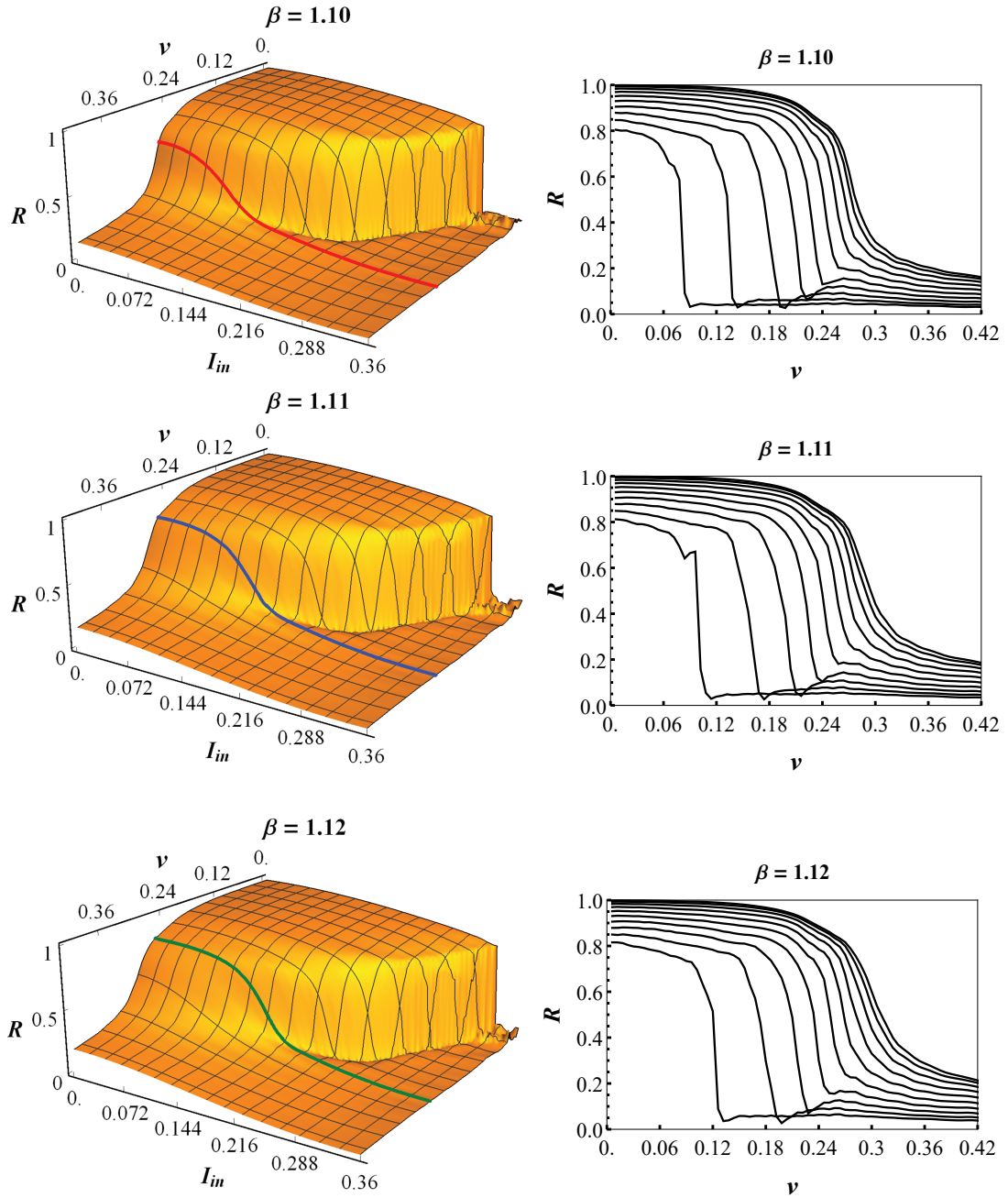


Figure 3.3: Modulated potential (non-reflectionless potential): 3D plots representing the dependence of the output intensity, R , on the input intensity I_{in} , and the signal soliton speed, ν for three values of β . Subfigures on the right correspond to constant- I_{in} cross-sections.

By fixing critical speed, $\nu_c = 0.33$ in Figure 3.3, we investigate the dependence of intensity of reflected soliton on the intensity of control soliton for all three cases of modulated potential. The three curves in Figure 3.4 represent each case of modulated potential shown in Figure 3.3 with fixed critical speed. In Figure 3.4, amplification M is shown in the right

subfigure corresponding to the slope of left subfigure. The figure shows that amplification factors $M \approx 17$ are achieved for the considered values of β . As mentioned previously, much larger amplification rates can be reached with values of β approaching 1.

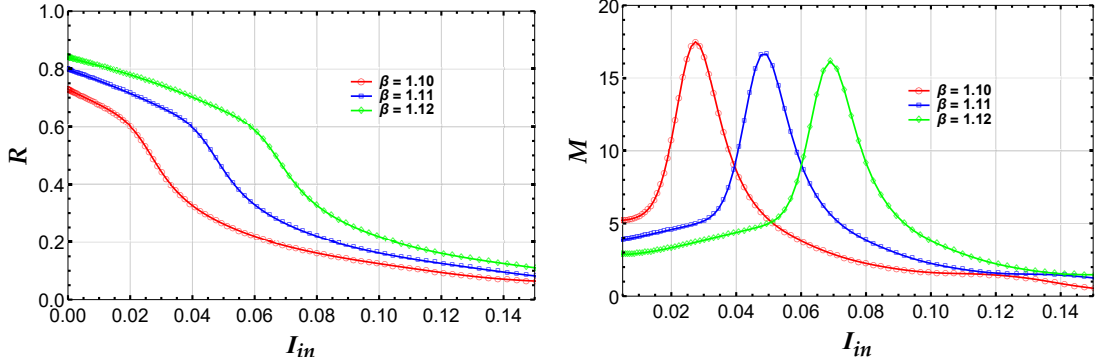


Figure 3.4: The left subfigure represents the relation between the output intensity, R , and the input intensity of control soliton, I_{in} , for three different cases of modified potential well $\beta = 1.10$, $\beta = 1.11$, and $\beta = 1.12$. The right subfigure shows the slope of left subfigure that determines amplification. For all curves the initial soliton speed is $v = 0.33$.

3.4 Conclusion

We exploit the sharp transition region between full reflectance and full transmittance to achieve optical signals amplification. We find that the transition region is highly sensitive to the intensity of the input control soliton. For reflectionless potential, the sensitivity is too high to be experimentally realized. Therefore, we modulate the reflectionless potential well to achieve a realistic performance of amplifier with a controllable amplification. We also show that amplification value can be controlled by the intensity of a control soliton located at the centre of potential well and the modulation of the potential well parameters, mainly its width. We performed a detailed numerical investigation of the effect of all parameters regimes in order to optimize the performance. The separations between the waveguides can be calculated and set to achieve such a potential profile, as previously was performed for logic gates and unidirectional flow [72]. We believe this to be an important and useful step towards achieving a soliton transistor and all-optical data processing. Figure 3.4 shows that the amplification factor is also dependent on the intensity of the input signal. This leads to nonlinear amplification, which we believe is not favorable from a

practical point of view. In an ideal situation, the amplification factor ought to be constant so that no modulation of the relative amplitudes or profile of the input signal is performed while amplifying it. We consider this as a challenge for a future work where we aim at obtaining an amplification scheme with constant amplification factor within a finite range of input signal intensities.

Chapter 4: Discrete Soliton Molecules

In this chapter, we consider a bound state of two discrete solitons in a two-dimensional waveguide array. Using numerical and variational calculations we investigate the effect of binding on the mobility of the two solitons, which we found to be marginal. Considering anisotropic waveguides, where coupling in one direction is stronger than in the other, we show that mobility is enhanced considerably along the weaker-coupling direction. We show also that a stable bound state of two solitons exists in such a setup where each one of the two solitons is located at a different waveguide. The stability of the resulting soliton molecule is provided by the Peierls-Nabarro potential and the mobility of the individual solitons is facilitated by the anisotropy. Considering a combination of two out-of-phase solitons we find that they form a metastable state of a single soliton that suddenly splits into two solitons propagating away from each other.

4.1 Introduction

This chapter is building on our previous work [65] where we have shown that discrete solitons become highly mobile in 2D waveguide arrays with anisotropic coupling strengths. Specifically, our main objectives include: i) studying the effect of the binding between the two solitons on their mobility, ii) calculating the force and potential of interaction between the two solitons, iii) calculating the PN potential for the two solitons and how the soliton-soliton interaction modulates it, and iv) investigating the possibility that a robust stable bound state between two solitons exists.

Stability and dynamics of discrete solitons are well described by the discrete nonlinear Schrödinger equation (DNLSE) which is nonintegrable but can be solved using variational, perturbative and numerical methods [166, 167, 168, 169, 170, 171, 172]. Using both numerical and variational calculations, we achieve all of the above-mentioned objectives, and specifically we show that a robust unpinned soliton molecule indeed exists

in anisotropic waveguides. Another interesting phenomenon is a soliton molecule *fission* where a bound state of two out-of-phase solitons suddenly splits into two solitons propagating away from each other.

The rest of the chapter is organised as follows. In Section 4.2 we present the DNLSE model that describes the evolution of the solitons. In Section 4.3, we solve the model numerically to obtain the equilibrium width and ground state energy of the two solitons. In Section 4.4, we present a variational calculation and calculate the energy functional and the PN potential. In this section, we reproduce the equilibrium properties of the soliton molecules obtained numerically, calculate the PN potential, and the soliton-soliton interaction. In Section 4.5, we investigate the soliton molecule and soliton fission in an anisotropic waveguide array. Finally, we end up with summarising our main results in Section 4.6.

4.2 Model Equation

The propagation of discrete solitons in two-dimensional waveguide arrays is described, within the tight-binding model [59], by the scaled 2D discrete nonlinear Schrödinger equation

$$\begin{aligned}
 i \frac{\partial}{\partial t} \Psi_{m,n} + (d_x \Psi_{m+1,n} + d_x \Psi_{m-1,n} + d_y \Psi_{m,n+1} + d_y \Psi_{m,n-1} - 2(d_x + d_y) \Psi_{m,n}) \\
 + \gamma |\Psi_{m,n}|^2 \Psi_{m,n} = 0,
 \end{aligned}
 \tag{4.1}$$

where $\Psi_{m,n}$ is the field envelope at the site (m,n) , γ is the strength of the nonlinearity which is considered here positive in order to analyse bright solitons, and the coupling coefficients between waveguides in the horizontal and vertical directions are represented by d_x and d_y , respectively, and t corresponds to the distance along the waveguides. We have already used this model in [65] to study the stability and mobility of single 2D discrete solitons in isotropic and anisotropic waveguides. Here, we consider a soliton molecule

instead of a single soliton in an anisotropic waveguide array such that the coupling between the waveguides along one direction is stronger than the other. There are three stationary 2D soliton types known in the literature for the isotropic version of Equation (4.1) which are named as the site-centered (SC), bond-centered (BC), and hybrid solitons. Some references might use other names. As we have pointed out recently [65], for the anisotropic case the hybrid soliton splits into two different forms namely, hybrid-X (HX), and hybrid-Y (HY). In principle, we can consider each soliton in the molecule to be any of these types. However, for simplicity, we consider both solitons to be the site-centered type.

The purpose of this work is to investigate the stability and mobility of such a discrete soliton molecule in 2D waveguide arrays. Specifically, we will investigate the effect of binding on mobility. It is established that a single 2D soliton exhibits very weak mobility in 2D waveguide arrays. The question we will address here is whether a 2D soliton molecule would be more mobile than a single soliton or not. The existence and mobility of the 2D solitons molecules will be investigated in both isotropic and anisotropic waveguide arrays. To that end, we consider, in general different horizontal and vertical coupling strengths. In reality this can be easily realized by modulating the waveguide separations. In the following two sections, we investigate this problem first numerically and then variationally. The numerical calculation leads to the equilibrium width and ground state energy. The variational calculation reproduces these results and helps to derive an analytical expression of the soliton-soliton and soliton-waveguide interaction potentials.

4.3 Equilibrium Width and Energy: Numerical Solution

In this section, we calculate the equilibrium properties of the soliton molecule and then study its mobility by solving the model Equation (4.1) numerically. This will allow us to find the possible stable soliton molecule states. We employ the finite difference method of [170] that is slightly modified to take into account the possibility of having an anisotropic waveguide array. We assume an $L \times L$ dimensional square lattice. The initial condition is

given in matrix form $[H]$ of the following type, namely

$$[H]_{M,N} = 2d_x + 2d_y - \gamma|\Psi_{M,N}|^2, \quad (4.2)$$

$$[H]_{M+1,N} = [H]_{M-1,N} = -d_x, \quad (4.3)$$

$$[H]_{M,N+1} = [H]_{M,N-1} = -d_y, \quad (4.4)$$

where, $M = m + (l - 1)n$ and $N = n + (l - 1)m$, $l = 1, 2, \dots, L$ for the square lattices of size $L \times L$. Solving the linear eigenvalue problem refines the prediction of $\Psi_{m,n}$ as the eigenfunction corresponding to the most negative eigenvalue. This procedure is repeated until the desired precision is obtained.

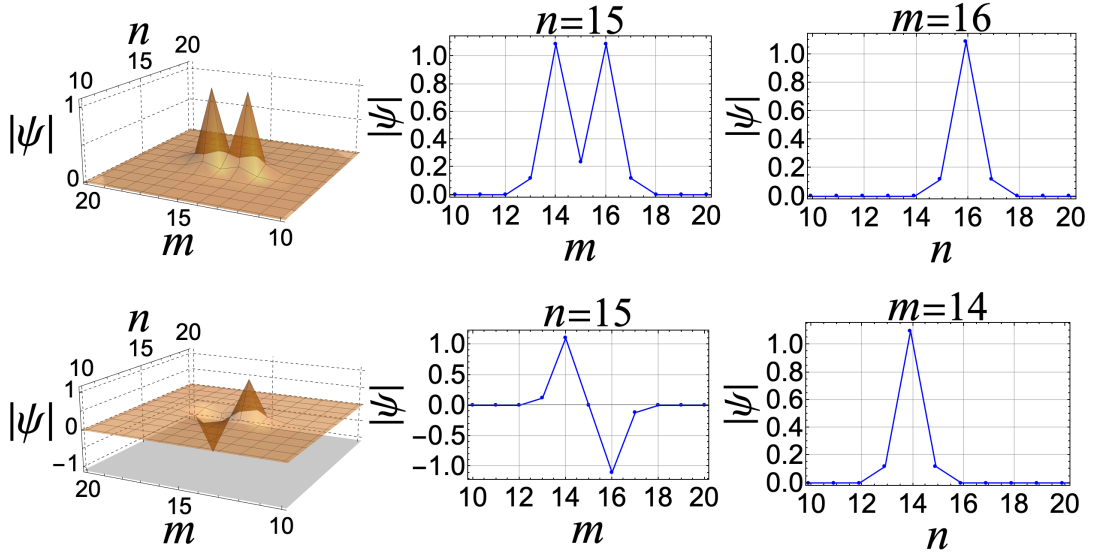


Figure 4.1: In-phase (upper panel) and out-of-phase (lower panel) soliton molecule profiles obtained by numerical solution of Equation (4.1) with isotropic waveguide array. The plots on the right hand side show the two cross-section profiles. Parameters used: $L = 30, P = 2, \gamma = 4, d_x = d_y = 0.5$.

For the initial profile, one can in principle choose a combination of any soliton type out of the four types of stationary soliton profiles. Here, for the sake of simplicity, we choose

only SC type trial functions, as follows

$$\Psi_{m,n} = A \left(e^{-\frac{(m-n_{1x})^2}{\eta_1^2} - \frac{(n-n_{1y})^2}{\eta_2^2}} + e^{-\frac{(m-n_{2x})^2}{\eta_1^2} - \frac{(n-n_{2y})^2}{\eta_2^2} + i\phi} \right), \quad (4.5)$$

where, A is the normalization constant and $n_{1x,1y}$ and $n_{2x,2y}$ are the coordinates peak positions of the first and second solitons, $\eta_{1,2}$ are the widths of the first and second soliton in horizontal and vertical directions respectively, and ϕ is the phase difference between the two solitons.

We solve the model Equation (4.1) using a trial function of the form given by Equation (4.5) to find the two ground state stationary soliton molecule states as shown in Figures 4.1 and 4.2. In these figures the upper panel displays the in-phase stationary profiles for a combination of two solitons and lower panel shows the out-of-phase profiles for an isotropic waveguide array. Considering anisotropic waveguide arrays by changing the coupling strength as, for instance, $d_x=2$ and $d_y=0.15$ leads to elongation of the width of the soliton molecule in one direction. A comparison of solitons cross-sections in isotropic and anisotropic waveguides is shown in Figure 4.3.

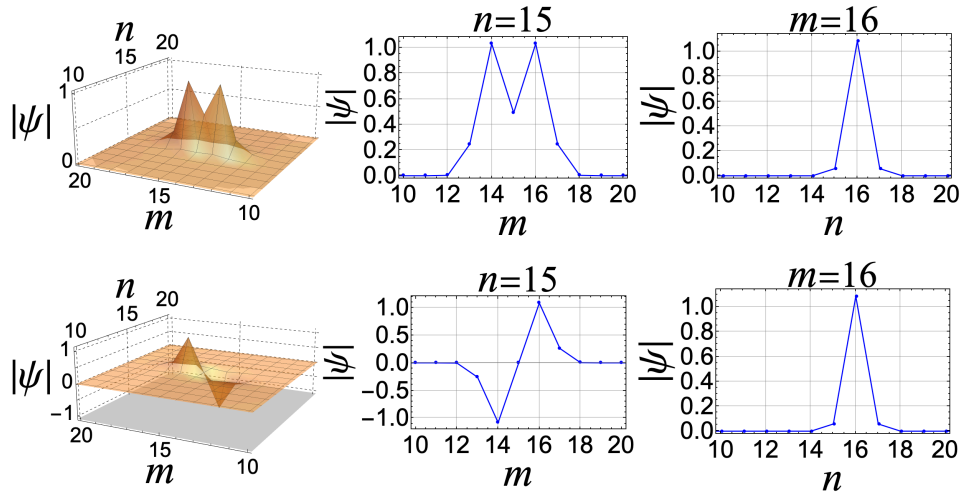


Figure 4.2: In-phase (upper panel) and out-of-phase (lower panel) soliton molecule profiles obtained by numerical solution of Equation (4.1) with anisotropic waveguide array. Parameters used are same as for the isotropic case in Figure 4.1 but with $d_x=1.0$ and $d_y=0.2$.

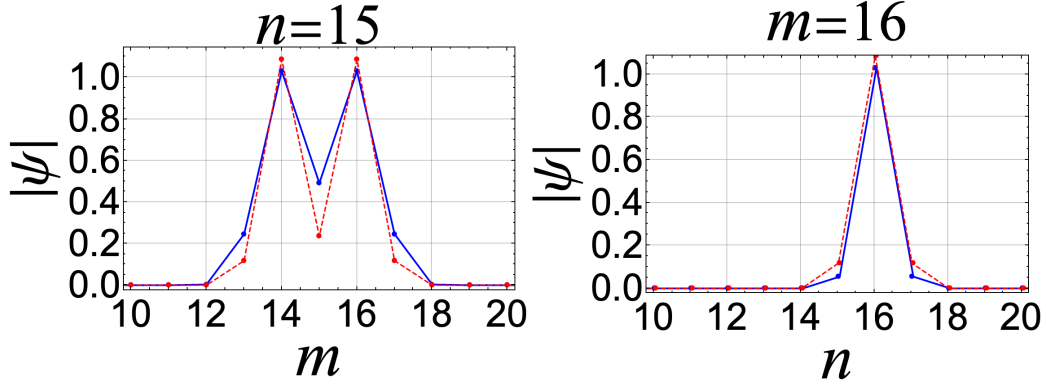


Figure 4.3: Comparison between the cross-sections of isotropic and anisotropic in-phase soliton-molecule profiles from Figures 4.1 and 4.2. Dashed red and solid blue lines correspond to isotropic and anisotropic waveguide arrays, respectively.

4.4 Variational Calculation

The advantage of using a variational calculation is to derive an analytical expression for Peierls-Nabarro (PN) potential which helps us to calculate the barrier in both horizontal and vertical directions. We start from the lagrangian corresponding to Equation (4.1) which takes the following form:

$$L = \sum_{m=-\infty}^{\infty} \sum_{n=-\infty}^{\infty} \left[\frac{i}{2} \left(\Psi_{m,n} \frac{\partial}{\partial t} \Psi_{m,n}^* - \Psi_{m,n}^* \frac{\partial}{\partial t} \Psi_{m,n} \right) - E \right], \quad (4.6)$$

where, the dispersion and nonlinear terms define the energy functional

$$E = - \sum_{m=-\infty}^{\infty} \sum_{n=-\infty}^{\infty} \left[\Psi_{m,n}^* (d_x \Psi_{m-1,n} + d_x \Psi_{m+1,n} + d_y \Psi_{m,n-1} + d_y \Psi_{m,n+1}) - 2(d_x + d_y) \Psi_{m,n} + \frac{1}{2} \gamma |\Psi_{m,n}|^4 \right]. \quad (4.7)$$

There are three kinds of trial functions which have been used widely in the literature to calculate the energy function namely, (i) gaussian, (ii) exponential and (iii) secant function. As mentioned in [173], using a secant trial function the summations in the lagrangian can not be performed in compact form and only asymptotic expressions can be obtained. This is not the case with exponential and gaussian trial functions where it is possible to perform the sums and generate a compact lagrangian form. Here we use the gaussian trial

function since it results in simpler expressions and requires no prior assumptions on the location of the peak of the solitons. This enables us to consider the hopping of the soliton across the sites of the waveguide. The exponential trial function will be used only in Section 4.5.2 to confirm the expression obtained for the potential of interaction in a soliton molecule obtained using the gaussian trial function.

We start the variational calculation by normalising the trial function given by Equation (4.5) to the constant power P

$$P = \sum_{m=-\infty}^{\infty} \sum_{n=-\infty}^{\infty} |\Psi_{m,n}|^2, \quad (4.8)$$

which gives A in terms of the elliptical function $\vartheta_3(x, y)$

$$A = \frac{\sqrt{P}}{\sqrt{\frac{\pi}{2} \sqrt{\eta_1 \eta_2} (A_1 + (A_2 + A_3))}}, \quad (4.9)$$

where,

$$\begin{aligned} A_1 &= \frac{\vartheta_3(-n_{1x}\pi, X_1) \vartheta_3(-n_{1y}\pi, X_2)}{\exp\left(-\frac{n_{1x}^2 + n_{2x}^2}{4\eta_1^2} - \frac{(n_{1y} - n_{2y})^2}{4\eta_2^2} - \frac{i\phi}{2}\right)}, \\ A_2 &= \left(1 + e^{2m\phi}\right) \vartheta_3\left(-\frac{1}{2}(n_{1x} + n_{2x})\pi, X_1\right) \times \vartheta_3\left(-\frac{1}{2}(n_{1y} + n_{2y})\pi, X_2\right) \\ &\quad \times \exp\left(-\frac{n_{1x}^2 - 4n_{1x}n_{2x} + n_{2x}^2}{2\eta_1^2} - \frac{(n_{1y} - n_{2y})^2}{2\eta_2^2} - i\phi\right), \\ A_3 &= \frac{\vartheta_3(-n_{2x}\pi, X_1) \vartheta_3(-n_{2y}\pi, X_2)}{\exp\left(-\frac{n_{1x}^2 + n_{2x}^2}{4\eta_1^2} - \frac{(n_{1y} - n_{2y})^2}{4\eta_2^2} - \frac{i\phi}{2}\right)}, \end{aligned}$$

and $X_1 = e^{-\frac{1}{2}\pi^2\eta_1^2}$ and $X_2 = e^{-\frac{1}{2}\pi^2\eta_2^2}$.

We then calculated the energy functional using of the above normalized trial function which is given in Appendix A. The variational and numerical equilibrium profiles of the isotropic waveguide array are shown in Figure 4.4.

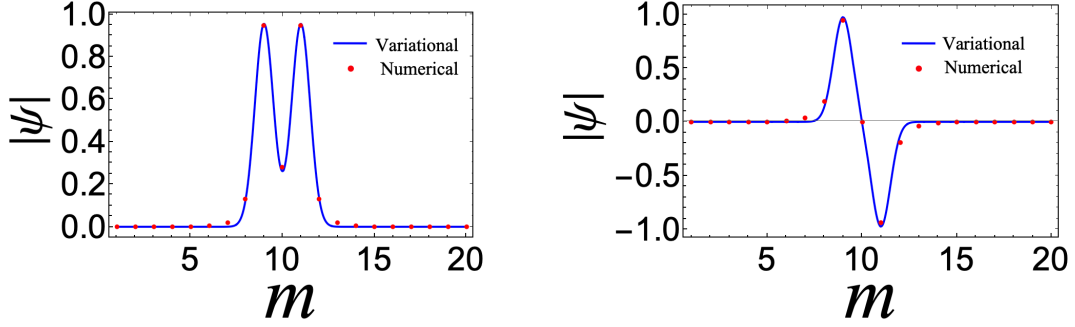


Figure 4.4: In-phase and out-of-phase isotropic soliton molecules obtained by both numerical (red dots) and variational method (blue solid line) for the choice of parameters $L = 20, P = 2, \gamma = 4, d_x = d_y = 0.5$ with the assumption of $\phi = 0$ and π to achieve in-phase (left) and out-of-phase (right) solitons.

The left and right subfigures are displaying the isotropic soliton molecule profiles for in phase, $\phi = 0$, and, out-of-phase, $\phi = \pi$, cases, respectively. Here, we fixed both solitons on the x -axis, $n_{1y} = n_{2y} = 0$, fixed the first soliton at origin, $n_{1x} = 0$, and left the position of the second soliton on the x -axis, n_{2x} , to vary. The figures show that, the variational and numerical profiles are in excellent agreement with each other.

4.4.1 Equilibrium Width and Energy

At this stage, the energy functional is a function of the two soliton peak positions and widths, i.e., $E = E(n_{1x}, n_{1y}, n_{2x}, n_{2y}, \eta_1, \eta_2)$. To find the solitons equilibrium widths, the energy needs to be minimized with respect to η_1 and η_2

$$\frac{\partial E}{\partial \eta_1} \Big|_{\eta_1 = \eta_{10}} = 0, \quad \frac{\partial E}{\partial \eta_2} \Big|_{\eta_2 = \eta_{20}} = 0, \quad (4.10)$$

where, η_{10} and η_{20} are the equilibrium widths. We assume $\eta_2 = \eta_1$ and then minimize the energy with respect η_1 . There are two possible schemes to achieve this: either by considering the trial function for a single soliton only or by fixing the first soliton at origin $n_{1x} = n_{1y} = 0$ while the second soliton is placed remotely: $n_{2x} = 0$ and $n_{2y} = \infty$. The equilibrium profiles for both schemes turns out to be the same, as it should be. By substituting η_{10} and η_{20} in the ansatz function, we find the equilibrium profiles while substituting them into the energy functional we obtain the PN potential as a function

of n_{2x} and n_{2y} . The profiles of PN potential for in-phase and out-of-phase solitons are displayed in Figures 4.5 and 4.6, respectively. To generate these plots, we set one soliton at origin ($n_{1x} = 0$ and $n_{1y} = 0$) and thus we obtained the PN potential in terms of the coordinates of the second soliton, $V_{PN} = V_{PN}(n_{2x}, n_{2y})$.

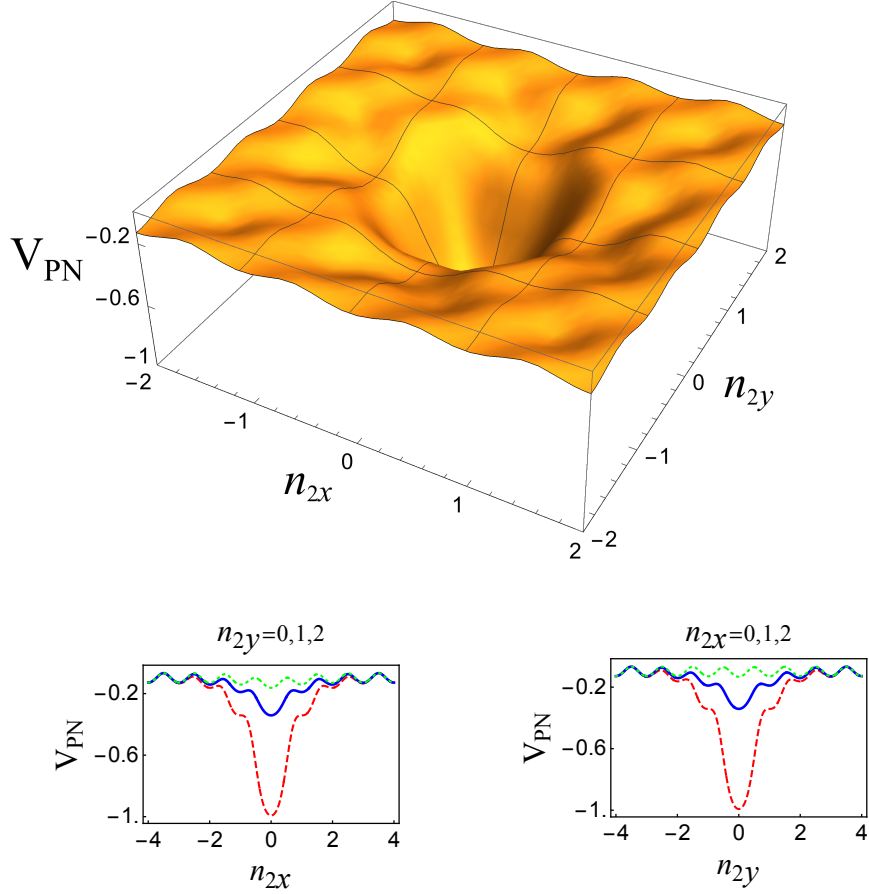


Figure 4.5: In-phase PN potential for the isotropic case (upper panel) and the two cross sections of the PN potential (lower panel). The parameters used are $P = 2$, $\gamma=4$, $n_{1x} = n_{1y}=0$, $\eta_1=\eta_{10}$ and $\eta_2=\eta_{20}$, $d_x=d_y=0.5$ with $\phi=0$. Red dashed corresponds to $n_{2y} = 0$ and $n_{2x} = 0$ for the left and right subfigures, respectively. Solid blue corresponds to $n_{2y} = 1$ and $n_{2x} = 1$, and dotted green corresponds to $n_{2y} = 2$ and $n_{2x} = 2$.

The numerical diagonalization scheme of the system given by Equations (5.30)-(4.4) generates at once the whole spectrum of eigenenergies and eigenfunctions including the ground state and excited states of the soliton molecule. This enables us to compare numerical ground state energy with the variational one, as in Figure 4.7. The variational calculation clearly captures the ground state of the soliton molecule for many soliton separations.

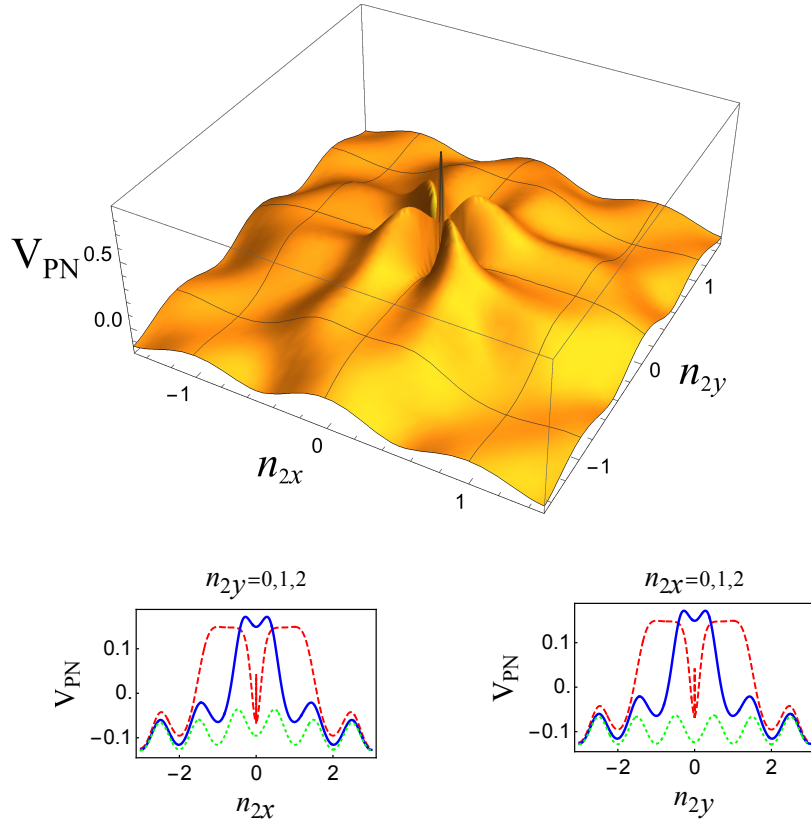


Figure 4.6: Out-of-phase PN potential for the isotropic case (upper panel), and its two cross-sections (lower panel). Parameters used are same as in Figure 4.5 but with $\phi = \pi$. Red dashed corresponds to $n_{2y} = 0$ and $n_{2x} = 0$ for the left and right subfigures, respectively. Solid blue corresponds to $n_{2y} = 1$ and $n_{2x} = 1$, and dotted green corresponds to $n_{2y} = 2$ and $n_{2x} = 2$.

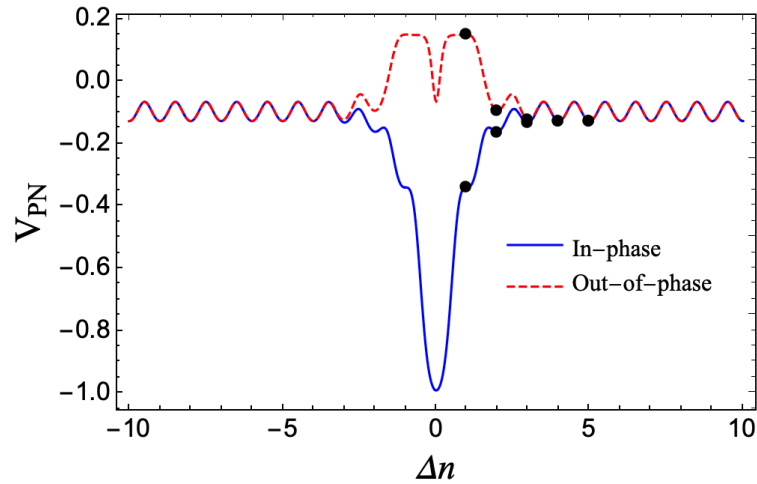


Figure 4.7: The PN potential for separation of solitons calculated variationally for two choices of phases: In-phase (blue solid line) and out-of-phase (red dashed line). Numerically calculated points are presented by black dots for the choice of parameters $P=2$, $\gamma=4$, $d_x=d_y=0.5$.

One can clearly notice in this figure the modulation brought by the interaction between solitons to the PN potential. When the two solitons are widely separated, the PN potential is periodic as for single solitons. However, when the solitons are close the PN potential acquires an additional potential well (barrier) for in-phase (out-of-phase) solitons.

4.4.2 Characteristics of PN Potential

To study the role of binding on mobility, we investigate the dependence of the PN potential on the location of the molecule, its orientation with respect to the direction of motion, and bond length. We plot the PN potential for varying molecule's center-of-mass with solitons' separation $\Delta n = 1, 2, 3, 4$ and 5, as shown in Figure 4.8.

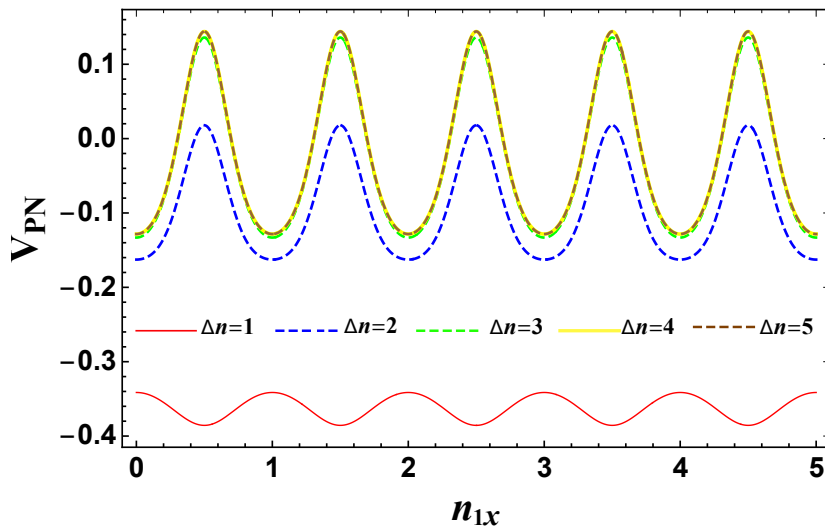


Figure 4.8: The PN potential versus the molecule's position for different solitons separation $\Delta n = n_{2x} - n_{1x}$. The parameters used are $P=2$, $\gamma=4$, $n_{2x} = n_{2y}=0$, $\eta_1=\eta_{10}$, $\eta_2=\eta_{20}$, $d_x = d_y=0.5$.

This figure, indicates that the PN potential is lowest for the two solitons with the closest separation. By increasing the separation between the two solitons, the barrier of the potential increases. For separations $\Delta n \geq 3$, the PN potential remains the same. Consequently, separations $\Delta n > 2$ will not effect the PN potential since the interaction between the two solitons becomes negligible. This figure suggests that, in principle, mobility should be enhanced for the two solitons with closest separation. However, numerical investigations

show that solitons are immobile for this case due to the increase in the barrier height.

Now, we investigate the mobility in terms of the molecule's direction of movement. We considered two trajectories: (i) parallel to the molecule's axis and (ii) at 45° with respect to the molecule's axis. Figure 4.9 show that when the two solitons are moved in the diagonal direction, the PN barrier becomes higher and it is harder now to move the solitons.

4.4.3 Soliton-Soliton Interaction

The PN potential is the sum of the soliton-soliton interaction potential and the interaction between the solitons and the waveguide array

$$V_{PN} = V_{SS} + V_{PN}^\infty, \quad (4.11)$$

where V_{SS} is the soliton-soliton interaction and V_{PN}^∞ is the limit of V_{PN} when the two solitons are widely separated such that their V_{SS} vanishes. We may thus calculate V_{SS} using for instance

$$V_{SS}(n_{2x}) = V_{PN} \Big|_{\substack{n_{1y}=0 \\ n_{2y}=0 \\ n_{1x}=0}} - V_{PN} \Big|_{\substack{n_{1y}=0 \\ n_{2y}=0 \\ n_{1x} \rightarrow \infty}}. \quad (4.12)$$

Figure 4.10 shows V_{SS} in terms of separation between solitons, namely n_{2x} since we have fixed one soliton at origin. While out-of-phase solitons repel, due to the potential barrier, the in-phase solitons attract and experience a molecular-type interaction potential. In principle, the soliton-soliton interaction allows for the formation of a soliton molecule. However, the magnitude of the potential depth (bond strength) is in this case much smaller than the PN potential barrier. Therefore, binding will have no effect on the mobility or pinning of solitons.

The concept of a soliton molecule in this case is excluded. On the other hand, we will show in the next section that when the two solitons are located at different waveguides

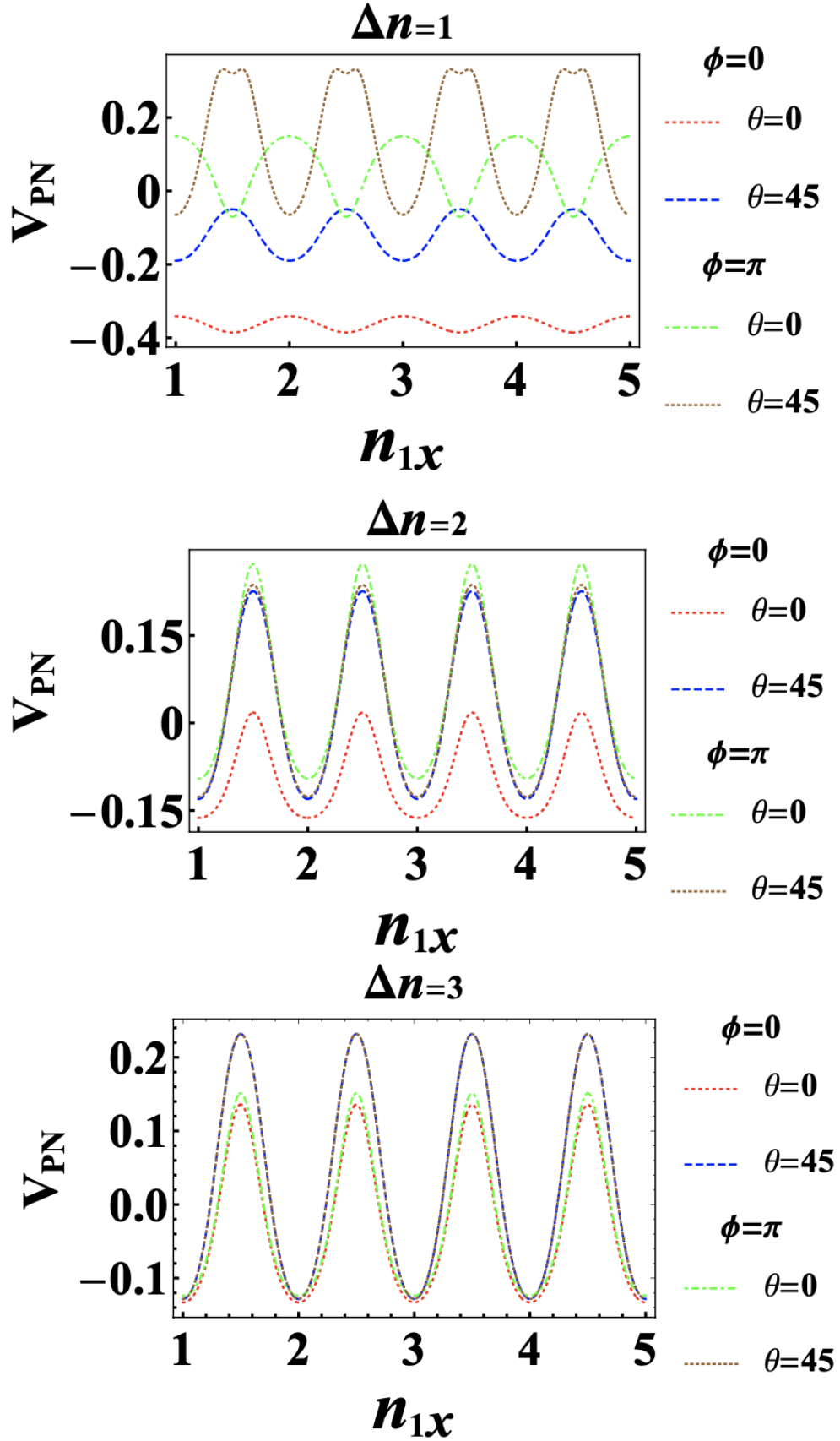


Figure 4.9: The PN potential for two orientations ($\theta=0$ (red dotted), $\theta=45$ (blue dashed)) for in-phase $\phi=0$ and ($\theta=0$ (green dot-dashed), $\theta=45$ (brown tiny-dashed)) for out-of-phase $\phi=\pi$ respectively with three different fixed separations $\Delta n = n_{2x} - n_{1x}=1$ (left), $\Delta n=2$ (middle) and $\Delta n=3$ (right). Parameters used are $P=2$, $\gamma=4$, and $d_x = d_y = 0.5$.

with high anisotropy, the soliton-soliton interaction will be dominant and a stable soliton molecule forms.

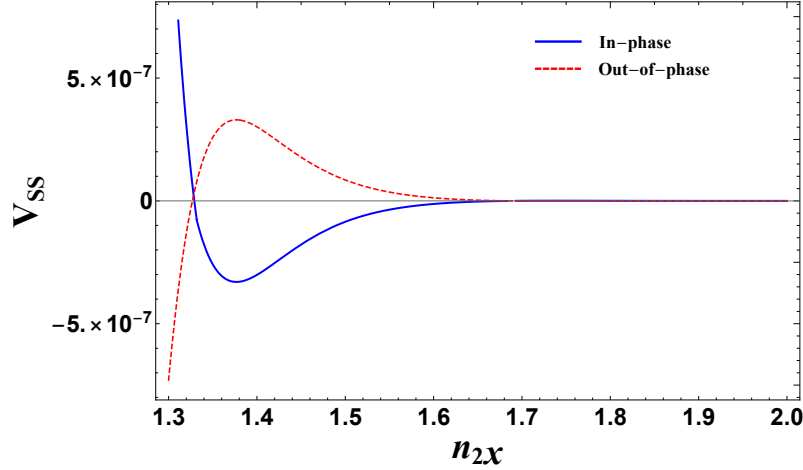


Figure 4.10: The soliton-soliton interaction given by Equation (4.12) for the choice of parameters $P=2$, $\gamma=17$, $d_x = d_y = 0.1$

4.5 Anisotropic Waveguide Arrays

We have shown in a recent work that 2D solitons become mobile in anisotropic waveguides [65]. We have also shown in the present paper that binding between solitons in an isotropic waveguide has no effect on their mobility. Therefore, we consider soliton molecules in anisotropic waveguides expecting the binding to enhance on their mobility.

4.5.1 Equilibrium Profiles and Mobility

The PN potentials for an in-phase and out-of-phase combination of two solitons with anisotropic waveguide array is shown in Figures 4.11 and 4.12, respectively. The figures show that mobility should be high in the horizontal direction compared to that in the vertical direction.

By comparing the cross sections of Figure 4.11 with Figure 4.5, we can see that the PN potential is not periodic as it was in the isotropic case. The variational and numerical equilibrium profiles of the anisotropic waveguide are shown in Figure 4.13. Agreement

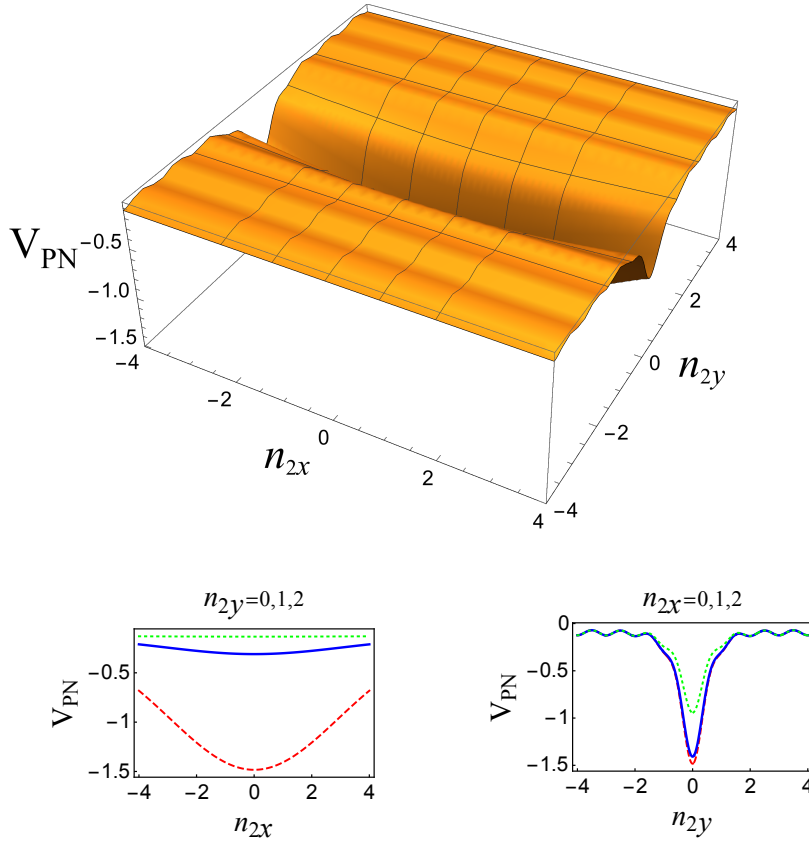


Figure 4.11: In-phase PN potential for the anisotropic case (upper panel) and its two cross section profiles (lower panel). The parameters used are $P = 2$, $\gamma=4$, $n_{1x} = n_{1y}=0$, $\eta_1=\eta_{10} = 3.86$ and $\eta_2=\eta_{20} = 0.760$, $d_x=3$, $d_y=0.15$ with $\phi=0$. Red dashed corresponds to $n_{2y} = 0$ and $n_{2x} = 0$ for the left and right subfigures, respectively. Solid blue corresponds to $n_{2y} = 1$ and $n_{2x} = 1$, and dotted green corresponds to $n_{2y} = 2$ and $n_{2x} = 2$.

between the variational and numerical profiles is clear in this figure.

4.5.2 Formation of Soliton Molecule

We have already found that 2D soliton molecules are completely immobile in isotropic waveguide arrays [65]. Hence, the anisotropy was invoked and therefore we consider anisotropic waveguide array with coupling in the horizontal (x -)direction to be much weaker than in the vertical (y -)direction.

With high anisotropy, the PN potential in the horizontal direction, V_{PNx} , is shown to be almost monotonic potential well with a global minimum at zero separation between the two solitons while the PN potential in the vertical direction, V_{PNy} , is oscillatory, as shown in Figure 4.11. The cross-sections of the PN potential shown in Figure 4.11 indicate that

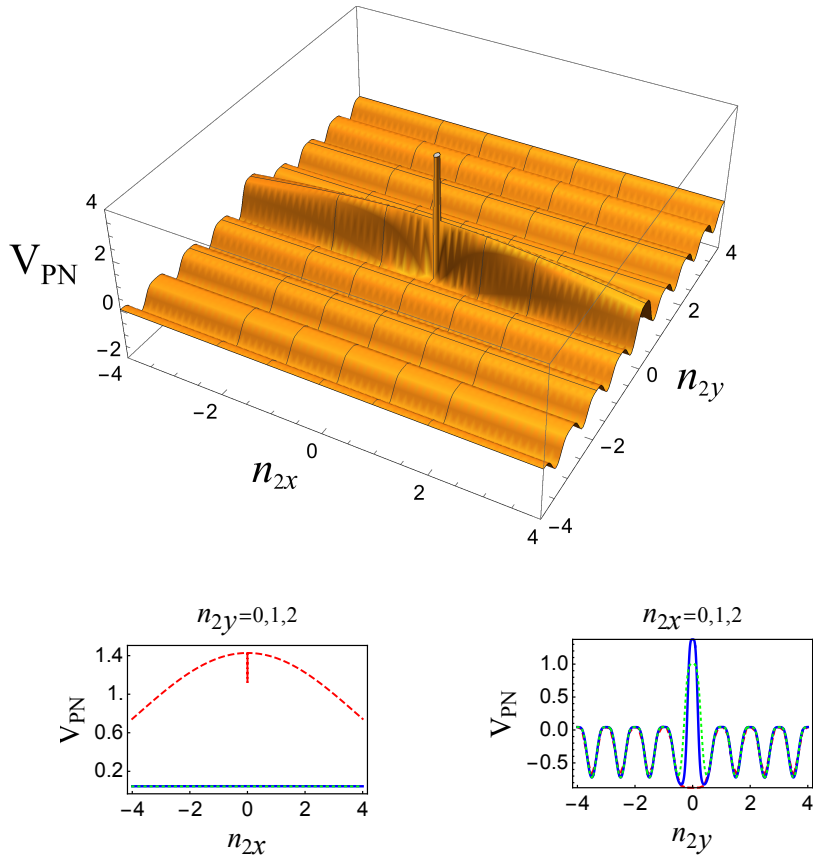


Figure 4.12: Out-of-phase PN potential for the anisotropic case (upper panel), and its two cross-section profiles (lower panel). Parameters used are the same as in Figure 4.11 but with $\phi = \pi$. Red dashed corresponds to $n_{2y} = 0$ and $n_{2x} = 0$ for the left and right subfigures, respectively. Solid blue corresponds to $n_{2y} = 1$ and $n_{2x} = 1$, and dotted green corresponds to $n_{2y} = 2$ and $n_{2x} = 2$.

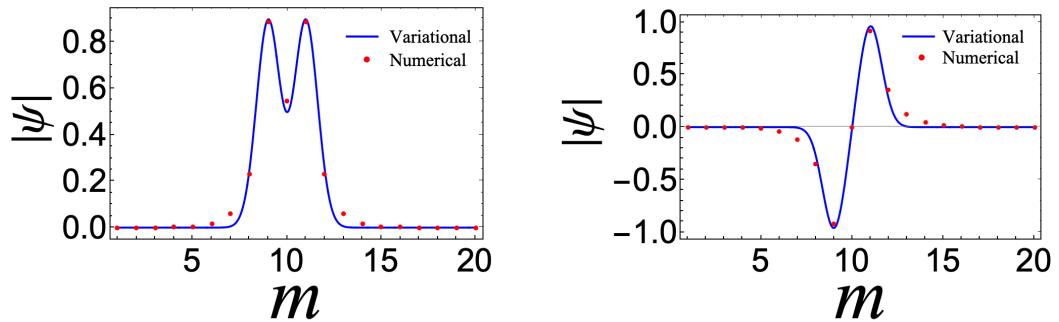


Figure 4.13: In-phase and out-of-phase anisotropic soliton molecules obtained by both numerical (red dots) and variational method (blue solid line) for the choice of parameters $L = 20, P = 2, \gamma = 4, dx = 2$ and $dy = 0.2$ with $\phi = 0$ (left) and π (right).

if the two solitons are located at the same waveguide, they will coalesce.

Locating the solitons at different waveguides prevents them from coalescing due to the potential barrier existing in between them. Nonetheless, the two solitons can still interact

through the overlap of their tails across the waveguides. Therefore, while the two solitons will be completely mobile in the horizontal direction, they are restricted to move only along their respective waveguides. This results in a special kind of a soliton molecule where the stability is provided by the PN potential and energy exchange is provided by the soliton-soliton interaction. Comparing Figures 4.11 and 4.12 shows that molecule formation is possible only for the in-phase solitons. Out-of-phase solitons are always expelled out of the waveguide because their force of interaction is repulsive.

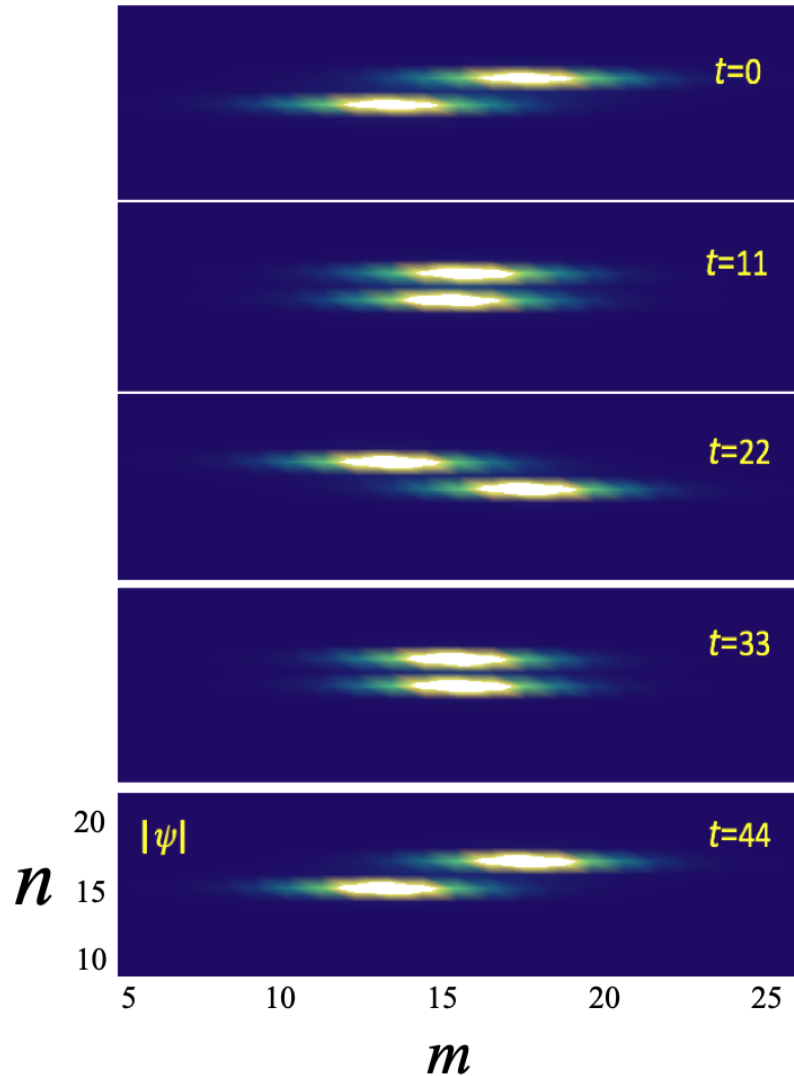


Figure 4.14: Soliton molecule in anisotropic PN potential (in-phase) given in Figure 4.11 along horizontal direction by means of numerical simulation of Equation (4.1) and using the parameters $L = 30$, $P=2$, $\gamma=3$, $d_x = 3$, $d_y = 0.15$. The two solitons are located initially at $n_{1x} = L/2 - 2$, $n_{2x} = L/2 + 2$, $n_{1y} = L/2$, $n_{2y} = L/2 + 2$.

Inspired by the above prediction of the variational calculation, we performed a numerical simulation of the two in-phase solitons separated initially by two waveguides in the y -direction and by an arbitrary nonzero initial separation in the x -direction. The dynamics of the solitons is then obtained by solving numerically the DNLSE, Equation (4.1). The resulting dynamics is shown in Figure 4.14. The two solitons oscillate around their center of mass indicating the formation of a soliton bound state. The trajectories of the two solitons are shown in Figure 4.15.

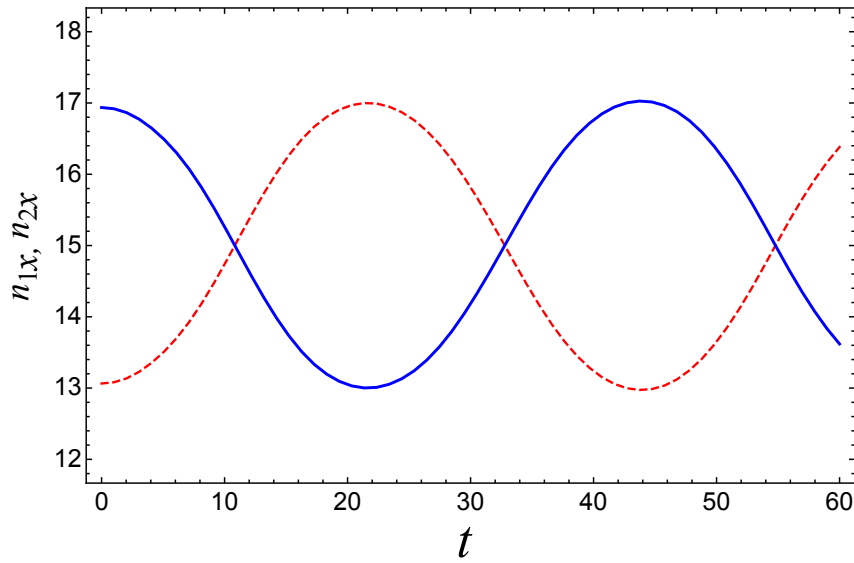


Figure 4.15: Trajectories of the two solitons corresponding to the soliton molecule of Figure 4.14.

The potential of interaction between the two solitons can be obtained from their trajectories. By calculating the soliton separation $\Delta n(t) = n_{2x}(t) - n_{1x}(t)$ and differentiating it twice to obtain the force $F = \mu d^2/dt^2 \Delta n(t)$, where μ is the *reduced effective mass* of the two solitons, we then calculate the potential by integrating the force with respect to $\Delta n(t)$,

$$V = - \int_{\Delta n_{x_{min}}}^{\Delta n_{x_{max}}} F(\Delta n) d(\Delta n), \quad (4.13)$$

where Δn_{min} and Δn_{max} are the minimum and maximum solitons separation.

In Figure 4.16, we show the potential calculated numerically from Equation (4.1). The potential is parabolic and the force of interaction is linear. This indicates that the soliton molecule can be modeled by a classical system of two masses attached to a spring. It

will be constructive to compare the numerical potential with the variational one. This is performed using both a gaussian ansatz, as given by Equation (4.5), and an exponential ansatz given by

$$\Psi_{m,n} = A \left(e^{-\frac{|m-n_{1x}|}{\eta_1} - \frac{|n-n_{1y}|}{\eta_2}} + e^{-\frac{|m-n_{2x}|}{\eta_1} - \frac{|n-n_{2y}|}{\eta_2} + i\phi} \right). \quad (4.14)$$

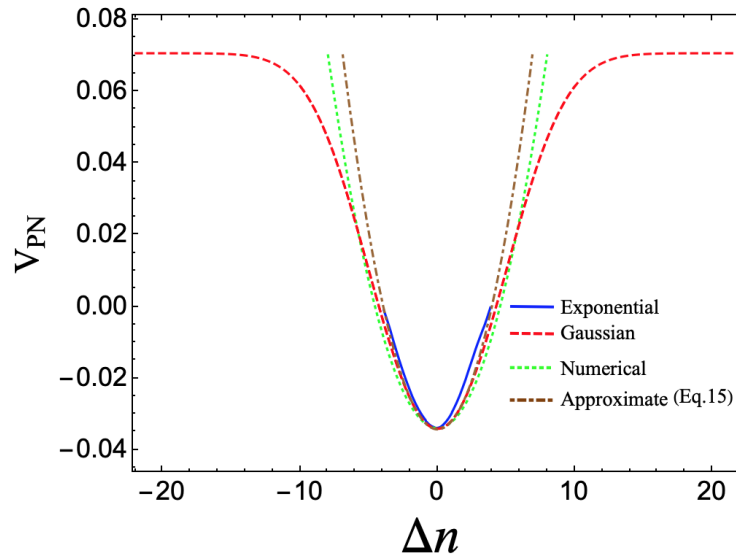


Figure 4.16: The potential of interaction between two solitons in a soliton molecule obtained by: i) the numerical solution of Equation (4.1) and the trajectories of the two solitons in Figure 4.15 (blue solid line), ii) variational calculation using a gaussian ansatz, Equation (4.5), (red dashed line), and iii) variational calculation using an exponential trial function, Equation (4.14), (green dotted line). The dashed-dotted line corresponds to the simplified analytical expression Equation (4.15). Parameters used are those of Figure 4.14.

Both trial functions lead to excellent agreement between the variational and numerical results, as Figure 4.16 clearly shows. It should be noted that an arbitrary constant of integration resulting from the integration in Equation (4.13) gave us the freedom to shift the numerical potential vertically in order to match the variational one. The curvature, on the other hand fits naturally. The above-mentioned analogy with the classical two-masses-spring system suggests that the potential of interaction between the solitons to be parabolic in terms of their separation. Indeed, an accurate simplified analytical expression for the potential of interaction between the two solitons in terms of their separation, Δn ,

can be derived by expanding the energy functional to the quadratic order, as given by

$$V_{PN} = V_0 + \frac{1}{2}k\Delta n^2, \quad (4.15)$$

where V_0 and k are given in terms of the parameters dx , dy , γ , and the soliton widths η_1 and η_2 , as detailed in Appendix 8. In a classical system of two masses attached to a spring, the period of oscillation is given by $\tau = 2\pi\sqrt{\mu/k}$. The period of the soliton molecule can thus be estimated for a specific setup. For instance, for the parameters used to generate the soliton molecule shown in Figure 4.14, the spring constant k can be calculated as given by Equation (A.12). The effective mass of a single soliton is given by the inverse of the second derivative of the energy with respect to the momentum, which in our case will be $2Pd_x$. The reduced mass of the two solitons is thus $\mu = 1/2d_x$. For the parameters of Figure 4.14, the estimate leads to $\tau \approx 39$, which is less the 10% off the numerical value of $\tau = 43.5$. This indicates that the force between the two solitons is indeed a Hooke-type of restoring force

$$F = -k\Delta n. \quad (4.16)$$

It should be noted, however that this applies for short solitons separations. For larger separations, the potential becomes constant and the force decays exponentially. This corresponds to the constant plateaus in the x -cross section of the V_{PN} potential for large solitons separation, as shown in Figures 4.16 and A.1.

4.5.3 Soliton Fission

We consider a soliton molecule of two out-of-phase solitons placed at different waveguides. Basically this is similar to the soliton molecule considered in the previous section but with out-of-phase solitons that are initially not separated from each other. Interestingly, we found this to be a metastable state with a long lifetime after which it suddenly splits into two solitons propagating away from each other. We named this behavior as

'soliton fission'. Figure 4.17 shows the splitting of the soliton molecule.

We see that the solitons remain coalescing up to $t = 80$ which is almost double the period of the soliton molecule of the previous case. The two solitons keep their coalescence as one soliton and exhibit only a small vibration in the amplitude. The soliton molecule then suddenly splits into two solitons propagating away from each other. Figure 4.18 shows the trajectories of two solitons before and after splitting.

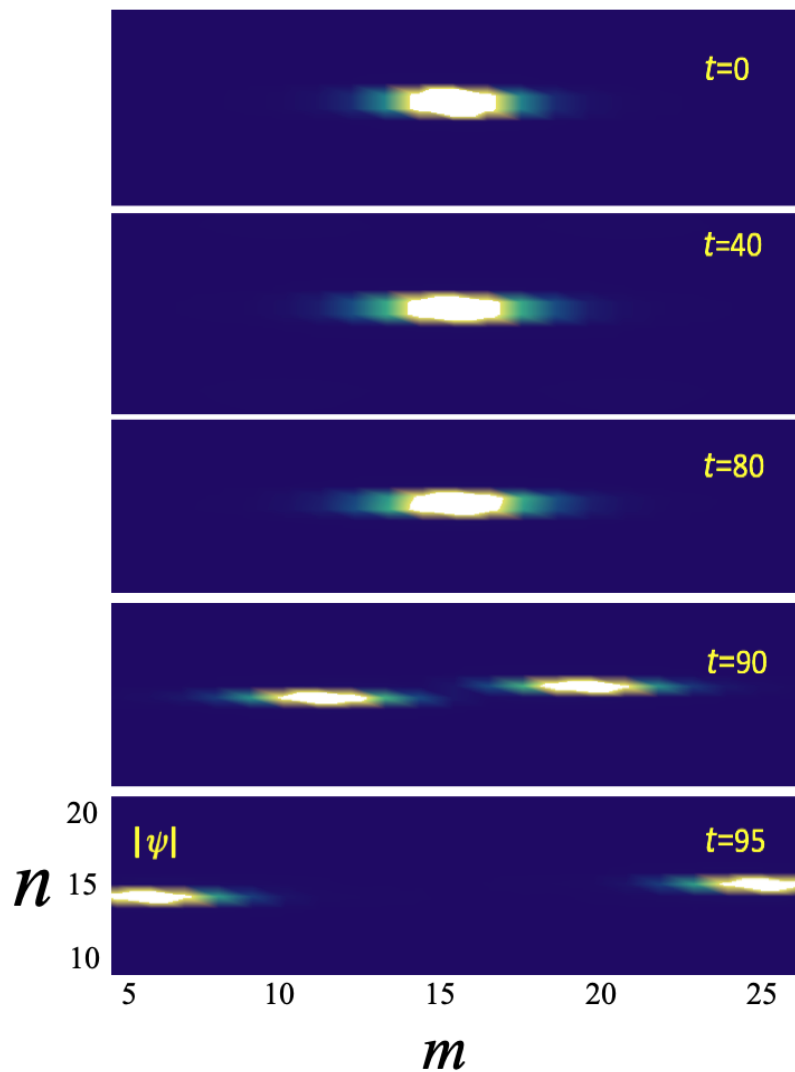


Figure 4.17: Splitting of the soliton molecule. Parameters used: $P=2$, $\gamma=4$, $d_x=3$, $d_y=0.15$, $\eta_1=3.86$ and $\eta_2=0.76$, $\phi=\pi$, and initial positions $n_{2x}=n_{1x}=L/2$, $n_{1y}=L/2$, $n_{2y}=L/2+1$.

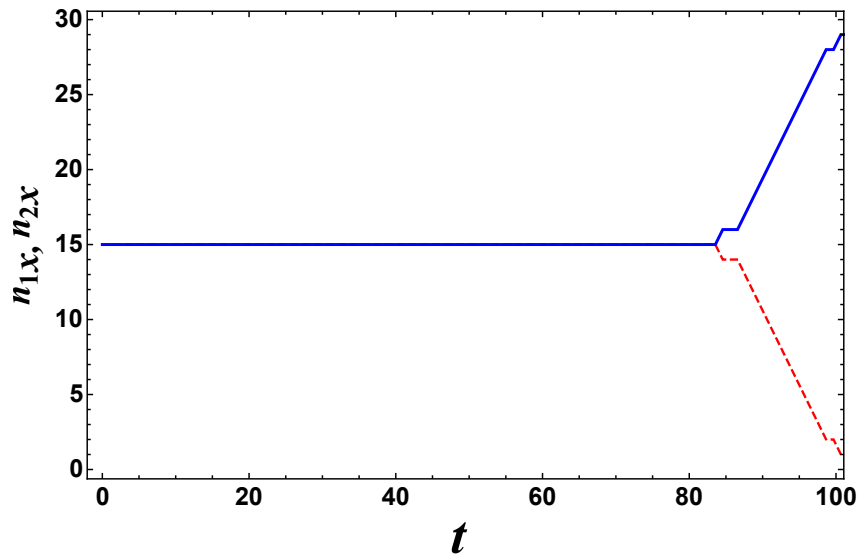


Figure 4.18: Trajectories of the two solitons forming the soliton molecule of Figure 4.17.

4.6 Conclusions

We have used both numerical and variational calculations to obtain the equilibrium profiles and ground state of discrete two-soliton molecules in 2D waveguide arrays. Using a gaussian variational trial function, Equation (4.5), with six variational parameters corresponding to the coordinates peak positions and widths of the two solitons, we calculated the PN potential and the interaction potential between the solitons. We have investigated the mobility of the soliton molecule and found that binding does not enhance on the mobility. Neither the bond length nor the direction of the molecule's motion had a tangible effect of the mobility. We have shown the existence of stable discrete soliton molecules in two-dimensional waveguide arrays. Analogy was made to the classical diatomic model with linear restoring force. A simplified expression for the force and potential of interaction were derived, Equations (4.15) and (4.16). We have also found a unique behavior of a meta stable state of a soliton molecule made of two out-of-phase solitons each placed in a different waveguide. Such a molecule shows a sudden splitting into two solitons propagating away from each other. We believe our results will be valuable for the all-optical applications using solitons to perform optical data processing.

Chapter 5: Mapping the Spin-1/2 System to 2D Manakov System

In this chapter, we find Skyrmion-like topological excitations for a two-dimensional spin-1/2 system. Expressing the spinor wavefunction in terms of a rotation operator maps the spin-1/2 system to a Manakov system. We employ both analytical and numerical methods to solve the resulting Manakov system. Using a generalized similarity transformation, we reduce the two-dimensional Manakov system to the integrable one-dimensional Manakov system. Solutions obtained in this manner diverge at the origin. We employ a power series method to obtain an infinite family of localized and nondiverging solutions characterized by a finite number of nodes. A numerical method is then used to obtain a family of localized oscillatory solutions with an infinite number of nodes corresponding to a skyrmion composed of concentric rings with intensities alternating between the two components of the spinor. We investigate the stability of the skyrmion solutions found here by calculating their energy functional in terms of their effective size. It turns out that indeed the skyrmion is most stable when the phase difference between the concentric rings is π , i.e., alternating between spin up and spin down. Our results are also applicable to doubly polarized optical pulses.

5.1 Introduction

We are motivated to investigate the behaviour and stability of two-dimensional topological excitations in spin-1/2 system through a novel approach. We start with the calculation of rotation operator which is used to map the spin 1/2 system into a Manakov system that is considered as a model of wave propagation in fiber optics and provides the spin texture of skyrmions. The challenge is to solve the obtained 2D Manakov system, in order to find the nontrivial spin texture. We solved the 2D Manakov system through various analytical and numerical techniques. We used similarity transformation and found all solutions to diverge at the origin, $\rho = 0$. Then, we found nondiverging densities through power series method but with trivial textures. Finally, we used a numerical method to find nondiverging

and nontrivial spin textures. The stability of these nondiverging and nontrivial skyrmions is also investigated. We show that the two spin states (spin up and spin down) are in fact responsible for the stability of two-dimensional topological excitations.

This chapter is organized as follows. In Section 5.2 we calculate the spinor wavefunction and texture for all the possible cases of rotations. Mapping the spin-1/2 system to a 2D Manakov system is described in Section 5.3. In Section 5.4, we solve the Manakov system to obtain nondiverging and nontrivial skyrmions. We applied similarity transformation in Section 5.4.1, power series method in Section 5.4.2 and numerical method in Section 5.4.3. The stability of the nondiverging and nontrivial skyrmions is investigated in Section 5.5. Finally, we conclude by summarizing our main results in Section 5.6.

5.2 Two-Dimensional Skyrmions

A spinor wavefunction contains two degrees of freedom: total density $n(\mathbf{r}, t)$ and the spinor $\zeta(\mathbf{r})$ which has two components since we consider spin-1/2. The total wavefunction is thus written as

$$\Psi(\mathbf{r}, t) = \sqrt{n(\mathbf{r}, t)} \zeta(\mathbf{r}), \quad (5.1)$$

which obeys the NLSE

$$i \frac{\partial}{\partial t} \Psi(\mathbf{r}, t) = -\nabla^2 \Psi(\mathbf{r}, t) - \gamma |\Psi(\mathbf{r}, t)|^2 \Psi(\mathbf{r}, t). \quad (5.2)$$

The spin part of the wavefunction, $\zeta(\mathbf{r})$, can be parametrized by a rotation operator as

$$\zeta(\mathbf{r}) = \exp \left\{ -\frac{i}{S} \boldsymbol{\omega}(\mathbf{r}) \cdot \mathbf{S} \right\} \zeta. \quad (5.3)$$

Here \mathbf{S} is the spin matrix, $\mathbf{S} = \sigma_x \hat{x} + \sigma_y \hat{y} + \sigma_z \hat{z}$, with σ_x , σ_y and σ_z being the Pauli matrices. This operator amounts to a rotation of the constant spin ζ around the vector $\boldsymbol{\omega}(\mathbf{r})$. Considering spherically symmetric spin textures and restricting the general rotation operator to be around the vector \mathbf{r} by an angle of $\omega(\mathbf{r})$ gives $\boldsymbol{\omega}(\mathbf{r}) = \omega(\mathbf{r}) \hat{\mathbf{r}}$ as depicted schematically

in Figure 5.1. Average spin at a position r is rotated by an angle $\omega(r)/S$ from its initial orientation. An explicit form of $\omega(r)$ determines a specific texture of the skyrmion. The constant spin ζ can be taken as any of the eigenvectors of the Pauli spin matrices, namely

$$\zeta_x = \frac{1}{\sqrt{2}} \begin{pmatrix} 1 \\ 1 \end{pmatrix}; \quad \text{eigenstate for } \sigma_x, \quad (5.4)$$

$$\zeta_y = \frac{1}{\sqrt{2}} \begin{pmatrix} 1 \\ i \end{pmatrix}; \quad \text{eigenstate for } \sigma_y, \quad (5.5)$$

$$\zeta_z = \begin{pmatrix} 1 \\ 0 \end{pmatrix}; \quad \text{eigenstate for } \sigma_z. \quad (5.6)$$

The rotation operator can be reduced to a useful formula as:

$$\exp \left\{ -\frac{i}{S} \omega(r) \hat{\mathbf{r}} \cdot \mathbf{S} \right\} = \mathbf{I} \cos[\omega(r)] - 2i(\hat{\mathbf{r}} \cdot \mathbf{S}) \sin[\omega(r)], \quad (5.7)$$

where \mathbf{I} is the identity matrix. Using this formula, the spinor wavefunction takes the form

$$\Psi(\mathbf{r}, t) = \sqrt{n(\mathbf{r}, t)} \times \begin{pmatrix} \cos[\omega(r)] - i \cos(\theta) \sin[\omega(r)] \\ \sin(\theta) \left(-i \cos(\phi) + \sin(\phi) \right) \sin[\omega(r)] \end{pmatrix}, \quad (5.8)$$

where we have taken $\zeta = \begin{pmatrix} 1 \\ 0 \end{pmatrix}$. It is then straightforward to obtain the spin texture in terms of the average spin components

$$\langle S_x \rangle = \zeta^\dagger(r) S_x \zeta(r), \quad (5.9)$$

$$\langle S_y \rangle = \zeta^\dagger(r) S_y \zeta(r), \quad (5.10)$$

$$\langle S_z \rangle = \zeta^\dagger(r) S_z \zeta(r). \quad (5.11)$$

In the present work, we restrict the investigation to two-dimensional spin textures. To obtain a two-dimensional spin texture, we consider the three possible planes, namely xz -, yz -, and xy -planes. We consider the three possible initial spinors, namely ζ_x , ζ_y , and ζ_z and the three possible rotation axes, namely x -, y -, and z -axes. We consider also an interesting case with rotations in the xy -plane around the ρ -axis. Inspecting all possible cases, we found only three fundamentally and nontrivial different types of textures. The first is constructed by spins rotated around a fixed axis normal to the plane. The second is obtained when the spins are rotated around a fixed axis parallel to the plane. The third is obtained when spins are rotated around ρ in the xy -plane. In the following we show the details for calculating the three spin textures. Considering rotations around x , y , z , or ρ -axis, we replace \hat{r} by \hat{x} , \hat{y} , \hat{z} , or $\hat{\rho}$, respectively.

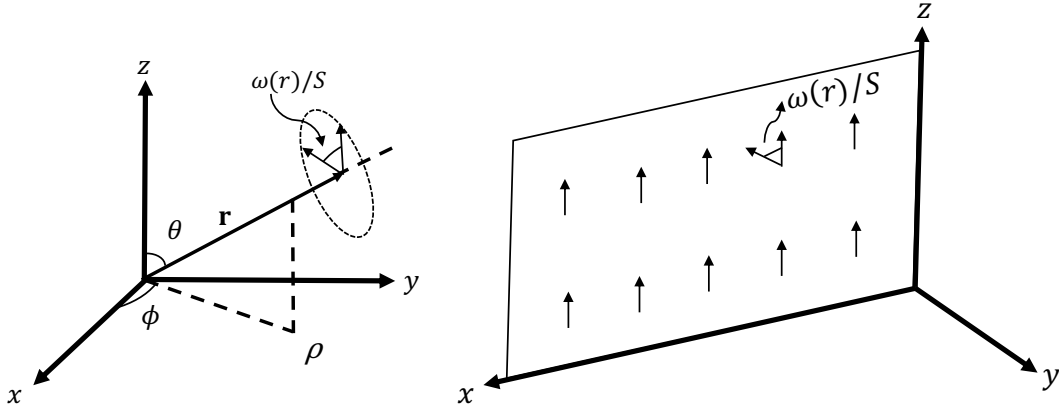


Figure 5.1: Schematic figure on left representing the action of the spin rotation operator for a maximally symmetric skyrmion while on right the rotation is around y -axis in xz -plane with initial spin along z -axis.

Rotations in the xz -plane: We consider rotations in xz -plane with axis of rotation being the x -axis, we choose the initial orientation along z -direction and hence use the eigenvector of S_z , namely, ζ_z , for the operation. The average spin components are given by

$$\langle S_x \rangle, \langle S_y \rangle, \langle S_z \rangle = \left(0, -\frac{\sin[2\omega(\rho)]}{2}, \frac{\cos[2\omega(\rho)]}{2} \right). \quad (5.12)$$

The spinor takes the form

$$\zeta(\mathbf{r}) = \begin{pmatrix} \cos[\omega(\rho)] \\ -i \sin[\omega(\rho)] \end{pmatrix}. \quad (5.13)$$

This corresponds to spin rotations out of the plane, i.e., around an axis parallel to the plane.

Considering rotations around the y -axis, the average spin components become

$$\langle S_x \rangle, \langle S_y \rangle, \langle S_z \rangle = \left(\frac{\sin[2\omega(\rho)]}{2}, 0, \frac{\cos[2\omega(\rho)]}{2} \right), \quad (5.14)$$

and the spinor becomes

$$\zeta(\mathbf{r}) = \begin{pmatrix} \cos[\omega(\rho)] \\ \sin[\omega(\rho)] \end{pmatrix}. \quad (5.15)$$

This spin texture corresponds to spin rotations within the plane, i.e., around an axis perpendicular to the plane. Considering the rotations around z -axis, we get:

$$\zeta(\mathbf{r}) = \begin{pmatrix} \cos[\omega(\rho)] - i \sin[\omega(\rho)] \\ 0 \end{pmatrix}, \quad (5.16)$$

and the average spin components are:

$$\langle S_x \rangle, \langle S_y \rangle, \langle S_z \rangle = (0, 0, 1/2), \quad (5.17)$$

which is trivial case because it corresponds to spin rotations around the same axis along which the spins are aligned, and thus will be ignored. The spinor and the average spin components for all the possible cases of rotations around fixed axes in xz -plane are listed in Table 5.1. Considering other planes leads basically to only these two spin textures.

Table 5.1: All possible cases of rotations in the xz -plane around three possible fixed axes of rotation, x -, y -, and z -axis, with three possible initial spin directions, ζ_x , ζ_y , ζ_z . The spinor wavefunction, $\zeta(\mathbf{r})$, and the average spin components, $\langle S_x \rangle$, $\langle S_y \rangle$ and $\langle S_z \rangle$, are calculated using Equations (5.8 - 5.11).

Rotations in xz -plane around fixed axes			
Axis of rotation	Initial Spin Orientation	$\zeta(\mathbf{r})$	$(\langle S_x \rangle, \langle S_y \rangle, \langle S_z \rangle)$
x -axis $\theta = \pi/2$, $\phi = 0$	ζ_x	$\begin{pmatrix} e^{-i\omega(\rho)} \zeta_x \\ \frac{\cos[\omega(\rho)] + \sin[\omega(\rho)]}{\sqrt{2}} \end{pmatrix}$	$(\frac{1}{2}, 0, 0)$
	ζ_y	$\begin{pmatrix} \frac{\cos[\omega(\rho)] + \sin[\omega(\rho)]}{\sqrt{2}} \\ i(\cos[\omega(\rho)] - \sin[\omega(\rho)]) \end{pmatrix}$	$(0, \frac{\cos[2\omega(\rho)]}{2}, \frac{\sin[2\omega(\rho)]}{2})$
	ζ_z	$\begin{pmatrix} \cos[\omega(\rho)] \\ -i \sin[\omega(\rho)] \end{pmatrix}$	$(0, -\frac{\sin[2\omega(\rho)]}{2}, \frac{\cos[2\omega(\rho)]}{2})$
y -axis $\theta = \pi/2$, $\phi = \pi/2$	ζ_x	$\begin{pmatrix} \frac{\cos[\omega(\rho)] - \sin[\omega(\rho)]}{\sqrt{2}} \\ \cos[\omega(\rho)] + \sin[\omega(\rho)] \end{pmatrix}$	$(\frac{\cos[2\omega(\rho)]}{2}, 0, -\frac{\sin[2\omega(\rho)]}{2})$
	ζ_y	$\begin{pmatrix} e^{-i\omega(\rho)} \zeta_y \\ \sqrt{2} \end{pmatrix}$	$(0, \frac{1}{2}, 0)$
	ζ_z	$\begin{pmatrix} \cos[\omega(\rho)] \\ \sin[\omega(\rho)] \end{pmatrix}$	$(\frac{\sin[2\omega(\rho)]}{2}, 0, \frac{\cos[2\omega(\rho)]}{2})$
z -axis $\theta = 0$, $\phi = \pi/2$	ζ_x	$\begin{pmatrix} \frac{\cos[\omega(\rho)] - i \sin[\omega(\rho)]}{\sqrt{2}} \\ \cos[\omega(\rho)] + i \sin[\omega(\rho)] \end{pmatrix}$	$(\frac{\cos[2\omega(\rho)]}{2}, \frac{\sin[2\omega(\rho)]}{2}, 0)$
	ζ_y	$\begin{pmatrix} \frac{\cos[\omega(\rho)] - i \sin[\omega(\rho)]}{\sqrt{2}} \\ i \cos[\omega(\rho)] - \sin[\omega(\rho)] \end{pmatrix}$	$(-\frac{\sin[2\omega(\rho)]}{2}, \frac{\cos[2\omega(\rho)]}{2}, 0)$
	ζ_z	$\begin{pmatrix} \sqrt{2} \\ e^{-i\omega(\rho)} \zeta_z \end{pmatrix}$	$(0, 0, \frac{1}{2})$

Table 5.2: All possible cases of rotations in the xy -plane around ρ with three possible initial spin directions, ζ_x , ζ_y , ζ_z . The spinor wavefunction, $\zeta(\mathbf{r})$, and the average spin components, $\langle S_x \rangle$, $\langle S_y \rangle$ and $\langle S_z \rangle$, are calculated using Equations (5.8 - 5.11).

Rotations in xy -plane around ρ			
Axis of rotation	Initial spin	$\zeta(\mathbf{r})$	$(\langle S_x \rangle, \langle S_y \rangle, \langle S_z \rangle)$
$\rho = \sqrt{x^2 + y^2}$ $(\theta = \pi/2)$	ζ_x	$\begin{pmatrix} \frac{\cos[\omega(\rho)] - ie^{-i\phi} \sin[\omega(\rho)]}{\sqrt{2}} \\ \cos[\omega(\rho)] - ie^{i\phi} \sin[\omega(\rho)] \end{pmatrix}$	$(\frac{\cos^2[\omega(\rho)] + \cos(2\phi) \sin^2[\omega(\rho)]}{2}, \frac{\sin(2\phi) \sin^2[\omega(\rho)]}{2}, -\frac{\sin(\phi) \sin[2\omega(\rho)]}{2})$
	ζ_y	$\begin{pmatrix} \frac{\cos[\omega(\rho)] + e^{-i\phi} \sin[\omega(\rho)]}{\sqrt{2}} \\ i(\cos[\omega(\rho)] - e^{i\phi} \sin[\omega(\rho)]) \end{pmatrix}$	$(\frac{\sin(2\phi) \sin^2[\omega(\rho)]}{2}, \frac{\cos^2[\omega(\rho)] - \cos(2\phi) \sin^2[\omega(\rho)]}{2}, \frac{\cos(\phi) \sin[2\omega(\rho)]}{2})$
	ζ_z	$\begin{pmatrix} \cos[\omega(\rho)] \\ e^{-i(\frac{\pi}{2} - \phi)} \sin[\omega(\rho)] \end{pmatrix}$	$(\frac{\sin(\phi) \sin[2\omega(\rho)]}{2}, -\frac{\cos(\phi) \sin[2\omega(\rho)]}{2}, \frac{\cos[2\omega(\rho)]}{2})$

Rotations in the xy -plane around ρ : We consider the rotations around $\rho = \sqrt{x^2 + y^2}$. Since the axis of rotation changes with ϕ , the spinor components and the texture demand also on ϕ , as listed in Table 5.2.

5.3 Mapping the Spin-1/2 System to 2D Manakov System

We have shown in the previous section that the spinor wavefunction of a skyrmion can be written in a specific form that corresponds to spin rotations. There are many such specific forms depending on the plane at which the spins are located in, the axis of spin rotations, and the initial spin orientation, as summarized by Tables 1 and 2. This procedure is effectively a change of variables amounting to a change in the representation from the spinor components, ψ_1 and ψ_2 , to the total density n and angle of rotation ω/S .

Considering one of these specific cases, namely spinors restricted to the xz -plane with spin rotations around the y -axis as shown schematically in Figure 5.1, the spinor becomes

$$\begin{pmatrix} \psi_1(\rho, \phi, t) \\ \psi_2(\rho, \phi, t) \end{pmatrix} = \sqrt{n(\rho, t)} \begin{pmatrix} e^{il_1\phi} \cos[\omega(\rho)] \\ e^{il_2\phi} \sin[\omega(\rho)] \end{pmatrix}, \quad (5.18)$$

where $\rho = \sqrt{x^2 + z^2}$ and ϕ is the angle between ρ and the z -axis. We have added the phase operator $e^{il\phi}$ to allow for non-zero angular momentum of any of the two components. This accounts for an acquired phase while spins are rotated. This spin-1/2 system is then mapped to a 2D Manakov system obtained by substituting the spinor (5.18) in the NLSE, (5.2),

$$\begin{aligned} i \begin{pmatrix} \psi_1(\rho, \phi, t) \\ \psi_2(\rho, \phi, t) \end{pmatrix}_t &= - \begin{pmatrix} \psi_1(\rho, \phi, t) \\ \psi_2(\rho, \phi, t) \end{pmatrix}_{\rho\rho} - \frac{1}{\rho} \begin{pmatrix} \psi_1(\rho, \phi, t) \\ \psi_2(\rho, \phi, t) \end{pmatrix}_{\rho} - \frac{1}{\rho^2} \begin{pmatrix} \psi_1(\rho, \phi, t) \\ \psi_2(\rho, \phi, t) \end{pmatrix}_{\phi\phi} \\ &\quad - \gamma(|\psi_1(\rho, \phi, t)|^2 + |\psi_2(\rho, \phi, t)|^2) \times \begin{pmatrix} \psi_1(\rho, \phi, t) \\ \psi_2(\rho, \phi, t) \end{pmatrix}. \end{aligned} \quad (5.19)$$

The problem then reduces to solving this system, which we describe in the next section. The solutions $\psi_1(\rho, \phi, t)$ and $\psi_2(\rho, \phi, t)$ can then be used in (5.18) to obtain two coupled equations for $n(\rho, t)$ and $\omega(\rho)$. Solving these equations gives the texture of the skyrmion through $\langle S_x \rangle$, $\langle S_y \rangle$, and $\langle S_z \rangle$, as well as its density profile, $n(\rho, t)$.

5.4 Solving the Manakov System

We present different methods of solving the Manakov system (5.19) in order to generate the non-trivial spin texture. All methods mentioned below are well known and powerful techniques in analytical and numerical analysis but our desired results are achieved by the numerical technique described in Section 5.4.3. The other methods paved the way for developing the numerical technique on a trial function, so we include them in this section. At first, we attempt to map the 2D Manakov system (5.19) into the 1D Manakov system which is integrable with many known solutions. While this leads to nontrivial skyrmion textures, the corresponding spinor densities diverge at $\rho = 0$. As an alternative approach we employ a power series method to find well-behaved spinor densities. However, the associated skyrmion texture turns out to be trivial for such a case. Finally, well-behaved spinor densities with nontrivial skyrmion textures are obtained by employing a trial function that takes into account the spin texture of a specific case of rotation as detailed in Tables 5.1 and 5.2, and then solving numerically the NLSE for $n(\rho, t)$ and $\omega(\rho)$.

5.4.1 Similarity Transformation

At first, we transform the 2D Manakov system into the fundamental 1D Manakov system via a simple similarity transformation. This will enable us then to find the new solutions of 2D Manakov system by using all known solutions of the fundamental 1D Manakov system. We start with the simplest case for the solution of 2D Manakov system, namely, the cylindrically symmetric solution. As there is no ϕ dependence in this case, corresponding to $l_1 = l_2 = 0$, we are left with

$$i \begin{pmatrix} \psi_1(\rho, t) \\ \psi_2(\rho, t) \end{pmatrix}_t = - \begin{pmatrix} \psi_1(\rho, t) \\ \psi_2(\rho, t) \end{pmatrix}_{\rho\rho} - \frac{1}{\rho} \begin{pmatrix} \psi_1(\rho, t) \\ \psi_2(\rho, t) \end{pmatrix}_\rho - \gamma(|\psi_1(\rho, t)|^2 + |\psi_2(\rho, t)|^2) \begin{pmatrix} \psi_1(\rho, t) \\ \psi_2(\rho, t) \end{pmatrix}. \quad (5.20)$$

To reduce this system into the integrable 1D Manakov system we apply the following simple transformation

$$\psi_{1,2} = \rho^n \Phi_{1,2} \quad (5.21)$$

to the above 2D Manakov system. The system then reduces to the fundamental 1D Manakov system for $n = -1/2$

$$\psi_{1,2} = \frac{1}{\sqrt{\rho}} \Phi_{1,2}. \quad (5.22)$$

For all solutions of the 1D Manakov system, $\Phi_{1,2}$, that are finite at $\rho = 0$, the solutions of 2D Manakov system $\psi_{1,2}$ diverge at $\rho = 0$. This applies to all known solutions of 1D Manakov system which we have used in Appendix 8, except the solution $(\Phi_1, \Phi_2) \sim (\tanh(\rho), \text{sech}(\rho))$. The $\tanh(\rho)$ part of this particular solution is zero at $\rho = 0$, and thus $\psi_1 \sim \Phi_1/\sqrt{\rho}$ does not diverge at $\rho = 0$. However, the other component $\psi_2 \sim \text{sech}(\rho)/\sqrt{\rho}$ diverges at $\rho = 0$. For all other solutions, both components diverge at $\rho = 0$. To establish the link between the solutions of the 1D and 2D Manakov systems in a rigorous manner, we consider the following most general form of a similarity transformation

$$\begin{aligned} p_1 \left[i \psi_{1_t} + b_{11} \left[\psi_{1_{\rho\rho}} + \frac{1}{\rho} \psi_{1_\rho} \right] + [b_{12} |\psi_1|^2 + b_{13} |\psi_2|^2] \psi_1 + [b_{14r} + ib_{14i}] \psi_1 \right] &= 0, \\ p_2 \left[i \psi_{2_t} + b_{21} \left[\psi_{2_{\rho\rho}} + \frac{1}{\rho} \psi_{2_\rho} \right] + [b_{22} |\psi_1|^2 + b_{23} |\psi_2|^2] \psi_2 + [b_{24r} + ib_{24i}] \psi_2 \right] &= 0, \end{aligned} \quad (5.23)$$

where $p_1, p_2, b_{11}, b_{21}, b_{12}, b_{22}, b_{13}, b_{23}, b_{14r}, b_{24r}, b_{14i}$, and b_{24i} are all functions of (ρ, t) , and are arbitrary real coefficients. We apply the following transformation on the system (5.23)

$$\begin{aligned} \Psi_1(\vec{r}, t) &= A(\rho, t) e^{iB_1(\rho, t)} F[P(\rho, t), T(\rho, t)], \\ \Psi_2(\vec{r}, t) &= A(\rho, t) e^{iB_2(\rho, t)} G[P(\rho, t), T(\rho, t)]. \end{aligned} \quad (5.24)$$

Here, $A(\rho, t)$, $B_1(\rho, t)$, $B_2(\rho, t)$, $P(\rho, t)$, and $T(\rho, t)$ are all defined as real functions. Substituting (5.24) in (5.23) and requiring the resulting equations to take the form of the following fundamental Manakov system

$$\begin{aligned} iF_t(P, T) + a_{11}F_{\rho\rho}(P, T) + [a_{12}|F(P, T)|^2 + a_{13}|G(P, T)|^2]F(P, T) &= 0, \\ iG_t(P, T) + a_{21}G_{\rho\rho}(P, T) + [a_{22}|F(P, T)|^2 + a_{23}|G(P, T)|^2]G(P, T) &= 0, \end{aligned} \quad (5.25)$$

gives a set of equations for the unknown functions. Solutions of these equations are relegated to Appendix 8. We listed few solutions for the 2D Manakov system obtained using this approach in Appendix 8. Here again, we end up with the solutions having divergences at $\rho = 0$ and therefore they will be discarded for no physical significance. Seeking solutions which are well-behaved at $\rho = 0$, we employ in the next section an Iterative Power Series (IPS) method [174].

5.4.2 Power Series Method

We apply the IPS method with a stationary solution given by

$$\begin{aligned} \psi_1(\rho, t) &= Z_1(\rho) e^{i\alpha_1 t}, \\ \psi_2(\rho, t) &= Z_2(\rho) e^{i\alpha_2 t}, \end{aligned} \quad (5.26)$$

where $Z_1(\rho)$ and $Z_2(\rho)$ are real functions and α_1 and α_2 are arbitrary real constants. Using this solution, Equation (5.20) renders to the following ordinary differential equations

$$\begin{aligned} \frac{1}{\rho} Z_1'(\rho) + Z_1''(\rho) + Z_1(\rho) [\gamma Z_2^2(\rho) - \alpha_1] + \gamma Z_1^3(\rho) &= 0, \\ \frac{1}{\rho} Z_2'(\rho) + Z_2''(\rho) + Z_2(\rho) [\gamma Z_1^2(\rho) - \alpha_2] + \gamma Z_2^3(\rho) &= 0. \end{aligned} \quad (5.27)$$

In the following, we give a brief algorithm description of the IPS method for obtaining a convergent power series solution to (5.27):

Expand $Z_1(\rho)$ and $Z_2(\rho)$ in power series around an arbitrary real initial point ρ_0 :

$$Z_1(\rho) = a_0 + a_1(\rho - \rho_0) + \sum_{n=2}^{n_{max}} a_n(\rho - \rho_0)^n,$$

$$Z_2(\rho) = b_0 + b_1(\rho - \rho_0) + \sum_{n=2}^{n_{max}} b_n(\rho - \rho_0)^n.$$

Set initial values $\{a_0, a_1\}$ and $\{b_0, b_1\}$ for $Z_1(\rho)$ and $Z_2(\rho)$, respectively.

Substitute in (5.27) to obtain the recursion relation for a_n and b_n in terms of $a_0, a_1, b_0,$ and b_1 .

Calculate $Z_1(\Delta), Z_1'(\Delta), Z_2(\Delta),$ and $Z_2'(\Delta)$, where $\Delta = (\rho - \rho_0)/I$ and I is an integer larger than 1.

Assign: $a_0 = Z_1(\Delta), a_1 = Z_1'(\Delta), b_0 = Z_2(\Delta),$ and $b_1 = Z_2'(\Delta)$.

Obtain a_n and b_n in terms of $a_0, a_1, b_0,$ and b_1 .

Repeat steps 2-6 I times.

At the I th step, a_0 will correspond to the power series of $Z_1(\rho)$ and b_0 will correspond to the power series of $Z_2(\rho)$.

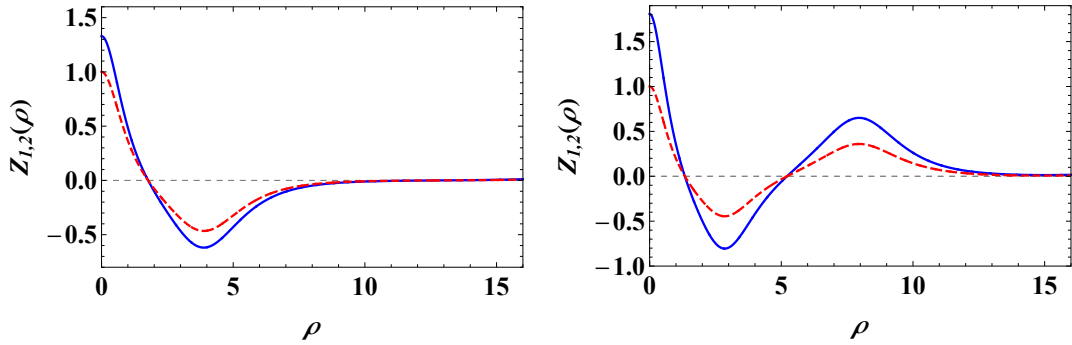


Figure 5.2: Stationary power series solutions of (5.27) with different number of nodes. Dashed (red) is $Z_1(\rho)$ and solid (blue) is $Z_2(\rho)$. The left subfigure is single-node solution with $a_0 = 1.3293391$, root at $r = 1.85$ and the right subfigure is double-node solution with $a_0 = 1.8079999$, roots at $r = 1.58, 5.45$. Parameters used are: $b_0 = 1, a_1 = b_1 = 0, \alpha_1 = \alpha_2 = 0.5, \gamma = 2, n_{max} = 2, I = 5000,$ and $\Delta = 0.0032$.

Employing the algorithm above, we obtain a family of infinite number of convergent solutions by tuning the parameter a_0 and fixing the other parameters. In Figure 5.2, we present two plots showing the single-node and double-node solutions obtained with $I = 5000$ and $n_{max} = 2$. Although this method provides an infinite number of non-divergent densities, due to the scalar symmetry between $\psi_1(\rho, t)$ and $\psi_2(\rho, t)$, the spin textures corresponding to these solutions which is proportional to ψ_2/ψ_1 , turn out to be trivial.

5.4.3 Numerical Solutions

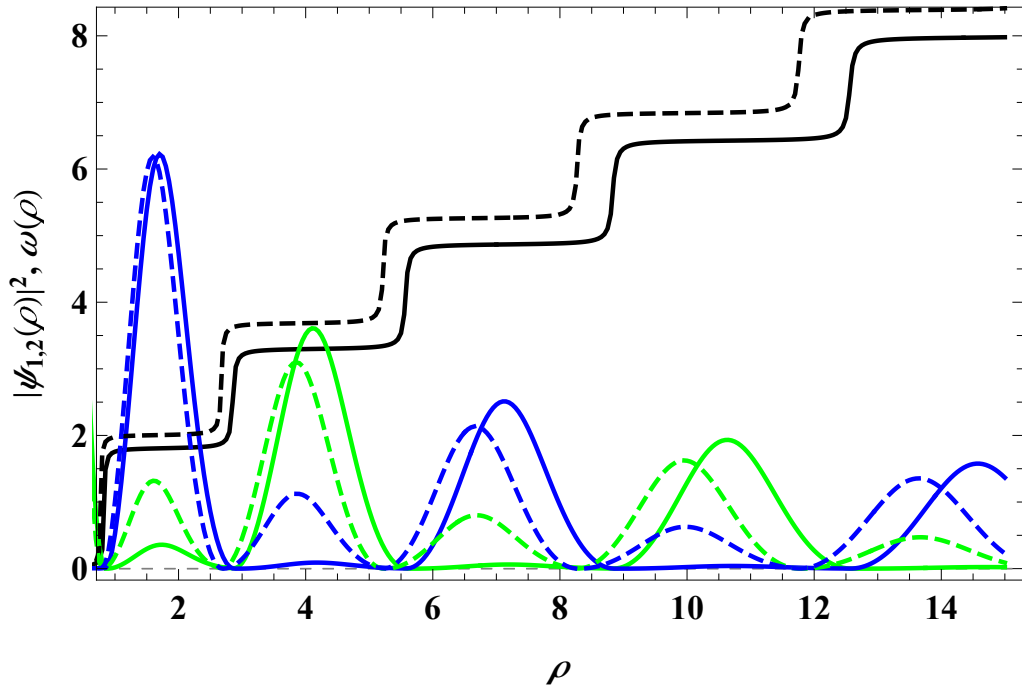


Figure 5.3: The numerical solutions of the spinor components given by Equation (5.28) of the system (5.29) and (5.30). The solutions correspond to alternating spin-up (green) and spin-down (blue) components of the spinor wave function. The black curve corresponds to $\omega(\rho)$. The solid and dashed curves correspond to the circle and square in Figure 5.10, which represent a stable and a metastable skyrmion, respectively. Parameters used are: $\gamma = c_1 = 1/2$, and $a_0 = 2.9$.

Here, we introduce a new procedure that leads to nondiverging and nontrivial spin textures. We start with a trial function which is constructed on the basis of the spinor wave function for rotation cases listed in Tables 5.1 and 5.2. For instance, we consider a case of rotation from Table 5.1 in xz -plane with initial spin along z -axis and y -axis is the axis of rotation.

Our ansatz, for this case becomes:

$$\begin{aligned}\psi_1(\rho, t) &= a(\rho) \cos[\omega(\rho)], \\ \psi_2(\rho, t) &= a(\rho) \sin[\omega(\rho)],\end{aligned}\tag{5.28}$$

where $a(\rho) = \sqrt{n(\rho)}$. Substituting this trial function into the system given in Equation (5.20) and then requesting the coefficients of $\cos[\omega(\rho)]$ and $\sin[\omega(\rho)]$ to vanish sep-

arately, we get two coupled equations in terms of $a(\rho)$ and $\omega(\rho)$

$$2a'(\rho)\omega'(\rho) + a(\rho)\left(\frac{\omega'(\rho)}{\rho} + \omega''(\rho)\right) = 0, \quad (5.29)$$

$$\gamma a^3(\rho) + \frac{a'(\rho)}{\rho} - a(\rho)\left(\frac{1}{4\rho^2} + \omega'^2(\rho)\right) + ra'(\rho) = 0. \quad (5.30)$$

We solve Equation (5.29) for $\omega(\rho)$ as

$$\omega(\rho) = \int \frac{c_1}{\rho a(\rho)^2} d\rho + c_2, \quad (5.31)$$

where c_1 and c_2 are constants of integration. By substituting the above relation for $\omega(\rho)$ in Equation (5.30), our problem (5.20) is reduced into the following single equation

$$c_1^2 - \gamma \rho^2 a^6 - \rho a^3 (a' + \rho a'') = 0. \quad (5.32)$$

We solve this equation for $a(\rho)$ numerically. The initial conditions used are $a(0) = a_0$ and $a'(0) = 0$. We choose a_0 as the tuning parameter for the calculation. The results are shown in Figure 5.3.

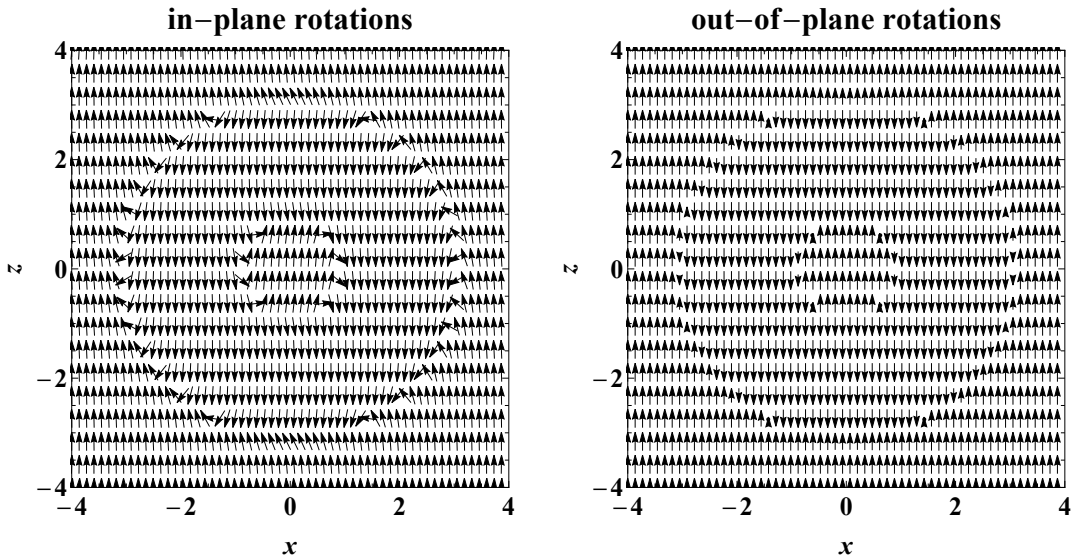


Figure 5.4: In-plane and out-of-plane vector representations of skyrmions in spin-1/2 system for the case of rotation in xz -plane around y -axis and x -axis, respectively with initial spin along z -axis. Parameters used are the same as in Figure 5.3.

Similarly, any of the rotation cases given in Tables 5.1 and 5.2 can be considered for the substitution of $\psi_1(\rho, t)$ and $\psi_2(\rho, t)$. It turns out, however, that all cases of rotations lead to the same Equation (5.32) with the same relation of $\omega(\rho)$ as given in Equation (5.31). All possible cases of rotations discussed in Table 5.1 correspond to the two fundamental types of skyrmions which represent rotation either in-plane or out-of-plane. The rotation of spin around its own axis is a trivial case.

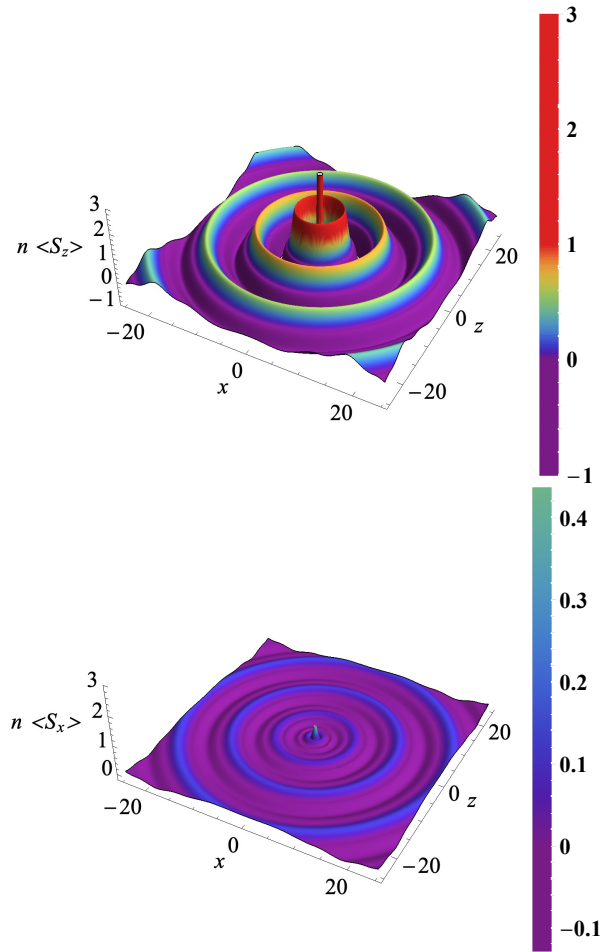


Figure 5.5: False-colour figures representing the average spin texture modulated by the total density, namely $n \langle S_z \rangle$ and $n \langle S_x \rangle$ for a skyrmion in a spin-1/2 system in xz -plane with initial spin along z -axis which is given in Table 5.1. The axis of rotation is y -axis. Parameters used are the same as in Figure 5.3.

The in-plane and out-of-plane spin textures $\langle S_x \rangle$ and $\langle S_z \rangle$ given by the expressions in Table 5.1 for the cases of rotation around y -axis and x -axis, respectively, with initial spin along z -axis are shown in Figure 5.4. These results are obtained from solving the Equation (5.32) numerically. The structure of $\langle S_y \rangle$ is trivial (constant/plain texture) for this

case. These spin textures are, however, modulated by the total density of both spin components. This kind of modulation is applicable for the adjustment of carrier distributions for current density change and light intensity [175] and also for the nonlinear resonator [176]. To show such modulations, we plot in Figure 5.5 the quantities $n \langle S_x \rangle$ and $n \langle S_z \rangle$ for the case of in-plane rotations. In order to find the spin texture of skyrmions for the cases of rotations around ρ in the xy -plane, as listed in Table 5.2, we follow the same procedure as discussed above. However, for the case of rotation around ρ , the spin texture will be dependent not only on the rotation angle $\omega(\rho)$ but also on the projection angle ϕ , as a result we expect fundamentally different skyrmions.

We consider the system (5.19) to be solved for this case which includes also ϕ dependence. Now, we take an example from Table 5.2 of the rotation around ρ in xy -plane with initial spin oriented along z -axis and the trial function becomes

$$\begin{aligned}\psi_1(\rho, \phi, t) &= a(\rho) e^{ik_1\phi} \cos[\omega(\rho)], \\ \psi_2(\rho, \phi, t) &= a(\rho) e^{ik_2\phi} \sin[\omega(\rho)] \times e^{-i(\pi/2-\phi)},\end{aligned}\quad (5.33)$$

where k_1 and k_2 are related as $k_1 = 1 + k_2$.

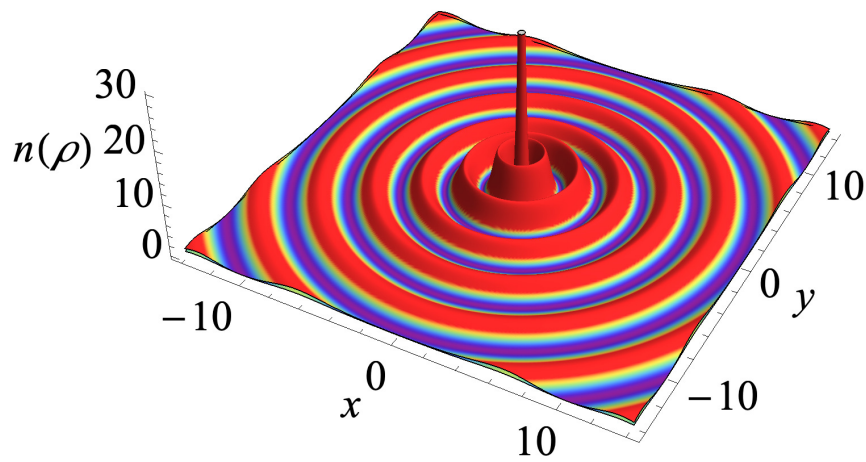


Figure 5.6: The total density for the case of rotation around ρ in xy -plane with initial spin along z -axis.

The total spinor densities for this case are shown in Figure 5.6. It is also noteworthy that all cases of rotation around ρ lead to the same Equation, (5.32). The spin texture for the case of rotation in xy -plane around ρ with initial spin along z -axis is given in Figure 5.7. It can be seen from the figure, that the $\langle S_z \rangle$ component has the same structure as in the previous case shown in Figure 5.4 because there is no ϕ dependence in this component. The vector representation of the skyrmions in spin-1/2 system for the above mentioned rotation is shown below in Figure 5.8. We found two other unique skyrmion textures for the case of rotation around ρ which are shown in Figure 5.9. The orientation of initial spin is along y -axis and the expressions for average spin components are given in Table 5.2. It is clear from the expressions of average spin components given in Table 5.2 that there are four distinguished textures for the case of rotation around ρ , as shown in Figures 5.7 and 5.9. For the case of axial symmetry as discussed in Table 5.1, we have only two fundamental skyrmion textures which are plotted in Figure 5.4.

5.5 Stability of the Non-Trivial Skyrmions

In order to investigate the stability of the skyrmions, we calculated the energy functional for both cases i.e rotation around fixed axes (axial symmetry) as given in Table 5.1 and rotations around ρ which is summarized in Table 5.2. The energy functional corresponding to system (5.19) reads

$$E = \int_0^{2\pi} d\phi \int_0^\infty \left[\alpha \left(|\Psi_1|^2 + |\Psi_2|^2 \right) - \frac{\gamma}{2} \left(|\Psi_1|^2 + |\Psi_2|^2 + 2|\Psi_1|^2 |\Psi_2|^2 \right) + |\Psi_{1\rho}|^2 + |\Psi_{2\rho}|^2 + \frac{1}{\rho^2} \left(|\Psi_{1\phi}|^2 + |\Psi_{2\phi}|^2 \right) \right] \rho d\rho. \quad (5.34)$$

We substitute the specific trial function in Equation (5.34) to find the expression for the energy functional of that specific case of rotation. For instance, we substitute the trial function (5.33) for the case of rotation around ρ in xy -plane with initial spin along z -axis in above relation and find the following expression with $k_1 = 1 + k_2$,

$$E = \int \left[-\frac{1}{2} \gamma a(\rho)^4 + a'(\rho)^2 + \frac{c_1^4}{\rho^2 a(\rho)^2} + \alpha a(\rho)^2 + \frac{a(\rho)^2 (1 + 2k_2 + k_2^2)}{\rho^2} \right] \rho d\rho. \quad (5.35)$$

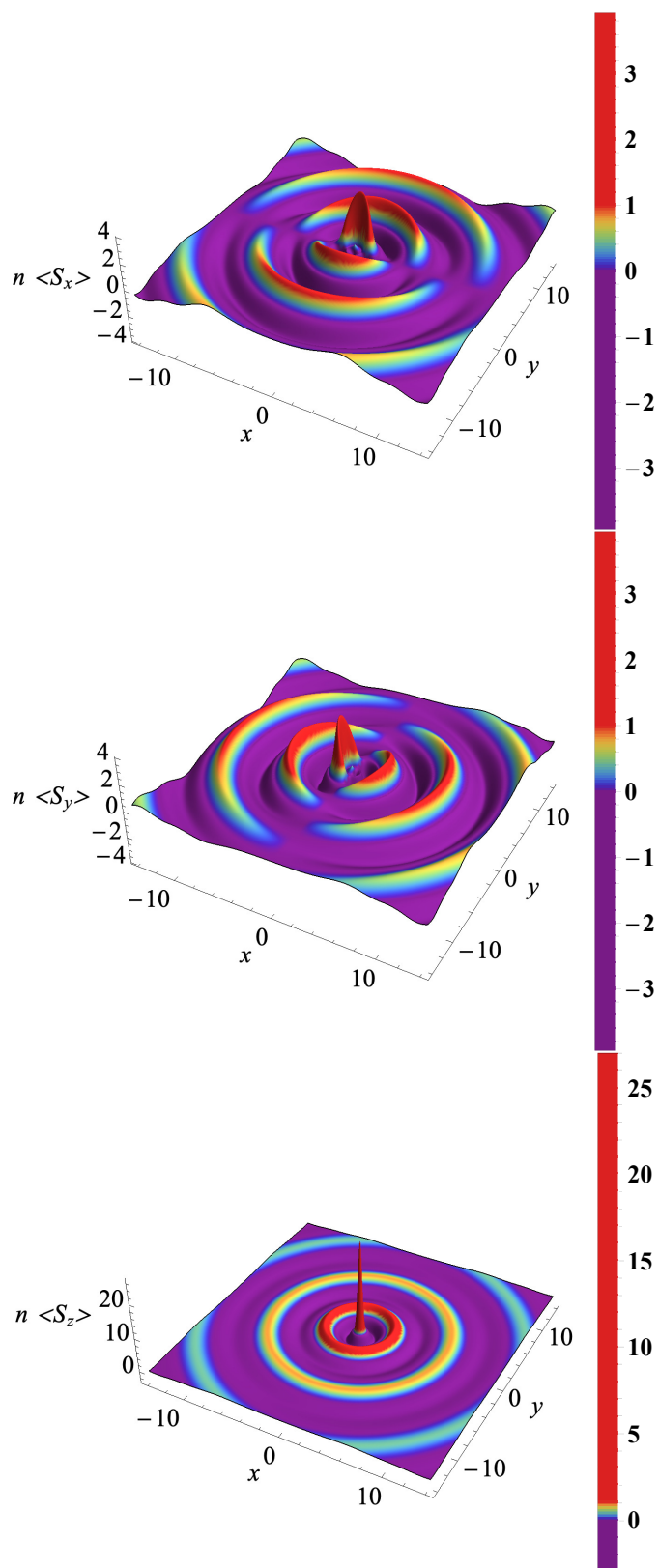


Figure 5.7: False-colour figures representing the average spin $n \langle S_x \rangle$, $n \langle S_y \rangle$, and $n \langle S_z \rangle$ for a skyrmion in a spin-1/2 system with the rotation around ρ in xy -plane. The initial spin orientation is along z -axis.

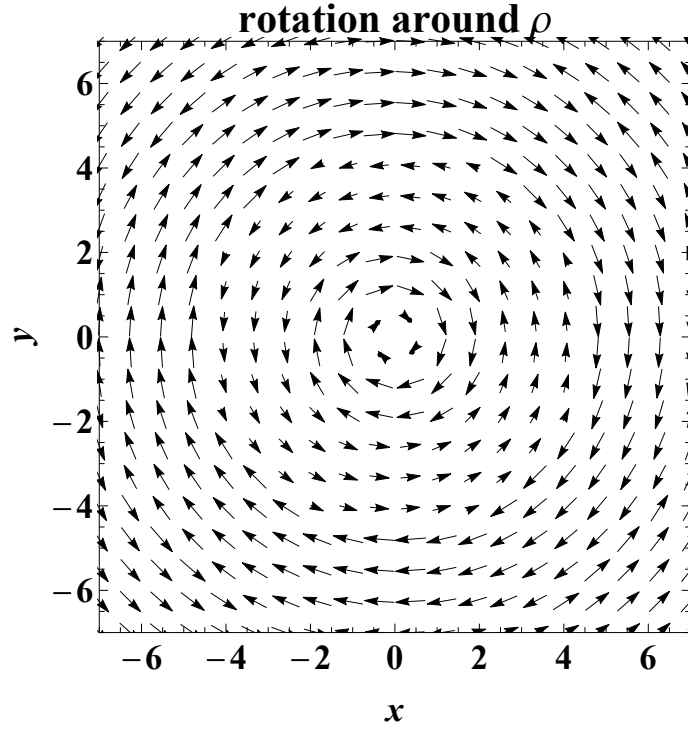


Figure 5.8: The vector representation of skyrmions in spin-1/2 system for the case of rotation around ρ in xy -plane with initial spin along z -axis.

While considering axial symmetry (5.20), for example, rotation around y -axis with initial spin along z -axis, we use the trial function (5.28) into (5.34) and obtain the following result for energy functional

$$E = \int \left[-\frac{1}{2} \gamma a(\rho)^4 + a'(\rho)^2 + \alpha a(\rho)^2 + \frac{c_1^4}{\rho^2 a(\rho)^2} \right] \rho d\rho. \quad (5.36)$$

We find a global minimum in the energy functional as well as many local minima. The local minima correspond to a state of concentric rings with spins alternating sharply between $1/2$ and $-1/2$. The total density within a ring is contributed by only one component of spin, either spin up or spin down. On the other hand, mixed states of spin in which the total density is contributed by both component of spin, i.e spin up and spin down correspond to a metastable skyrmion. The profile of the two spin components corresponding to a stable and a metastable skyrmion (circle and square on the energy curve in Figure 5.10) are shown in Figure 5.3.

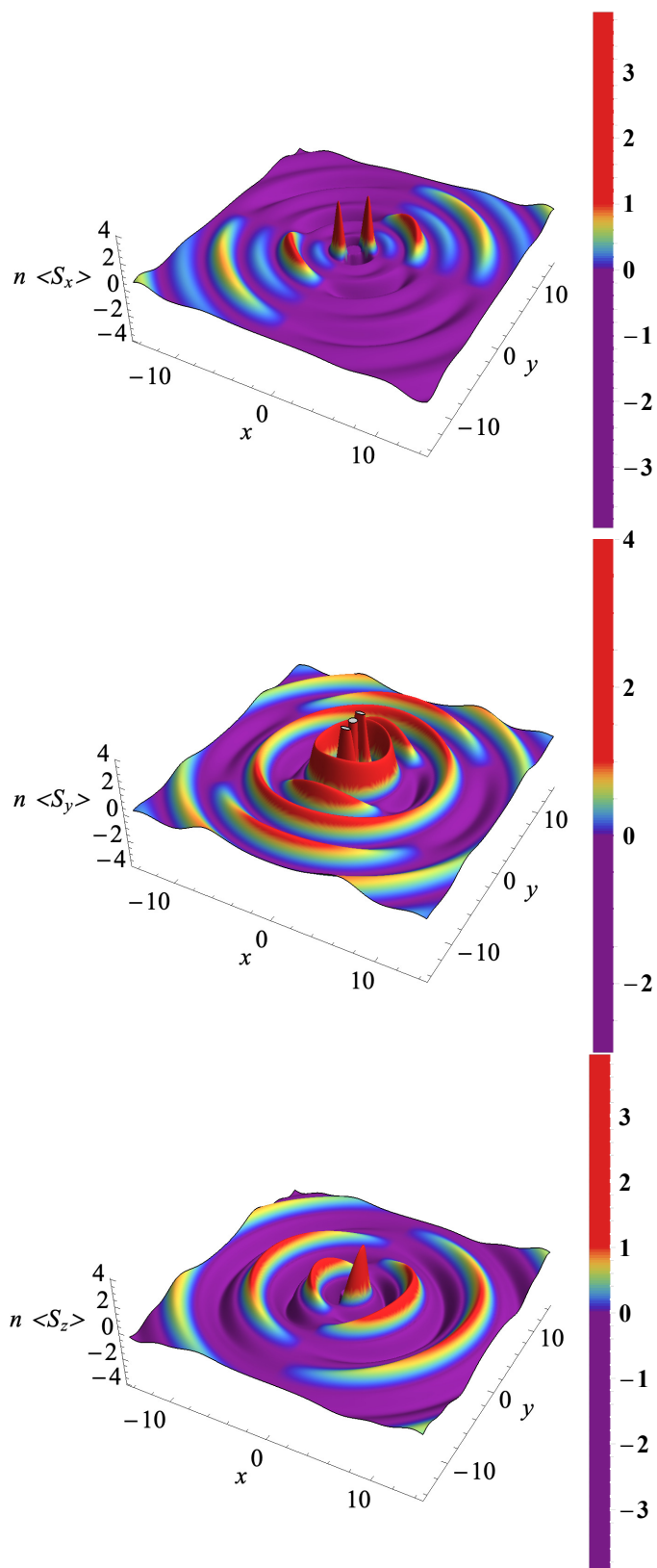


Figure 5.9: False-colour figures representing the average spin $n \langle S_x \rangle$, $n \langle S_y \rangle$, and $n \langle S_z \rangle$ for a skyrmion in a spin-1/2 system with the rotation around ρ in xy -plane. The initial spin orientation is along y -axis.

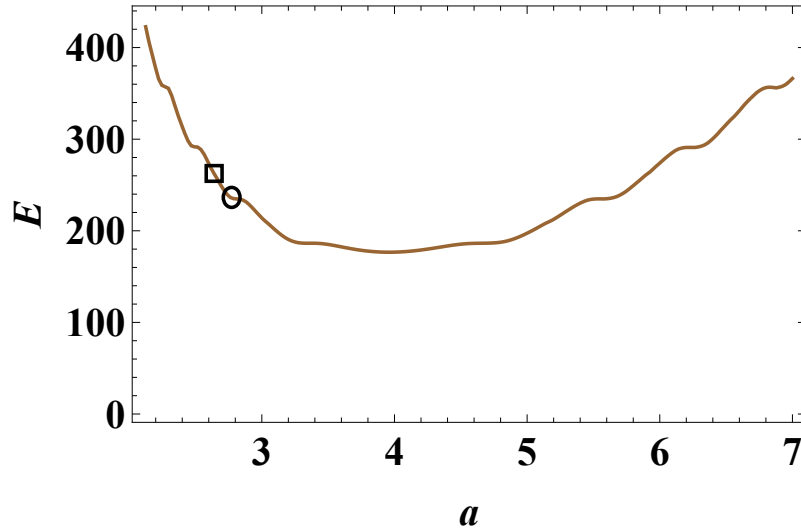


Figure 5.10: The energy for the case of rotation around y -axis with initial spin along z -axis.

5.6 Conclusion

We mapped the spin-1/2 system to a 2D Manakov system through a rotation operator that gives the spin texture of skyrmions. We have investigated all possible 2D skyrmion textures, as listed in Tables 1 and 2. We solved the 2D Manakov system using various analytical and numerical methods. While the similarity transformation method maps all solutions of the integrable 1D Manakov system to the 2D Manakov system, the solutions of the latter turn out to diverge at $\rho = 0$. Nondiverging solutions were then obtained using a power series method. However, the spin texture associated with these solutions turned out to be trivial, i.e., no texture. Finally, we considered a numerical solution of a system of coupled equations for the skyrmion density, $n(\rho, \phi)$, and texture, $\omega(\rho, \phi)$. This led to nondiverging and nontrivial spin textures. Then, we investigated the stability of these nontrivial nondiverging skyrmions by calculating their energy functional in terms of their effective size. It turned out that stable skyrmions correspond to concentric rings of spin components alternating between spin up and spin down. Metastable states, where energy is either increasing or decreasing with skyrmion size, correspond to concentric rings of mixed spin components.

Our results show that, in contrast with the established fact that in two dimensions lo-

calized solutions of the NLSE are unstable, the two spin states stabilize each other against collapse and allow for nontrivial stable two-dimensional topological excitations. Our results are also applicable to doubly polarized optical pulses. We strongly believe that this work is an important addition to the effort of realizing topological excitations.

Chapter 6: Unidirectional Flow and Unidirectional Segregation

In this chapter, we investigate the dynamics of two component bright-bright (BB) solitons through reflectionless double barrier and double well potentials in the framework of a Manakov system governed by the coupled nonlinear Schrödinger equations. The objective is to achieve unidirectional flow and unidirectional segregation/splitting, which may be used in the design of optical data processing devices. We observe how the propagation of composite BB soliton is affected by the presence of interaction coupling between the two components passing through the asymmetric potentials. We consider Gaussian and Rosen-Morse double potential barriers in order to achieve the unidirectional flow. Moreover, we observe a novel phenomenon which we name "*Polarity Reversal*" in the unidirectional flow. In this situation, the polarity of the diode is reversed. To understand the physics underlying these phenomena, we perform a variational calculation where we also achieve unidirectional segregation/splitting using an asymmetric double square potential well. Our comparative study between analytical and numerical analysis lead to an excellent agreement between the two methods.

6.1 Introduction

In this chapter, we are motivated to investigate the scattering of composite solitons which are solutions of the coupled nonlinear Schrödinger equations (NLSE) known also as Manakov system [178], in the presence of external potentials. The combination of bright-bright (BB) solitons which are exact solutions of the Manakov system are used as an initial pulse and then we observe the effect of interaction coupling on the two components during their time evolution. We consider two types of potentials for numerical simulations. One is an asymmetric Rosen-Morse (RM) double barrier potential and the other one is an asymmetric Gaussian double barrier potential. We obtain unidirectional flow in the presence of interaction and observed an exciting behavior which we coined "*Polarity Reversal*" in unidirectional flow, which is characterized by polarity reversal of the diode.

Another main objective of our work is to investigate unidirectional segregation of the composite solitons, i.e. composite solitons splitting into two components such that one component is fully transmitted and the other is fully reflected by an asymmetric potential when propagating from one direction and remain unaffected when transmitted from the opposite direction. We investigate the regimes of unidirectional flow and unidirectional splitting/segregation by calculating transport coefficients in terms of the parameters of the potentials. We also perform an alternative study to enrich our results of unidirectional segregation using a variational calculation [179, 180] and obtained an excellent agreement between analytical and numerical methods.

The rest of the chapter is organized as follows. In Section 6.2, we present the setup and theoretical model. In Section 6.3, we show how the dynamics of the propagation of composite BB solitons through asymmetric barrier is affected by the presence of strong interaction coupling between the two components. In Section 6.4, we use variational calculation and numerical method to perform a comparative study of the unidirectional segregation. Finally, in Section 6.5, we summarize our main results.

6.2 Theoretical Model

In the presence of an external scalar potential $V(x)$ the dynamics of bright-bright solitons is governed by the Manakov system of equations,

$$\begin{aligned} i\psi_{1t} &= -\frac{1}{2}\psi_{1xx} + s[g_1|\psi_1|^2 + g_{12}|\psi_2|^2]\psi_1 + V(x)\psi_1, \\ i\psi_{2t} &= -\frac{1}{2}\psi_{2xx} + s[g_2|\psi_2|^2 + g_{12}|\psi_1|^2]\psi_2 + V(x)\psi_2. \end{aligned} \quad (6.1)$$

where ψ_j , with $j = 1, 2$ denotes the wavefunction of the individual components. Repulsive or attractive interactions are accounted for by $s = +1$ or -1 , respectively. The nonlinear local interaction strength of the components ψ_1 and ψ_2 are represented by g_1 and g_2 , respectively. The strength of the interaction coupling the two components is g_{12} and $V(x)$ is the external scalar potential. Since the main focus will be on the effect of the nonlinear interaction g_{12} , we set $s = -1, g_1 = g_2 = 1$ and restrict g_{12} to $[-1, 1]$. In addition, we

consider also the special case where we set $g_1 \neq g_2$ for $g_{12} = 0$ and $g_{12} = -0.5$. With these restrictions on the nonlinearities, the Manakov system describes the composite bright-bright (BB) soliton. For our study, we choose two different types of the potential, $V(x)$, which have similar profiles. One is the asymmetric double Gaussian barrier of the form

$$V(x) = V_1 \exp\left[-\frac{(x-x_1)^2}{2\sigma^2}\right] + V_2 \exp\left[-\frac{(x-x_2)^2}{2\sigma^2}\right], \quad (6.2)$$

where $V_{1,2}$, σ , and $x_{1,2}$ determine the height, width, and position of the center of the first and second potential barrier, respectively. The second type of the potential $V(x)$ is of the form

$$V(x) = V_1 \operatorname{sech}^2[\alpha_1(x-x_1)] + V_2 \operatorname{sech}^2[\alpha_2(x-x_2)], \quad (6.3)$$

which is a combination of two RM potentials. Here, $V_{1,2}$, $\alpha_{1,2}$, and $x_{1,2}$ determine the height, inverse width, and position of the center of the first and second potential barrier, respectively. Both potentials are asymmetric double barriers and we chose slightly different heights for both potentials to achieve unidirectional behaviour. The profiles of the Gaussian and RM asymmetric double potentials indicated by the solid green and red dot-dashed curves, respectively are displayed in Figure 6.1. In our numerical simulation we prepared an initial state far away from the potential region and then let it propagate in real time. We always choose our initial wave functions as the exact solutions of the homogeneous version of Equation (6.1), namely

$$\begin{aligned} \psi_1(x, 0) &= A e^{iv_1 x} \operatorname{sech}[A(x-x_0)], \\ \psi_2(x, 0) &= A e^{iv_2 x} \operatorname{sech}[A(x-(x_0+\delta))]. \end{aligned} \quad (6.4)$$

where $v_{1,2}$, x_0 are the initial center-of-mass velocity and position, respectively, and δ is a very small shift in the initial position of the component 2, A is an arbitrary real normalization constant that we set to unity. For our investigation, we fixed the separation between the BB soliton components, $\delta = 0.001$.

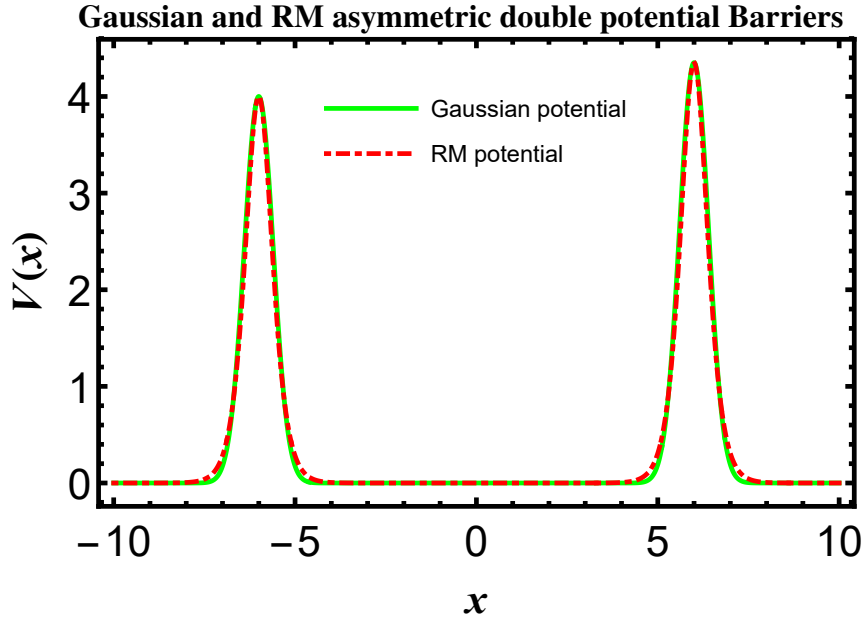


Figure 6.1: The Gaussian and Rosen-Morse asymmetric double potential barriers plotted for the Equations (6.2 & 6.3), indicated by solid green and red dot-dashed curves, respectively. The potential barriers are plotted for the parameters: $V_1 = 4$, $V_2 = 4.35$, $\sigma = 0.4$, $\alpha_1 = \alpha_2 = 2$, $x_1 = -6$ and $x_2 = 6$.

Now, we present the numerical results of our calculation for the transport coefficients: For the left-to-right-moving soliton with a single potential barrier, we define the reflectance, transmittance and trapping coefficients as follows:

$$\begin{aligned}
 R_i &= \frac{1}{N} \int_{-\infty}^{-l_i} dx |\psi_i(x,t)|^2, \\
 T_i &= \frac{1}{N} \int_{l_i}^{\infty} dx |\psi_i(x,t)|^2, \\
 L_i &= \frac{1}{N} \int_{-l_i}^{l_i} dx |\psi_i(x,t)|^2,
 \end{aligned} \tag{6.5}$$

respectively, where $l_i \approx 5/\alpha_i$, $i = 1, 2$, from the centre of the barrier and N is the normalization of the total soliton intensity given by $N = \int_{-\infty}^{\infty} (|\psi_1|^2 + |\psi_2|^2) dx$. For right-to-left-moving soliton, R and T are interchanged but L remains the same. Here, l_i represents the position of measurement of reflectance or transmission, set at a value slightly greater than the position of the boundary of the barrier, which we represented in terms of the inverse width of the barrier (α_i). For the considered two potential barriers in series, we choose $-l_i$ to the left of the left barrier and l_i to the right of the right barrier.

6.3 Propagation of Bright-Bright Solitons through RM Potential Barriers

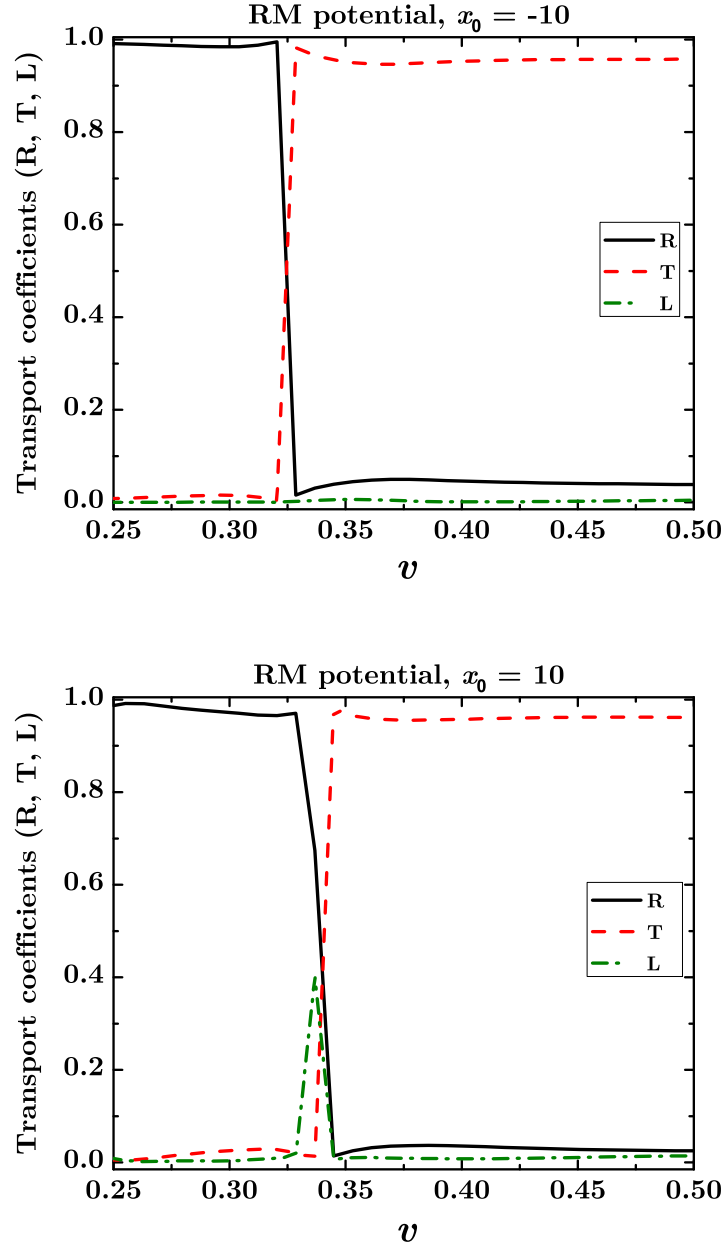


Figure 6.2: Transport coefficients in terms of velocity for the propagation of the ψ_1 component through asymmetric RM potential barriers for $g_1 = g_2 = 1$, and $g_{12} = 0$ from $x_0 = -10$ (upper panel) and $x_0 = 10$ (lower panel). Solid black line represents reflectance, R , dashed red line represents transmission, T , and dash-dotted green line represents trapping, L .

The dynamics of the bright-bright solitons described by the two-component Manakov system scattering through an asymmetric RM potential barriers positioned in series with slight difference in the height of the two barriers and finite separation will be presented

in this section. As both RM and Gaussian asymmetric potential barriers portray similar behavior throughout the analysis, we explain the entire study using RM potential in this section. In order to avoid redundancy, the results through an asymmetric Gaussian double potential barrier are given in Appendix 8. For our numerical investigation, we consider $V_1 = 4$, $V_2 = 4.35$, $\sigma = 0.4$, $\alpha_1 = \alpha_2 = 2$ and $x_1 = -6, x_2 = 6$. The evolution of BB solitons are investigated under the following scenarios: (i) in the absence of mean field coupling, $g_{12} = 0$, (ii) in the presence of an attractive coupling, $g_{12} > 0$, and (iii) in the presence of a repulsive coupling, $g_{12} < 0$.

6.3.1 Unidirectional Flow for Uncoupled Components with $g_{12} = 0$

The propagation of the BB solitons through an asymmetric RM potential barriers with $g_{12} = 0$ is displayed in Figure 6.2 for initial propagation from locations along the axis $x_0 = -10$ and $x_0 = 10$. Figure 6.2 displays the transport coefficients namely, reflectance, R , transmittance, T and trapping, L , in terms of velocity for the left and right moving BB soliton components through an asymmetric RM double barrier potential indicated by solid black, dashed red and dotted green lines, respectively, for the component ψ_1 . The corresponding curves for ψ_2 are identical with those of ψ_1 . This is obvious because $g_{12} = 0$. The transport coefficients obtained reveal the existence of a particular initial velocity value above which there is a sudden drop in reflectance to its minimum value and a sudden rise in the transmittance to its maximum value for both components. Furthermore, this critical velocity required for maximum transmittance appears to be different for right moving and left moving BB solitons.

For the right moving BB solitons scattered through RM potential barriers, this critical velocity is found to be $v_c = 0.324$ whereas that for the left moving BB solitons $v_c = 0.339$. Such differences in critical velocities for soliton propagation in opposite directions enables the realization of soliton diode using asymmetric RM potential wells [45]. While comparing the case of asymmetric potential wells in [45] with the present study, it is observed that the same functionality can be realized through the RM potential barriers.

Moreover, the present scheme with RM potential barriers displays larger velocity window of $0.324 \leq v \leq 0.338$ for the diode functionality compared to the case of [45] with a smaller velocity window $0.3275 \leq v \leq 0.3375$.

The trapping of solitons within a very narrow velocity window about the critical velocity, as shown by the green dotted curves in Figure 6.2 correspond to an unstable trapped state at the center of the potential barrier. The peak at the transition region corresponds to a nonlinear trapped mode by a stationary bound state of the potential. Physically, it corresponds to an unstable equilibrium that separates full transmission from full (quantum) reflection. The transition is so sharp such that the peak is very narrow. Further, trapping of solitons is absent for the right moving solitons from $x = -10$, but a small velocity range over which soliton trapping is found for the left moving solitons from $x = 0$. This trapping of left moving soliton appears as a peak near to the critical velocity as indicated by the lower panel of the Figure 6.2.

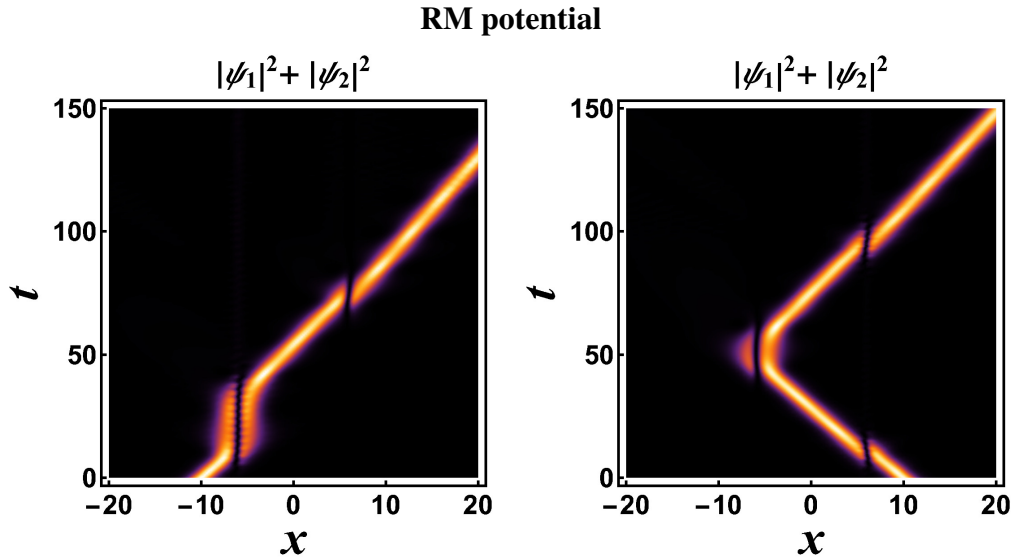


Figure 6.3: Propagation of composite BB soliton through asymmetric RM potential barriers for $g_1 = g_2 = 1$, and $g_{12} = 0$ at $v = 0.324$. Both components are identical. Left and right subfigures are results of initial propagation from $x_0 = -10$ and $x_0 = 10$, respectively.

Figure 6.3 portray the spatiotemporal evolution of the composite BB solitons for a particular initial velocity. In Figure 6.3, the left subfigure describes the propagation of the BB soliton components ψ_1 and ψ_2 with a critical velocity $v_c = 0.324$, incident from $x_0 = -10$

through asymmetric RM double potential barriers. The BB soliton components are first transmitted through the left barrier ($V_1 = 4.0$) positioned at $x_0 = -6$ and then transmitted through the right barrier ($V_2 = 4.35$) positioned at $x_0 = 6$ with an overall transmittance $T \approx 0.97$.

Considering the right subfigure of Figure 6.3 for the left moving BB solitons from $x_0 = 10$, BB solitons are first transmitted through the right barrier (V_2) positioned at $x_0 = 6$ and then reflected to the right by the left barrier (V_1) positioned at $x_0 = -6$ and finally transmitted through the right barrier to the left barrier with an overall reflectance, $R \approx 0.97$. This asymmetrical behavior in the flow of solitons is due to the appreciable velocity reduction of the BB solitons while crossing the first barrier, which plays a decisive role on overall transmission or reflection. For the case of right propagating BB solitons, it suffers a small velocity reduction when it transmits through the first barrier (V_1). But this reduced velocity is still sufficient to transmit through the second barrier (V_2) and propagates through to the right. On the other hand, the left moving BB solitons suffers an appreciable velocity reduction when it transmits through its first large barrier (V_2). This velocity reduction is high enough such that the soliton velocity is less than the critical velocity to overcome the second barrier which makes it impossible to transmit through the second barrier (V_1) and results in its reflection towards the right. This unidirectional flow portrays the diode behavior of the composite BB solitons through RM potential barriers similar to the one which we have realized in our previous analysis for a single soliton propagation through an asymmetrical RM potential wells [45].

Furthermore, we observed a maximum transmission at few lower velocities for $g_{12} = 0$ for right moving soliton but no soliton trapping as indicated by the appearance of green dot-dashed spike in the lower panel of the Figure 6.2. On the other hand for the left moving soliton there exists trapping as well as maximum transmission for certain lower velocities with $g_{12} \simeq 1$.

6.3.2 Polarity Reversal in Unidirectional Flow with $g_{12} > 0$

The role of the attractive mean field coupling ($g_{12} > 0$) on the propagation of BB solitons through the asymmetrical RM potential barriers will be addressed in this section. Since, both components ψ_1 and ψ_2 exhibit an identical behavior for both directions of propagation, we have described our results with the component ψ_1 , to avoid redundancy. Figure 6.4 describes the transmission and reflection coefficients of the component ψ_1 passing through the RM potential barriers from $x_0 = \pm 10$, versus the velocity and positive mean field coupling.

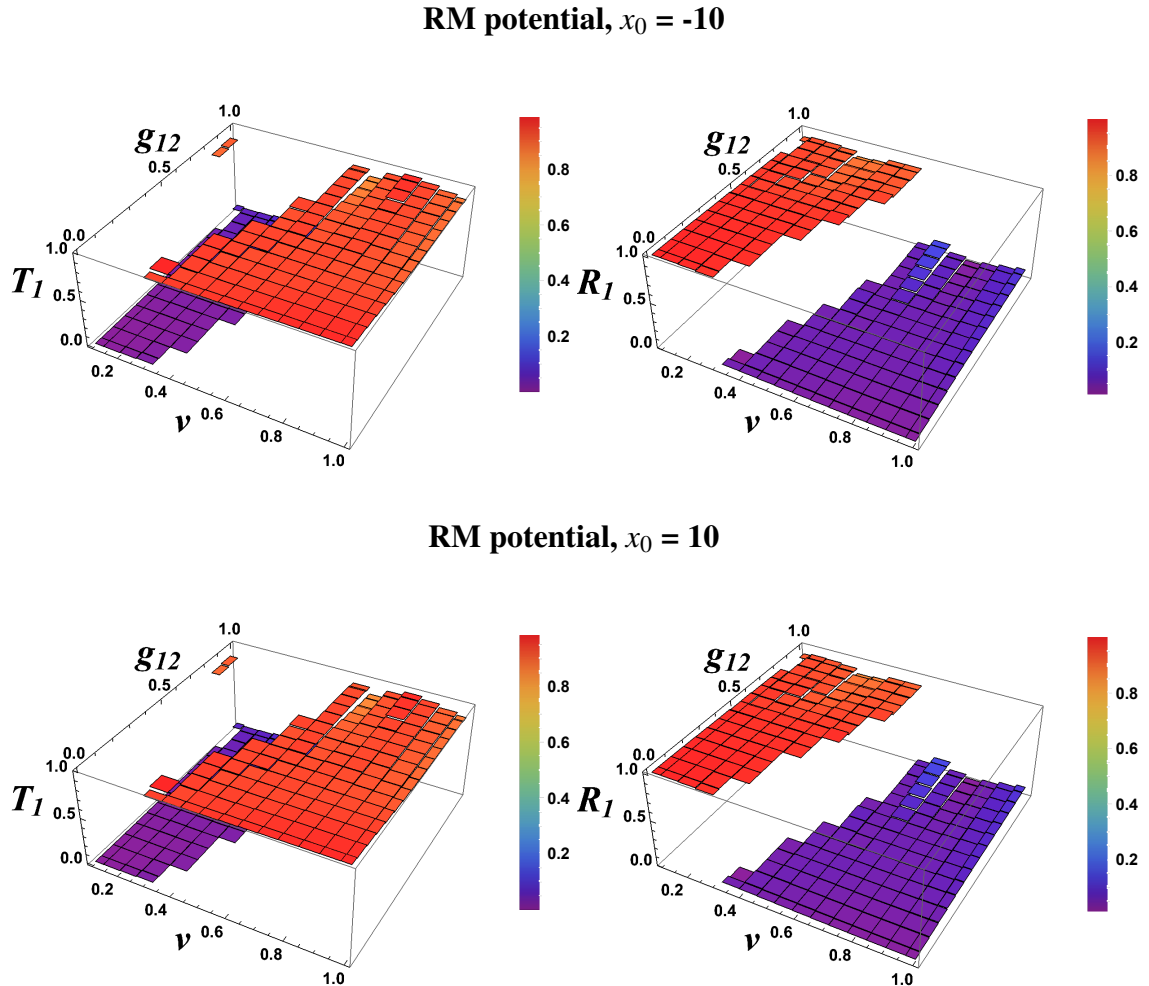


Figure 6.4: Transmission and reflection coefficients of the component ψ_1 for $g_1 = g_2 = 1$, propagating from $x_0 = -10$ (upper two) and $x_0 = 10$ (lower two) through RM potential barriers versus v and g_{12} .

In our numerical investigation, we considered varying the incident velocity of the BB solitons from 0.1 to 1 and g_{12} was varied from 0 to 1. The results obtained illustrate that

reflection dominates over the transmission for the composite solitons with incident velocities $v \leq 0.36$ for RM barriers throughout the entire range of g_{12} values. For this range of the incident velocities, reflection is observed to be around ≈ 0.98 . A sharp transition from the maximum reflection ($R \approx 0.98$) to the maximum transmission ($T \approx 0.94$) is obtained for the BB solitons with an initial incident velocity of $v = 0.363$ for $g_{12} = 0.1$. This critical velocity is found to be larger than that for the case with $g_{12} = 0$, where a minimum critical velocity of 0.324 is required to reach maximum transmission through RM potential barriers. This indicates that the presence of g_{12} coupling introduces a shift in the critical velocity required to reach maximum transmission. For a further increase in g_{12} value, a further shift in the velocity, v , is required for maximum transmission to hold.

Next, the propagation dynamics of the BB solitons from $x_0 = 10$ is considered which is shown in the lower two panels of Figure 6.4. Like the previous case, here also reflection is found to dominate for BB solitons with incident velocities $v \leq 0.39$ (for RM barriers). Thereafter, it shows a sudden sharp transition from higher reflection ($R \approx 0.95$) to the higher transmission ($T \approx 0.95$) for incident velocities $v = 0.391$ for RM potential barriers. Here also, a shift in critical incident velocity is observed with the shift in g_{12} which allows the diode functionality similarly to the case of $g_{12} = 0$. The important characteristic noticed here is a reverse shift in critical velocity (reduction in critical velocity) for $g_{12} \geq 0.35$, for the left moving solitons. The velocity window for the diode functionality at different g_{12} values are tabulated in Table 6.1. For this direction of propagation of BB solitons, the trapping is also found to be negligible.

Furthermore, we have explored an exciting phenomenon, which we referred to as "*polarity reversal for an optical diode*" and is observed for both kinds of potential barriers considered. In our investigation, we observed that for the right-moving soliton there is a critical velocity over which there is a sudden jump from mostly reflectance to mostly transmittance. A similar behavior exists for the right-moving soliton for another critical velocity. Moreover, it is observed that there exists different critical velocity for the

left- and right-moving solitons for full transmission. As a result, there exists an appreciable velocity window or velocity range for which there is almost full transmittance in one direction and nearly zero transmittance in the other direction, i.e., the soliton shows directional propagation for this set of parameters. This behavior (unidirectional flow of solitons) is similar to the diode effect in semiconductor physics. This behavior is observed in forward direction for up to $g_{12} = 0.323$ and 0.312 for RM asymmetric potential barriers and Gaussian asymmetric potential barriers, respectively (i.e. The right moving solitons, undergoes full transmission and the left moving solitons undergoes full reflection over the obtained velocity window).

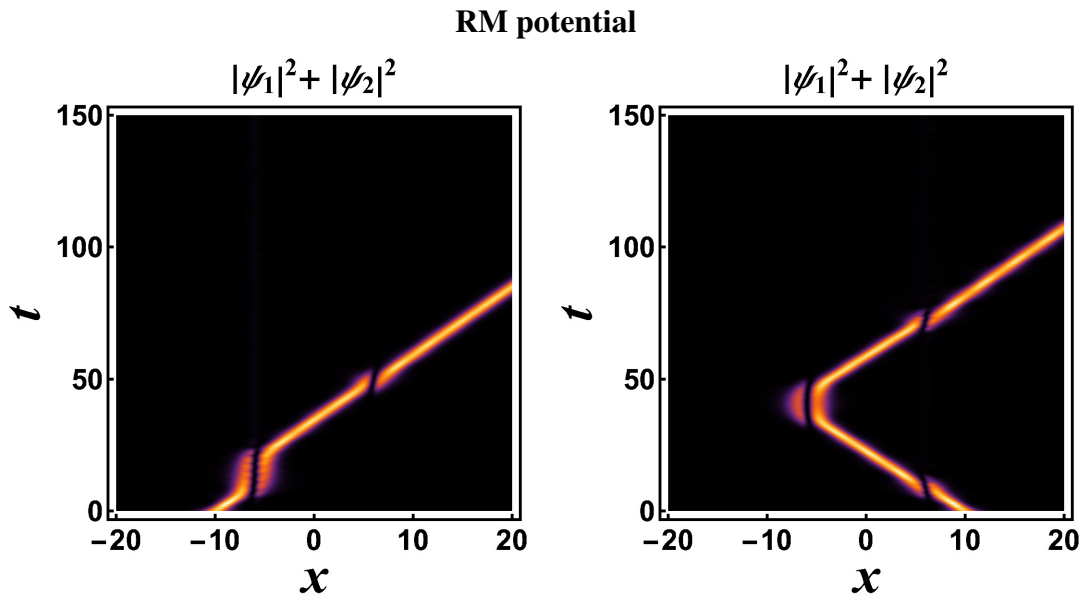


Figure 6.5: Propagation of composite BB soliton through asymmetric RM potential barriers for $g_1 = g_2 = 1$, and $g_{12} = 0.3$ at $v = 0.418$. Both components are identical. Left and right subfigures are results of initial propagation from $x_0 = -10$ and $x_0 = 10$, respectively.

On the other hand, for g_{12} values above 0.33 and 0.317 for RM asymmetric potential barriers and Gaussian asymmetric potential barriers, respectively, we observed the exact reversal in behavior of diode effect (i.e. The left moving solitons, undergoes full transmission and the right moving solitons undergoes full reflection over the obtained velocity window irrespective of the barrier height. This variation in propagation behavior of right and left moving soliton due the effect of interaction coupling, we refer to as “polarity reversal of the optical diode or polarity reversal in unidirectional flow”). The “right po-

larity" corresponds to the unidirectional flow towards the right direction in which right moving composite BB solitons transmit through both potential barriers and left moving composite solitons reflect through the potential barrier V_1 while "*left polarity*" corresponds to the unidirectional flow towards left direction in which right moving composite BB solitons reflect through the potential barrier V_1 and left moving composite solitons transmit through both potential barriers.

From the spatiotemporal plots, it is observed that for lower coupling $g_{12} \leq 0.323$ (for RM potential), both components exhibit the diode behavior with "*right polarity*" as shown in Figure 6.5 obtained for $g_{12} = 0.3$ which is similar to the one achieved in the case $g_{12} = 0$. For $g_{12} = 0.324 - 0.329$, it is observed that a full transmission exists for BB solitons propagating from both directions with maximum transmission for the critical incident velocities $v \geq 0.424$ through RM potential barriers. For $v < 0.424$, it exhibits maximum reflection for both right and left moving composite BB solitons as shown in Figure 6.6. Further, for $g_{12} \geq 0.33$ (for RM potential), exactly the reverse phenomena is achieved for $g_{12} \leq 0.3$, i.e., the right moving BB solitons passing through a smaller barrier (V_1) towards the larger barrier (V_2) is getting reflected while that for left moving BB solitons passing through larger barrier (V_2) towards the smaller barrier (V_1) is getting transmitted. Hence, the polarity of unidirectional flow is reversed from right to left polarity which can be seen by comparing Figure 6.7 with Figure 6.5 for RM potential. This phenomena is purely due to the increase in g_{12} above certain critical value 0.329 (for RM potential), which is demonstrated by Figure 6.8. Moreover, for an attractive interaction ($g_{12} > 0$), the results do not display any segregation or splitting of the BB soliton components and both components remain intact throughout the propagation.

6.3.3 Unidirectional Segregation with $g_{12} < 0$

The influence of repulsive mean field coupling on the propagation of the BB solitons through an asymmetric RM potential barriers will be examined in this section. We find segregation or splitting of composite BB solitons scattering through asymmetric double

potential barriers in the presence of a repulsive coupling ($g_{12} < 0$). We also found unidirectional segregation, i.e., the composite BB soliton components undergo segregation while passing through the potential barriers for propagation in one particular direction and remains intact for incident propagation from the opposite direction. The reflection coefficients of the components of the BB solitons versus velocity and g_{12} for the initial propagation from $x_0 = \pm 10$ through RM potential barriers are shown in Figure 6.9.

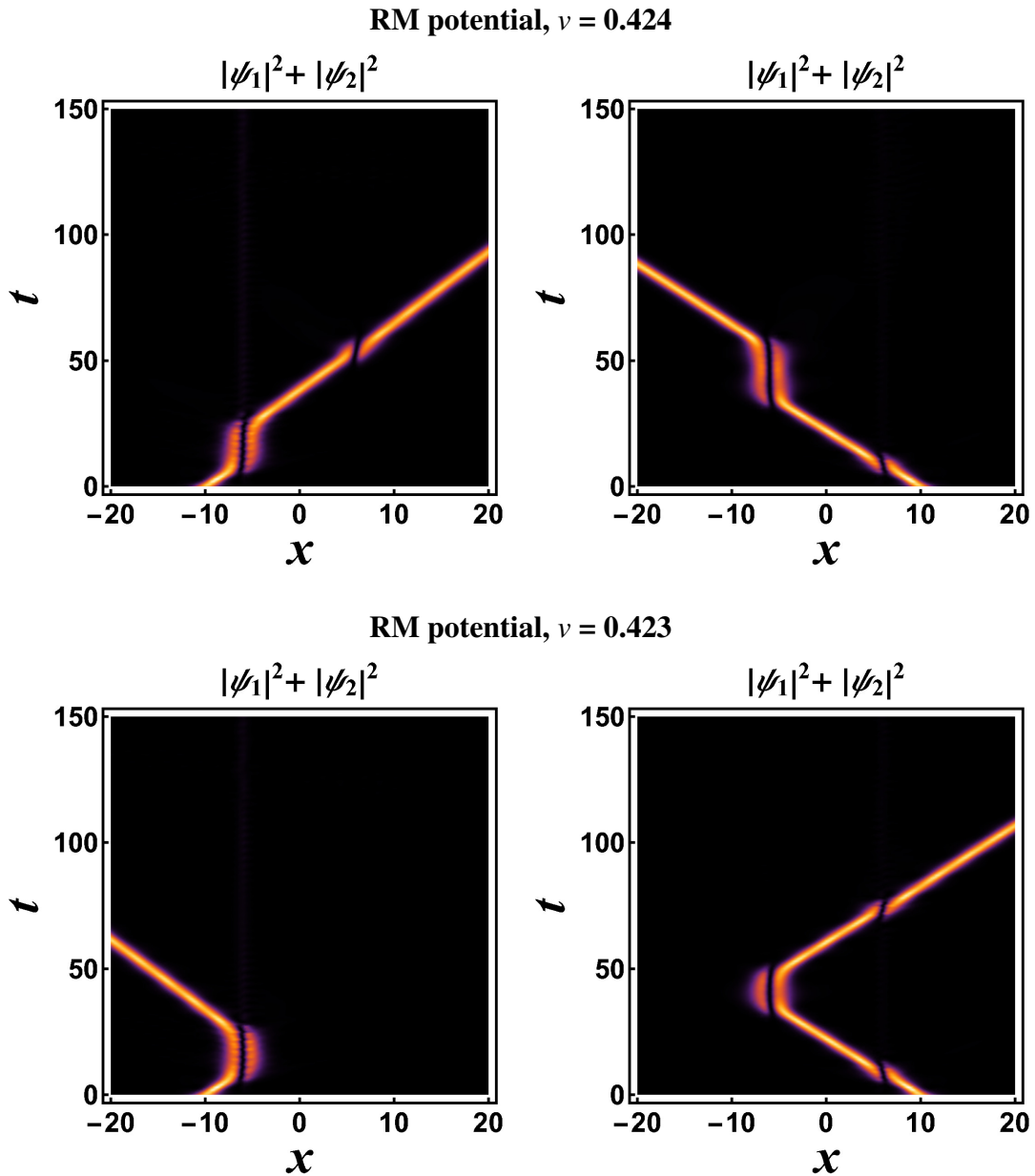


Figure 6.6: Propagation of composite BB soliton through asymmetric RM potential barriers for $g_1 = g_2 = 1$, and $g_{12} = 0.325$. Upper panel shows full transmission at $\nu = 0.424$ while lower panel shows full reflection at $\nu = 0.423$, from both left and right directions. There is no unidirectional flow in the range of coupling strength $0.324 \leq g_{12} \leq 0.329$.

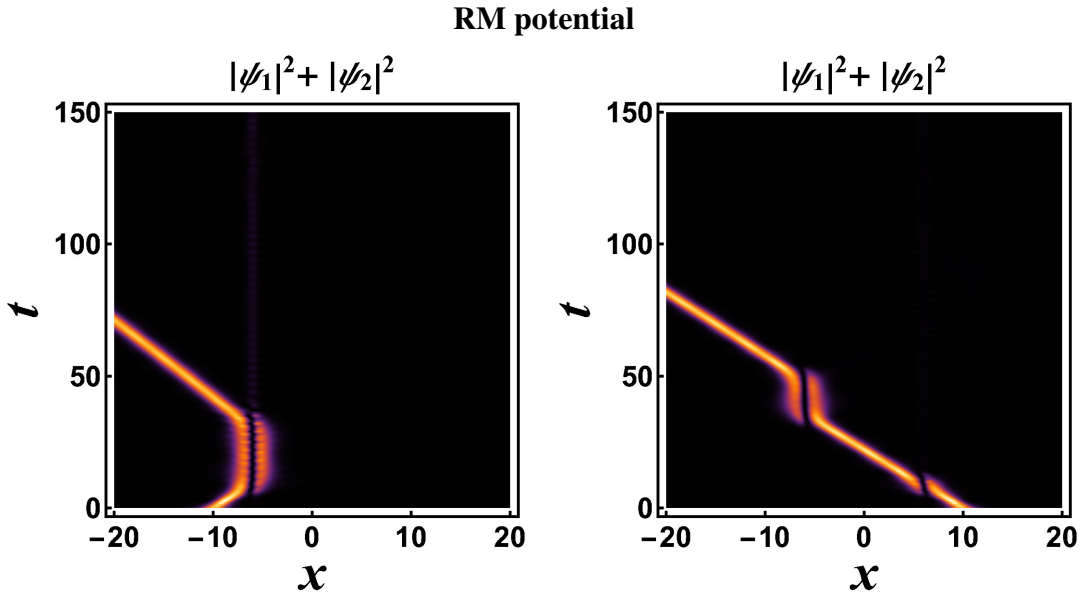


Figure 6.7: Propagation of composite BB soliton through asymmetric RM potential barriers for $g_1 = g_2 = 1$, and $g_{12} = 0.33$ at $v = 0.425$. Both components are identical. Left and right subfigures are results of initial propagation from $x_0 = -10$ and $x_0 = 10$, respectively. The polarity reversal phenomenon in unidirectional flow is achieved by comparing with Figure 6.5.

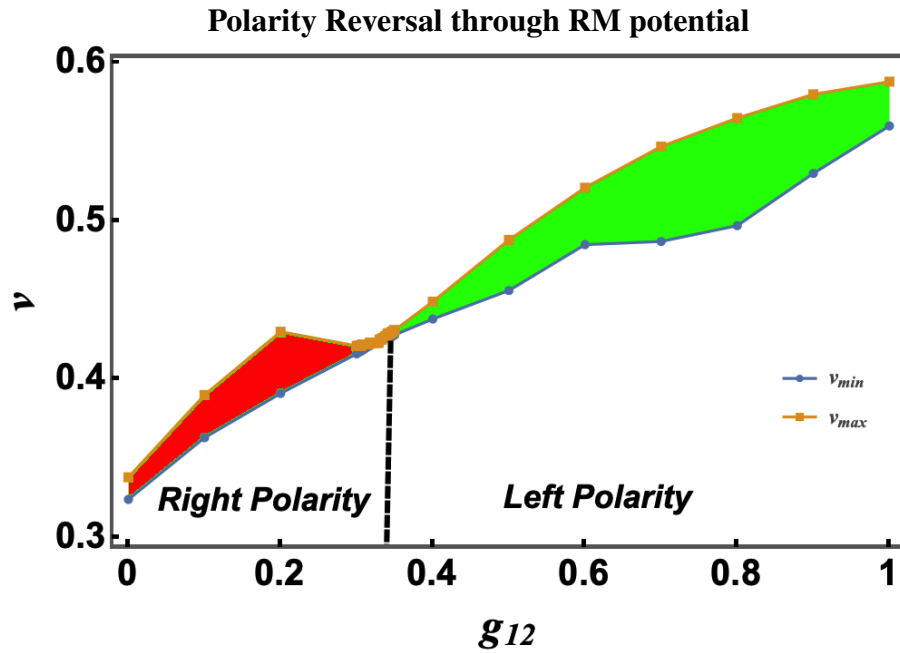


Figure 6.8: Borders of velocity window for the unidirectional flow (v_{min}, v_{max}) vs g_{12} with $g_1 = g_2 = 1$, through the RM potential barriers. Full reflection for $v \leq 0.423$ and full transmission for $v \geq 0.424$ is obtained with the range of coupling strength $0.324 \leq g_{12} \leq 0.329$, hence no unidirectional flow is observed at this specific range of g_{12} . Away from this point of $g_{12} = 0.329$, we find polarity reversal in unidirectional flow. The shaded region shows the velocity window for the unidirectional flow. The red color shows the right polarity while the green color shows the left polarity of the unidirectional flow. The data used to generate this figure is listed in Table 6.1.

Table 6.1: The velocity window for unidirectional flow of composite BB solitons with different coupling strengths. For the RM potential barriers with the range of coupling strength $0.324 \leq g_{12} \leq 0.329$ with $g_1 = g_2 = 1$, we find full reflection for $v \leq 0.424$ and full transmission for $v \geq 0.425$, hence no unidirectional flow is observed at this specific range of g_{12} . Away from this point, we find polarity reversal in unidirectional flow.

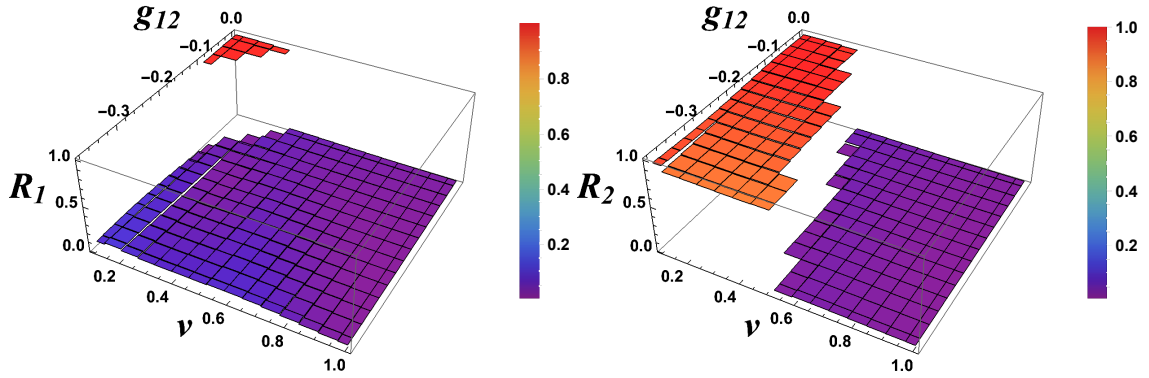
Unidirectional flow with composite BB solitons		
Interaction strength	Velocity window	
g_{12}	$v_{min} \leq v \leq v_{max}$	
0	$0.324 \leq v \leq 0.338$	<i>Right polarity</i>
0.1	$0.363 \leq v \leq 0.39$	
0.2	$0.391 \leq v \leq 0.430$	
0.3	$0.416 \leq v \leq 0.421$	
0.301-0.303	$0.417 \leq v \leq 0.421$	
0.304-0.306	$0.418 \leq v \leq 0.421$	
0.307	$0.418 \leq v \leq 0.422$	
0.308-0.310	$0.419 \leq v \leq 0.422$	
0.311-0.313	$0.420 \leq v \leq 0.422$	
0.314-0.316	$0.421 \leq v \leq 0.422$	
0.317-0.320	$0.421 \leq v \leq 0.423$	
0.321-0.323	0.423	
0.324-0.329	no unidirectional flow	
0.33-0.333	0.425	<i>Left polarity</i>
0.334-0.336	0.426	
0.337-0.339	$0.426 \leq v \leq 0.427$	
0.34	$0.426 \leq v \leq 0.428$	
0.341	$0.427 \leq v \leq 0.429$	
0.342	$0.427 \leq v \leq 0.428$	
0.343-0.345	$0.427 \leq v \leq 0.429$	
0.346-0.347	$0.427 \leq v \leq 0.43$	
0.348	$0.428 \leq v \leq 0.43$	
0.349-0.35	$0.428 \leq v \leq 0.431$	
0.4	$0.438 \leq v \leq 0.449$	
0.5	$0.456 \leq v \leq 0.488$	
0.6	$0.485 \leq v \leq 0.521$	
0.7	$0.487 \leq v \leq 0.547$	
0.8	$0.497 \leq v \leq 0.565$	
0.9	$0.53 \leq v \leq 0.580$	
1	$0.56 \leq v \leq 0.588$	

We consider varying the incident velocity of the BB solitons from 0.1 to 1 and g_{12} varying from 0 to -0.38 for our numerical investigation. In Figure 6.9, the top surface describes the reflection coefficient of the component ψ_1 and the bottom one describes the reflection coefficient of the component ψ_2 . When the incident velocity is low ($v = 0.1$) with g_{12} up to -0.16, reflection is found to be predominant for both the components. In the range $-0.36 \leq g_{12} \leq -0.21$, at $v = 0.1$, the reflection of the component ψ_1 is ≈ 0.05 and that for the component ψ_2 is ≈ 0.96 . This demonstrates the nearly full separation of the com-

ponents, i.e., the component ψ_1 undergoes maximum transmission and the component ψ_2 undergoes maximum reflection. For further decrease in g_{12} from -0.36 to -0.5 , we start to have trapping and T_1 gradually reduces and reaches a minimum value of 0.6 ($R_1 = 0.4$) for $g_{12} = -0.5$, while that of T_2 shows slight increase and reaches a transmission ≈ 0.17 ($R_2 = 0.83$). For lower g_{12} values down to -0.35 , the R_1 is found to be low but thereafter increases to the maximum of ≈ 0.4 for further reduction in g_{12} values. The R_2 shows a sharp transition from maximum to minimum at velocity $v = 0.25$ for $-0.35 < g_{12} \leq -0.1$. In case $g_{12} > -0.35$ this transition region shifts to lower velocities around 0.2 . In case of R_2 , this transition to the minimum reflection is gradual and complete drop in reflection occurs at the velocity $v = 0.45$. With this increase in incident velocity $v \geq 0.45$, the reflection for both the components are observed to be minimum for the entire range of the g_{12} values. The obtained results illustrate that repulsion dominates for lower velocities and higher g_{12} values. The obtained results demonstrate almost similar dynamics as the one obtained for the propagation from $x_0 = -10$. But a greater reflection window for the component ψ_2 over the mid g_{12} values for velocity ≈ 0.3 is noticed. Also, a shift in the incident velocity $v \geq 0.55$, required for the minimum reflection is observed.

Furthermore, we report here a phenomenon of unidirectional segregation as is demonstrated in Figure 6.10. This unidirectional segregation is obtained for BB soliton components passing through an asymmetrical RM potential barriers with barriers positioned at $x_1 = -4$ and $x_2 = 4$ with incident velocity $v = 0.34$ in the range $-0.0045 \leq g_{12} \leq -0.0033$. For the right moving BB solitons incident from the initial position at $x_0 = -15$, both components undergo transmission through both barriers and reach the right side with $T_1 = T_2 = 0.98$. On the other hand, for a left moving BB solitons, the component ψ_1 passes through both barriers and shows complete transmission $T_1 = 0.98$ and reaches the left side. Whereas the component ψ_2 passes through the first barrier and gets reflected by second barrier, then it again transmits through the first barrier and reaches the right side with a reflectance $R_1 = 0.98$.

RM potential, $x_0 = -10$



RM potential, $x_0 = 10$

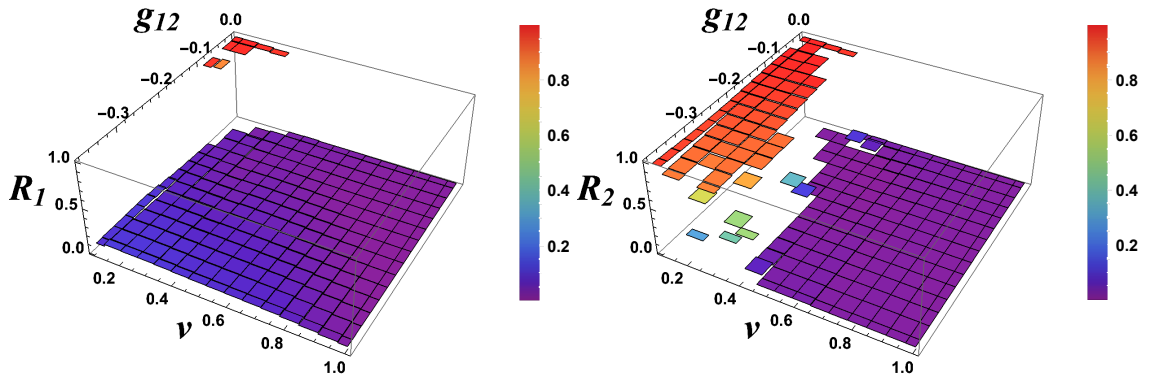


Figure 6.9: Reflection coefficients of the components ψ_1 and ψ_2 propagating through RM potential barriers from $x_0 = -10$ (upper two) and $x_0 = 10$ (lower two) versus ν and g_{12} . Other parameters are $g_1 = 1$ and $g_2 = 1$.

This transition is found to be very sensitive to the parameters of the designed reflectionless potential and the transmitted components of the right moving BB solitons are found to remain intact in a certain time interval, thereafter one of the components is out of phase with respect to the other component with a small phase shift but both the components continue along the same trajectory. This sensitive behavior paves the way to perform a variational calculation in order to achieve unidirectional segregation and to understand the physics underlying this phenomenon which we will discuss in the Section 6.4.

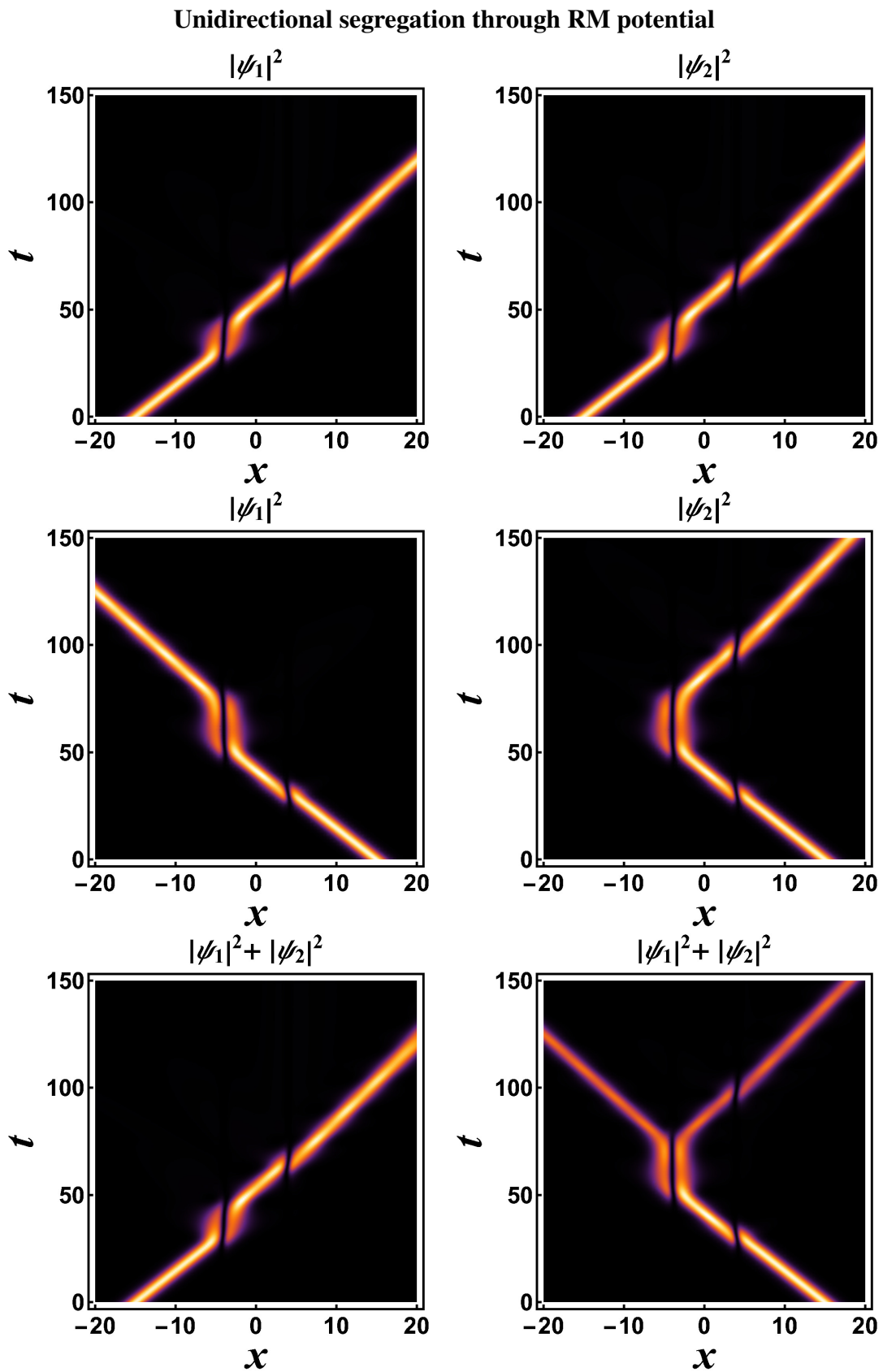


Figure 6.10: Propagation of components through asymmetric RM potential barriers for $g_1 = g_2 = 1$, and $g_{12} = -0.004$ at $v = 0.34$. The parameter of initial position $x_0 = \pm 15$ is used. Unidirectional segregation of composite BB soliton is achieved.

6.3.4 Special Case: $g_1 \neq g_2$

In this section, we investigate the influence of the nonlinear local interaction strength of each component on the BB solitons dynamics (i) in absence of interaction coupling ($g_{12} = 0$) and (ii) in presence of the repulsive interaction coupling ($g_{12} < 0$), respectively. For our study, we consider varying the nonlinear local interaction strength of the component ψ_1 , by varying g_1 from 1.05 to 1.5 and the velocity is varied from 0.1 to 1.

(a) For $g_{12} = 0$

The results obtained for the propagation of BB solitons through the asymmetric RM potential barriers in the absence of interaction coupling ($g_{12} = 0$), with g_1 varying from 1.05 to 1.5 is illustrated in the Figure 6.11 for initial propagation from $x_0 = \pm 10$. In Figure 6.11, the top two plots display the results of reflectance of the components ψ_1 and ψ_2 , respectively of the BB solitons propagating from the initial position $x_0 = -10$. The lower two plots provide the results of the transmittance of the components ψ_1 and ψ_2 , respectively of the BB solitons propagating from the initial position $x_0 = -10$. For $g_1 = 1.05$, the value of R_1 is found to be maximum up to the velocity $v = 0.346$, thereafter it makes a sharp transition from maximum reflectance to the minimum. On the other hand the R_2 maintains its maximum value up to the velocity $v = 0.307$ and thereafter reaches sharp minimum. We infer that the increase in nonlinear local interaction strength introduces a shift in the velocity required for maximum reflectance. The subsequent shift in the velocity shift for maximum reflectance R_1 is observed for g_1 values 1.14, 1.31 and 1.42, respectively. A similar behavior for shift in velocity to achieve maximum T_1 is also observed, as displayed in the third plot of Figure 6.11. Next, considering the propagation of the BB solitons from $x_0 = 10$, for extremely low velocities, there exist nonlinear modes with energy trapping around $\approx 0.2\%$ throughout the variation of g_1 , as shown by Figure 6.12. Moreover, the present case also displays that the existence of the shift in the velocity throughout which the maximum reflectance of R_1 is maintained. The reflectance is found to be maximum up to the velocity v equals to 0.32, thereafter it undergoes a sharp transition from maxi-

mum reflection to minimum reflection at $g_1 = 1.05$. Thereafter, it displays the right shift in the velocity for maximum reflectance as obtained for the propagation from $x_0 = -10$, but at different g_1 values. Furthermore, for the present case, we also have identified the regimes of the unidirectional segregation as in our previous section. Here, for the g_1 values from 1.03 to 1.1, the system exhibits the unidirectional segregation for the BB soliton components propagating from initial positions, $x_0 = \pm 15$ with barrier positions, ± 4 . The unidirectional flow obtained for these parameters at $v = 0.34$ is illustrated in Figure 6.13. In this case, for the right propagating BB solitons, ψ_1 undergo complete reflection in first barrier meanwhile the component ψ_2 undergoes full transmission crossing both barriers. On the other hand, the left moving solitons undergo full reflection at the first barrier.

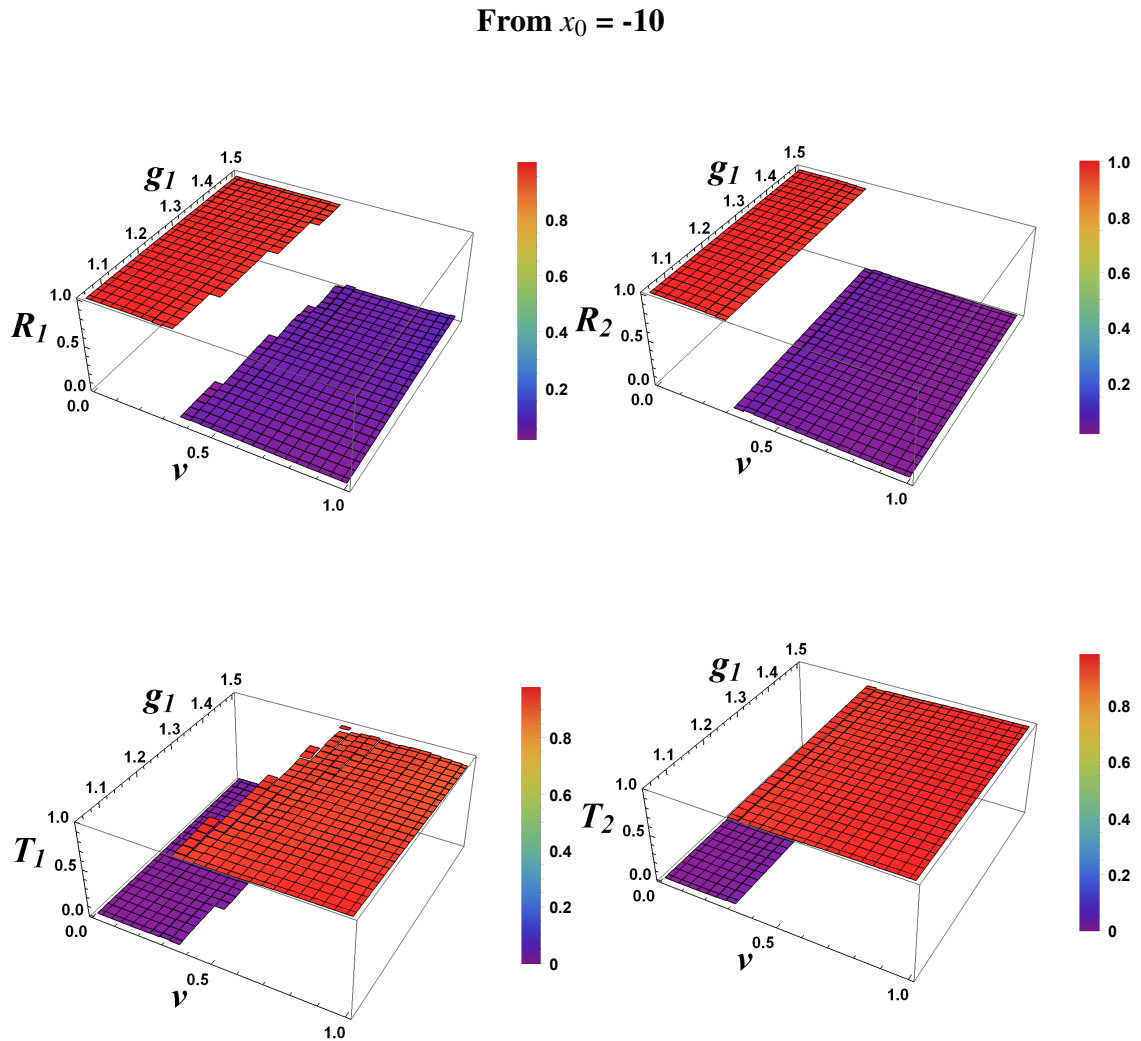


Figure 6.11: Reflection and transmission coefficients of the components ψ_1 and ψ_2 propagating through RM potential barriers from $x_0 = -10$ versus v and g_1 . The parameters used are $g_{12} = 0$ and $g_2 = 1$.

From $x_0 = 10$

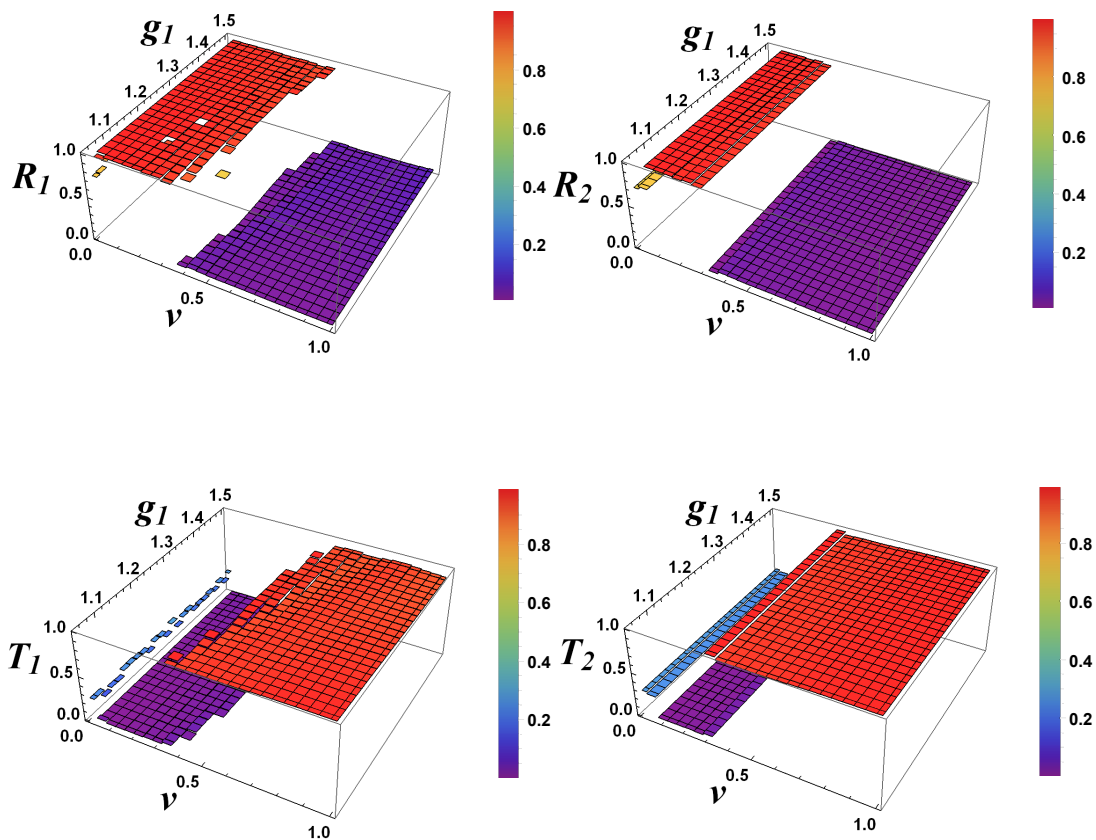


Figure 6.12: Reflection and transmission coefficients of the components ψ_1 and ψ_2 propagating through RM potential barriers from $x_0 = 10$ versus ν and g_1 . The parameters used are $g_{12} = 0$ and $g_2 = 1$.

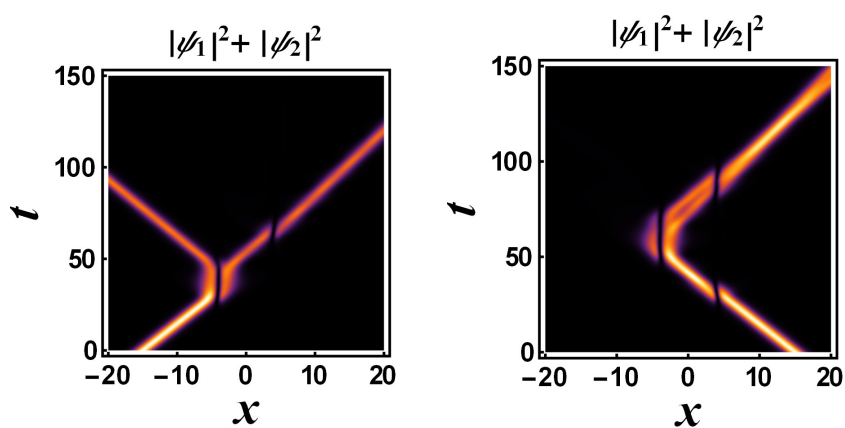


Figure 6.13: Propagation of components through asymmetric RM potential barriers at $\nu = 0.34$. The parameter of initial position $x_0 = \pm 15$ is used. Unidirectional segregation of composite BB soliton is achieved. Other parameters used are $g_{12} = 0$, $g_1 = 1.05$, and $g_2 = 1$.

(b) For $g_{12} = -0.5$

Additionally, in order to understand the influence of the nonlinear local interaction coupling in presence of repulsive interaction coupling, here, we consider the case $g_{12} = -0.5$. The dynamics of the BB solitons through the RM potential barriers is investigated for g_1 varying from 1.05 to 1.5. The results obtained for the BB solitons propagating from $x_0 = -10$ is provided by the Figure 6.14. For lower velocities and low g_1 values ($g_1 < 1.16$), there exist few nonlinear trapping modes. But for higher g_1 values above 1.16, the nonlinear trapping modes are absent. Here also the shift in velocity for maximum reflectance of R_1 is found to increase with increasing g_1 . After certain g_1 value above 1.3, the velocity required for maximum reflectance becomes constant. Next considering R_2 , for lower velocities and lower g_1 values, more trapping modes are observed. For g_1 values above 1.2, the trapping is found to reduce but with around 90% reflectance. As the velocity increases, reflectance decreases and reaches up to 50%, with around 50% trapping until the velocity equals to 0.4. During this regime, the reflectance is constant for the all g_1 values. For further increase in the velocity, the reflection as well as trapping found to reduce gradually and reaches minimum. From the transmittance plots of Figure 6.14, it is illustrated that the dynamics of transmittance of the components are complementary to that of the reflectance of the components. Next, the propagation of BB solitons from $x_0 = 10$ is considered in the Figure 6.15. It is observed that the existence of the nonlinear trapping modes are high for the left moving solitons propagating from $x_0 = 10$, where it encounters the large barrier first. But for higher g_1 values, trapping is found to be minimum. Here also the results demonstrate the shift in velocity for maximum reflectance of R_1 , with increase in the g_1 values. Further increase in the velocity above 0.3, the reflectance drops from maximum to minimum sharply. On the other hand, R_2 portrays, almost similar dynamical behavior as that of R_1 , but the drop in reflectance is shifted to the lower velocity, $v = 0.2$. Here, also the transmittance of the components show more or less opposite behavior as that of the reflectance of the respective components. From the results, it is observed that g_{12} increases the number of nonlinear modes and reduces the

transmission of the component around 50%.

Furthermore, from the density plots shown by Figure 6.16, g_{12} was found to suppress the unidirectional segregation obtained with same numerical values considered for the case $g_{12} = 0$ and results in bidirectional segregation. For the BB solitons propagating from $x_0 = -15$, the component ψ_1 undergoes full reflection while the component ψ_2 undergoes full transmission. Similarly for the BB solitons propagating from $x_0 = 15$, we also found that the component ψ_1 shows full reflection and the component ψ_2 shows full transmission. Moreover, from our results, we found that even an extremely small value of $g_{12} = -0.004$ is sufficient to suppress the unidirectional segregation.

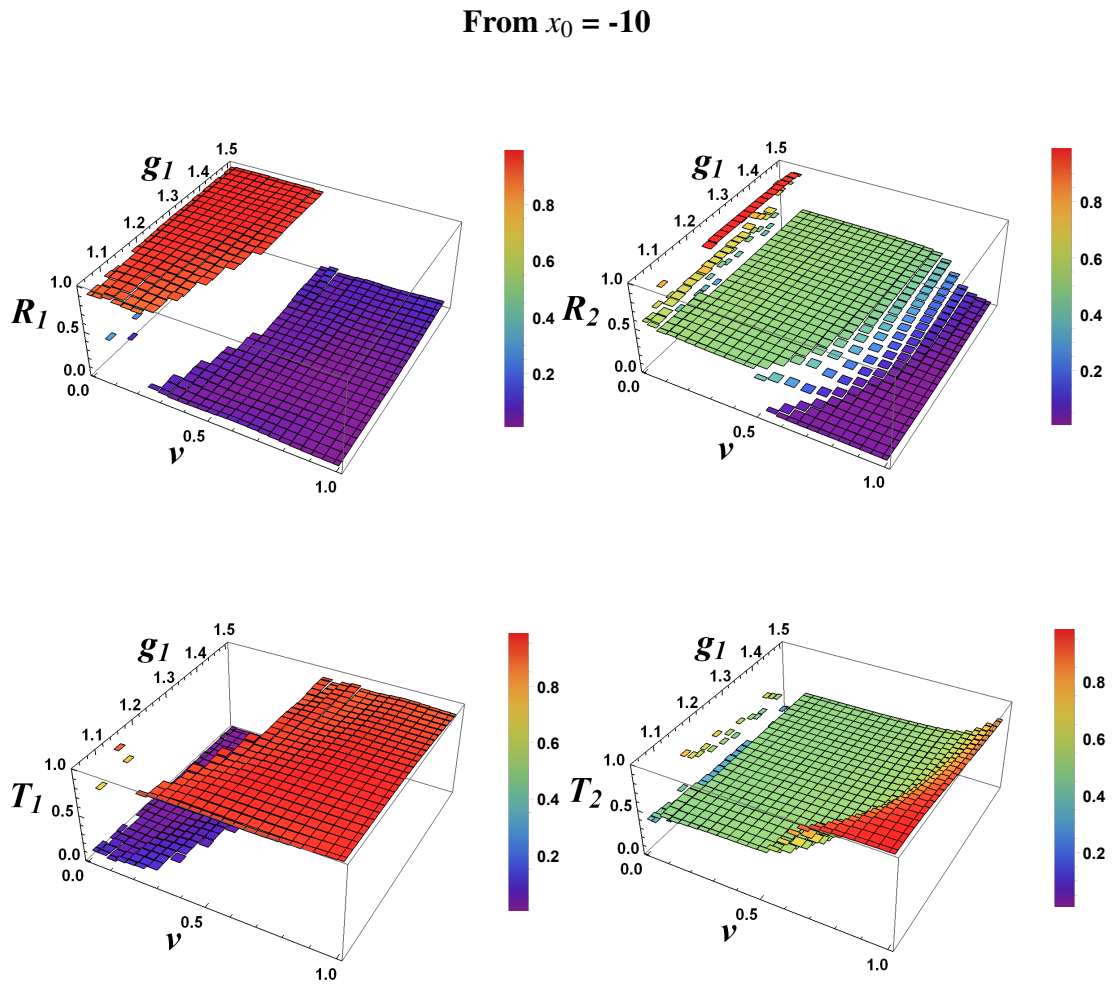


Figure 6.14: Reflection and transmission coefficients of the components ψ_1 and ψ_2 propagating through RM potential barriers from $x_0 = -10$ versus ν and g_1 . The parameters used are $g_{12} = -0.5$ and $g_2 = 1$.

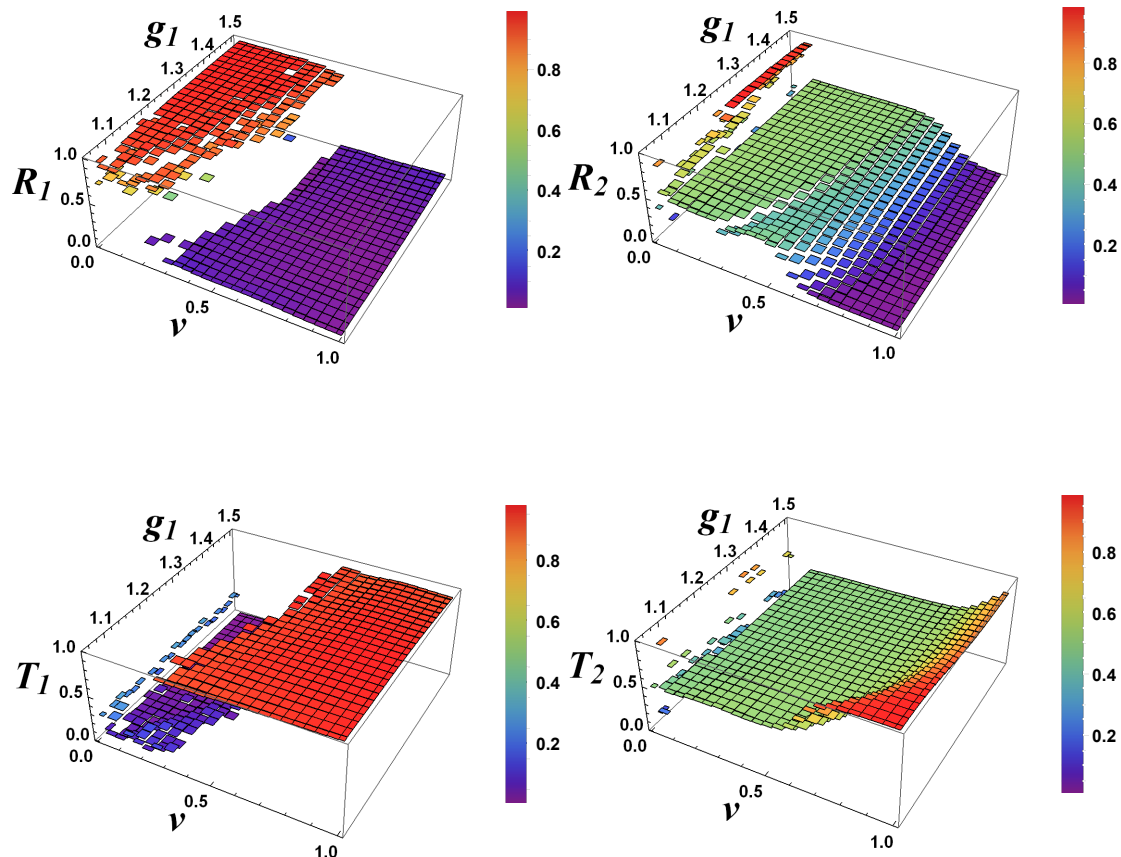
From $x_0 = 10$ 

Figure 6.15: Reflection and transmission coefficients of the components ψ_1 and ψ_2 propagating through RM potential barriers from $x_0 = 10$ versus ν and g_1 . The parameters used are $g_{12} = -0.5$ and $g_2 = 1$.

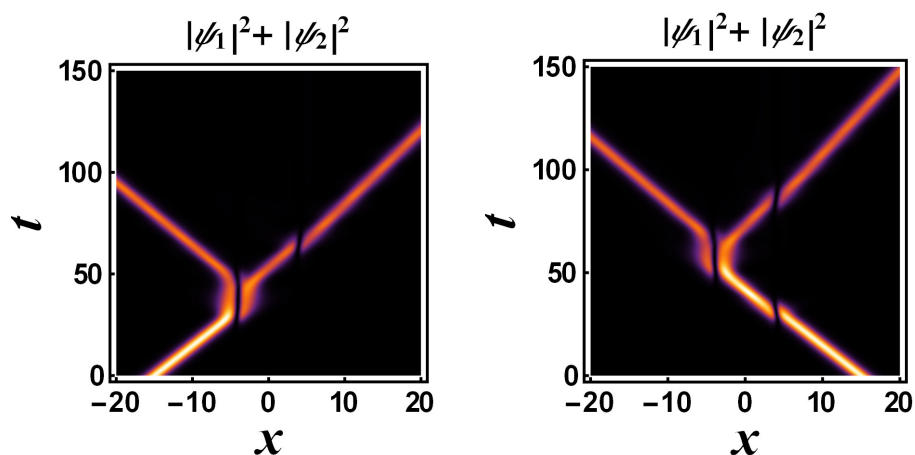


Figure 6.16: Propagation of components through asymmetric RM potential barriers at $\nu = 0.34$. The parameter of initial position $x_0 = \pm 15$ is used. Bidirectional segregation of composite BB soliton is observed. Other parameters used are $g_{12} = -0.5$, $g_1 = 1.05$, and $g_2 = 1$.

6.4 Variational Approach Versus Numerical Computation

We use a comparative analysis between numerical computation and variational approach to validate our results for the unidirectional segregation of composite BB soliton. In this section, we will show how our numerical results for the computation of the unidirectional segregation are in excellent agreement with those generated by the variational approach.

The starting point of our analysis is the Lagrangian density,

$$\begin{aligned} \mathcal{L} = & \frac{i}{2} \left(\psi_1^* \frac{\partial \psi_1}{\partial t} - \psi_1 \frac{\partial \psi_1^*}{\partial t} \right) - \frac{1}{2} \left| \frac{\partial \psi_1}{\partial x} \right|^2 + \frac{g_1}{2} |\psi_1|^4 + \frac{i}{2} \left(\psi_2^* \frac{\partial \psi_2}{\partial t} - \psi_2 \frac{\partial \psi_2^*}{\partial t} \right) - \frac{1}{2} \left| \frac{\partial \psi_2}{\partial x} \right|^2 \\ & + \frac{g_2}{2} |\psi_2|^4 + g_{12} |\psi_1|^2 |\psi_2|^2 + V(x) [|\psi_1|^2 + |\psi_2|^2]. \end{aligned} \quad (6.6)$$

Using the Euler-Lagrange equation with Equation (6.6) we obtain the following coupled NLSE,

$$\begin{aligned} i \frac{\partial \psi_1}{\partial t} + \frac{1}{2} \frac{\partial^2 \psi_1}{\partial x^2} + [g_1 |\psi_1|^2 + g_{12} |\psi_2|^2 + V(x)] \psi_1 &= 0, \\ i \frac{\partial \psi_2}{\partial t} + \frac{1}{2} \frac{\partial^2 \psi_2}{\partial x^2} + [g_2 |\psi_2|^2 + g_{12} |\psi_1|^2 + V(x)] \psi_2 &= 0, \end{aligned} \quad (6.7)$$

which is identical to Equation (6.1). We adopt the following variational ansatz as the BB soliton solutions to Equation (6.7)

$$\begin{aligned} \psi_1(x, t) &= A \operatorname{sech} \left(\frac{x + \xi_1}{a} \right) e^{i[\phi + v_1(x + \xi_1) + b(x + \xi_1)^2]}, \\ \psi_2(x, t) &= A \operatorname{sech} \left(\frac{x + \xi_2}{a} \right) e^{i[\phi + v_2(x + \xi_2) + b(x + \xi_2)^2]}. \end{aligned} \quad (6.8)$$

The variational parameters $A(t)$, $\xi_{1,2}(t)$, $a(t)$, $\phi(t)$, $v_{1,2}(t)$, and $b(t)$ represent the amplitude, center-of-mass position, width, phase, velocity, and the chirp of the solitons, respectively. We use the normalization condition,

$$\int_{-\infty}^{\infty} dx |\psi|^2 = 2A^2 a = N, \quad (6.9)$$

to reduce the number of variational parameters by one variable where we define the amplitude as a function of the width, a , and the normalization constant, N . The potential in Equation (6.7) for both components takes the form,

$$V(x) = l_{00} + l_{01} \left[\Theta(x - q_1) - \Theta(x - q_2) \right] + l_{02} \left[\Theta(x - q_3) - \Theta(x - q_4) \right], \quad (6.10)$$

where $\Theta(x)$ is the Heaviside unit step function, l_{00} , l_{01} , l_{02} , q_1 , q_2 , and q_3 are potential parameters to be suitably selected for numerical computations. The choice of this particular potential simplifies the analytical calculations but will not limit the validity of our main results. Due to the fact that soliton scattering through a potential well causes its width to shrink while soliton scattering through a potential barrier will cause its width to expand substantially, then we selected the usage of potential well rather than barrier in our present variational approach.

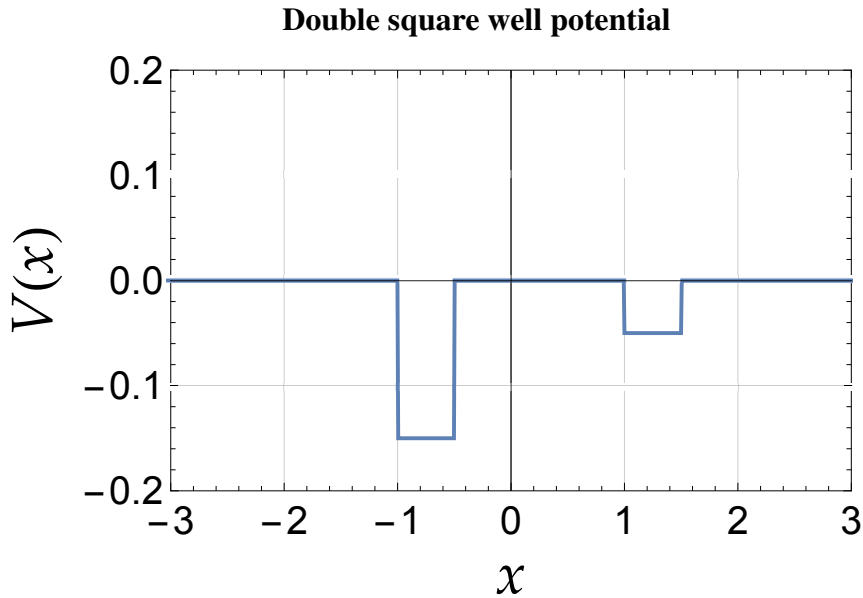


Figure 6.17: Asymmetric double well potential. We plot the potential, Equation (6.10), with parameters: $l_{00} = 0$, $l_{01} = -0.15$, $l_{02} = -0.05$, $q_1 = -1$, $q_2 = -0.5$, $q_3 = 1$, $q_4 = 1.5$.

The double square well potential, Equation (6.10), captures the essential features of the Gaussian and Rosen-Morse double potential barriers where it allows for a unidirectional flow too [47]. In Figure 6.17, we plot the potential. In this section we are using the parameters: $g_1 = g_2 = 1$, $g_{12} = 0.05$, $l_{00} = 0$, $l_{01} = -0.15$, $l_{02} = -0.05$, $q_1 = -1$, $q_2 =$

-0.5 , $q_3 = 1$, $q_4 = 1.5$, for the variational and numerical calculations unless otherwise noted. In our analysis, we fix the potential position and change the launching point of the vector soliton such that when we set $\beta = -1$ ($\beta = 1$), the BB soliton is coming from the right (left) of the potential in Figure 6.17. Inserting our variational ansatz Equation (6.8), into the Lagrangian density, Equation (6.6), and integrating with respect to x from $-\infty$ to ∞ , results in the effective Lagrangian of the system as a function of the variational parameters,

$$\begin{aligned}
L = & -\frac{N}{3a^2} + \frac{(g_1 + g_2)N^2}{6a} - \frac{1}{3}N\pi^2 a^2 b^2 - \frac{1}{2}N(v_1^2 + v_2^2) - \frac{1}{6}N\pi^2 a^2 b' \\
& - N(v_1 \xi_1' + v_2 \xi_2' + 2\phi') \\
& + \frac{1}{2}N \left\{ 2l_{00} + l_{01} \left[-\tanh\left(\frac{q_1 + \xi_1}{a}\right) + \tanh\left(\frac{q_2 + \xi_1}{a}\right) \right] \right. \\
& + l_{02} \left[-\tanh\left(\frac{q_3 + \xi_1}{a}\right) + \tanh\left(\frac{q_4 + \xi_1}{a}\right) \right] \left. \right\} \\
& + \frac{1}{2}N \left\{ 2l_{00} + l_{01} \left[-\tanh\left(\frac{q_1 + \xi_2}{a}\right) + \tanh\left(\frac{q_2 + \xi_2}{a}\right) \right] \right. \\
& + l_{02} \left[-\tanh\left(\frac{q_3 + \xi_2}{a}\right) + \tanh\left(\frac{q_4 + \xi_2}{a}\right) \right] \left. \right\} \\
& + \frac{g_{12}N^2}{a^2} \operatorname{csch}^2\left(\frac{\xi_1 - \xi_2}{a}\right) \left[a - (\xi_1 - \xi_2) \operatorname{coth}\left(\frac{\xi_1 - \xi_2}{a}\right) \right]. \tag{6.11}
\end{aligned}$$

Applying the Euler-Lagrange equations for each variational parameter yields a system of ordinary differential equations that describe their time evolution (See Appendix 8). In Figure 6.18, we plot the BB soliton's trajectory calculated from the variational approach (solid lines) and compare the result to the numerical calculation for soliton velocity $v = 0.2$. We find that even when we allow for an internal oscillation between the two components in BB soliton, the agreement is good between the two methods.

The transport coefficients, given in Equation (6.5), can be used to calculate also the reflectance, R , transmittance, T , and trapping, L , of the BB soliton obtained from the variational calculations in terms of velocity. In this case, the integration limits will be from the box edge to the potential position for R and T depending on whether the soliton comes from right or left. For the trapping coefficient, the integration covers the potential area only.

Unidirectional segregation by variational and numerical method

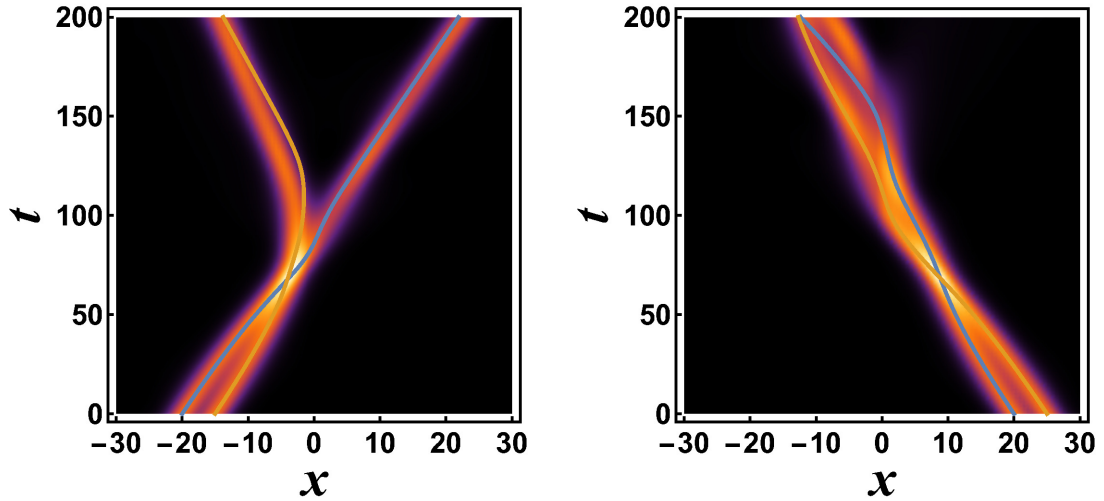


Figure 6.18: Propagation of components through asymmetric double square well potential, see Figure 6.17, for $g_{12} = 0.05$ at $v = 0.2$. Solid lines are results from variational calculation. Intensity plots are results of numerical calculation. Unidirectional segregation of composite BB soliton is achieved with an excellent agreement between variational and numerical method.

Variational calculation for right moving two component solitons

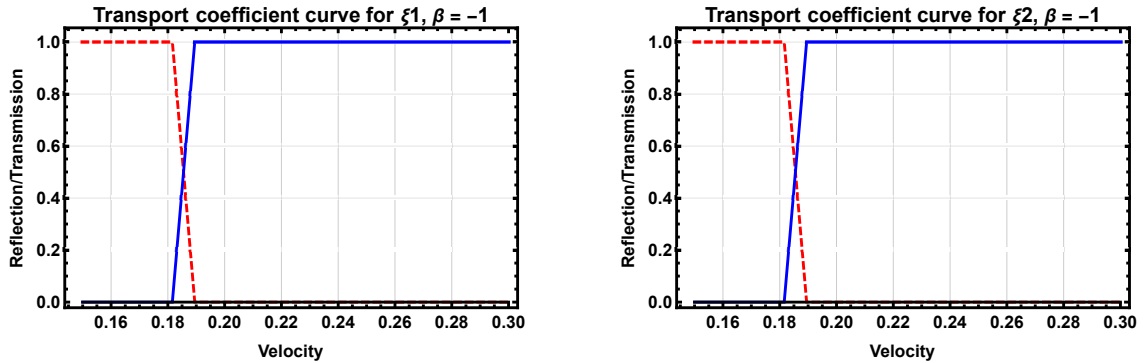


Figure 6.19: Analytically calculated transport coefficients in terms of velocity for the propagation of two right moving components through asymmetric double square potential well for $g_{12} = 0.05$. Upper panel shows first component while lower panel shows second component of the initial wave functions (6.8). There is no segregation in this direction.

In Figure 6.19, we see that for $\beta = -1$ (i.e., sending the BB soliton from the right), the transport coefficient curves are the same for the two components. That is, the two components move through the potential without segregation. But in Figure 6.20, for $\beta = 1$, (i.e., sending the BB soliton from the left) we find that there is a window for the splitting of the two components when the velocity range is $0.17 < v < 0.27$. For example, a BB soliton with $v = 0.2$ as in Figure 6.18, should split in one direction and not the other as seen from Figures 6.19 and 6.20. In Figures 6.21 and 6.22, we plot the transport coefficients for the

numerical simulation of a BB soliton interacting with the same potential. We find a good agreement between the results obtained from the numerical simulation compared to the variational analysis predictions.

Variational calculation for left moving two component solitons

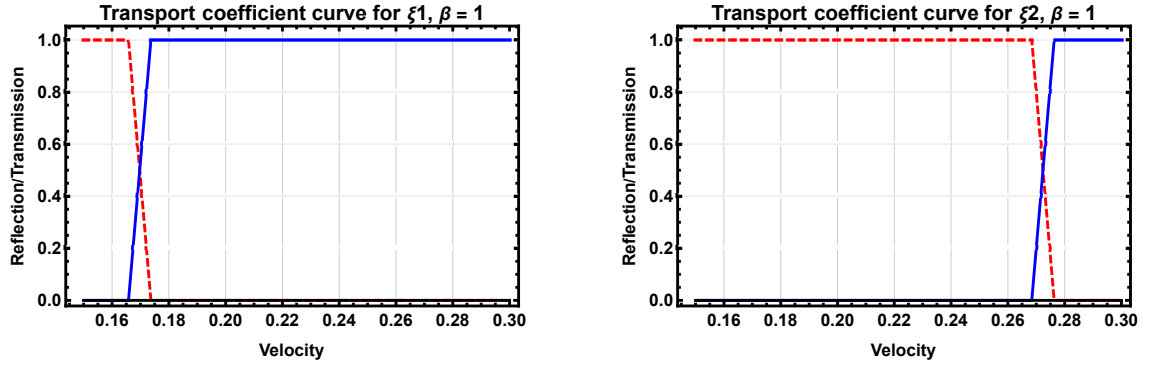


Figure 6.20: Analytically calculated transport coefficients in terms of velocity for the propagation of two left moving components through asymmetric double square potential well for $g_{12} = 0.05$. Upper panel shows first component while lower panel shows second component of the initial wave functions (6.8). Segregation is observed in this direction.

Numerical calculation for right moving two component solitons

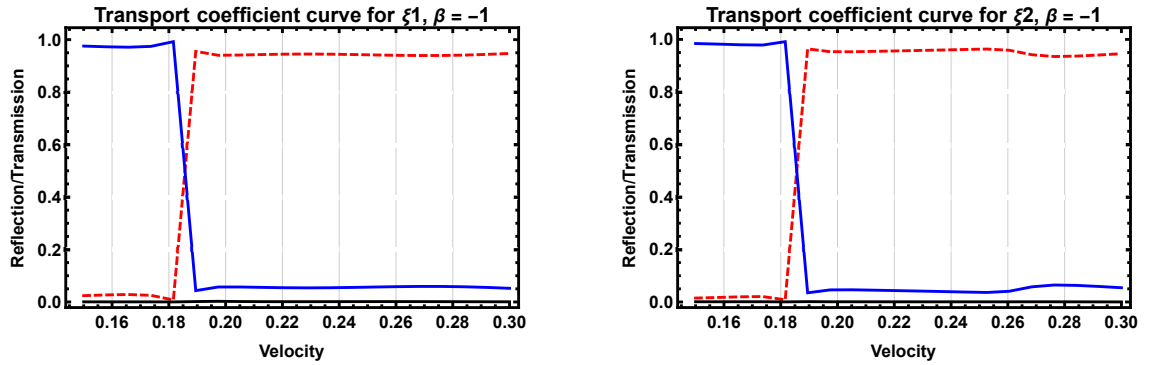


Figure 6.21: Numerically calculated transport coefficients in terms of velocity for the propagation of two right moving components through asymmetric double square potential well for $g_{12} = 0.05$. Upper panel shows first component while lower panel shows second component of the initial wave functions (6.8). There is no segregation in this direction.

6.5 Results and Discussion

We summarize our main results: Firstly, we achieved unidirectional flow of composite BB soliton passing through asymmetric double potential barriers in the absence of nonlinear coupling ($g_{12} = 0$). Our results for the unidirectional flow are achieved with potential

barriers rather than potential wells, as in [45]. Secondly, we achieved also a unidirectional flow of composite BB soliton in the presence of attractive mean field inter-component coupling, i.e., $g_{12} > 0$ using the two selected potentials. Interestingly, we find a change in polarity in unidirectional flow for $g_{12} > 0.329$ for RM potential and $g_{12} > 0.316$ for Gaussian potential. Both components of the BB soliton remained invariant throughout the propagation. Thirdly, we found segregation or splitting of composite BB soliton into its two components in the presence of repulsive mean field interaction coupling, $g_{12} < 0$, through both types of considered potentials. We also observed the shuttle motion between the barriers in our study. However, we restricted ourselves to the parameter regime for the unidirectional flow and segregation.

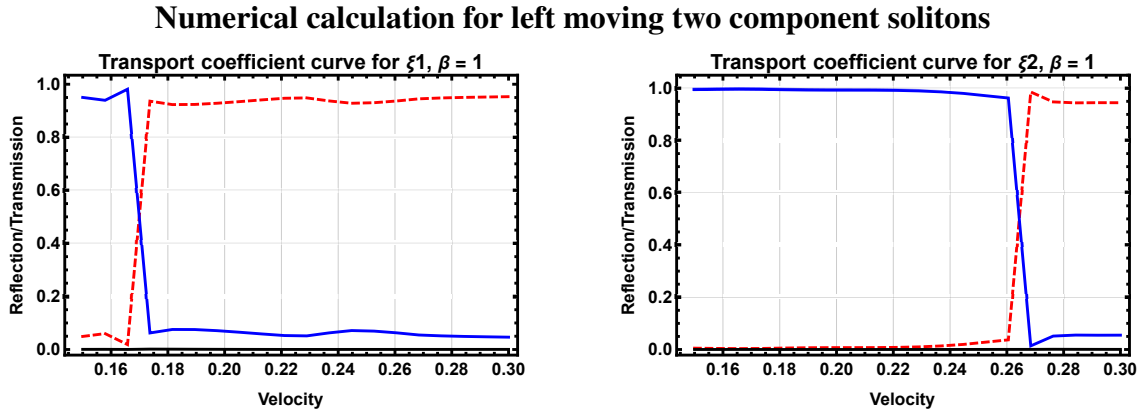


Figure 6.22: Numerically calculated transport coefficients in terms of velocity for the propagation of two left moving components through asymmetric double square potential well for $g_{12} = 0.05$. Upper panel shows first component while lower panel shows second component of the initial wave functions (6.8). Segregation is observed in this direction.

In addition, we achieved unidirectional segregation by varying nonlinear strength of one of the components (g_1) in the absence of nonlinear interaction coupling ($g_{12} = 0$). Further, we realised that an extremely small value of repulsive coupling ($g_{12} = -0.004$) can destroy unidirectional segregation for such a case and results in bidirectional segregation. We also found unidirectional segregation of composite BB soliton using variational calculations and compared our results with numerical computations. We obtained an excellent agreement between analytical and numerical analysis. Our results are applicable to all-optical data processing and we believe that this work is an important contribution to the

effort made towards the realization of optical devices e.g., optical diode, interferometer. Another application would be the realization of quantum logic gates where two solitons are usually needed to code a qubit. The scattering dynamics of the two solitons through the potential may set up a protocol equivalent to a two-qubit logic gate such as CNOT gate.

Chapter 7: All-Optical Quantum Controlled-NOT Gate

In this chapter, we present a protocol for the quantum controlled-NOT gate which is based on two qubits operation by investigating the soliton scattering through a reflectionless potential well in an optical system. We consider the set up of two input solitons with different intensities scattered by a reflectionless potential well with a control soliton placed at the centre of the potential. The two input solitons correspond to the target qubit while presence or absence of control soliton corresponds to the control qubit. We achieve the desired performance of the quantum logic gate by exploiting the intensity difference between the two input solitons and we find this to be possible within a finite width of a velocity of incidence for the two solitons. The calculation of transport coefficients ensures the feasibility of building a quantum controlled-NOT gate. This protocol demonstrates the prospect of soliton scattering by a potential well for quantum information processing.

7.1 Introduction

Here, we propose a novel model to implement the quantum CNOT operation, through a two-soliton scattering in a reflectionless potential well and the presence of control signal soliton in the considered potential well. Our proposed system is not only well decoupled from the previous systems considered but also much simpler and easier to implement the above functionality within a significant velocity and parameter range. The aim of the present work is to construct a quantum controlled-NOT gate using soliton scattering by a reflectionless potential well. We introduce a control soliton placed at the centre of the potential well, which provides more control on the parameters involved in the scattering through the potential. As quantum controlled-NOT gate is two qubit logic gate, it can not be realised with a single soliton. We use two solitons as one input qubit (target) with different intensities. We achieve the desired performance by exploiting a difference in their intensities. The presence or absence of control soliton is considered as the other qubit (control) of the quantum logic gate.

The rest of the chapter is organized as follows. In Section 7.2, we present the setup and theoretical model. In Section 7.3, we show how the quantum controlled-NOT gate can be achieved by using soliton scattering through a reflectionless potential well. Finally, in Section 7.4, we summarize our main results.

7.2 Theoretical Framework and Setup

In the presence of an external potential, $V(x)$, the dynamics of bright solitons is governed by the one-dimensional nonlinear Schrödinger equation, which can be written in the standard dimensionless form as

$$i \frac{\partial}{\partial t} \psi(x, t) = \left[-\frac{1}{2} \frac{\partial^2}{\partial x^2} + V(x) + g |\psi(x, t)|^2 \right] \psi(x, t), \quad (7.1)$$

where, we choose the potential, $V(x)$, of the form

$$V(x) = -V_0 \operatorname{sech}[\alpha(x - x_0)]^2. \quad (7.2)$$

Here, V_0 , α , and x_0 determine the depth, inverse width, and the position of the center of the potential well, respectively. This potential, which is known as the Pöschl-Teller potential, belongs to the class of reflectionless potentials which may transmit without reflection in the linear regime. We use the parameters of potential as: $V_0 = 4$, $\alpha = \sqrt{V_0}$, and $x_0 = 0$. The factor g in Equation (7.1) denotes the mean-field interaction strength and we consider $g = -1$. In our numerical simulation, we prepare an initial state far away from the potential region and propagate it in real time. We consider two propagating solitons as a single qubit (signal/target) and one stationary soliton (control) embedded in the potential well referred to as control soliton. We choose our initial wave function as the exact solution of the homogenous version of Equation (7.1), namely

$$\psi(x, t) = u_1 \operatorname{sech} [u_1(vt - x + x_1)] e^{\frac{1}{2}i((u_1^2 - v^2)t + 2v(x - x_1))}$$

$$\begin{aligned}
& + u_2 \operatorname{sech} [u_2(vt - x + x_2)] e^{\frac{1}{2}i((u_2^2 - v^2)t + 2v(x - x_2))} \\
& + u_3 \operatorname{sech} [u_3(v_0t - x + x_3)] e^{\frac{1}{2}i((u_3^2 - v_0^2)t + 2v_0(x - x_3))}, \tag{7.3}
\end{aligned}$$

where $u_{1,2}$, $x_{1,2}$, and v represent intensity, initial center-of-mass position and velocity of two signal solitons, respectively. The intensity of control soliton is represented by u_3 which is chosen greater than $u_{1,2}$. As control soliton is stationary and located at the origin, where v_0 , and x_3 take the value zero. Our initial protocol can be summarised as

$$\Psi = \Psi_{s1} + \Psi_{s2} + \Psi_c, \tag{7.4}$$

where Ψ_{s1} and Ψ_{s2} are input signal solitons, collectively considered as one qubit, and Ψ_c is the control soliton. The evolution time is taken long enough for the scattered solitons to be far away from the potential. Then, we calculate the reflectance, trapping, and transmittance coefficients. We define the reflectance, trapping and transmittance coefficients as follows:

$$\begin{aligned}
R &= \frac{1}{N} \int_{-\infty}^{-l} |\Psi(x,t)|^2 dx \\
L &= \frac{1}{N} \int_{-l}^l |\Psi(x,t)|^2 dx \\
T &= \frac{1}{N} \int_l^{\infty} |\Psi(x,t)|^2 dx, \tag{7.5}
\end{aligned}$$

respectively, where $l \approx 5/\alpha$, and N is the normalization of the total soliton intensity given by $N = \int_{-\infty}^{\infty} |\Psi(x,t)|^2 dx$. Here, l represents the position of measurement of reflectance or transmission, set at a value slightly greater than the position of the boundary of the potential well, which we represented in terms of the inverse width of the potential α . The limits in the integrations of the transport coefficients are set such that we obtain individual transport coefficients for each one of the two signal solitons.

7.3 The CNOT Gate Protocol

The controlled NOT gate (also C-NOT or CNOT) is a quantum logic gate that is an essential component in the construction of a gate-based quantum computer. It can be used to entangle and disentangle Einstein-Podolsky-Rosen (EPR) states. Any quantum circuit can be simulated to an arbitrary degree of accuracy using a combination of CNOT gates and single qubit rotations. The action of the CNOT gate can be represented by the matrix:

$$CNOT = \begin{bmatrix} 1 & 0 & 0 & 0 \\ 0 & 1 & 0 & 0 \\ 0 & 0 & 0 & 1 \\ 0 & 0 & 1 & 0 \end{bmatrix} \quad (7.6)$$

The CNOT gate operates on a quantum register consisting of 2 qubits. The CNOT gate flips the second qubit (the target qubit) if and only if the first qubit (the control qubit) is $|1\rangle$. The truth table for the CNOT gate is given in Table 7.1.

Table 7.1: Truth table for CNOT gate

Before		After	
Control	Target	Control	Target
$ 0\rangle$	$ 0\rangle$	$ 0\rangle$	$ 0\rangle$
$ 0\rangle$	$ 1\rangle$	$ 0\rangle$	$ 1\rangle$
$ 1\rangle$	$ 0\rangle$	$ 1\rangle$	$ 1\rangle$
$ 1\rangle$	$ 1\rangle$	$ 1\rangle$	$ 0\rangle$

In our protocol we consider two solitons of different amplitudes separated by a certain finite distance which represents the target qubit. The presence or absence of control soliton represents the control qubit. Our scheme for the propagation of two solitons having different intensities or amplitudes through a reflectionless potential well is shown in Figure 7.1. We observe that when the two solitons propagate with the same velocity, v , through a reflectionless potential well in the absence of control soliton, they transmit fully without any change in their path. So, we conclude that there is no change in target qubit in the absence of control soliton as shown in upper panel of Figure 7.1. The dashed double lines at the center of the schematic figure represent the potential. The thin red line between dashed

double lines represents the presence of control soliton which is shown in the lower panel of Figure 7.1.

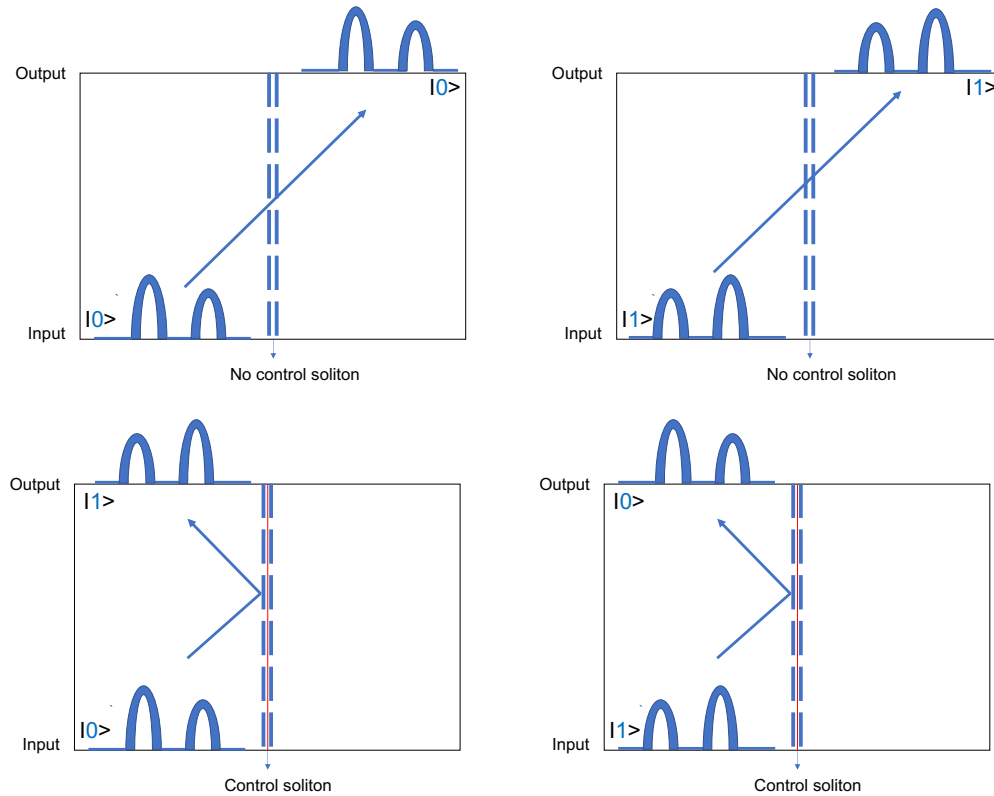


Figure 7.1: Schematic figure representing the solitons' scattering implementation of the controlled-NOT gate. Upper panel: No change in target at output in the absence of control soliton and both solitons show full transmittance through the potential well which is represented by dashed double line at origin. Lower panel: Flip of target at output in the presence of control soliton which is represented by thin red line between dashed double lines of potential.

By introducing the control soliton, we observe a flip in the intensities of the two incoming solitons as they scatter off the potential. This is because, the soliton closer to the potential well will experience reflectance earlier than the other soliton. We follow a similar scheme of controlling the scattering of the target two solitons by introducing a control soliton into a potential well as described in [34]. The input for control qubit of the quantum gate is taken as $|1\rangle$, if there is a control soliton in the potential well and $|0\rangle$ otherwise. The other input qubit for target is designed through the combination of two solitons with different intensities, one of the combinations is taken as $|1\rangle$ and its opposite combination (flip) is taken as $|0\rangle$, as shown in the schematic figure. The output is taken from the scattered

solitons where both target solitons can be reflected, transmitted, trapped or split i.e., one soliton reflects and the other soliton transmitted. It should be noted that we use throughout all numerical calculated solitons that are in-phase with each other. We realize that phase differences may affect the output of the scattering of solitons. Therefore, we chose for simplicity not to incorporate this additional factor in our protocol.

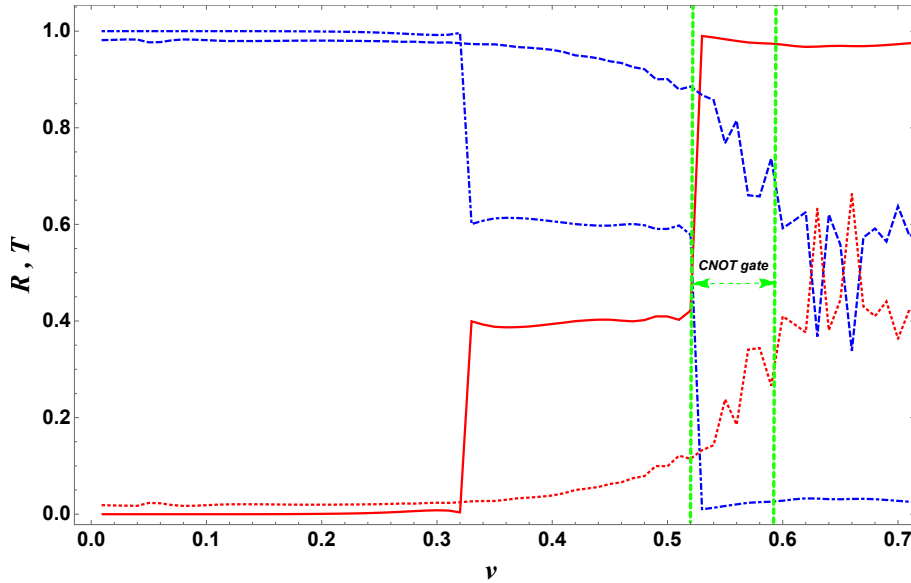


Figure 7.2: Transport Coefficients of CNOT gate: Dashed and dashed-Dotted (blue) curves correspond to total reflectance R . Solid and dotted (red) curves correspond to total transmittance T of the two target solitons. Dashed dotted blue curve and red solid curve correspond to transport coefficients, R, T , in the absence of control soliton while dashed blue and dotted red curves correspond to transport coefficients, R, T , in the presence of control soliton. The working window of velocity for quantum controlled-NOT gate is $0.524 \leq v \leq 0.590$ and is highlighted by the two green vertical dashed borders. The parameters used are $u_{1,2} = 1, 1.5, u_3 = 2, x_1 = -20$, and $x_2 = -40$.

A preliminary investigation of the scattering outcomes in terms of the potential and soliton parameters including potential depth, width, location, soliton initial speed, phase, and type, gives an idea of the ranges of parameters for which the useful applications could be obtained. The transport coefficients curves for the quantum controlled-NOT gate are presented in Figure 7.2 which show a reasonably wide window of velocity for the operation of CNOT gate. The working window of velocity ($0.524 \leq v \leq 0.590$) for quantum CNOT gate is highlighted through the green dashed borders. The parameters used are $u_{1,2} = 1, 1.5, u_3 = 2, x_1 = -20$, and $x_2 = -40$.

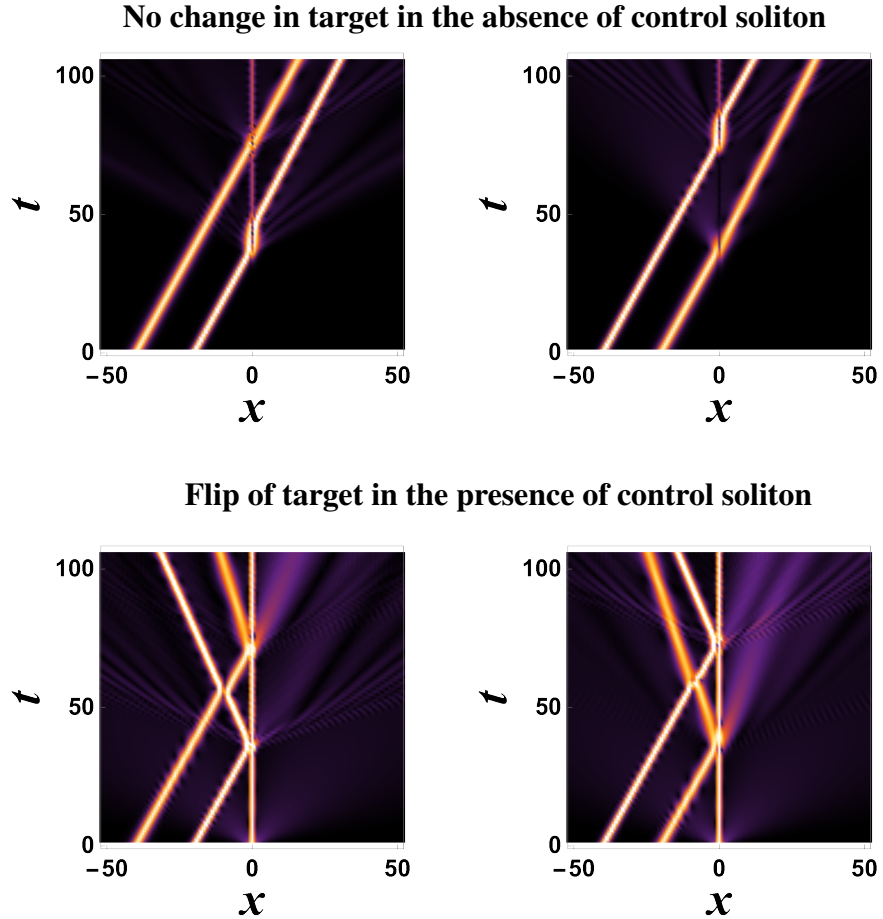


Figure 7.3: Upper panel: Both solitons show full transmittance through the potential well in the absence of control soliton and we observe no change in target. Lower panel: Both solitons reflect through the potential well in the presence of control soliton and we observe a flip in target. The parameters used are $u_{1,2} = 1, 1.5$, $u_3 = 2$, $v = 0.525$, $x_1 = -20$, and $x_2 = -40$.

It can be seen from Figure 7.2 that both target solitons show full reflectance, i.e., $R \approx 1$, for $v < 0.32$ in the absence of control soliton i.e., control qubit = $|0\rangle$. After that, they start splitting through the potential well and one soliton reflects and the other one transmits for $v \leq 0.524$ which makes the first border of velocity window for quantum controlled-NOT gate. After this critical velocity, both target solitons show full transmittance, i.e., $T \approx 1$, which is desired to achieve CNOT gate. We observe no change in the combination of two scattered solitons of different intensities which is also shown in upper panel of Figure 7.3 at velocity $v = 0.525$. Furthermore, by introducing the control soliton i.e., control qubit = $|1\rangle$, target solitons reflect till $v = 0.590$ which makes the second border of velocity window for CNOT gate as mentioned in Figure 7.2. Beyond this value of velocity, they also show splitting through the potential well. We observe a flip in target at output as the

two solitons undergo scattering by a reflectionless potential well which is shown in lower panel of Figure 7.3 at the same velocity $v = 0.525$. The initial profiles of target solitons at $t = 0$ and the final profiles after scattering at $t = t_f$ are shown in Figure 7.4.

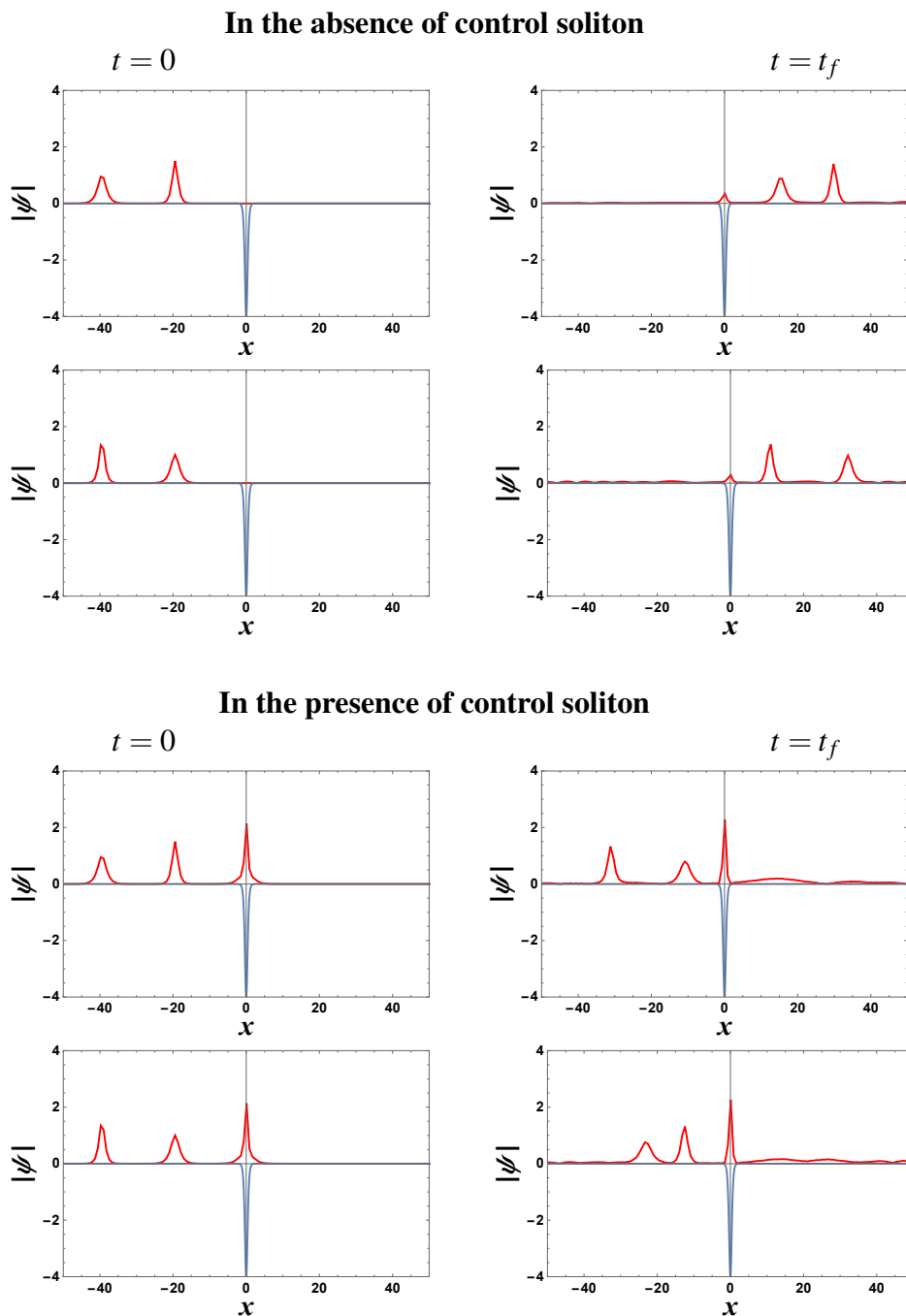


Figure 7.4: Initial and final profiles of target solitons corresponding to Figure 7.3. Here left panel is showing initial profiles of target solitons in the absence and presence of control soliton respectively i.e., at $t = 0$ and right panel shows profiles of target solitons after scattering at $t = t_f = 100$ for each case. The parameters used are the same as in Figure 7.3.

7.4 Discussion and Conclusion

We have shown that by using soliton scattering through a reflectionless potential well, a quantum controlled-NOT gate can be achieved. We introduce a control soliton located at the centre of the potential well, which provides the desired control on the outcome of scattering. Since quantum controlled-NOT gate is a two-qubit logic gate, we use two incoming solitons as one input qubit while the other qubit is represented by a control soliton. We achieve the desired performance by exploiting a difference in the intensities of the two incoming solitons. We find full transmittance of the scattered solitons in the absence of control soliton for a specific velocity window and full reflectance in the presence of control soliton. In addition, we observe an intensity flip in input solitons after scattering through potential well in the presence of control soliton. We find this to be possible within a considerable finite width of a velocity of incidence. Furthermore, we also observe that the working velocity window for quantum controlled-NOT gate can be shifted to lower or higher values by changing the intensity difference in the two input solitons.

A major advancement would be the development of the three single-qubit logic gates within the setup and protocol described here. This is so since together with the controlled-NOT gate, the three single-qubit gates form a complete set from which any other quantum logic gate can be constructed. We believe this proposal will be a useful step towards achieving all-optical quantum logic gates.

Chapter 8: Conclusion and Recommendations

The dissertation investigates the study of all-optical data processing through solitons in waveguides arrays and optical fibers by employing analytical and numerical methods. In Chapter 2, we have shown that by modifying the setup of the previously-proposed OR gate in a waveguide array, an XOR gate can be obtained. The modification includes the introduction of a third potential well in addition to the two potential wells in the OR gate. A control soliton is injected into the new potential well. The role of the new potential well and its control soliton is to disperse the (11) output signal from the (10) and (01) outputs exploiting a difference in their center-of-mass speed. We found this to be possible within a finite width of a velocity of incidence that is comparable with that of the OR gate. We have also shown how the AND, OR, and XOR gates can be connected to result in half and full adders. We believe this proposal will be a useful step towards achieving all-optical data processing.

In Chapter 3, we exploit the sharp transition region between full reflectance and full transmittance to achieve optical signals amplification. We find that the transition region is highly sensitive to the intensity of the input control soliton. For reflectionless potential, the sensitivity is too high to be experimentally realized. Therefore, we modulate the reflectionless potential well to achieve a realistic performance of amplifier with a controllable amplification. We also show that amplification value can be controlled by the intensity of a control soliton located at the centre of potential well and the modulation of the potential well parameters, mainly its width. We performed a detailed numerical investigation of the effect of all parameters regimes in order to optimize the performance. The separations between the waveguides can be calculated and set to achieve such a potential profile. We believe this to be an important and useful step towards achieving a soliton transistor and all-optical data processing. Our result shows that the amplification factor is also dependent on the intensity of the input signal. This leads to nonlinear amplification, which we believe is not favorable from a practical point of view. In an ideal situation, the

amplification factor ought to be constant so that no modulation of the relative amplitudes or profile of the input signal is performed while amplifying it. We consider this as a challenge for a future work where we aim at obtaining an amplification scheme with constant amplification factor within a finite range of input signal intensities.

In Chapter 4, we have used both numerical and variational calculations to obtain the equilibrium profiles and ground state of discrete two-soliton molecules in 2D waveguide arrays. Using a gaussian variational trial function, with six variational parameters corresponding to the coordinates peak positions and widths of the two solitons, we calculated the PN potential and the interaction potential between the solitons. We have investigated the mobility of the soliton molecule and found that binding does not enhance on the mobility. Neither the bond length nor the direction of the molecule's motion had a tangible effect of the mobility. We have shown the existence of stable discrete soliton molecules in two-dimensional waveguide arrays. Analogy was made to the classical diatomic model with linear restoring force. We have also found a unique behavior of a meta stable state of a soliton molecule made of two out-of-phase solitons each placed in a different waveguide. Such a molecule shows a sudden splitting into two solitons propagating away from each other. We believe our results will be valuable for the all-optical applications using solitons to perform optical data processing.

In Chapter 5, we mapped the spin-1/2 system to a 2D Manakov system through a rotation operator that gives the spin texture of skyrmions and we have investigated all possible 2D skyrmion textures. We solved the 2D Manakov system using various analytical and numerical methods. While the similarity transformation method maps all solutions of the integrable 1D Manakov system to the 2D Manakov system, the solutions of the latter turn out to diverge at $\rho = 0$. Nondiverging solutions were then obtained using a power series method. However, the spin texture associated with these solutions turned out to be trivial, i.e., no texture. Finally, we considered a numerical solution of a system of coupled equations for the skyrmion density, $n(\rho, \phi)$, and texture, $\omega(\rho, \phi)$. This led to nondiverging

and nontrivial spin textures. Then, we investigated the stability of these nontrivial nondiverging skyrmions by calculating their energy functional in terms of their effective size. It turned out that stable skyrmions correspond to concentric rings of spin components alternating between spin up and spin down. Metastable states, where energy is either increasing or decreasing with skyrmion size, correspond to concentric rings of mixed spin components. Our results show that, in contrast with the established fact that in two dimensions localized solutions of the NLSE are unstable, the two spin states stabilize each other against collapse and allow for nontrivial stable two-dimensional topological excitations. Our results are also applicable to doubly polarized optical pulses. We strongly believe that this chapter is an important addition to the effort of realizing topological excitations.

We summarize our main results of chapter 6: Firstly, we achieved unidirectional flow of composite BB soliton passing through asymmetric double potential barriers in the absence of nonlinear coupling ($g_{12} = 0$). We considered two types of potentials for our numerical simulations. We choose asymmetric RM and Gaussian double barrier potentials. Our results for the unidirectional flow are achieved with potential barriers rather than potential wells. Secondly, we achieved also a unidirectional flow of composite BB soliton in the presence of attractive mean field inter-component coupling, i.e., $g_{12} > 0$ using the two selected potentials. Interestingly, we find a change in polarity in unidirectional flow for $g_{12} > 0.329$ for RM potential and $g_{12} > 0.316$ for Gaussian potential. Both components of the BB soliton remained invariant throughout the propagation. Thirdly, we found segregation or splitting of composite BB soliton into its two components in the presence of repulsive mean field interaction coupling, $g_{12} < 0$, through both types of considered potentials. We also observed the shuttle motion between the barriers in our study. However, we restricted ourselves to the parameter regime for the unidirectional flow and segregation. In addition, we achieved unidirectional segregation by varying nonlinear strength of one of the components (g_1) in the absence of nonlinear interaction coupling ($g_{12} = 0$). Further, we realised that an extremely small value of repulsive coupling ($g_{12} = -0.004$) can destroy the unidirectional segregation for such a case and results

in bidirectional segregation. We also found unidirectional segregation of composite BB soliton using variational calculations and compared our results with numerical computations. We obtained an excellent agreement between analytical and numerical analysis. Our results are applicable to all-optical data processing and we strongly believe that this work is an important contribution to the effort made towards the realization of optical devices e.g., optical diode, interferometer. Another application would be the realization of quantum logic gates where two solitons are usually needed to code a qubit. The scattering dynamics of the two solitons through the potential may set up a protocol equivalent to a two-qubit logic gate such as CNOT gate.

In Chapter 7, we have shown that by using soliton scattering through a reflectionless potential well, a quantum controlled-NOT gate can be achieved. We introduce a control soliton located at the centre of the potential well, which provides the desired control on the outcome of scattering. Since quantum controlled-NOT gate is a two-qubit logic gate, we use two incoming solitons as one input qubit while the other qubit is represented by a control soliton. We achieve the desired performance by exploiting a difference in the intensities of the two incoming solitons. We find full transmittance of the scattered solitons in the absence of control soliton for a specific velocity window and full reflectance in the presence of control soliton. In addition, we observe an intensity flip in input solitons after scattering through potential well in the presence of control soliton. We find this to be possible within a considerable finite width of a velocity of incidence. Furthermore, we also observe that the working velocity window for quantum controlled-NOT gate can be shifted to lower or higher values by changing the intensity difference in the two input solitons. A major advancement would be the development of the three single-qubit logic gates within the setup and protocol described here. This is so since together with the controlled-NOT gate, the three single-qubit gates form a complete set from which any other quantum logic gate can be constructed. We believe this proposal will be a useful step towards achieving all-optical quantum logic gates.

References

- [1] G. P. Agrawal, "Nonlinear Fiber Optics", Fifth Edition. Academic press, 2012.
- [2] B. P. Pal, "Guided wave optical components and devices", Academic press, 1st edition, 2006.
- [3] A. Hasegawa, and M. Matsumoto, "Optical Solitons in Fibers", Springer, 2003.
- [4] A. Yariv, "Coupled-mode theory for guided-wave optics", *IEEE J. Quan. Elec.*, 9, 919, 1973.
- [5] Y. S. Kivshar and B. A. Malomed, "Interaction of solitons in tunnel-coupled optical fibers", *Opt. Lett.*, 14, 1365, 1989.
- [6] P. L. Chu, G. D. Peng, and B. A. Malomed, "Analytical solution to soliton switching in nonlinear twin-core fibers", *Opt. Lett.*, 18, 328, 1993.
- [7] S. Konar, S. Jana, and M. Mishra, "Induced focusing and all optical switching in cubic quintic nonlinear media", *Opt. Commun.*, 255, 114, 2005.
- [8] N. Akhmediev and A. Ankiewicz, "Dissipative solitons: From optics to biology and medicine", Springer, 2008.
- [9] N.N. Rao, P.K. Shukla, and M.Y. Yu, "Dust-acoustic waves in dusty plasmas", *Planetary and Space Sci.*, 38, 543, 1990.
- [10] O. Aharony, S. S. Gubser, J. Maldacena, H. Ooguri, and Y. Oz, "Large N field theories, string theory and gravity", *Phys. Rep.*, 323, 183, 2000.
- [11] K. Dysthe, H. E. Krogstad, and P. Mller, "Oceanic rogue waves", *Annual Rev. Fluid Mechanics*, 40, 287, 2008.
- [12] P. Pedri and L. Santos, "Two-dimensional bright solitons in dipolar Bose-Einstein condensates", *Phys. Rev. Lett.*, 95, 200404, 2005.
- [13] R. V. J. Raja, K. Senthilnathan, K. Porsezian and K. Nakkeeran, "Efficient pulse compression using tapered photonic crystal fiber at 850 nm", *IEEE J. Quan. Elec.*, 46, 1795, 2010.
- [14] Y. Xu, X. Chen, and Y. Zhu, "High sensitive temperature sensor using a liquid-core optical fiber with small refractive index difference between core and cladding materials", *Sensors*, 8, 1872, 2008.
- [15] A. Scott, "Encyclopedia of nonlinear science", Routledge, 2005.
- [16] A. Hasegawa and Y. Kodama, "Solitons in optical communications", Oxford: Oxford Univ. Press, 1995.
- [17] L. Mollenauer and J. Gordon, "Solitons in optical fibers", Boston: Academic Press, 2006.
- [18] N. Akhmediev and A. Ankiewicz, "Solitons: Nonlinear Pulses and Beams", London: Chapman and Hall, 1997.

- [19] G. Agrawal, "Nonlinear fiber optics", 3rd ed, San Diego: Academic Press, 2001.
- [20] Y. S. Kivshar and G. P. Agrawal. "Optical Solitons: From fibers to photonic crystals", Academic Press, San Diego, 2003.
- [21] R. Keil, M. Heinrich, F. Dreisow, T. Pertsch, A. Tünnermann, S. Nolte, D. Christodoulides and A. Szameit, "All-optical routing and switching for three-dimensional photonic circuitry", *Sci. Rep.*, 1, 94, 2011.
- [22] A. Politi, M. Cryan, J. Rarity, S. Yu and J. O'Brien, "Silica-on-Silicon Waveguide Quantum Circuits", *Science*, 320, 646, 2008.
- [23] J. Sabini, N. Finlayson and G. Stegeman, "All optical switching in non linear X junctions", *Appl. Phys. Lett.*, 55, 1176, 1989.
- [24] P. Chu, Y. Kivshar, B. Malomed, G. Peng and M. Quiroga-Teixeiro, "Soliton controlling, switching, and splitting in nonlinear fused-fiber couplers", *J. Opt. Soc. Am. B*, 12, 898, 1995.
- [25] M. Peccianti, C. Conti, G. Assanto, A. De Luca, and C. Umeton, "All-optical switching and logic gating with spatial solitons in liquid crystals", *Appl. Phys. Lett.*, 81, 3335, 2002.
- [26] A. Piccardi, A. Alberucci, U. Bortolozzo, S. Residori, and G. Assanto, "Soliton gating and switching in liquid crystal light valve", *Appl. Phys. Lett.*, 96, 071104, 2010.
- [27] W. Krolikowski and Y. Kivshar, "Soliton-based optical switching in waveguide arrays", *J. Opt. Soc. Am. B*, 13, 876, 1996.
- [28] Y. Wu, "All-optical logic gates by using multibranch waveguide structure with localized optical nonlinearity", *IEEE J. Sel. Top. Quantum Electron*, 11, 307, 2005.
- [29] Y. Wu, M. Huang, M. Chen, R. Tasy, "All-optical switch based on the local nonlinear Mach-Zehnder interferometer", *Opt. Express*, 15, 9883, 2007.
- [30] K. M. Aghdami, M. Golshani, and R. Kheradmand, "Two-dimensional discrete cavity solitons: switching and all-optical gates", *IEEE Photon. J.*, 4, 1147, 2012.
- [31] D. Christodoulides and E. Eugenieva, "Blocking and Routing Discrete Solitons in Two-Dimensional Networks of Nonlinear Waveguide Arrays", *Phys. Rev. Lett.*, 87, 23, 2001.
- [32] J. Scheuerand, M. Orenstein, "All-optical gates facilitated by soliton interactions in a multilayered Kerr medium", *J. Opt. Soc. Am. B*, 22, 1260, 2005.
- [33] A. Javed, A. Shaheen, and U. Al Khawaja, "Amplifying optical signals with discrete solitons in waveguide arrays", *Phys. Lett. A*, 384, 126654, 2020.
- [34] A. Shaheen, A. Javed, and U. Al Khawaja, "Adding binary numbers with discrete solitons in waveguide arrays", *Phys. Scr.*, 95, 085107, 2020.
- [35] P. S. Vinayagam, A. Javed, and U. A. Khawaja, "Stable discrete soliton molecules in two-dimensional waveguide arrays", *Phys. Rev. A*, 98, 063839, 2018.
- [36] J. Taylor, "Optical Solitons -Theory and Experiment", Cambridge: Cambridge Univ. Press, 1992.

- [37] M. Stratmann, T. Pagel, and F. Mitschke, “Experimental observation of temporal soliton molecules”, *Phys. Rev. Lett.*, 95, 143902, 2005.
- [38] A. Hause, H. Hartwig, M. Bohm, and F. Mitschke, “Binding mechanism of temporal soliton molecules”, *Phys. Rev. A*, 78, 063817, 2008.
- [39] A. Hause, H. Hartwig, B. Seifert, H. Stolz, M. Bohm, and F. Mitschke, “Phase structure of soliton molecules”, *Phys. Rev. A*, 75, 063836, 2007.
- [40] U. Al Khawaja and H. Stoof, “Formation of matter-wave soliton molecules”, *New J. Phys.*, 13, 085003, 2011.
- [41] A. Sukhorukov, “Reflectionless potentials and cavities in waveguide arrays and coupled-resonator structures”, *Opt. Lett.*, 35, 989, 2010.
- [42] S. Lepri and G. Casati, “Asymmetric Wave Propagation in Nonlinear Systems”, *Phys. Rev. Lett.*, 106, 164101, 2011.
- [43] U. Al Khawaja and A. Sukhorukov, “Unidirectional flow of discrete solitons in waveguide arrays”, *Opt. Lett.*, 40, 2719, 2015.
- [44] U. Al Khawaja, S. Al-Marzoug, and H. Bahlouli, “Unidirectional flow of discrete solitons in optical waveguide arrays with modulated nonlinearity”, *Phys. Lett. A*, 384, 126625, 2020.
- [45] U. Al Khawaja and M. Asad-uz-zaman, “Directional flow of solitons with asymmetric potential wells: Soliton diode”, *Europhys. Lett.*, 101, 50008, 2013.
- [46] U. Al Khawaja, S. Al-Marzoug, H. Bahlouli and Y. Kivshar, “Unidirectional soliton flows in PT-symmetric potentials”, *Phys. Rev. A*, 88, 023830, 2013.
- [47] M. Alotaibi, S. Al-Marzoug, H. Bahlouli and U. Khawaja, “Unidirectional flow of solitons with nonlinearity management”, *Phys. Rev. E*, 100, 042213, 2019.
- [48] D. N. Christodoulides, and R. I. Joseph, “Discrete self-focusing in nonlinear arrays of coupled waveguides”, *Opt. Lett.*, 13, 794, 1988.
- [49] H. S. Eisenberg, Y. Silberberg, R. Morandotti, A. R. Boyd, and J. S. Aitchison, “Discrete spatial optical solitons in waveguide arrays”, *Phys. Rev. Lett.*, 81, 3383, 1998.
- [50] C. Mejía-Cortés, R. A. Vicencio, and B. A. Malomed, “Mobility of solitons in one-dimensional lattices with the cubic-quintic nonlinearity”, *Phys. Rev. E*, 88, 052901, 2013.
- [51] A. B. Aceves, C. De Angelis, T. Peschel, R. Muschall, F. Lederer, S. Trillo, and S. Wabnitz, “Discrete self-trapping, soliton interactions, and beam steering in nonlinear waveguide arrays”, *Phys. Rev. E*, 53, 1172, 1996.
- [52] R. Carretero-González, J. D. Talley, C. Chong, B. A. Malomed, “Multistable solitons in the cubic–quintic discrete nonlinear Schrödinger equation”, *Physica D*, 216, 77, 2006.
- [53] I. E. Papacharalampous, P. G. Kevrekidis, B. A. Malomed, and D. J. Frantzeskakis, “Soliton collisions in the discrete nonlinear Schrödinger equation”, *Phys. Rev. E*, 68, 046604, 2003.

- [54] Y. S. Kivshar and B. A. Malomed, “Dynamics of solitons in nearly integrable systems”, *Rev. Mod. Phys.*, 61, 763, 1989.
- [55] Y. S. Kivshar and D. K. Campbell, “Peierls-Nabarro potential barrier for highly localized nonlinear modes”, *Phys. Rev. E*, 48, 3077, 1993.
- [56] L. Brizhik, A. Eremko, L. Cruzeiro-Hansson, and Y. Olkhovska, “Soliton dynamics and Peierls-Nabarro barrier in a discrete molecular chain”, *Phys. Rev. B*, 61, 1129, 2000.
- [57] P. G. Kevrekidis, I. G. Kevrekidis, A. R. Bishop, and E. S. Titi, “Continuum approach to discreteness”, *Phys. Rev. E*, 65, 046613, 2002.
- [58] M. Johansson, P. Jason, *Breather Mobility and the Peierls-Nabarro Potential: Brief Review and Recent Progress*. In: J. F. R. Archilla, N. Jiménez, V. J. Sánchez-Morcillo, L. M. García-Raffi (eds) Quodons in Mica. Springer Series in Materials Science, Springer, 2015.
- [59] I. L. Garanovich, S. Longhi, A. A. Sukhorukov, Y. S. Kivshar, “Light propagation and localization in modulated photonic lattices and waveguides”, *Physics Reports*, 518, 1, 2012.
- [60] J. W. Fleischer, M. Segev, N. K. Efremidis, and D. N. Christodoulides, “Observation of two-dimensional discrete solitons in optically induced nonlinear photonic lattices”, *Nature*, 422, 147, 2003.
- [61] R. Keil, M. Heinrich, F. Dreisow, T. Pertsch, A. Tünemann, S. Nolte, D. N. Christodoulides, and A. Szameit, “All-optical routing and switching for three-dimensional photonic circuitry”, *Sci. Rep.*, 1, 94, 2011.
- [62] K. M. Aghdami, M. Golshani, and R. Kheradmand, “Two-dimensional discrete cavity solitons: switching and all-optical gates”, *IEEE Photon. J.*, 4, 1147, 2012.
- [63] D. N. Christodoulides and E. D. Eugenieva, “Blocking and routing discrete solitons in two-dimensional networks of nonlinear waveguide arrays”, *Phys. Rev. Lett.*, 87, 233901, 2001.
- [64] P. G. Kevrekidis, K. Ø. Rasmussen, and A. R. Bishop, “Two-dimensional discrete breathers: Construction, stability, and bifurcations”, *Phys. Rev. E*, 61, 2006, 2000.
- [65] U. Al Khawaja, P. S. Vinayagam, and S. M. Al-Marzoug, “Enhanced mobility of discrete solitons in anisotropic two-dimensional waveguide arrays with modulated separations”, *Phys. Rev. A*, 97, 023820, 2018.
- [66] L. Hadžievski, A. Maluckov, M. Stepić, and D. Kip, “Power controlled soliton stability and steering in lattices with saturable nonlinearity”, *Phys. Rev. Lett.*, 93, 033901, 2004.
- [67] R. A. Vicencio and M. Johansson, “Discrete soliton mobility in two-dimensional waveguide arrays with saturable nonlinearity”, *Phys. Rev. E*, 73, 046602, 2006.
- [68] P. G. Kevrekidis, B. A. Malomed, A. Saxena, A. R. Bishop, and D. J. Frantzeskakis, “Solitons and vortices in two-dimensional discrete nonlinear Schrödinger systems with spatially modulated nonlinearity”, *Phys. Rev. E*, 91, 043201, 2015.

- [69] V. A. Brazhnyi and B. A. Malomed, "Localization and delocalization of two-dimensional discrete solitons pinned to linear and nonlinear defects", *Phys. Rev. E*, 83, 016604, 2011.
- [70] Z. Chen, J. Liu, S. Fu, Y. Li, and B. A. Malomed, "Discrete solitons and vortices on two-dimensional lattices of PT-symmetric couplers.", *Opt. Exp.*, 22, 29679, 2014.
- [71] A. Hause, H. Hartwig, M. Bohm, and F. Mitschke, "Binding mechanism of temporal soliton molecules", *Phys. Rev. A*, 78, 063817, 2008.
- [72] S. V. Manakov, "On the theory of two-dimensional stationary self-focusing of electromagnetic waves," *J. Exp. Theor. Phys.*, 38, 248, 1974.
- [73] M. R. Gupta, B. K. Som, and B. Dasgupta, "Coupled nonlinear Schrödinger equations for Langmuir and electromagnetic waves and extension of their modulational instability domain," *J. Plasma Phys.*, 25, 499, 1981.
- [74] Y. Chen and H. A. Haus, "Solitons and polarization mode dispersion," *Opt. Lett.*, 25, 290, 2000.
F. K. Abdullaev, B. A. Umarov, M. R. B. Wahiddin, and D. V. Navotny, "Dispersion-managed solitons in a periodically and randomly inhomogeneous birefringent optical fiber," *J. Opt. Soc. Am.*, 17, 1117, 2000.
- [75] C. Xie, M. Karlsson, P. A. Andrekson, and H. Sunnerud, "Statistical analysis of soliton robustness to polarisation-mode dispersion," *Electron. Lett.*, 36, 1575, 2000.
- [76] J. U. Kang, G. I. Stegeman, J. S. Aitchison, and N. Akhmediev, "Observation of Manakov spatial solitons in AlGaAs planar waveguides," *Phys. Rev. Lett.*, 76, 3699, 1996.
- [77] K. Xu, Y. Chen, T. A. Okhai, and L. W. Snyman, "Micro optical sensors based on avalanching silicon light-emitting devices monolithically integrated on chips," *Opt. Mater. Express*, 9, 3985, 2019.
- [78] M. Tajiri and M. Hagiwara, "Similarity solutions of the two-dimensional coupled nonlinear Schrödinger equation," *J. Phys. Soc. Jpn.*, 52, 3727, 1983.
- [79] E. Arévalo, "Solitary wave solutions as a signature of the instability in the discrete nonlinear Schrödinger equation," *Phys. Rev. Lett.*, 102, 224102, 2009.
- [80] H.Q. Zhang, X.H. Meng, T. Xu, L. L. Li, and B. Tian, "Interactions of bright solitons for the (2+ 1)-dimensional coupled nonlinear Schrödinger equations from optical fibres with symbolic computation," *Phys. Scr.*, 75, 537, 2007.
- [81] Y. P. Wang, B. Tian, W. R. Sun, and D. Y. Liu, "Analytic study on the mixed-type solitons for a (2+ 1)-dimensional N-coupled nonlinear Schrödinger system in nonlinear optical-fiber communication," *Commun. Nonlinear Sci. Numer. Simul.*, 22, 1305, 2015.
- [82] Y. J. Cai, C. L. Bai, and Q. L. Luo, "Exact soliton solutions for the (2+ 1)-dimensional coupled higher-order Nonlinear Schrödinger equations in birefringent optical-fiber communication," *Commun. Theor. Phys.*, 67, 273, 2017.
- [83] S. T. Ji and X. S. Liu, "Generating ring dark solitons in two-component Bose–Einstein condensates," *Phys. Lett. A*, 378, 524, 2014.

- [84] J. Stockhofe, P. G. Kevrekidis, D. J. Frantzeskakis, and P. Schmelcher, “Dark–bright ring solitons in Bose–Einstein condensates,” *J. Phys. B*, 44, 191003, 2011.
- [85] J. Hudock, P. G. Kevrekidis, B. A. Malomed, and D. N. Christodoulides, “Discrete vector solitons in two-dimensional nonlinear waveguide arrays: Solutions, stability, and dynamics,” *Phys. Rev. E*, 67, 056618, 2003.
- [86] J. W. Fleischer, M. Segev, N. K. Efremidis, and D. N. Christodoulides, “Observation of two-dimensional discrete solitons in optically induced nonlinear photonic lattices,” *Nature*, 422, 147, 2003.
- [87] H. N. Hassan and M. A. El-Tawil, “Solving cubic and coupled nonlinear Schrödinger equations using the homotopy analysis method,” *J. Appl. Math. Mech.*, 7, 41, 2011.
- [88] F. Kh Abdullaev and E. N. Tsoy, “The evolution of optical beams in self-focusing media,” *Physica D*, 161, 67, 2002.
- [89] U. Al Khawaja and H. T. C. Stoof, “Skyrmion physics in Bose-Einstein ferromagnets,” *Phys. Rev. A*, 64, 043612, 2001.
- [90] U. Al Khawaja and H. T. C. Stoof, “Skyrmions in a ferromagnetic Bose–Einstein condensate,” *Nature*, 411, 918, 2001.
- [91] H. T. C. Stoof, E. Vliegen, and U. Al Khawaja, “Monopoles in an antiferromagnetic Bose-Einstein condensate,” *Phys. Rev. Lett.*, 87, 120407, 2001.
- [92] J. Noh, W. A. Benalcazar, S. Huang, M. J. Collins, K. P. Chen, T. L. Hughes, and M. C. Rechtsman, “Topological protection of photonic mid-gap defect modes,” *Nat. Photonics*, 12, 408, 2018.
- [93] Y. Ke, X. Qin, F. Mei, H. Zhong, Y. S. Kivshar, and C. Lee, “Topological phase transitions and thouless pumping of light in photonic waveguide arrays,” *Laser Photonics Rev.*, 10, 995, 2016.
- [94] K. Forinash, M. Peyrard, and B. Malomed, “Interaction of discrete breathers with impurity modes”, *Phys. Rev. E*, 49, 3400, 1994.
- [95] X. Cao and B. Malomed, “Soliton-defect collisions in the nonlinear Schrödinger equation” *Phys. Lett. A*, 206, 177, 1995.
- [96] D. J. Frantzeskakis, G. Theocharis, F. K. Diakonov, P. Schmelcher, and Y. S. Kivshar, “Interaction of dark solitons with localized impurities in Bose-Einstein condensates”, *Phys. Rev. A*, 66, 053608, 2002.
- [97] A. E. Miroshnichenko, S. Flach, and B. Malomed, “Resonant scattering of solitons”, *Chaos*, 13, 874, 2003.
- [98] V. Ahufinger, A. Mebrahtu, R. Corbalan, and A. Sanpera, “Quantum switches and quantum memories for matter-wave lattice solitons”, *New J. Phys.*, 9, 4, 2007.
- [99] C. Weiss and Y. Castin, “Creation and Detection of a Mesoscopic Gas in a Nonlocal Quantum Superposition”, *Phys. Rev. Lett.*, 102, 010403, 2009.
- [100] A. I. Streltsov, O. E. Alon, and L. S. Cederbaum, “Scattering of an attractive Bose-Einstein condensate from a barrier: Formation of quantum superposition states”, *J. Phys. B*, 42, 091004, 2009.

- [101] Y. S. Kivshar, ZhangFei, and L. Vázquez, “Resonant soliton-impurity interactions”, *Phys. Rev. Lett.*, 67, 1177, 1991.
- [102] R. H. Goodman, P. J. Holmes, and M. I. Weinstein, “Strong NLS soliton defect interactions”, *Physica D*, 192, 215, 2004.
- [103] H. Sakaguchi and M. Tamura, “Scattering and trapping of nonlinear Schrödinger solitons in external potentials”, *J. Phys. Soc. Jpn.*, 73, 503, 2004.
- [104] K. T. Stoychev, M. T. Primatarowa, and R. S. Kamburova, “Resonant scattering of nonlinear Schrödinger solitons from potential wells”, *Phys. Rev. E*, 70, 066622, 2004.
- [105] L. Morales-Molina and R. A. Vicencio, “Trapping of discrete solitons by defects in nonlinear waveguide arrays”, *Opt. Lett.*, 31, 966, 2006.
- [106] C. Lee and J. Brand, “Enhanced quantum reflection of matter-wave solitons”, *Europhys. Lett.*, 73, 321, 2006.
- [107] T. Ernst and J. Brand, “Resonant trapping in the transport of a matter-wave soliton through a quantum well”, *Phys. Rev. A*, 81, 033614, 2010.
- [108] A. B. Aceves, J. V. Moloney, and A. C. Newell, “Theory of light-beam propagation at nonlinear interfaces. I. Equivalent-particle theory for a single interface”, *Phys. Rev. A*, 39, 1809, 1989.
- [109] Y. S. Kivshar, A. M. Kosevich, and O. A. Chubykalo, “Radiative effects in the theory of beam propagation at nonlinear interfaces”, *Phys. Rev. A*, 41, 1677, 1990.
- [110] S. L. Cornish, N. G. Parker, A. M. Martin, T. E. Judd, R. G. Scott, T. M. Fromhold, and C. S. Adams, “Quantum reflection of bright matter-wave solitons” *Physica D*, 238, 1299, 2009.
- [111] T. A. Pasquini, Y. Shin, C. Sanner, M. Saba, A. Schirotzek, D. E. Pritchard, and W. Ketterle, “Quantum Reflection from a Solid Surface at Normal Incidence”, *Phys. Rev. Lett.*, 93, 223201, 2004.
- [112] T. A. Pasquini, M. Saba, G.B. Jo, Y. Shin, W. Ketterle, D. E. Pritchard, T. A. Savas, and N. Mulders, “Low Velocity Quantum Reflection of Bose-Einstein Condensates”, *Phys. Rev. Lett.*, 97, 093201, 2006.
- [113] J. Cuevas, P. G. Kevrekidis, B. A. Malomed, P. Dyke, and R. G. Hulet, “Interactions of solitons with a Gaussian barrier: splitting and recombination in quasi-one-dimensional and three-dimensional settings”, *New. J. Phys.*, 15, 063006, 2013.
- [114] W. Liu, Y. N. Zhu, M. Liu, B. Wen, S. Fang, H. Teng, M. Lei, L. M. Liu, and Z. Wei, “Optical properties and applications for MoS₂-Sb₂Te₃-MoS₂ heterostructure materials”, *Photonics Res.*, 6, 220, 2018.
- [115] W. Liu, L. Pang, H. Han, Z. Shen, M. Lei, H. Teng, and Z. Wei, “Dark solitons in WS₂ erbium-doped fiber lasers”, *Photonics Res.*, 4, 111, 2016.
- [116] W. Liu, L. Pang, H. Han, M. Liu, M. Lei, S. Fang, H. Teng, and Z. Wei, “Tungsten disulfide saturable absorbers for 67 fs mode-locked erbium-doped fiber lasers”, *Opt. Express*, 25, 2950, 2017.

- [117] W. Liu, L. Pang, H. Han, K. Bi, M. Lei, and Z. Wei, "Tungsten disulphide for ultrashort pulse generation in all-fiber lasers", *Nanoscale*, 9, 5806, 2017.
- [118] Y. Yan, W. Liu, Q. Zhou, and A. Biswas, "Dromion-like structures and periodic wave solutions for variable-coefficients complex cubic-quintic Ginzburg-Landau equation influenced by higher-order effects and nonlinear gain", *Nonlinear Dyn.*, 99, 1313, 2020.
- [119] W. Liu, W. Yu, C. Yang, M. Liu, Y. Zhang, and M. Lei, "Analytic solutions for the generalized complex Ginzburg-Landau equation in fiber lasers", *Nonlinear Dyn.*, 89, 2933, 2017.
- [120] C. Wang, Z. Nie, W. Xie, J. Gao, Q. Zhou, and W. Liu, "Dark soliton control based on dispersion and nonlinearity for third-order nonlinear Schrödinger equation", *Optik*, 184, 370, 2019.
- [121] X. Fan, T. Qu, S. Huang, X. Chen, M. Cao, Q. Zhou, and W. Liu, "Analytic study on the influences of higher-order effects on optical solitons in fiber laser", *Optik*, 186, 326, 2019.
- [122] J. A. Fernandez-de la Garza, and S. López-Aguayo, "Stable Legendre-Lorentzian solitons in localized optical potentials", *J. Opt.*, 23, 055501, 2021.
- [123] M. A. Cruz-Gomez, D. López-Aguayo, and S. Lopez-Aguayo, "Two-dimensional solitons in Laguerre-Gaussian potentials", *J. Opt.*, 22, 015504, 2019.
- [124] U. Felix-Rendon, and S. Lopez-Aguayo, "Solitons in-symmetric optical Mathieu lattices", *J. Opt.*, 20, 015606, 2017.
- [125] U. Al Khawaja, S. M. Al-Marzoug, and H. Bahlouli, "All-optical switches, unidirectional flow, and logic gates with discrete solitons in waveguide arrays", *Opt. Express*, 24, 11062, 2016.
- [126] S. Li and F. Dou, "Matter-wave interactions in two-component Bose-Einstein condensates", *Europhys. Lett.*, 111, 30005, 2015.
- [127] C. L. Grimshaw, S. A. Gardiner, and B. A. Malomed, "Splitting of two-component solitary waves from collisions with narrow potential barriers", *Phys. Rev. A*, 101, 043623, 2020.
- [128] S. Lepri, and G. Casati, "Asymmetric wave propagation in nonlinear systems", *Phys. Rev. Lett.*, 106, 164101, 2011.
- [129] S. Lepri, and B. A. Malomed, "Symmetry breaking and restoring wave transmission in diode-antidiode double chains", *Phys. Rev. E*, 87, 042903, 2013.
- [130] X. D. Bai, B. A. Malomed, and F. G. Deng, "Unidirectional transport of wave packets through tilted discrete breathers in nonlinear lattices with asymmetric defects", *Phys. Rev. E*, 94, 032216, 2016.
- [131] H. Sakaguchi, and B. A. Malomed, "Matter-wave soliton interferometer based on a nonlinear splitter", *New J. Phys.*, 18, 025020, 2016.
- [132] O. Maor, N. Dror, and B. A. Malomed, "Holding spatial solitons in a pumped cavity with the help of nonlinear potentials", *Opt. Lett.*, 38, 5454, 2013.

- [133] M. A. Nielsen, and I. Chuang, “Quantum computation and quantum information”, 2002.
- [134] D. Wecker, B. Bauer, B. K. Clark, M. B. Hastings, and M. Troyer, “Gate-count estimates for performing quantum chemistry on small quantum computers”, *Phys. Rev. A*, 90, 022305, 2014.
- [135] D. P. DiVincenzo, and D. Loss, “Quantum information is physical. Superlattices and Microstructures”, 23, 419, 1998.
- [136] A. I. Maïmistov, “Reversible logic elements as a new field of application of optical solitons”, *Quantum Electronics*, 25, 1009, 1995.
- [137] Q. A. Turchette, C. J. Hood, W. Lange, H. Mabuchi, and H. J. Kimble, “Measurement of conditional phase shifts for quantum logic”, *Phys. Rev. Lett.*, 75, 4710, 1995.
- [138] M. H. Jakubowski and K. Steiglitz, “State transformations of colliding optical solitons and possible application to computation in bulk media”, *Phys. Rev. E*, 58, 6752, 1998.
- [139] A. Adamatzky, “New Media for Collision-Based Computing. In: Adamatzky A. (eds) Collision-Based Computing”, Springer, London, 2002.
- [140] A. Janutka, “Simulation of quantum logic via collisions of vector solitons”, *J. Phys. A: Math. Gen.*, 39, 12505, 2006.
- [141] A. Janutka, “Error of quantum-logic simulation via vector-soliton collisions”, *J. Phys. A: Math. Gen.*, 40, 10813, 2007.
- [142] A. Janutka, “Quantum-like information processing using vector solitons”, *J. Phys. A: Math. Gen.*, 41, 375202, 2008.
- [143] J. N. Kutz, P. Holmes, S. G. Evangelides, and J. P. Gordon, “Hamiltonian dynamics of dispersion-managed breathers”, *J. Opt. Soc. Am. B*, 15, 87, 1998.
- [144] P. K. A. Wai, and K. Nakkeeran, “On the uniqueness of Gaussian ansatz parameters equations: generalized projection operator method”, *Phys. Lett. A*, 332, 239, 2004.
- [145] R. V. J. Raja, K. Porsezian, S. K. Varshney, and S. Sivabalan, “Modeling photonic crystal fiber for efficient soliton pulse propagation at 850 nm”, *Opt. Commun.*, 283, 5000, 2010.
- [146] A. B. Moubissi, K. Nakkeeran, P. T. Dinda, and T. C. Kofane, “Non-Lagrangian collective variable approach for optical solitons in fibres”, *J. Phys. A: Math. Gen.*, 34, 129, 2001.
- [147] A. Kamagate, P. Grelu, P. T. Dinda, J. M. Soto-Crespo, and N. Akhmediev, “Stationary and pulsating dissipative light bullets from a collective variable approach”, *Phys. Rev. E*, 79, 1, 2009.
- [148] A. Bondeson, M. Lisak, and D. Anderson, “Soliton perturbations: a variational principle for the soliton parameters”, *Phys. Scr.*, 20, 479, 1979.
- [149] D. Anderson, “Variational approach to nonlinear pulse propagation in optical fibers”, *Phys. Rev. A*, 27, 3135, 1983.

- [150] C. Pare, and M. Florjanczyk, “Approximate model of soliton dynamics in all-optical couplers”, *Phys. Rev. A*, 41, 6287, 1990.
- [151] K. Saitoh, and M. Koshiba, “Full-vectorial imaginary-distance beam propagation method based on a finite element scheme: application to photonic crystal fibers”, *IEEE J. Quan. Elec.*, 38, 927, 2002.
- [152] S. S. A. Obayya, B. M. A. Rahman and K. T. V. Grattan, “Accurate finite element modal solution of photonic crystal fibres”, *IEEE Proc. Optoelectron.*, 152, 241, 2005.
- [153] M. J. Ablowitz, and J. Ladik, “A nonlinear difference scheme and inverse scattering”, *Stud. Appl. Math.*, 55, 213, 1976.
- [154] M. J. Ablowitz, and J. Ladik, “On the solution of a class of nonlinear partial difference equations”, *Stud. Appl. Math.*, 57, 1, 1977.
- [155] T. R. Taha, and M. J. Ablowitz, “Analytical and numerical aspects of certain nonlinear evolution equations IV. Numerical, modified Korteweg-de Vries equation”, *J. Comput. Phys.*, 77, 540, 1988.
- [156] A. Hasegawa, and F. Tappert, “Transmission of stationary nonlinear optical pulses in dispersive dielectric fibers. I. Anomalous dispersion”, *Appl. Phys. Lett.*, 23, 142, 1973.
- [157] I. Garanovich, S. Longhi, A. Sukhorukov and Y. Kivshar, “Light propagation and localization in modulated photonic lattices and waveguides”, *Physics Reports*, 518, 79, 2012.
- [158] M. Bellec, G. Nikolopoulos and S. Tzortzakis, “Faithful communication Hamiltonian in photonic lattices”, *Opt. Lett.*, 37, 4504, 2012.
- [159] J. Cuevas, G. James, P.G. Kevrekidis, B.A. Malomed and B. Sanchez-Rey, “Approximation of solitons in the discrete NLS equation”, *J. Nonlinear Math. Phys.*, 15, 124, 2008.
- [160] E. Yaghoubi, L. A. Bakhtiar, A. Adami, S. Hamidi and M. Hosseinzadeh, “All optical OR/AND/XOR gates based on nonlinear directional coupler”, *J. Opt.*, 43, 146, 2014.
- [161] E. R. Pashaki and M. Shalchian, “Design and simulation of an ultra-low power high performance CMOS logic: DMTGDI”, *Integration*, 55, 1494, 2016.
- [162] C. Jin and O. Wada, “Photonic switching devices based on semiconductor nanostructures”, *J. Phys. D*, 47, 133001, 2014.
- [163] A. T. Motcheyo, J. T. Tchameu, M. S. Siewe and C. Tchawoua, “Homoclinic nonlinear band gap transmission threshold in discrete optical waveguide arrays”, *Commun Nonlinear Sci Numer Simul*, 50, 29, 2017.
- [164] A. T. Motcheyo, M. Kimura, Y. Doi and C. Tchawoua, “Supratransmission in discrete one-dimensional lattices with the cubic–quintic nonlinearity”, *Nonlinear Dyn.*, 95, 2461, 2019.
- [165] A. T. Motcheyo, C. Tchawoua, M. S. Siewe and J. T. Tchameu, “Multisolitons and stability of two hump solitons of upper cutoff mode in discrete electrical transmission line”, *Phys. Lett. A*, 375, 1104, 2011.

- [166] P. G. Kevrekidis *The Discrete Nonlinear Schrödinger Equation Mathematical Analysis, Numerical Computations and Physical Perspectives*, Springer eBooks, 2009.
- [167] B. Malomed and M. I. Weinstein, "Soliton dynamics in the discrete nonlinear Schrödinger equation", *Phys. Lett. A*, 220, 91, 1996.
- [168] B. A. Malomed, in: *Progress in Optics* 43, 71-194 ed. by E. Wolf: North Holland, 2002.
- [169] Y. V. Kartashov, B. A. Malomed, L. Torner, "Solitons in nonlinear lattices", *Rev. Mod. Phys.*, 83, 247 2011 Erratum, *Rev. Mod. Phys.*, 83, 405, 2011.
- [170] P.G Kevrekidis, K. Ø. Rasmussen, and A. R. Bishop, "The discrete nonlinear Schrödinger equation: a survey of recent results", *Int. J. Mod. Phys. B*, 15, 2833, 2001.
- [171] U. Peschel, R. Morandotti, J. M. Arnold, J. S. Aitchison, H. S. Eisenberg, Y. Silberberg, T. Pertsch, and F. Lederer, "Optical discrete solitons in waveguide arrays. 2. Dynamic properties", *J. Opt. Soc. Am. B.*, 19, 2637, 2002.
- [172] H. S. Eisenberg, R. Morandotti, Y. Silberberg, J. M. Arnold, G. Pennelli, and J. S. Aitchison, "Optical discrete solitons in waveguide arrays. I. Soliton formation", *J. Opt. Soc. Am. B.*, 19, 2938, 2002.
- [173] U. Al Khawaja, S. M. Al-Marzoug, and H. Bahlouli, "Peierls–Nabarro potential profile of discrete nonlinear Schrödinger equation", *Commun. N. Sci. Num. Sim.*, 46, 74, 2017.
- [174] L. Y. Al Sakkaf, Q. M. Al-Mdallal, and U. Al Khawaja, "A Numerical Algorithm for Solving Higher-Order Nonlinear BVPs with an Application on Fluid Flow over a Shrinking Permeable Infinite Long Cylinder," *Complexity*, 2018, 11, 2018.
- [175] K. Xu, "Silicon MOS optoelectronic micro-nano structure based on reverse-biased PN junction," *Phys. Status Solidi A*, 216, 1800868, 2019.
- [176] A. Leuch, L. Papariello, O. Zilberberg, C. L. Degen, R. Chitra, and A. Eichler, "Parametric symmetry breaking in a nonlinear resonator," *Phys. Rev. Lett.*, 117, 214101, 2016.
- [177] U. Al Khawaja and L. Al Sakkaf, *Handbook of Exact Solutions to the Nonlinear Schrödinger Equations*, London, IOP publishing, 2019.
- [178] S. Manakov, "On the theory of two-dimensional stationary self-focusing of electromagnetic waves", *JETP*, 38, 248, 1974.
- [179] A. Bondeson, M. Lisak, and D. Anderson, "Soliton Perturbations: A Variational Principle for the Soliton Parameters", *Phys. Scr.*, 20, 479, 1979.
- [180] D. Anderson, "Variational approach to nonlinear pulse propagation in optical fibers", *Phys. Rev. A*, 27, 3135, 1983.

List of Publications

1. P. S. Vinayagam, Amaria Javed, and U. Al Khawaja, “Stable discrete soliton molecules in two-dimensional waveguide arrays”, *Phys. Rev. A*, 98, 063839, 2018. <https://doi.org/10.1103/PhysRevA.98.063839>
2. Amaria Javed, L. Al Sakkaf, and U. Al Khawaja, “Families of Skyrmions in Two-Dimensional Spin-1/2 Systems”, *IEEE J. Sel. Top. Quantum Electron*, 26, 1, 2020. <https://ieeexplore.ieee.org/document/9093166>
3. Amaria Javed, Alaa Shaheen, and U. Al Khawaja “Amplifying optical signals with discrete solitons in waveguide arrays”, *Phys. Lett. A*, 384, 126654, 2020. <https://doi.org/10.1016/j.physleta.2020.126654>
4. Alaa Shaheen, Amaria Javed, and U. Al Khawaja “Adding Binary Numbers with Discrete Solitons in Waveguide Arrays”, *Phys. Scr.*, 95, 085107, 2020. <https://doi.org/10.1088/1402-4896/aba2b2>
5. Amaria Javed, T. Uthayakumar, M. O. D. Alotaibi, S. M. Al-Marzoug, H. Bahlouli, and U. Al Khawaja “Unidirectional flow of composite bright-bright solitons through asymmetric double potential barriers and wells”, *Commun. Nonlinear Sci. Numer. Simul.*, 103, 105968, 2021. <https://doi.org/10.1016/j.cnsns.2021.105968>
6. Amaria Javed, T. Uthayakumar, and U. Al Khawaja “Simulating an all-optical quantum controlled-NOT gate using soliton scattering by a reflectionless potential well”, *Phys. Lett. A*, 429, 127949, 2022. <https://doi.org/10.1016/j.physleta.2022.127949>

Appendices

Appendix A: Energy Functional

A.1 Variational Energy Functional

The energy functional calculated using the trial function Equation (4.5) in Equation (4.7) is given by

$$E = \frac{1}{8}A^4\pi\gamma\eta_1\eta_2E_1 - A^2\left[-(d_x + d_y)\pi\eta_1\eta_2E_2 + \frac{1}{2}d_x\pi\eta_1\eta_2E_3 + \frac{1}{2}d_y\pi\eta_1\eta_2E_4\right], \quad (\text{A.1})$$

where

$$\begin{aligned} E_1 &= -\left(4e^{2i\phi} + e^{4i\phi} + 1\right)\vartheta_3\left(-\frac{1}{2}(n_{1x} + n_{2x})\pi, e^{-\frac{1}{4}\pi^2\eta_1^2}\right) \\ &\quad \vartheta_3\left(-\frac{1}{2}(n_{1y} + n_{2y})\pi, e^{-\frac{1}{4}\pi^2\eta_2^2}\right) \\ &\quad \times \exp\left(-\frac{n_{1x}^2}{\eta_1^2} + \frac{2n_{1x}n_{2x}}{\eta_1^2} - \frac{2i\eta_2^2\phi + n_{1y}^2 - 2n_{1y}n_{2y} + n_{2y}^2}{\eta_2^2} - \frac{n_{2x}^2}{\eta_1^2}\right) \\ &\quad - 2\left(1 + e^{2i\phi}\right) \\ &\quad \times \left(\vartheta_3\left(-\frac{1}{4}(3n_{1x} + n_{2x})\pi, e^{-\frac{1}{4}\pi^2\eta_1^2}\right)\vartheta_3\left(-\frac{1}{4}(3n_{1y} + n_{2y})\pi, e^{-\frac{1}{4}\pi^2\eta_2^2}\right)\right. \\ &\quad \left.+ \vartheta_3\left(-\frac{1}{4}(n_{1x} + 3n_{2x})\pi, e^{-\frac{1}{4}\pi^2\eta_1^2}\right) \times \vartheta_3\left(-\frac{1}{4}(n_{1y} + 3n_{2y})\pi, e^{-\frac{1}{4}\pi^2\eta_2^2}\right)\right) \\ &\quad \times \exp\left(-\frac{1}{4\eta_1^2\eta_2^2}\eta_2^2(4i\eta_1^2\phi + 3n_{1x}^2 - 6n_{1x}n_{2x} + 3n_{2x}^2) + 3\eta_1^2n_{1y}^2\right. \\ &\quad \left.- 6\eta_1^2n_{1y}n_{2y} + 3\eta_1^2n_{2y}^2\right) - \vartheta_3\left(-n_{1x}\pi, e^{-\frac{1}{4}\pi^2\eta_1^2}\right)\vartheta_3\left(-n_{1y}\pi, e^{-\frac{1}{4}\pi^2\eta_2^2}\right) \\ &\quad - \vartheta_3\left(-n_{2x}\pi, e^{-\frac{1}{4}\pi^2\eta_1^2}\right) \times \vartheta_3\left(-n_{2y}\pi, e^{-\frac{1}{4}\pi^2\eta_2^2}\right), \quad (\text{A.2}) \end{aligned}$$

$$\begin{aligned} E_2 &= \left(1 + e^{2i\phi}\right)\vartheta_3\left(-\frac{1}{2}(n_{1x} + n_{2x})\pi, e^{-\frac{1}{2}\pi^2\eta_1^2}\right)\vartheta_3\left(-\frac{1}{2}(n_{1y} + n_{2y})\pi, e^{-\frac{1}{2}\pi^2\eta_2^2}\right) \\ &\quad \times \exp\left(\frac{n_{1x}n_{2x}}{\eta_1^2} + \frac{1}{2}\left(-\frac{n_{1x}^2}{\eta_1^2} - \frac{(n_{1y} - n_{2y})^2}{\eta_2^2} - \frac{n_{2x}^2}{\eta_1^2} - 2i\phi\right)\right) \\ &\quad + \vartheta_3\left(-n_{1x}\pi, e^{-\frac{1}{2}\pi^2\eta_1^2}\right)\vartheta_3\left(-n_{1y}\pi, e^{-\frac{1}{2}\pi^2\eta_2^2}\right) \\ &\quad + \vartheta_3\left(-n_{2x}\pi, e^{-\frac{1}{2}\pi^2\eta_1^2}\right)\vartheta_3\left(-n_{2y}\pi, e^{-\frac{1}{2}\pi^2\eta_2^2}\right), \quad (\text{A.3}) \end{aligned}$$

$$E_3 = e^{-\frac{1}{2\eta_1^2}}\left(\vartheta_3\left(-\frac{1}{2}(2n_{1x} + 1)\pi, e^{-\frac{1}{2}\pi^2\eta_1^2}\right)\vartheta_3\left(-n_{1y}\pi, e^{-\frac{1}{2}\pi^2\eta_2^2}\right)\right)$$

$$\begin{aligned}
& + \vartheta_3\left(\frac{\pi}{2} - n_{1x}\pi, e^{-\frac{1}{2}\pi^2\eta_1^2}\right) \\
& \times \vartheta_3\left(-n_{1y}\pi, e^{-\frac{1}{2}\pi^2\eta_2^2}\right) + \vartheta_3\left(-\frac{1}{2}(2n_{2x}+1)\pi, e^{-\frac{1}{2}\pi^2\eta_1^2}\right) \vartheta_3\left(-n_{2y}\pi, e^{-\frac{1}{2}\pi^2\eta_2^2}\right) \\
& + \vartheta_3\left(\frac{\pi}{2} - n_{2x}\pi, e^{-\frac{1}{2}\pi^2\eta_1^2}\right) \vartheta_3\left(-n_{2y}\pi, e^{-\frac{1}{2}\pi^2\eta_2^2}\right) \\
& + \left(e^{\frac{n_{1x}(n_{2x}+2)}{\eta_1^2}} + e^{\frac{(n_{1x}+2)n_{2x}}{\eta_1^2} + 2i\phi}\right) \\
& \times \left(\vartheta_3\left(-\frac{1}{2}(n_{1x}+n_{2x}-1)\pi, e^{-\frac{1}{2}\pi^2\eta_1^2}\right) \vartheta_3\left(-\frac{1}{2}(n_{1y}+n_{2y})\pi, e^{-\frac{1}{2}\pi^2\eta_2^2}\right)\right) \\
& + \vartheta_3\left(-\frac{1}{2}(n_{1x}+n_{2x}+1)\pi, e^{-\frac{1}{2}\pi^2\eta_1^2}\right) \vartheta_3\left(-\frac{1}{2}(n_{1y}+n_{2y})\pi, e^{-\frac{1}{2}\pi^2\eta_2^2}\right) \\
& \times \exp\left(\frac{1}{2}\left(-\frac{n_{1x}^2+2n_{1x}+(n_{2x}+1)^2}{\eta_1^2} - \frac{2i\eta_2^2\phi+n_{1y}^2-2n_{1y}n_{2y}+n_{2y}^2}{\eta_2^2}\right)\right), \quad (\text{A.4})
\end{aligned}$$

$$\begin{aligned}
E_4 & = e^{-\frac{1}{2\eta_2^2}} \left(\vartheta_3\left(-n_{1x}\pi, e^{-\frac{1}{2}\pi^2\eta_1^2}\right)\right. \\
& \times \left(\vartheta_3\left(-\frac{1}{2}(2n_{1y}+1)\pi, e^{-\frac{1}{2}\pi^2\eta_2^2}\right) + \vartheta_3\left(\frac{\pi}{2} - n_{1y}\pi, e^{-\frac{1}{2}\pi^2\eta_2^2}\right)\right) \\
& + \vartheta_3\left(-n_{2x}\pi, e^{-\frac{1}{2}\pi^2\eta_1^2}\right) \left(\vartheta_3\left(-\frac{1}{2}(2n_{2y}+1)\pi, e^{-\frac{1}{2}\pi^2\eta_2^2}\right)\right. \\
& + \left.\vartheta_3\left(\frac{\pi}{2} - n_{2y}\pi, e^{-\frac{1}{2}\pi^2\eta_2^2}\right)\right) \\
& + \vartheta_3\left(-\frac{1}{2}(n_{1x}+n_{2x})\pi, e^{-\frac{1}{2}\pi^2\eta_1^2}\right) \\
& \times \exp\left(\frac{1}{2}\left(-\frac{(n_{1x}-n_{2x})^2}{\eta_1^2} - \frac{2i\eta_2^2\phi+n_{1y}^2+2n_{1y}(n_{2y}+1)+n_{2y}^2+2n_{2y}+1}{\eta_2^2}\right)\right) \\
& \times \left(\left(e^{\frac{2n_{1y}(n_{2y}+1)}{\eta_2^2}} + e^{\frac{2(i\eta_2^2\phi+n_{1y}n_{2y}+n_{2y})}{\eta_2^2}}\right) \vartheta_3\left(-\frac{1}{2}(n_{1y}+n_{2y}-1)\pi, e^{-\frac{1}{2}\pi^2\eta_2^2}\right)\right) \\
& \times \exp\left(\frac{1}{2}\left(-\frac{n_{1x}^2+n_{2x}^2}{\eta_1^2} - \frac{2i\eta_2^2\phi+n_{1y}^2+2n_{1y}(n_{2y}+1)+n_{2y}^2+2n_{2y}+1}{\eta_2^2}\right)\right) \\
& + \left(e^{\frac{2(n_{1y}+1)n_{2y}}{\eta_2^2}} + e^{\frac{2(i\eta_2^2\phi+n_{1y}n_{2y}+n_{1y})}{\eta_2^2}}\right) \vartheta_3\left(-\frac{1}{2}(n_{1y}+n_{2y}+1)\pi, e^{-\frac{1}{2}\pi^2\eta_2^2}\right) \\
& \times \exp\left(\frac{1}{2}\left(-\frac{n_{1x}^2+n_{2x}^2}{\eta_1^2} - \frac{2i\eta_2^2\phi+n_{1y}^2+2n_{1y}(n_{2y}+1)+n_{2y}^2+2n_{2y}+1}{\eta_2^2}\right)\right). \quad (\text{A.5})
\end{aligned}$$

A.2 Simplified PN Potential

The above full form of potential, Equation (A.1), can be simplified by expanding in powers of the small quantities $e^{-\pi^2\eta_1^2/4}$ and $e^{-\pi^2\eta_2^2/4}$, as follows

$$\begin{aligned}
V_{PNx} = & -\frac{1}{4}\pi\eta_1\eta_2e^{\frac{2n_{2y}}{\eta_2^2}} \left[4d_x \left(-2e^{-\frac{n_{2x}^2}{2\eta_1^2} - \frac{n_{2y}(n_{2y}+4)}{2\eta_2^2}} + e^{-\frac{(n_{2x}-1)^2}{2\eta_1^2} - \frac{n_{2y}(n_{2y}+4)}{2\eta_2^2}} \right. \right. \\
& + \left. \left. e^{-\frac{(n_{2x}+1)^2}{2\eta_1^2} - \frac{n_{2y}(n_{2y}+4)}{2\eta_2^2}} + 2e^{-\frac{1}{2\eta_1^2} - \frac{2n_{2y}}{\eta_2^2}} - 2e^{-\frac{2n_{2y}}{\eta_2^2}} \right) \right. \\
& + d_y \left(4e^{-\frac{n_{2x}^2}{2\eta_1^2} - \frac{(n_{2y}+1)^2}{2\eta_2^2}} - 8e^{-\frac{n_{2x}^2}{2\eta_1^2} - \frac{n_{2y}(n_{2y}+4)}{2\eta_2^2}} - 8e^{-\frac{2n_{2y}}{\eta_2^2}} + 8e^{-\frac{4n_{2y}+1}{2\eta_2^2}} \right) \\
& + 3 \left(3e^{-\frac{n_{2x}^2}{\eta_1^2} - \frac{n_{2y}(n_{2y}+2)}{\eta_2^2}} + 4e^{-\frac{3n_{2x}^2}{4\eta_1^2} - \frac{n_{2y}(3n_{2y}+8)}{4\eta_2^2}} + e^{-\frac{2n_{2y}}{\eta_2^2}} + e^{-\frac{1}{4}\pi^2\eta_2^2 - \frac{2n_{2y}}{\eta_2^2}} \right) \\
& \left. + 18\cos(\pi n_{2y})e^{-\frac{\pi^2\eta_2^2}{4} - \frac{n_{2x}^2}{\eta_1^2} - \frac{n_{2y}(n_{2y}+2)}{\eta_2^2}} + 3e^{-\frac{1}{4}\pi^2\eta_2^2 - \frac{2n_{2y}}{\eta_2^2}} \cos(2\pi n_{2y}) \right] \quad (A.6)
\end{aligned}$$

and

$$\begin{aligned}
V_{PNy} = & -\frac{1}{4}\pi\eta_1\eta_2e^{\frac{2n_{2y}}{\eta_2^2}} \left[4d_x \left(-2e^{-\frac{n_{2x}^2}{2\eta_1^2} - \frac{n_{2y}(n_{2y}+4)}{2\eta_2^2}} + 2e^{-\frac{1}{2\eta_1^2} - \frac{2n_{2y}}{\eta_2^2}} - 2e^{-\frac{2n_{2y}}{\eta_2^2}} \right. \right. \\
& + \left. \left. 2e^{-\frac{n_{2y}(n_{2y}+4)}{2\eta_2^2}} \right) + d_y \left(8e^{-\frac{4n_{2y}+1}{2\eta_2^2}} - 8e^{-\frac{2n_{2y}}{\eta_2^2}} \right) \right. \\
& + 3 \left(e^{-\frac{2n_{2y}}{\eta_2^2}} + 3e^{-\frac{n_{2y}(n_{2y}+2)}{\eta_2^2}} + 4e^{-\frac{n_{2y}(3n_{2y}+8)}{4\eta_2^2}} + e^{-\frac{1}{4}\pi^2\eta_2^2 - \frac{2n_{2y}}{\eta_2^2}} \right) \\
& + 12e^{\frac{1}{4}\left(-\pi^2\eta_2^2 - \frac{n_{2y}(3n_{2y}+8)}{\eta_2^2}\right)} \cos\left(\frac{\pi n_{2y}}{2}\right) + 18e^{-\frac{1}{4}\pi^2\eta_2^2 - \frac{n_{2y}(n_{2y}+2)}{\eta_2^2}} \cos(\pi n_{2y}) \\
& \left. + 12e^{\frac{1}{4}\left(-\pi^2\eta_2^2 - \frac{n_{2y}(3n_{2y}+8)}{\eta_2^2}\right)} \cos\left(\frac{3\pi n_{2y}}{2}\right) + 3e^{-\frac{1}{4}\pi^2\eta_2^2 - \frac{2n_{2y}}{\eta_2^2}} \cos(2\pi n_{2y}) \right], \quad (A.7)
\end{aligned}$$

where V_{PNx} and V_{PNy} are the V_{PN} in the horizontal and vertical directions, respectively. To further simplify this expression, we consider a highly anisotropic waveguide, such as $d_x=3$, $d_y=0.15$. The equilibrium widths, $\eta_{10,20}$, are then calculated by minimizing the potential with respect to the widths $\eta_{1,2}$ which gives $\eta_{10}=3.86$, $\eta_{20}=0.76$. This further simplifies the potential as follows.

$$V_{PNx} = c_1 - c_2 \left(e^{2c_3n_{2x}} + 1 \right) e^{-n_{2x}(c_3+c_4n_{2x})} - c_5e^{c_3n_{2x}^2} + c_8e^{-c_4n_{2x}^2} - c_6e^{c_7n_{2x}^2}, \quad (A.8)$$

where, $c_1 = -6.81008$, $c_2 = 11.249948$, $c_3 = -0.06711$, $c_4 = 0.03355$,
 $c_5 = 1.90572$, $c_6 = 7.54659$, $c_7 = -0.05033$, $c_8 = 23.04872$, and

$$V_{PNy} = -c_1 + e^{n_{2y}(c_2 - c_3 n_{2y})} (c_4 - c_5 \cos(\pi n_{2y})) + e^{n_{2y}(c_2 - c_6 n_{2y})} \left(c_7 - c_8 \cos\left(\frac{\pi n_{2y}}{2}\right) - c_8 \cos\left(\frac{3\pi n_{2y}}{2}\right) \right) - c_9 \cos(2\pi n_{2y}) \quad (\text{A.9})$$

where, $c_1 = -5.14794$, $c_2 = 8.88178 \times 10^{-16}$, $c_3 = 1.7313$, $c_4 = -20.73639$, $c_5 = 9.97285$,
 $c_6 = 1.29847$, $c_7 = -27.64852$, $c_8 = 6.64856$, $c_9 = 1.66214$

In Figures A.1 and A.2 we plot the approximate and full potential to see that they still agree very well.

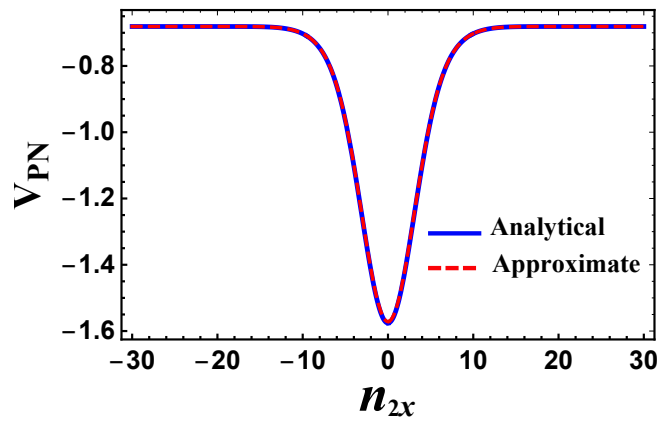


Figure A.1: The PN potential, given by Equation (A.1), is shown by the blue solid line and the simplified form for the horizontal direction, given by Equation (A.8), is plotted by the red dashed line for the choice of parameters $P=2$, $\gamma=4$, $d_x=3$, $d_y=0.15$, $\eta_{10}=3.86$ and $\eta_{20}=0.76$ and $n_{2y}=1$.

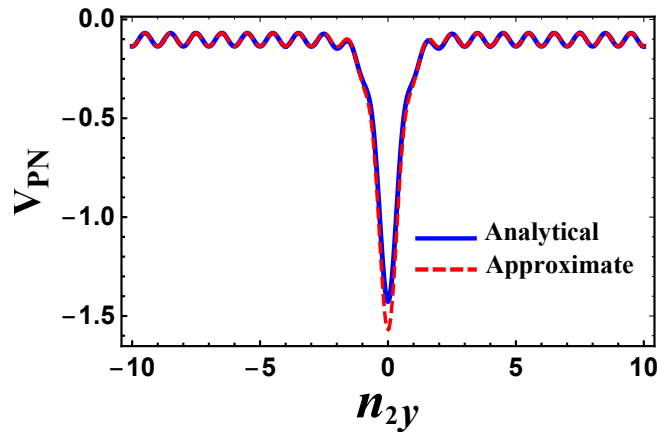


Figure A.2: The full and approximate PN potential given by Equations (A.1) and (A.9) are plotted using blue solid and red dashed lines, respectively, for the same parameters used in Figure A.1 but with $n_{2x}=1$.

A.3 V_{PN} for Soliton Molecule

The variational energy functional Equation (A.1) can be simplified for the special case of a soliton molecule where one soliton is restricted to move along the waveguide $n_{1y} = -1$ and the other soliton moves along the waveguide $n_{2y} = 1$, and thus the separation between the two solitons is essentially determined by $\Delta n = n_{2x} - n_{1x}$. The energy functional is therefore given in terms of the solitons separation as

$$\begin{aligned}
V_{PN} = & \frac{1}{D} P \left(2e^{\frac{1}{2} \left(-\frac{2\Delta n+1}{\eta^2} - \frac{5}{\eta^2} \right)} \left(2\vartheta_3 \left(0, e^{-\frac{1}{2}\pi^2\eta_1^2} \right) \vartheta_3 \left(0, e^{-\frac{1}{2}\pi^2\eta_2^2} \right) \right. \right. \\
& + e^{\frac{\Delta n^2}{2\eta^2} + \frac{2}{\eta^2}} \left(\vartheta_3 \left(-\pi, e^{-\frac{1}{2}\pi^2\eta_2^2} \right) \right. \\
& \times \left. \left. \vartheta_3 \left(-\frac{\pi\Delta n}{2}, e^{-\frac{1}{2}\pi^2\eta_1^2} \right) + \vartheta_3 \left(\pi, e^{-\frac{1}{2}\pi^2\eta_2^2} \right) \vartheta_3 \left(\frac{\pi\Delta n}{2}, e^{-\frac{1}{2}\pi^2\eta_1^2} \right) \right) \right) \\
& \times \left(-e^{\frac{2\Delta n+1}{2\eta^2}} \vartheta_3 \left(0, e^{-\frac{1}{2}\pi^2\eta_1^2} \right) \right. \\
& \times \left(d_y \left(1 + e^{\frac{4}{\eta^2}} \right) \left(\vartheta_3 \left(-\frac{\pi}{2}, e^{-\frac{1}{2}\pi^2\eta_2^2} \right) + \vartheta_3 \left(\frac{\pi}{2}, e^{-\frac{1}{2}\pi^2\eta_2^2} \right) \right) \right. \\
& - 4(d_x + d_y) e^{\frac{5}{2\eta^2}} \vartheta_3 \left(0, e^{-\frac{1}{2}\pi^2\eta_2^2} \right) \left. \right) \\
& - e^{\frac{5}{2\eta^2}} \left(d_x \left(1 + e^{\frac{2\Delta n}{\eta^2}} \right) \vartheta_3 \left(0, e^{-\frac{1}{2}\pi^2\eta_2^2} \right) \left(\vartheta_3 \left(-\frac{\pi}{2}, e^{-\frac{1}{2}\pi^2\eta_1^2} \right) \right. \right. \\
& + \left. \left. \vartheta_3 \left(\frac{\pi}{2}, e^{-\frac{1}{2}\pi^2\eta_1^2} \right) \right) \right) \\
& + e^{\frac{1}{2} \left(\frac{\Delta n(\Delta n+2)}{\eta^2} + \frac{3}{\eta^2} \right)} \left(d_y e^{\frac{1}{2\eta^2}} \vartheta_3 \left(-\frac{3\pi}{2}, e^{-\frac{1}{2}\pi^2\eta_2^2} \right) \vartheta_3 \left(-\frac{\pi\Delta n}{2}, e^{-\frac{1}{2}\pi^2\eta_1^2} \right) \right. \\
& - 2d_x e^{\frac{1}{2} \left(\frac{1}{\eta^2} + \frac{1}{\eta^2} \right)} \\
& \times \left. \vartheta_3 \left(-\pi, e^{-\frac{1}{2}\pi^2\eta_2^2} \right) \vartheta_3 \left(-\frac{\pi\Delta n}{2}, e^{-\frac{1}{2}\pi^2\eta_1^2} \right) - 2d_y e^{\frac{1}{2} \left(\frac{1}{\eta^2} + \frac{1}{\eta^2} \right)} \right. \\
& \times \left. \vartheta_3 \left(-\pi, e^{-\frac{1}{2}\pi^2\eta_2^2} \right) \vartheta_3 \left(-\frac{\pi\Delta n}{2}, e^{-\frac{1}{2}\pi^2\eta_1^2} \right) \right) \\
& + d_y e^{\frac{1}{2\eta^2}} \vartheta_3 \left(-\frac{\pi}{2}, e^{-\frac{1}{2}\pi^2\eta_2^2} \right) \vartheta_3 \left(-\frac{\pi\Delta n}{2}, e^{-\frac{1}{2}\pi^2\eta_1^2} \right) + d_y e^{\frac{1}{2\eta^2}} \vartheta_3 \left(\frac{\pi}{2}, e^{-\frac{1}{2}\pi^2\eta_2^2} \right) \\
& \times \vartheta_3 \left(\frac{\pi\Delta n}{2}, e^{-\frac{1}{2}\pi^2\eta_1^2} \right) \\
& + d_y e^{\frac{1}{2\eta^2}} \vartheta_3 \left(\frac{3\pi}{2}, e^{-\frac{1}{2}\pi^2\eta_2^2} \right) \vartheta_3 \left(\frac{\pi\Delta n}{2}, e^{-\frac{1}{2}\pi^2\eta_1^2} \right) + d_x e^{\frac{1}{2\eta^2}} \vartheta_3 \left(-\pi, e^{-\frac{1}{2}\pi^2\eta_2^2} \right) \\
& \times \vartheta_3 \left(-\frac{1}{2}\pi(\Delta n + 1), e^{-\frac{1}{2}\pi^2\eta_1^2} \right) \\
& + e^{\frac{1}{2\eta^2}} \vartheta_3 \left(\pi, e^{-\frac{1}{2}\pi^2\eta_2^2} \right) \left(d_x \vartheta_3 \left(\frac{1}{2}\pi(\Delta n - 1), e^{-\frac{1}{2}\pi^2\eta_1^2} \right) \right.
\end{aligned}$$

$$\begin{aligned}
& - 2(d_x + d_y)e^{\frac{1}{2\eta_1^2}} \vartheta_3\left(\frac{\pi\Delta n}{2}, e^{-\frac{1}{2}\pi^2\eta_1^2}\right) + d_x \vartheta_3\left(\frac{1}{2}\pi(\Delta n + 1), e^{-\frac{1}{2}\pi^2\eta_1^2}\right) \\
& + d_x e^{\frac{1}{2\eta_2^2}} \vartheta_3\left(-\pi, e^{-\frac{1}{2}\pi^2\eta_2^2}\right) \vartheta_3\left(\frac{1}{2}(\pi - \pi\Delta n), e^{-\frac{1}{2}\pi^2\eta_1^2}\right) \\
& - \frac{1}{\pi\eta_1\eta_2} P\gamma\left(6\vartheta_3\left(0, e^{-\frac{1}{4}\pi^2\eta_1^2}\right)\right. \\
& \times \left.\vartheta_3\left(0, e^{-\frac{1}{4}\pi^2\eta_2^2}\right)\right. \\
& + \left.e^{\frac{\Delta n^2}{4\eta_1^2} + \frac{1}{\eta_2^2}} \left(e^{\frac{3\Delta n^2}{4\eta_1^2} + \frac{3}{\eta_2^2}} \vartheta_3\left(-\pi, e^{-\frac{1}{4}\pi^2\eta_2^2}\right) \vartheta_3\left(-\frac{\pi\Delta n}{2}, e^{-\frac{1}{4}\pi^2\eta_1^2}\right)\right.\right. \\
& + \left.4\vartheta_3\left(-\frac{\pi}{2}, e^{-\frac{1}{4}\pi^2\eta_2^2}\right) \vartheta_3\left(-\frac{\pi\Delta n}{4}, e^{-\frac{1}{4}\pi^2\eta_1^2}\right)\right. \\
& + \left.4\vartheta_3\left(\frac{\pi}{2}, e^{-\frac{1}{4}\pi^2\eta_2^2}\right) \vartheta_3\left(\frac{\pi\Delta n}{4}, e^{-\frac{1}{4}\pi^2\eta_1^2}\right)\right. \\
& \left.\left.+ e^{\frac{3\Delta n^2}{4\eta_1^2} + \frac{3}{\eta_2^2}} \vartheta_3\left(\pi, e^{-\frac{1}{4}\pi^2\eta_2^2}\right) \vartheta_3\left(\frac{\pi\Delta n}{2}, e^{-\frac{1}{4}\pi^2\eta_1^2}\right)\right)\right)
\end{aligned}$$

where,

$$\begin{aligned}
D & = 2\left(2\vartheta_3\left(0, e^{-\frac{1}{2}\pi^2\eta_1^2}\right) \vartheta_3\left(0, e^{-\frac{1}{2}\pi^2\eta_2^2}\right) + e^{\frac{\Delta n^2}{2\eta_1^2} + \frac{2}{\eta_2^2}} \left(\vartheta_3\left(-\pi, e^{-\frac{1}{2}\pi^2\eta_2^2}\right)\right.\right. \\
& \times \left.\left.\vartheta_3\left(-\frac{\pi\Delta n}{2}, e^{-\frac{1}{2}\pi^2\eta_1^2}\right) + \vartheta_3\left(\pi, e^{-\frac{1}{2}\pi^2\eta_2^2}\right) \vartheta_3\left(\frac{\pi\Delta n}{2}, e^{-\frac{1}{2}\pi^2\eta_1^2}\right)\right)\right)^2.
\end{aligned}$$

For highly anisotropic waveguides the soliton width in the x -direction is at least more than several waveguides and the soliton width in the y -direction is less than or of order a one waveguide. Consequently, the quantity $e^{-\pi^2\eta_1^2/4}$ is very small and hence

$$\vartheta_3(n\pi, e^{-\pi^2\eta_1^2/4}) \approx 1, \quad (\text{A.10})$$

with arbitrary real n . On the other hand the $\vartheta_3(n\pi, e^{-\pi^2\eta_2^2/4})$ function can be expanded in powers of $e^{-\pi^2\eta_2^2/4}$, as

$$\vartheta_3(n\pi, e^{-\pi^2\eta_2^2/4}) \approx \begin{cases} 1 + 2e^{-\pi^2\eta_2^2/4}, & \text{integer } n \\ 1 - 2e^{-\pi^2\eta_2^2/4}, & \text{half-integer } n \end{cases} \quad (\text{A.11})$$

Expanding in powers of Δn and employing the above-mentioned approximations (A.10) and (A.11), the potential can be put in a parabolic form (4.15), where the spring constant k is given by

$$\begin{aligned}
k & = \frac{1}{2a^3 b^2 \eta_1^4} e^{-c/2} P \left[2ab e^{-\frac{1}{2\eta_1^2}} \left((e^{2c} - 1)^2 \left(e^{\frac{\pi^2}{2c}} - 2 \right) d_y e^{\frac{1}{2\eta_1^2}} \eta_1^2 - 2ab e^{c/2} d_x \right) \right. \\
& - \frac{1}{\pi\eta_2} e^{\frac{3c}{2} + \frac{3\pi^2}{4c}} \\
& \times \left. \left(-6e^c + 6e^{2c} + 2e^{3c} + e^{\frac{\pi^2}{4c}} - 3e^{c+\frac{\pi^2}{4c}} - 3e^{2c+\frac{\pi^2}{4c}} + e^{3c+\frac{\pi^2}{4c}} - 2 \right) P\gamma\eta_1 \right],
\end{aligned}$$

(A.12)

and the constant energy background is given by

$$\begin{aligned}
 V_0 = & \frac{1}{8a^2b^2} P \left[8abe^{-\frac{5c}{2} - \frac{1}{2\eta_1^2}} \left(2abe^{5c/2} d_x \left(e^{\frac{1}{2\eta_1^2}} - 1 \right) + \left(4e^{5c/2} + 6e^{4c} + 4e^{9c/2} - e^{\frac{\pi^2}{2c}} \right. \right. \right. \\
 & + \left. \left. 2e^{\frac{5c}{2} + \frac{\pi^2}{2c}} - 3e^{4c + \frac{\pi^2}{2c}} + 2e^{\frac{9c}{2} + \frac{\pi^2}{2c}} + 2 \right) d_y e^{\frac{1}{2\eta_1^2}} \right) - \frac{1}{\pi\eta_1\eta_2} 2e^{\frac{3\pi^2}{4c}} \left(-8e^c + 2e^{4c} + 3e^{\frac{\pi^2}{4c}} \right. \\
 & \left. \left. + 4e^{c + \frac{\pi^2}{4c}} + e^{4c + \frac{\pi^2}{4c}} + 6 \right) \gamma P \right],
 \end{aligned}
 \tag{A.13}$$

where $a = e^{\frac{2}{\eta_1^2}} + 1$, $b = e^{\frac{\pi^2\eta_2^2}{2}} + 2$ and $c = \frac{1}{\eta_2^2}$.

Appendix B: Solutions of the 2D Manakov System

Using the similarity transformation described in Section 5.4.1, we found many new solutions for the 2D Manakov system (5.19), here we mentioned only two of them for their significance. The full list of solution is compiled by [177].

Solution-1

$$\psi_1(\rho, t) = \frac{1}{\sqrt{\rho}} \tanh\left(\sqrt{\frac{3}{8}} \rho\right) e^{-i(1-3t)} \quad (\text{B.1})$$

$$\psi_2(\rho, t) = \sqrt{\frac{5}{2}} \frac{1}{\sqrt{\rho}} \operatorname{sech}\left(\sqrt{\frac{3}{8}} \rho\right) e^{\frac{15}{8}i(-1+t)} \quad (\text{B.2})$$

The choice of parameters are $a_{11} = -1$, $a_{12} = 2$, $a_{21} = 1$, and $a_{13} = a_{22} = a_{23} = \frac{1}{2}$. See Figure B.1.

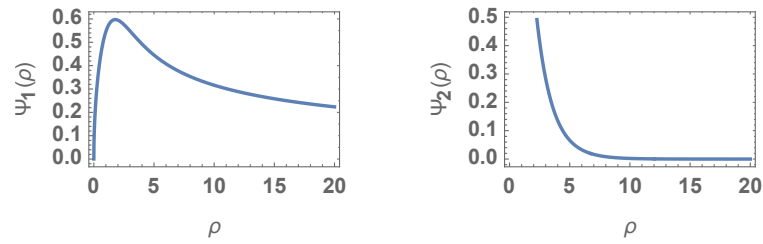


Figure B.1: Graphical representation of $\psi_1(\rho)$ and $\psi_2(\rho)$ for solution-1.

Solution-2

$$\psi_1(\rho, t) = \frac{1}{3\sqrt{\rho}} \left(-2 + 3 \operatorname{sech}^2[\rho]\right) e^{2i(1-t)} \quad (\text{B.3})$$

$$\psi_2(\rho, t) = \frac{1}{\sqrt{\rho}} \operatorname{sech}^2[\rho] e^{-2i(1-t)} \quad (\text{B.4})$$

The parameters are $a_{11} = a_{21} = 1$, $a_{12} = a_{22} = -\frac{9}{2}$, and $a_{13} = a_{23} = \frac{9}{2}$. See Figure B.2.

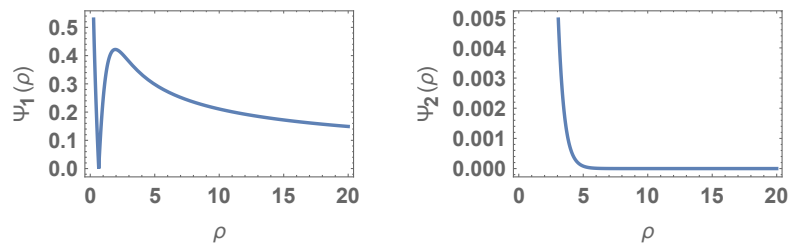


Figure B.2: Graphical representation of $\psi_1(\rho)$ and $\psi_2(\rho)$ for solution-2.

Appendix C: Similarity Transformation

The results of all the unknown quantities in (5.24) and all the coefficients in (5.23) are listed below:

For $\Psi_1(\vec{r}, t)$:

$$\begin{aligned}
 T(\rho, t) &= g_1(t), \\
 p_1(\rho, t) &= \frac{1}{e^{iB_1(\rho, t)} A(\rho, t) g_1'(t)}, \\
 b_{11}(\rho, t) &= \frac{a_{11} g_1'(t)}{P_\rho^2(\rho, t)}, \\
 b_{12}(\rho, t) &= \frac{a_{12} g_1'(t)}{A^2(\rho, t)}, \\
 b_{13}(\rho, t) &= \frac{a_{13} g_1'(t)}{A^2(\rho, t)}, \\
 A(\rho, t) &= \frac{g_2(t)}{\sqrt{\rho P_\rho(\rho, t)}}, \\
 B_1(\rho, t) &= -\int \frac{P_t(\rho, t) P_\rho(\rho, t)}{2 a_{11} g_1'(t)} d\rho + g_3(t), \\
 b_{14i}(\rho, t) &= -\frac{g_2'(t)}{g_2(t)} + \frac{P_{\rho t}(\rho, t)}{P_\rho(\rho, t)}, \\
 b_{14r}(\rho, t) &= \frac{1}{4 a_{11} g_1'^2(t)} \left[2 \int P_t(\rho, t) P_\rho(r, t) d\rho g_1''(t) \right. \\
 &\quad \left. - g_1'(t) \left(2 \int (I) d\rho + P_t^2(\rho, t) - \frac{N}{\rho^2 P_\rho^4(\rho, t)} \right) \right] + g_3'(t). \tag{C.1}
 \end{aligned}$$

where $I = P_{tt}(\rho, t) P_\rho(\rho, t) + P_t(\rho, t) P_{\rho t}(\rho, t)$, and $N = a_1^2 g_1'^2(t) [P_\rho^2(\rho, t) + 3\rho^2 P_{\rho\rho}^2(\rho, t) - 2\rho^2 P_\rho(\rho, t) P_{\rho\rho\rho}(\rho, t)]$.

For $\Psi_2(\vec{r}, t)$:

$$\begin{aligned}
 T(\rho, t) &= g_1(t), \\
 p_2(\rho, t) &= \frac{1}{e^{iB_2(\rho, t)} A(\rho, t) g_1'(t)}, \\
 b_{21}(\rho, t) &= \frac{a_{21} g_1'(t)}{P_\rho^2(\rho, t)}, \\
 b_{22}(\rho, t) &= \frac{a_{22} g_1'(t)}{A^2(\rho, t)}, \\
 b_{23}(\rho, t) &= \frac{a_{23} g_1'(t)}{A^2(\rho, t)},
 \end{aligned}$$

$$\begin{aligned}
A(\rho, t) &= \frac{g_2(t)}{\sqrt{\rho P_\rho(\rho, t)}}, \\
B_2(\rho, t) &= -\int \frac{P_t(\rho, t) P_\rho(\rho, t)}{2 a_{21} g_1'(t)} d\rho + g_3(t), \\
b_{24i}(\rho, t) &= -\frac{g_2'(t)}{g_2(t)} + \frac{P_{\rho t}(\rho, t)}{P_\rho(\rho, t)}, \\
b_{24r}(\rho, t) &= \frac{1}{4 a_{21} g_1''(t)} \left[2 \int P_t(\rho, t) P_\rho(r, t) d\rho g_1''(t) \right. \\
&\quad \left. - g_1'(t) \left(2 \int (I) d\rho + P_t^2(\rho, t) - \frac{N}{\rho^2 P_\rho^4(\rho, t)} \right) \right] + g_3'(t). \tag{C.2}
\end{aligned}$$

where $I = P_{tt}(\rho, t) P_\rho(\rho, t) + P_t(\rho, t) P_{\rho t}(\rho, t)$, and $N = a_1^2 g_1'^2(t) [P_\rho^2(\rho, t) + 3\rho^2 P_{\rho\rho}^2(\rho, t) - 2\rho^2 P_\rho(\rho, t) P_{\rho\rho\rho}(\rho, t)]$. Here a_{11} , a_{12} , a_{13} , a_{21} , a_{22} and a_{23} are all arbitrary real constants.

Appendix D: Asymmetric Gaussian Potential Barriers

The transport coefficients for the Gaussian double potential barriers are shown in Figure D.1. For the right moving BB solitons scattered through Gaussian barriers, the critical velocity $v_c = 0.369$ whereas that for the left moving BB solitons $v_c = 0.377$. Furthermore, the velocity window for our new scheme with Gaussian barriers ($0.365 \leq v \leq 0.372$) is very much comparable to the previous study of Gaussian potential wells [45] ($0.304 \leq v \leq 0.310$).

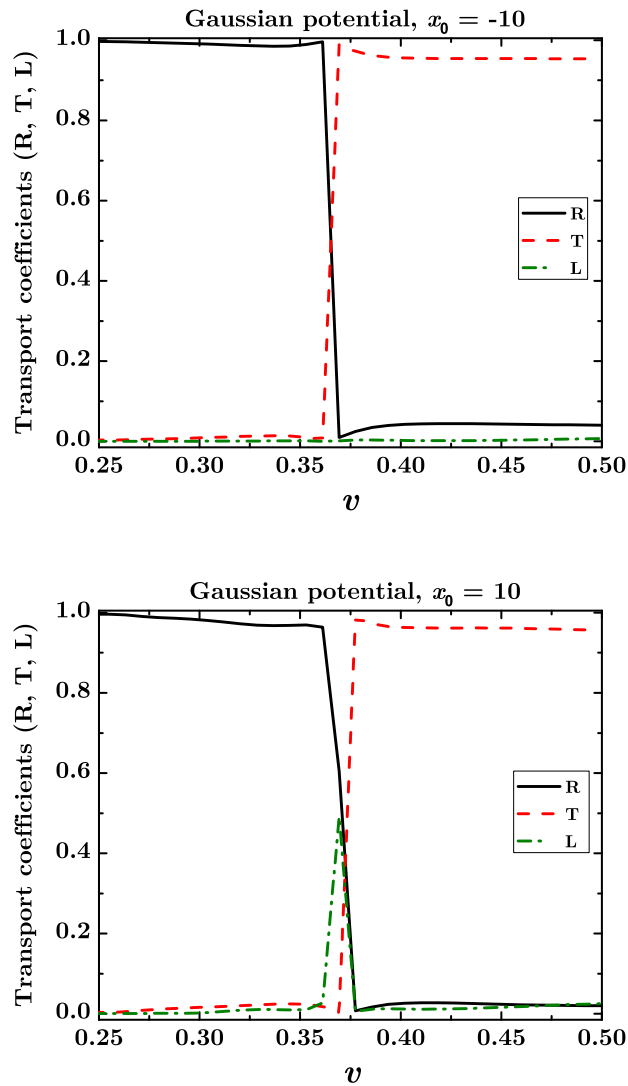


Figure D.1: Transport coefficients in terms of velocity for the propagation of the ψ_1 component through asymmetric Gaussian barriers for $g_1 = g_2 = 1$, $g_{12} = 0$ from $x_0 = -10$ (upper panel) and $x_0 = 10$ (lower panel).

D.1 Unidirectional Flow for Uncoupled Components with $g_{12} = 0$

The unidirectional flow is also achieved for uncoupled components of BB solitons through Gaussian double potential barriers. Figure D.2 shows the propagation of the BB soliton components ψ_1 and ψ_2 with a critical velocity $v_c = 0.368$, incident from $x_0 = \mp 10$ through asymmetric Gaussian double barrier potentials.

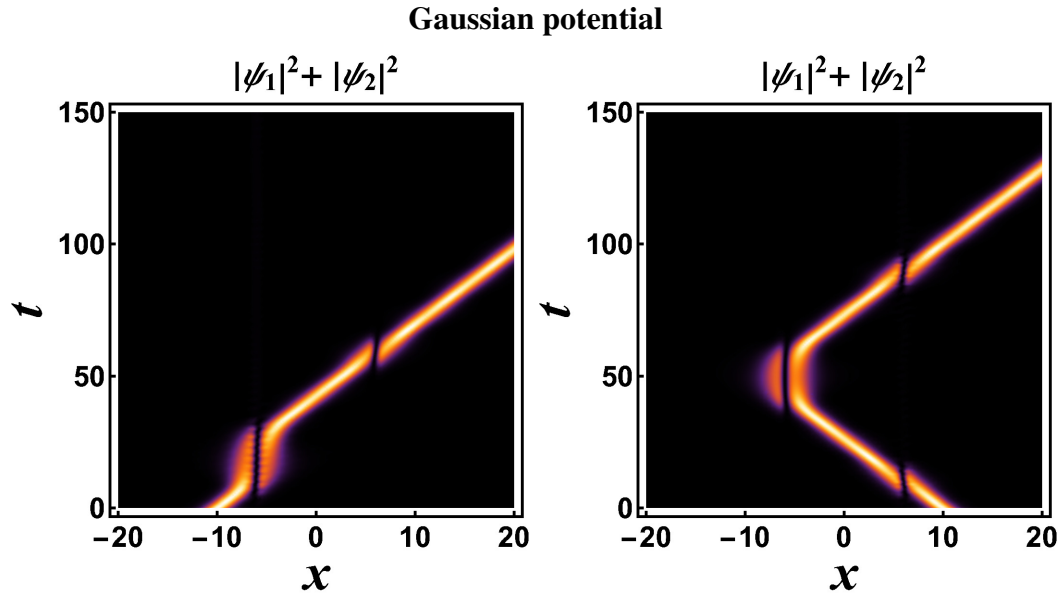
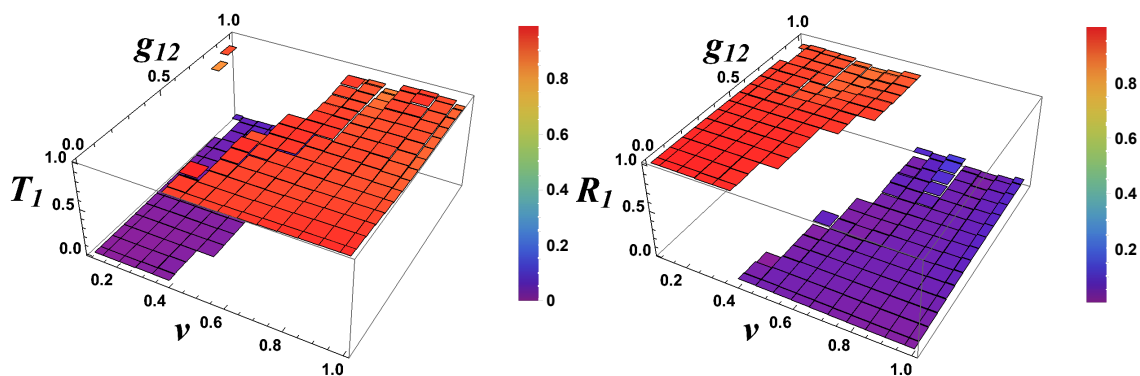


Figure D.2: Propagation of composite BB soliton through asymmetric Gaussian potential barriers for $g_{12} = 0$ with $g_1 = g_2 = 1$ at $v = 0.368$. Both components are identical. Left and right subfigures are results of initial propagation from $x_0 = -10$ and $x_0 = 10$, respectively.

D.2 Polarity Reversal in Unidirectional Flow with $g_{12} > 0$

The important characteristic of *polarity reversal* is also observed through the propagation of BB solitons via the asymmetrical Gaussian double potential barriers. Figure D.3 describes the transmission and reflection coefficients of the component ψ_1 passing through the RM potential barriers from $x_0 = \pm 10$, versus the velocity and positive mean field coupling. From the spatiotemporal plots, it is observed that for lower coupling $g_{12} \leq 0.312$, both components exhibit the diode behavior with "right polarity" as shown in Figure D.4 obtained for $g_{12} = 0.3$ which is similar to the one achieved in the case $g_{12} = 0$.

Gaussian potential, $x_0 = -10$



Gaussian potential, $x_0 = 10$

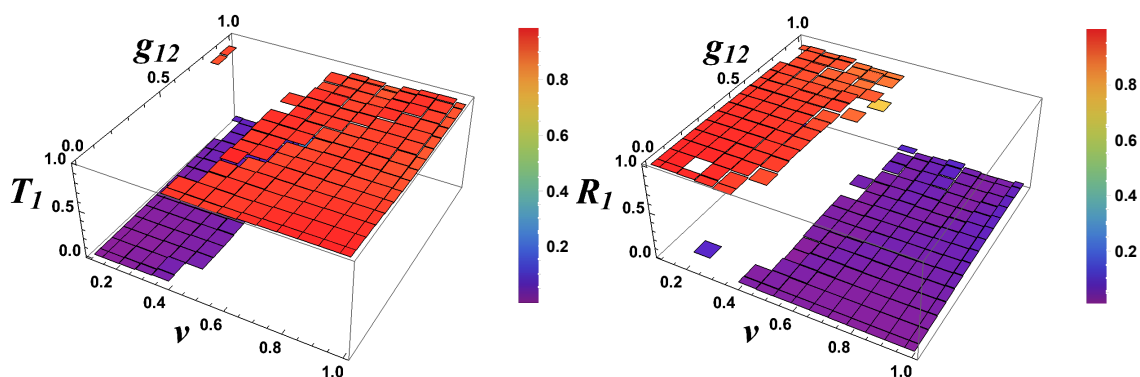


Figure D.3: Transmission and reflection coefficients of the component ψ_1 propagating from $x_0 = -10$ (upper two) and $x_0 = 10$ (lower two) through Gaussian barriers versus ν and g_{12} . Other parameters are $g_1 = g_2 = 1$.

Gaussian potential

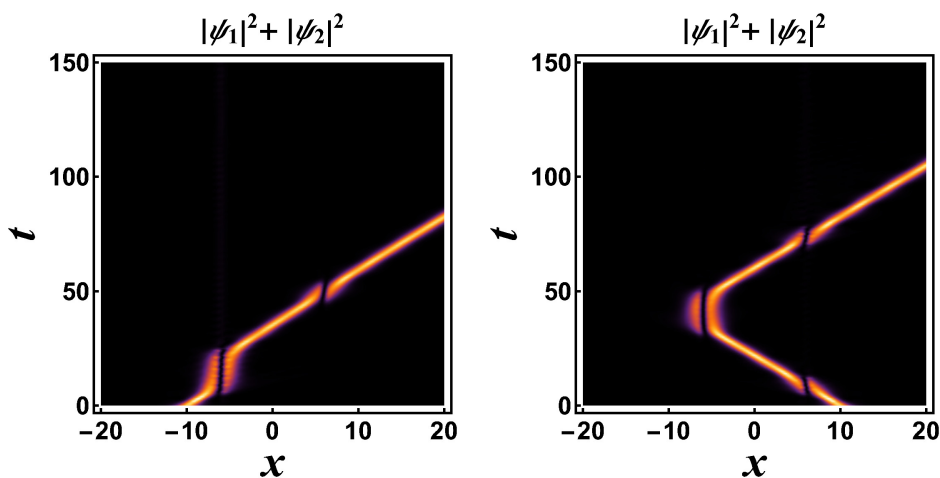


Figure D.4: Propagation of composite BB soliton through asymmetric Gaussian potential barriers for $g_{12} = 0.3$ with $g_1 = g_2 = 1$ at $\nu = 0.452$. Both components are identical. Left and right subfigures are results of initial propagation from $x_0 = -10$ and $x_0 = 10$, respectively.

Table D.1: The velocity window for unidirectional flow of composite BB solitons with different coupling strengths. For the Gaussian potential barriers with the range of coupling strength $0.313 \leq g_{12} \leq 0.316$ with $g_1 = g_2 = 1$, we find full reflection for $v \leq 0.453$ and full transmission for $v \geq 0.454$, hence no unidirectional flow is observed at this specific range of g_{12} . Away from this point, we find polarity reversal in unidirectional flow.

Unidirectional flow with composite BB solitons		
Interaction strength	Velocity window	
g_{12}	$v_{min} \leq v \leq v_{max}$	
0	$0.365 \leq v \leq 0.372$	<i>Right polarity</i>
0.1	$0.402 \leq v \leq 0.413$	
0.2	$0.43 \leq v \leq 0.45$	
0.3	$0.451 \leq v \leq 0.454$	
0.308	$0.452 \leq v \leq 0.453$	
0.309-0.312	0.453	
0.313-0.316	no unidirectional flow	
0.317-0.320	0.454	<i>Left polarity</i>
0.321	$0.454 \leq v \leq 0.455$	
0.325	$0.454 \leq v \leq 0.456$	
0.35	$0.456 \leq v \leq 0.462$	
0.4	$0.462 \leq v \leq 0.476$	
0.5	$0.471 \leq v \leq 0.5$	
0.6	$0.487 \leq v \leq 0.539$	
0.7	$0.473 \leq v \leq 0.564$	
0.8	$0.502 \leq v \leq 0.583$	
0.9	$0.532 \leq v \leq 0.598$	
1	$0.558 \leq v \leq 0.608$	

For Gaussian potential barriers, we observe no unidirectional flow in the range of interaction coupling $0.313 \leq g_{12} \leq 0.316$ where the composite BB solitons propagating from both directions show full transmission for $v \geq 0.457$, while it exhibits maximum reflection for both right and left moving composite BB solitons for $v < 0.457$ as shown in Figure D.5. The velocity window for the diode functionality at different g_{12} values are tabulated in Table D.1. Further, for $g_{12} \geq 0.317$, exactly the reverse phenomena is achieved through Gaussian potential barriers and the polarity of unidirectional flow is reversed from right to left polarity which can be seen by comparing Figure D.6 with Figure D.4. This phenomena is purely due to the increase in g_{12} above certain critical value 0.316, which is demonstrated by Figure D.7.

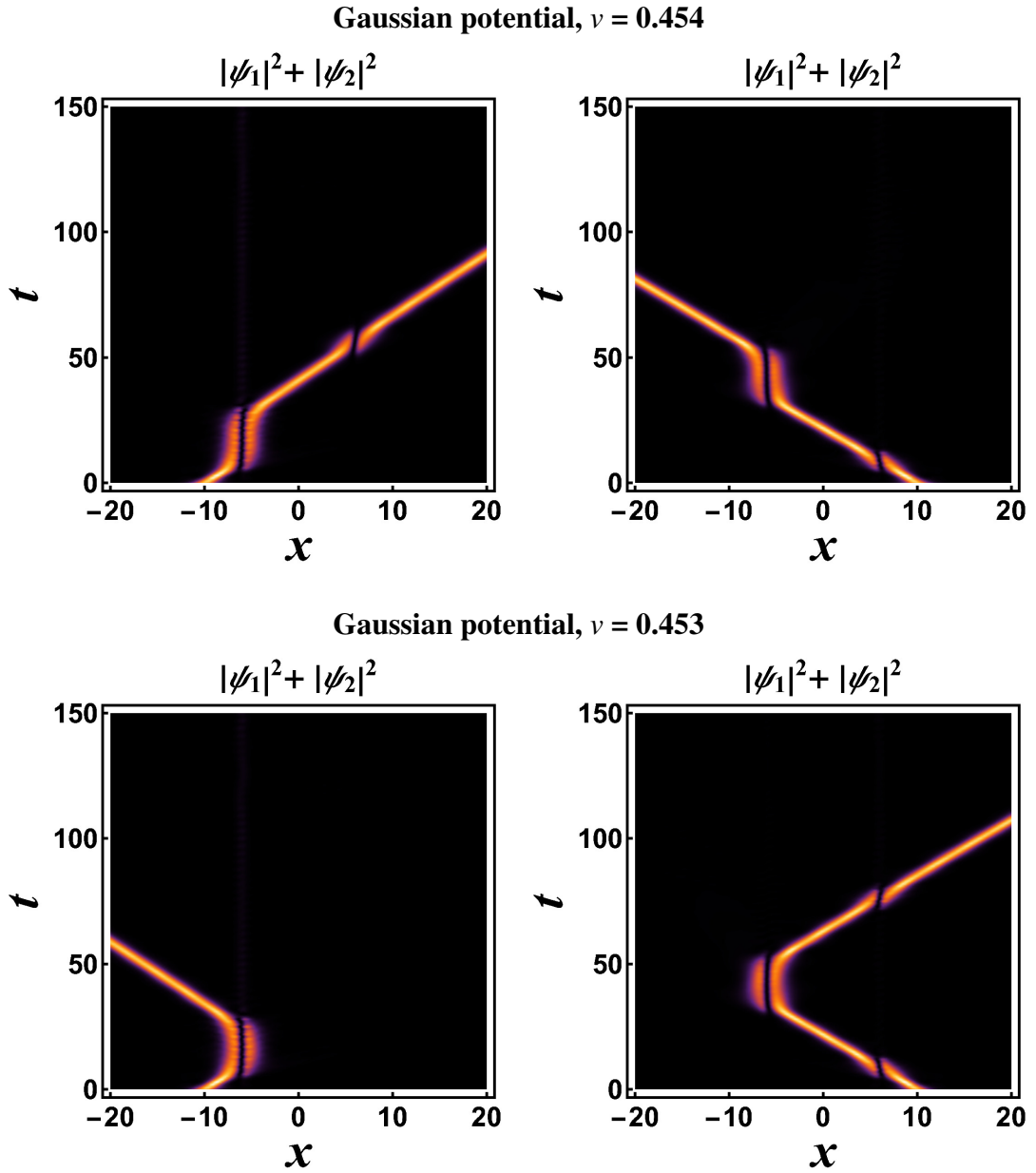


Figure D.5: Propagation of composite BB soliton through asymmetric Gaussian potential barriers for $g_{12} = 0.315$ with $g_1 = g_2 = 1$. Upper panel shows full transmission at $\nu = 0.454$ while lower panel shows full reflection at $\nu = 0.453$, from both left and right directions. There is no unidirectional flow in the range of coupling strength $0.313 \leq g_{12} \leq 0.316$.

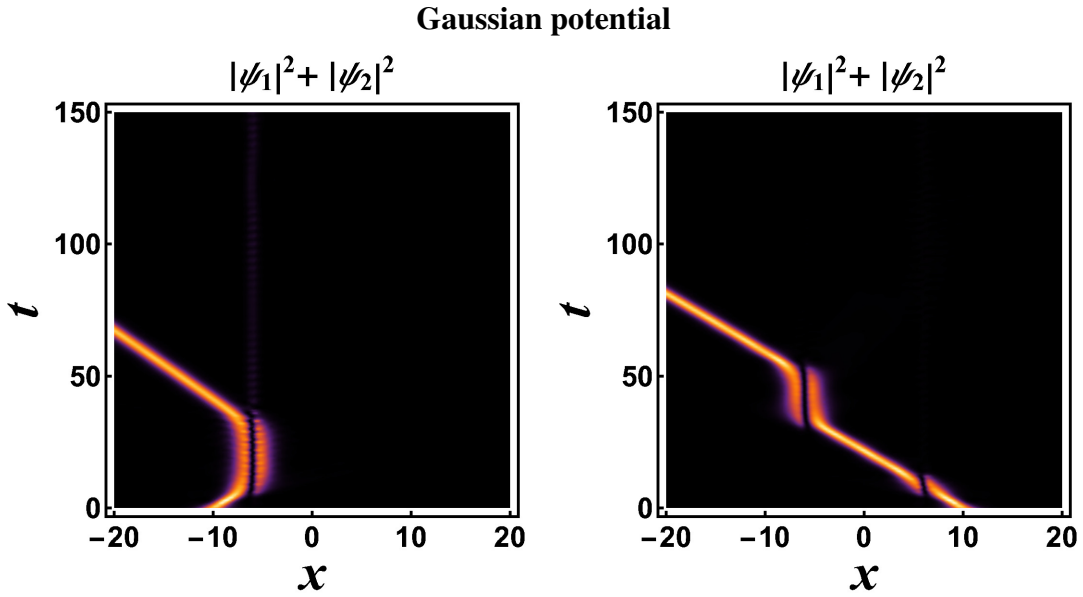


Figure D.6: Propagation of composite BB soliton through asymmetric Gaussian potential barriers for $g_{12} = 0.317$ with $g_1 = g_2 = 1$ at $v = 0.454$. Both components are identical. Left and right subfigures are results of initial propagation from $x_0 = -10$ and $x_0 = 10$, respectively. The polarity reversal phenomenon in unidirectional flow is achieved by comparing with Figure D.4

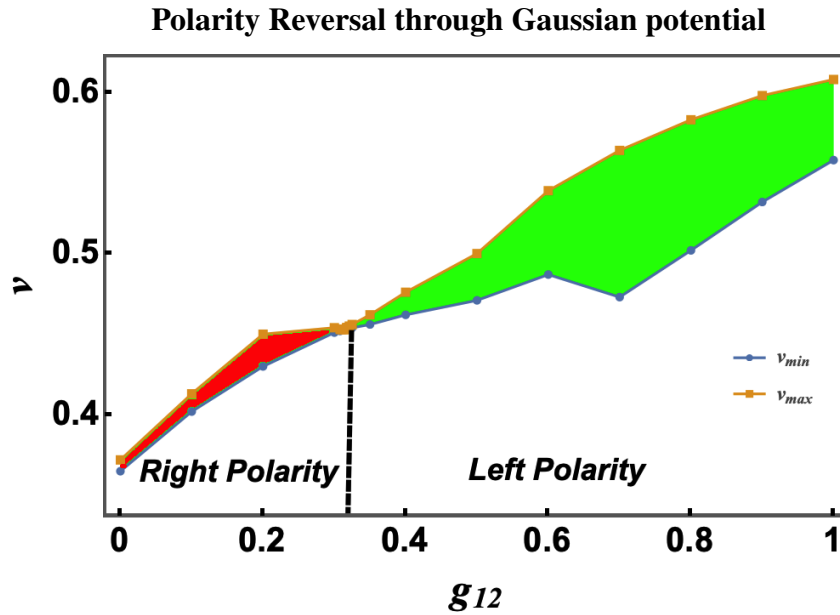


Figure D.7: Borders of velocity window for the unidirectional flow (v_{min}, v_{max}) vs g_{12} through the Gaussian potential barriers with $g_1 = g_2 = 1$. Full reflection for $v \leq 0.453$ and full transmission for $v \geq 0.454$ is obtained with the range of coupling strength $0.313 \leq g_{12} \leq 0.316$, hence no unidirectional flow is observed at this specific range of g_{12} . Away from this point of $g_{12} = 0.316$, we find polarity reversal in unidirectional flow. The shaded region shows the velocity window for the unidirectional flow. The red color shows the right polarity while the green color shows the left polarity of the unidirectional flow. The data used to generate this figure is listed in Table D.1.

D.3 Unidirectional Segregation with $g_{12} < 0$

Almost the same behavior is observed in the variation of reflection coefficients for the BB soliton components propagating through Gaussian potential barriers from $x_0 = \pm 10$ versus velocity and g_{12} values which is shown in Figure D.8.

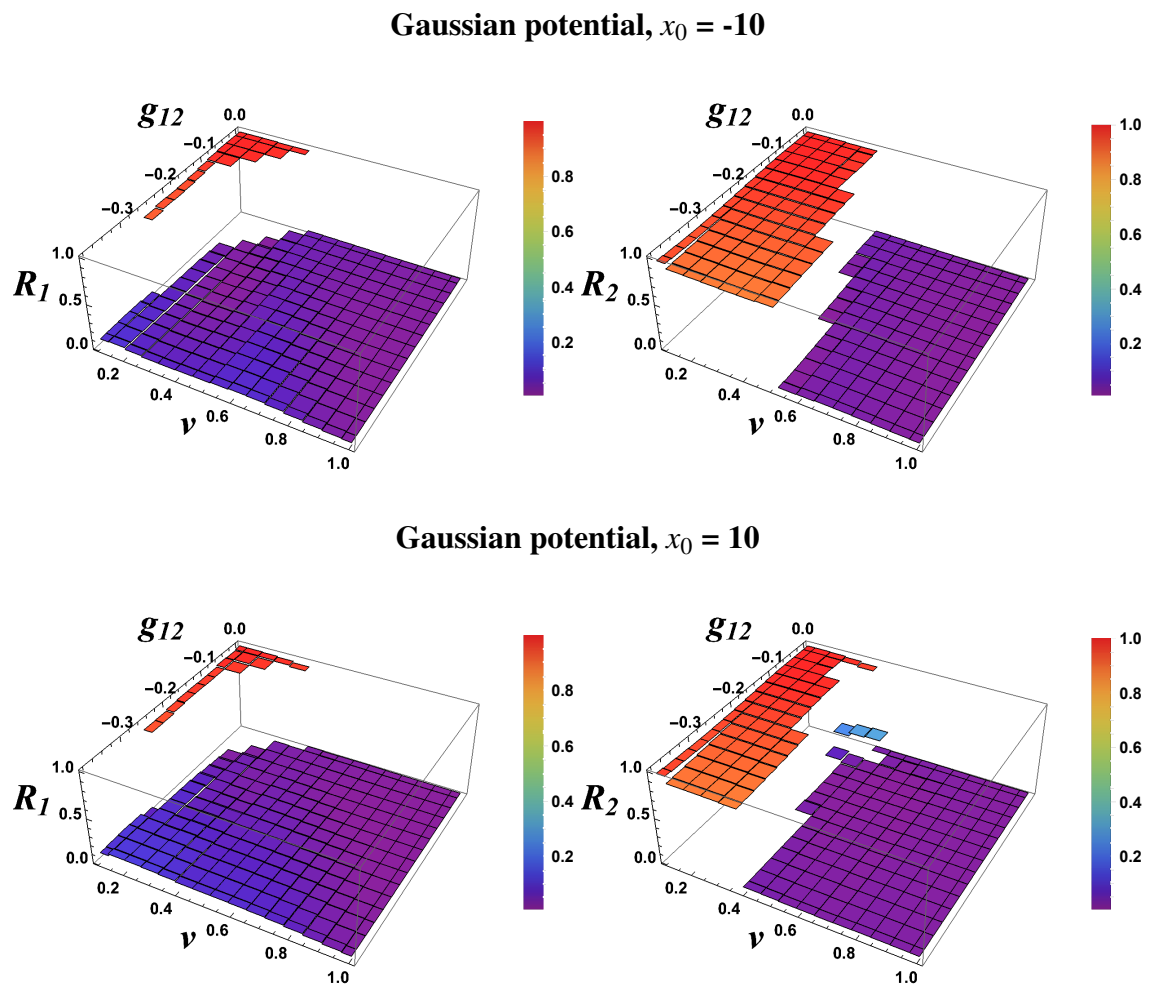


Figure D.8: Reflection coefficients of the components ψ_1 and ψ_2 propagating through Gaussian potential barriers from $x_0 = -10$ (upper two) and $x_0 = 10$ (lower two) versus v and g_{12} . Other parameters are $g_1 = g_2 = 1$.

Appendix E: Equations of Motion

Using the effective Lagrangian, Equation (6.11), the Euler–Lagrange equations lead to the following equations of motion for the variational parameters,

$$\begin{aligned}
& \frac{g_{12}N^2}{a^3} \operatorname{csch}^2\left(\frac{\xi_1 - \xi_2}{a}\right) \left[a - 4(\xi_1 - \xi_2) \coth\left(\frac{\xi_1 - \xi_2}{a}\right) \right] \\
& + \frac{g_{12}N^2}{a^4} (\xi_1 - \xi_2)^2 \operatorname{csch}^4\left(\frac{\xi_1 - \xi_2}{a}\right) \\
& \times \left[2 + \cosh\left(2\frac{\xi_1 - \xi_2}{a}\right) \right] + \frac{Nl_{01}}{2a^2} \left[-(q_2 + \xi_1) \operatorname{sech}^2\left(\frac{q_2 + \xi_1}{a}\right) \right. \\
& + (q_1 + \xi_1) \operatorname{sech}^2\left(\frac{q_1 + \xi_1}{a}\right) \\
& - (q_2 + \xi_2) \operatorname{sech}^2\left(\frac{q_2 + \xi_2}{a}\right) + (q_1 + \xi_2) \operatorname{sech}^2\left(\frac{q_1 + \xi_2}{a}\right) \left. \right] \\
& + \frac{Nl_{02}}{2a^2} \left[-(q_4 + \xi_1) \operatorname{sech}^2\left(\frac{q_4 + \xi_1}{a}\right) \right. \\
& + (q_3 + \xi_1) \operatorname{sech}^2\left(\frac{q_3 + \xi_1}{a}\right) - (q_4 + \xi_2) \operatorname{sech}^2\left(\frac{q_4 + \xi_2}{a}\right) \\
& + (q_3 + \xi_2) \operatorname{sech}^2\left(\frac{q_3 + \xi_2}{a}\right) \left. \right] \\
& + \frac{2N}{3a^3} - \frac{(g_1 + g_2)N^2}{6a^2} - \frac{1}{3}N\pi^2 a (2b^2 + b') = 0, \tag{E.1}
\end{aligned}$$

$$\begin{aligned}
& \frac{3g_{12}N^2}{a^2} \coth\left(\frac{\xi_1 - \xi_2}{a}\right) \operatorname{csch}^2\left(\frac{\xi_1 - \xi_2}{a}\right) \\
& + \frac{Nl_{01}}{2a} \left[-\operatorname{sech}^2\left(\frac{q_1 + \xi_1}{a}\right) + \operatorname{sech}^2\left(\frac{q_2 + \xi_1}{a}\right) \right] \\
& + \frac{Nl_{02}}{2a} \left[-\operatorname{sech}^2\left(\frac{q_3 + \xi_1}{a}\right) + \operatorname{sech}^2\left(\frac{q_4 + \xi_1}{a}\right) \right] \\
& - \frac{g_{12}N^2}{a^3} (\xi_1 - \xi_2) \operatorname{csch}^4\left(\frac{\xi_1 - \xi_2}{a}\right) \\
& \times \left[2 + \cosh\left(2\frac{\xi_1 - \xi_2}{a}\right) \right] + Nv'_1 = 0, \tag{E.2}
\end{aligned}$$

$$\begin{aligned}
& -\frac{3g_{12}N^2}{a^2} \coth\left(\frac{\xi_1 - \xi_2}{a}\right) \operatorname{csch}^2\left(\frac{\xi_1 - \xi_2}{a}\right) \\
& + \frac{Nl_{01}}{2a} \left[-\operatorname{sech}^2\left(\frac{q_1 + \xi_2}{a}\right) + \operatorname{sech}^2\left(\frac{q_2 + \xi_2}{a}\right) \right] \\
& + \frac{Nl_{02}}{2a} \left[-\operatorname{sech}^2\left(\frac{q_3 + \xi_2}{a}\right) + \operatorname{sech}^2\left(\frac{q_4 + \xi_2}{a}\right) \right] \\
& + \frac{g_{12}N^2}{a^3} (\xi_1 - \xi_2) \operatorname{csch}^4\left(\frac{\xi_1 - \xi_2}{a}\right) \\
& \times \left[2 + \cosh\left(2\frac{\xi_1 - \xi_2}{a}\right) \right] + Nv'_2 = 0, \tag{E.3}
\end{aligned}$$

$$-Nv_1 - N\xi'_1 = 0, \tag{E.4}$$

$$-Nv_2 - N\xi'_2 = 0, \tag{E.5}$$

$$-\frac{2}{3}N\pi^2 a^2 b + \frac{1}{3}N\pi^2 a d' = 0. \tag{E.6}$$